

University of Warwick institutional repository: <http://go.warwick.ac.uk/wrap>

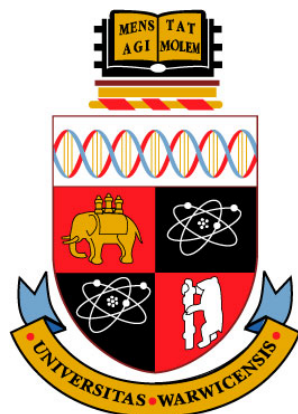
A Thesis Submitted for the Degree of PhD at the University of Warwick

<http://go.warwick.ac.uk/wrap/34621>

This thesis is made available online and is protected by original copyright.

Please scroll down to view the document itself.

Please refer to the repository record for this item for information to help you to cite it. Our policy information is available from the repository home page.



**Multinuclear Solid State NMR of Novel Bioactive
Glass and Nanocomposite Tissue Scaffolds**

by
Claudia Adriana Turdean-Ionescu

Thesis

Submitted to the University of Warwick

for the degree of

Doctor of Philosophy

Department of Physics

October 2010

THE UNIVERSITY OF
WARWICK

CONTENTS

CONTENTS	ii
LIST OF TABLES	v
LIST OF FIGURES	vi
ACKNOWLEDGEMENTS	x
DECLARATIONS	xi
ABSTRACT	xiii
ABBREVIATIONS	xiv
1	1
INTRODUCTION	1
1.1. Bioactive materials.....	1
1.1.1. Historical background	1
1.1.2. Bone structure	2
1.1.3. Bioactive glasses	3
1.1.3.1. Melt-derived bioactive glasses.....	4
1.1.3.2. Sol-gel derived bioactive glasses	4
1.1.4. Glass structure and bioactivity	6
1.1.5. Bioactive reaction mechanism of HCA layer deposition: Hench's hypothesis.....	8
1.2. Sol-gel method, a non-conventional route to obtain biomaterials	11
1.2.1. Sol-gel hydrolysis and condensation reactions	11
1.2.1.1. Precursors	12
1.2.1.2. Water-to-alkoxide ratio (R).....	13
1.2.1.3. Effect of catalysts.....	13
1.2.1.4. Steric and inductive effects	14
1.2.1.5. Solvent effects.....	15
1.2.1.6. Transesterification, reesterification, and hydrolysis	15
1.2.2. Mechanism of reactions	16
1.2.3. Structural evolution	18
1.3. Characterisation methodology	19
2	23
NMR THEORETICAL BACKGROUND	23
2.1. Introduction	23
2.2. The NMR Hamiltonian	23
2.3. Internal interaction mechanisms	25
2.3.1. The chemical shift interaction.....	25
2.3.2. Dipole-dipole coupling	28
2.3.3. The J-coupling.....	30
2.3.4. The nuclear electric quadrupole interaction.....	31
2.4. Magic angle spinning (MAS).....	34
2.5. Combined rotation and multiple-pulse spectroscopy	36
2.6. Cross-polarisation	37
2.7. Two-dimensional methods	40
2.8. Relaxation mechanism	42
3	45

EXPERIMENTAL ASPECTS	45
3.1. Introduction	45
3.2. NMR experimental setup	45
3.3. Pulse sequences	48
3.3.1. Single pulse experiment	49
3.3.2. Pulsed echo experiment	50
3.3.3. Cross polarisation and heteronuclear decoupling	51
3.3.4. Homonuclear decoupling	53
3.3.5. Two-dimensional NMR techniques	54
3.3.5.1. Homonuclear correlation	54
3.3.5.2. Heteronuclear correlation	57
3.3.5.3. Multiple-quantum MAS (MQMAS)	59
3.4. Experimental parameters of NMR nuclei	61
3.5. Synthesis of sol-gel derived biomaterials	66
3.5.1. Sol-gel synthesis of 70S30C bioactive glasses	67
3.5.2. Sol-gel synthesis of 58S bioactive glasses	68
3.5.3. Organic-inorganic nanocomposite scaffolds	69
3.5.3.1. Silica-gelatin hybrid scaffolds	69
3.5.3.2. Silica-calcium oxide- (γ -PGA) organic-inorganic hybrids	70
3.6. Bioactive media used to test in-vitro bioactivity	71
4	73
SOL-GEL 70S30C BIOACTIVE GLASSES	73
4.1. Introduction	73
4.2. Experiment details	74
4.3. Results and discussion	75
4.3.1. Nanostructure evolution of 70S30C sol-gel bioactive glasses	75
4.3.2. Inhomogeneity characterisation in 70S30C sol-gel bioactive glasses	85
4.3.3. Tailoring the nanoporosity of 70S30C sol-gel derived bioactive glasses by using trimethylethoxysilane	89
4.4. Conclusions	98
5	100
SOL-GEL 58S (SiO₂-CaO-P₂O₅) DERIVED BIOACTIVE GLASSES	100
5.1. Introduction	100
5.2. Experimental details	101
5.3. Results and discussion	101
5.4. Conclusions	126
6	128
ORGANIC-INORGANIC NANOCOMPOSITE SCAFFOLDS	128
6.1. Introduction	128
6.2. Experiment details	129
6.3. Results and discussion	130
6.3.1. Class I and class II of organic-inorganic hybrid nanocomposites in the SiO ₂ -gelatin systems	130
6.3.2. Silica-calcium oxide- (γ -PGA) organic-inorganic hybrids	147
6.4. Conclusions	157
7	159
INHIBITIVE EFFECT OF SERUM PROTEINS IN THE MECHANISM OF APATITE GROWTH ON BIOACTIVE GLASSES	159
7.1. Introduction	159

7.2. Experiment details.....	160
7.3. Results and discussion	161
7.4. Conclusions	185
8	187
OVERALL CONCLUSIONS AND FUTURE DIRECTIONS	187
8.1. Overall conclusions.....	187
8.2. Future directions	190
9	192
REFERENCES.....	192

LIST OF TABLES

Table 3.1. NMR parameters for different transitions of a quadrupolar nucleus with $I = 3/2$.	59
Table 3.2. Physical properties of the NMR nuclei studied in this thesis	61
Table 3.3. Primary reference compounds for the isotopes studied.	65
Table 3.4. The dosage of trimethylethoxysilane per 35 ml of normal 70S30C of TMS-A and TMS-B sub-groups (TT represents the mole ratio of TMES/TEOS).	68
Table 3.5. Concentration (mM) and pH of SBF and human plasma	72
Table 4.1. Amount of hydrogen in mol/g of samples as determined by ^1H NMR.	76
Table 4.2. ^{29}Si MAS NMR data for measured samples, giving the spectral deconvolution into different Q^n species.	78
Table 4.3. ^{29}Si CP MAS NMR data at a contact time of 5 ms of SiO_2 -CaO sol-gel samples (xerogels and thermal treated samples).	78
Table 4.4. Hydrogen content in mol/g calculated from ^1H MAS NMR spectra.	87
Table 4.5. ^{29}Si MAS NMR data of 70S30C bioactive glass (traditional method), giving the spectral deconvolution into different Q^n species.	88
Table 4.6. ^{29}Si MAS NMR data for measured samples, giving the spectral deconvolution into different Q^n species.	88
Table 4.7. The H contents of non-stabilised and stabilised TMS-70S30C and T-70S30C calculated from ^1H NMR spectra.	92
Table 5.1. The hydrogen content and peak position as determined from ^1H NMR spectra.	102
Table 5.2. Peak position from ^{13}C CP MAS NMR spectra.	109
Table 5.3. ^{31}P MAS NMR data for measured samples, giving the spectral deconvolution into different species.	114
Table 5.4. ^{29}Si MAS NMR data for measured samples, giving the spectral deconvolution into different Q^n species.	121
Table 6.1. ^{29}Si MAS NMR data of class I and class II organic-inorganic hybrids, giving the spectral deconvolution into different T^n and Q^n species.	131
Table 6.2. ^{29}Si MAS NMR data of class II silica-calcium oxide- γ -PGA hybrids, giving the spectral deconvolution into different T^n and Q^n species.	149
Table 7.1. ^{31}P MAS NMR data for measured samples, giving the spectral deconvolution into different species.	165
Table 7.2. ^{29}Si MAS NMR data for measured samples, giving the spectral deconvolution into different Q^n species.	174
Table 7.3. ^{23}Na MQMAS data of BG sample.	184

LIST OF FIGURES

Figure 1.1. Hierarchical organization of bone.	2
Figure 1.2. (a) Crystalline silica, (b) Amorphous silica, (c) Effect of introduction of Ca^{2+} cations in a silica network.....	7
Figure 1.3. Schematic of osteoblast cell cycle.	10
Figure 1.4. The $\text{R}'_n\text{Si}(\text{OEt})_f$ functionality spectrum	13
Figure 1.5. Inductive effects of substituents attached to silicon.	15
Figure 1.6. Scheme of acid-catalyzed gel (a), desiccated xerogel (b).....	18
Figure 1.7. Scheme of base-catalyzed gel (a), desiccated xerogel (b).	18
Figure 1.8. Summary of the various methods for investigating the structure, texture and bioactivity of sol-gel derived bioactive materials.	20
Figure 2.1. Energy level diagram for $I = 1/2$	24
Figure 2.2. Typical chemical shift-dominated NMR powder patterns.....	28
Figure 2.3. Powder pattern lineshape for a pair of through space dipole-dipole coupled spin $1/2$ nuclei.....	30
Figure 2.4. Schematic energy level diagram for a spin $I = 3/2$ nucleus showing the effect of the Zeeman, first-order and second-order quadrupolar interactions upon the four energy levels.....	32
Figure 2.5. The effect of the first-order quadrupolar interaction to the NMR lineshape for a nucleus with spin $I = 3/2$	33
Figure 2.6. Schematic representation of the MAS experiment.	35
Figure 2.7. The effect of the second-order quadrupolar interaction	36
Figure 2.8. (a) Schematic representation of the CP sequence for $^1\text{H} \rightarrow \text{X}$. (b) The changes of the energy levels from the laboratory frame and in the rotating frame ...	38
Figure 2.9. Time intervals in a basic two-dimensional experiment.	41
Figure 2.10. Schematic 2D (a) SQ-SQ and (b) DQ-SQ correlation spectra.	42
Figure 3.1. a) The basic components of a pulsed FT NMR spectrometer and b) The relationship between the time and frequency domains of an r.f. pulse of frequency ν_0 (Hz) and duration τ_p	46
Figure 3.2. A single pulse sequence.....	49
Figure 3.3. A pulse echo sequence.....	51
Figure 3.4. Cross polarisation (CP) pulse sequence.....	52
Figure 3.5. Pulse sequence of continuous 1D windowed homonuclear decoupling for obtaining a directly detected high-resolution ^1H spectrum.	54
Figure 3.6. Pulse sequences for the symmetry-based POST-C7 sequence.	56
Figure 3.7. Pulse sequence and coherence transfer pathway diagram for the ^1H DQ CRAMPS	56
Figure 3.8. Pulse sequence and coherence transfer pathway diagram for the SQ-SQ HETCOR.....	58
Figure 3.9. MQMAS pulse sequence and the coherence pathways.	60
Figure 3.10. Q^n species in sol-gel silicate glasses.....	63
Figure 3.11. T^n species in silicate glasses obtained by sol-gel process.....	63
Figure 3.12. Phosphate tetrahedral sites that can exist in phosphate glasses.....	64
Figure 3.13. The structure of alkoxides used in the sol-gel synthesis.....	66
Figure 3.14. Process flow chart for the synthesis of 70S30C sol-gel derived glasses.	67
Figure 3.15. Schematic of the reactions for the hybrid synthesis.	70

Figure 3.16. Calcium salt form of γ -PGA.	71
Figure 4.1. ^1H MAS NMR spectra of 100S no stabilization, 70S no stabilization, 100S (x4) and 70S30C (x8).	76
Figure 4.2. ^{29}Si MAS NMR spectra of 100S, and 70S30C, respectively, not stabilised and stabilised samples.	77
Figure 4.3. Fit of the 100S Non-stabilised: (a) difference between spectrum and simulation, (b) deconvolution in 3 peaks, (c) spectrum and (d) the simulation.	79
Figure 4.4. ^{29}Si CP MAS NMR spectra of 100S, and 70S30C, respectively, non stabilised and stabilised samples, at a contact time of 5 ms.	81
Figure 4.5. ^{13}C CP MAS NMR spectra of 100S (a), and 70S30C (b), respectively, not stabilised samples, at a contact time of 5 ms.	83
Figure 4.6. Schematic illustration of evolution of calcium distribution.	84
Figure 4.7. Cross-section of a 70S30C monolith.	85
Figure 4.8. ^1H MAS NMR spectra of samples taken from the translucent and opaque regions of traditional 70S30C monoliths.	86
Figure 4.9. ^{29}Si MAS NMR spectra of samples in the translucent and opaque regions of traditional 70S30C monoliths.	87
Figure 4.10. ^{29}Si MAS NMR spectra of non-stabilised TMS-B4 and the two components (upper and lower) observed in non-stabilised TMS-A4.	90
Figure 4.11. ^1H MAS NMR spectra of non-stabilised TMS-B4 and the two components (upper and lower) observed in non-stabilised TMS-A4.	91
Figure 4.12. ^1H MAS NMR spectra of non-stabilised TMS-B samples with different TT ratio.	92
Figure 4.13. ^{29}Si MAS NMR spectra of non-stabilised T-70S30C and TMS-B series samples with various TT ratio.	93
Figure 4.14. ^1H MAS NMR spectra of stabilised TMS-A4 upper, TMS-B2 and T-70S30C samples.	95
Figure 4.15. ^{29}Si MAS NMR spectra of stabilised TMS-A4 upper, TMS-B2 and T-70S30C samples.	96
Figure 4.16. Schematic illustration of ‘‘nano-cluster’’ formed by excessive TMES in the sol of TMS-B2 [3].	97
Figure 5.1. ^1H MAS NMR spectra of 58S samples synthesised via inorganic route.	102
Figure 5.2. ^1H MAS NMR spectra of 58S samples synthesised via alkoxide route (a and b).	103
Figure 5.3. ^{13}C CP MAS NMR spectra of 58S samples synthesised from nitrate as calcium precursor,	107
Figure 5.4. ^{13}C CP MAS NMR spectra of 58S samples synthesised from CME as calcium precursor (a) and the carbonate region (b).	108
Figure 5.5. Possible surface carbonate-like species.	109
Figure 5.6. ^{31}P MAS NMR spectra of 58S Nitrate samples.	113
Figure 5.7. A comparison between ^{31}P MAS and ^{31}P CP MAS spectra of 58S Nitrate 130 (a) and 58S Nitrate 400 (b) samples, respectively.	113
Figure 5.8. The ^{31}P MAS NMR spectra of samples synthesised via alkoxide route.	118
Figure 5.9. ^{29}Si MAS NMR spectra of 58S samples synthesised by inorganic (a) and alkoxide (b) routes.	120
Figure 6.1. ^{29}Si MAS NMR spectra of silica-gelatin, class I hybrids.	130

Figure 6.2. ^{29}Si MAS NMR spectra of class II silica-gelatin hybrids with 30% (a) and 60% (b) of gelatin for different C factors.....	134
Figure 6.3. ^{13}C CP MAS NMR spectra of class I hybrids.	136
Figure 6.4. The structures of the most representative amino acids in the gelatin molecules	137
Figure 6.5. ^{13}C CP MAS NMR spectra of class II organic-inorganic hybrids containing 30% gelatin.....	138
Figure 6.6. ^{13}C CP MAS NMR spectra of class II hybrid nanocomposites containing 60% gelatin in silica matrix for different C factors.....	138
Figure 6.7. (a) ^1H MAS NMR spectra at 12.5 kHz of silica-gelatin class I hybrids. (b) A comparison between spectra obtained at 12.5 kHz, 30 kHz and CRAMPS for the 60G sample.	140
Figure 6.8. Homonuclear decoupled spectra using DUMBO-1 for 60% gelatin in a silica network	141
Figure 6.9. ^1H MAS NMR spectra recorded at 30 kHz (a) and homonuclear-decoupled spectra using windowed DUMBO-1 at 12.5 kHz (b) of hybrids with 30% gelatin.....	142
Figure 6.10. Two-dimensional ^1H (500 MHz) DQ CRAMPS spectrum of hybrids with C-factor 0 (a) and 500 (b) for 30% gelatin.....	144
Figure 6.11. Two-dimensional ^1H (500 MHz) DQ CRAMPS spectrum of hybrids with C-factor 0 (a) and 1500 (b) for 60% gelatin.....	145
Figure 6.12. ^{29}Si MAS NMR spectra of (a) hybrids for X_{EC} ranging from 1 to 100 using HF as catalyst and (b) a comparison between gels made with HF, at room temperature and 60 °C with and without calcium for $X_{\text{EC}}=2$	148
Figure 6.13. ^{13}C CP MAS NMR of silica-CaO-(γ -PGA) hybrids for $X_{\text{EC}}=1$ gelled with HF at room temperature and at 60 °C (a) and for different X_{EC} (1, 2, 5 and 10) gelled with HF (b).	151
Figure 6.14. ^{13}C CP MAS NMR of silica-(γ -PGA) hybrids without calcium for $X_{\text{EC}}=2$ gelled with HF at room temperature and at 60 °C.	152
Figure 6.15. ^1H MAS NMR spectra of (a) hybrids for X_{EC} ranging from 1 to 10 using HF as catalyst and (b) hybrids made with HF, at room temperature and 60 °C without calcium for $X_{\text{EC}}=2$	153
Figure 6.16. (a) A comparison between ^{13}C CP MAS NMR spectra for $X_{\text{EC}}=2$ when CaCl_2 (2ECCa RT) and calcium salt of γ -PGA (2EC CaPGA Aged) have been used and (b) ^1H MAS at 12.5 kHz and CRAMPS using windowed DUMBO-1 sequence spectra of 2EC CaPGA aged sample.....	155
Figure 6.17. ^{43}Ca MAS NMR of silica-CaO-PGA hybrids when CaCl_2 and CaPGA have been used	156
Figure 7.1. ^1H MAS NMR spectra of BG (a) and TG (b) glasses, as synthesised and immersed in pSBF and sSBF for 2h, 1d and 7d, respectively.....	161
Figure 7.2. ^{13}C CP MAS NMR spectra of TG and BG glasses (a), with the carbonate and organic carbonyl region (b) fitted (dash lines).	163
Figure 7.3. ^{31}P MAS NMR spectra of BG (a) and TG (b) for different soaking times in SBF.	166
Figure 7.4. The variation of linewidths (ppm) of the 3 ppm resonance with soaking time (h) in pSBF and sSBF for BG and TG samples.	168
Figure 7.5. ^1H - ^{31}P HETCOR of pSBF 7d TG (a) and sSBF 7d TG (b).....	169
Figure 7.6. ^{29}Si MAS NMR spectra of BG (a) and TG (b) as-synthesised and immersed in SBF for different periods of time.	173

Figure 7.7. ^1H - ^{29}Si HETCOR spectra of pSBF 7d TG (a) and sSBF 7d TG (b) samples.....	178
Figure 7.8. ^{23}Na MAS NMR spectra recorded at 14.1 T and a spinning speed of 10 kHz for the BG sample, as-received and immersed in pSBF and sSBF	180
Figure 7.9. ^{23}Na MAS NMR spectra recorded at 14.1T and a spinning speed of 10 and 20 kHz for BG and pSBF 2h BG samples.....	182
Figure 7.10. ^{23}Na MQMAS spectra recorded at 14.1 T and a spinning speed of 20 kHz of BG (a) and pSBF 2h BG (b) samples.....	183
 Scheme 6.1. The possibilities for the reactions of the epoxide group.....	 133

ACKNOWLEDGEMENTS

This work would not have been possible without the help of many people and their knowledge shared with me.

First, I would like to express my sincere appreciation to my supervisors, Prof. Mark E. Smith and Dr. John V. Hanna, for their insightful support throughout this research effort which was such a rewarding experience.

Most cordial thanks go to Dr. Kevin Pike for introducing me in the solid-state NMR field and for his friendship and to Dr. Andrew Howes for giving me both technical and moral support. I would like to express my appreciation to Prof. Christian Bonhomme from University Pierre and Marie Curie, Paris for all his support and help during my last months at Warwick. I am also very thankful to all my colleagues from the NMR group who helped me throughout my PhD, such as Dr. Thomas Kemp, Dr. Dinu Iuga, Dr. Amy Webber, Jonathan Bradley and Dr. Eugeny Kryukov.

Dr. Julian Jones' group, in particular Dr. Sen Lin, Dr. Gowsihan Poologasundarampillai, Oliver Mahony, Bobo Yu and Esther Valliant from Imperial College, London, is gratefully acknowledged for a fruitful collaboration and for providing me with such high quality samples.

The financial support offered by the University of Warwick through a postgraduate research scholarship is greatly acknowledged. EPSRC is thanked for funding the work on sol-gel bioactive glasses.

My last and warmest thanks go to my husband, my parents and my brother who supported me with their love and patience, for a much longer period than three years.

Thank you!

DECLARATIONS

The work contained in this thesis was carried out in the Department of Physics of the University of Warwick from July 2007 to July 2010, under the supervision of Professor Mark E. Smith and Dr. John V. Hanna. It is the result of my own independent research except where specifically referenced in the text and has not been previously submitted for any other degree.

The results presented throughout Chapter 4 have been published [1-3], while parts of the results from Chapter 6 have been published or submitted to publications [4-6]. A complete list of publications to which the author has contributed during this project is given below:

1. S. Lin, C. Ionescu, K. J. Pike, M. E. Smith, J. R. Jones, Nanostructure evolution and calcium distribution in sol–gel derived bioactive glass, *J. Mater. Chem.*, **2009**, *19*, 1276-1282.
2. S. Lin, C. Ionescu, S. Baker, M. E. Smith, J. R. Jones, Characterisation of the inhomogeneity of sol–gel-derived SiO₂–CaO bioactive glass and a strategy for its improvement, *J. Sol-Gel Sci. Technol.*, **2010**, *53*, 255-262.
3. S. Lin, C. Ionescu, E. M. Valliant, J. V. Hanna, M. E. Smith, J. R. Jones, Tailoring the nanoporosity of sol–gel derived bioactive glass using trimethylethoxysilane, *J. Mater. Chem.*, **2010**, *20*, 1489-1496.
4. O. Mahony, O. Tsigkou, C. Ionescu, C. Minelli, L. Ling, R. Hanly, M. E. Smith, M. M. Stevens, J. R. Jones, Silica-Gelatin Hybrids with Tailorable Degradation and Mechanical Properties for Tissue Regeneration, *Adv. Funct. Mater.*, **2010**, *20*, 3835-3845.
5. G. Poologasundarampillai, C. Ionescu, O. Tsigkou, M. Murugesan, R. G. Hill, M. M. Stevens, J. V. Hanna, M. E. Smith J. R. Jones, Synthesis of bioactive class II

poly(γ -glutamic acid)/silica hybrids for bone tissue regeneration, *J. Mater. Chem.*, **2010**, *20*, 8952-8961.

6. G. Poologasundarampillai, B. Yu, S. Yue, P. D. Lee, C. Ionescu, J. V. Hanna, M. E. Smith, R. D. Hamilton, T. Kasuga, J. R. Jones, Inorganic/organic hybrid nanocomposite scaffolds for bone regeneration, submitted to *Biomaterials*.

Other papers are under preparation and will be submitted for publication in the near future.

ABSTRACT

Sol-gel derived bioactive glasses are promising candidates for bone regeneration, where bone is a natural nanocomposite of collagen (organic polymer) and hydroxyapatite (inorganic mineral) with a complex hierarchical structure and excellent mechanical properties. Solid-state NMR is a sensitive probe and offers atomic-level information on the structure of sol-gel derived bioactive glasses. In this thesis, a multinuclear solid state NMR approach, as part of an extensive study, has been applied to a key range of sol-gel derived materials related to novel nanocomposites to act as tissue scaffolds.

The nanostructure evolution of sol-gel derived bioactive glasses 70S30C (70 mol% SiO₂ and 30 mol% CaO) was characterised by ²⁹Si, ¹H and ¹³C CP MAS NMR. Calcium was found to be incorporated into the silica network during the stabilisation stage and to increase its disorder. The inhomogeneity found within 70S30C bioactive glass monoliths showed that the calcium concentration was higher in the outer region of the monolith caused by the way calcium only enters into the structure after breakdown of the nitrate. Trimethylsilylation reaction mechanisms used to tailor the nanoporosity of sol-gel derived 70S30C bioactive glass was also studied. The ²⁹Si NMR results showed that the modification processes affected the atomic scale structure of the glass, such as Qⁿ structure and network connectivity. ¹H and ¹³C NMR was used to follow the loss of hydroxyls and organic groups directly.

The study was extended to 58S (60 mol% SiO₂, 36 mol% CaO, 4 mol% P₂O₅) systems and compared for two synthesis routes: inorganic and alkoxide. Via the inorganic route high temperatures were needed for calcium incorporation, while via alkoxide route calcium was found to be incorporated at low temperatures. Reactive surface Ca ions were involved in the formation of different types of carbonates for the two routes. The addition of P₂O₅ to the silica-calcium oxide system results in a scavenging of calcium ions by phosphate groups to give orthophosphate and pyrophosphate units.

Solid-state NMR of new organic-inorganic hybrid scaffolds, class II, in the silica-gelatin and silica-calcium oxide-poly(γ -glutamic acid) (γ -PGA) systems indicates that 3-glycidoxypropyltrimethoxysilane (GPTMS) provides a covalent link between the organic and inorganic networks and increased the inorganic condensation. ¹H-¹H intra- and intermolecular proximities have been identified using ¹H DQ (double-quantum) CRAMPS (combined rotation and multiple pulse spectroscopy) techniques. ¹³C NMR results indicate that an efficient promotion of epoxide ring opening of GPTMS was reached by either gelatin or γ -PGA. ⁴³Ca NMR identified different calcium environments in the hybrid systems.

The last part of this thesis is focused on the comparison studies in the mechanism of apatite growth on both melt-derived (*Bioglass*[®]) and sol-gel derived (*TheraGlass*[®]) bioactive glass surfaces. By using a combination of ¹H, ¹³C, ³¹P, ²⁹Si and ²³Na, using one and two dimensional NMR spectroscopy, the inhibitive effects of serum proteins in the mechanism of the apatite growth was revealed. The solid-state NMR experimental data support the hydroxycarbonate apatite formation mechanism proposed by Hench. Apatite formation takes place from the largely amorphous phosphate ions initially deposited on the glass surface. Serum proteins adsorbed on the glass surface have been found to significantly inhibit the apatite formation. Multiple sodium sites have been identified in *Bioglass*[®] composition with the formation of a more ordered local structure on increasing immersion time.

ABBREVIATIONS

1D, one dimensional;
2D, two dimensional;
ADC, analogue-to-digital converter
CME, calcium methoxyethoxide;
CP, cross polarisation;
CRAMPS, combined rotation and multiple-pulse spectroscopy;
CS, chemical shielding;
CSA, chemical shift anisotropy;
CT, central transition;
CYCLOPS, cyclically ordered phase sequence;
DQ / DQC, double quantum coherence;
DTA, differential thermal analysis;
DUMBO, decoupling under mind bogging optimisation;
EFG, electric field gradient;
EXAFS, extended X-ray absorption fine structure;
FID, free induction decay;
FT, Fourier transform;
FSLG, frequency-switched Lee-Goldburg;
FWHM, full-width half-maximum;
GPTMS, 3-glycidoxypropyltrimethoxysilane;
HAp, hydroxyl apatite;
HCA, hydroxycarbonate apatite;
HETCOR, heteronuclear correlation;
ICP, inductive coupled plasma;
INEPT, insensitive nuclear enhancement by polarisation transfer;
IR, infra red;
LG, Lee-Goldburg;
MAS, magic angle spinning;
MQ, multiple quantum;
NBO, non bridging oxygen

NMR, nuclear magnetic resonance;
PAS, principal axis system;
PCL, poly(ϵ -caprolactone);
PEO, poly(ethylene oxide);
 γ -PGA, poly(γ -glutamic acid);
PMLG, phase-modulated Lee-Goldburg;
PMMA, poly(methylmethacrylate);
POST-C7, permutationally offset stabilized C7;
PVA, poly(vinylalcohol);
r.f., radio-frequency;
SBF, simulated body fluid;
s/n, signal to noise;
SPINAL, small phase incremental alternation;
SQ, single-quantum;
ST, satellite transition;
TEOS, tetraethylorthosilicate;
TEP, triethylphosphate;
TGA, thermogravimetric analysis;
TMES, trimethylethoxysilane
TPPI, two pulse phase incremented;
TT ratio, TMES:TEOS ratio;
UV-VIS, ultraviolet visible;
XANES, X-ray absorption near edge structure

1.

INTRODUCTION

1.1. Bioactive materials

1.1.1. Historical background

“A bioactive material is one that elicits a specific biological response at the interface of the material which results in the formation of a bond between the tissues and the material” [7]. Historically, the function of biomaterials has been to *replace* diseased or damaged tissues. The objective of the first man-designed biomaterials for bone and tooth repair was bio-inertness, owing to their absent or weak interaction with living tissues upon implantation. Usually denoted as *first generation biomaterials*, they were investigated from the beginnings of 1960s and included metals or alloys (titanium, stainless steel, cobalt–chrome) and dense or porous ceramics (Al_2O_3 (alumina) and ZrO_2 (zirconia)) [8]. Alumina and zirconia are still used in surgical implants for the manufacture of prostheses components where inertness and other specific properties such as wear resistance are required [9].

The *second generation biomaterials* developed around 1970 [7]. The aim of these bioceramics was a favourable interaction with the living body, a bioactive and/or resorbable behaviour. The most significant second generation bioceramics are crystalline calcium phosphates, bioactive glasses and glass-ceramics clinically used for applications such as the bone tissue augmentation, bone cements or the coating of metallic implants [10-17].

At the end of the 20th Century, it was clear that bioceramics by themselves could not give a complete response to the clinical needs of biomaterials for implants. Bioceramics with more demanding properties were required. This led to the arrival of so-called *third generation bioceramics* able to induce regeneration and repair of living tissues based on gene activation [18-22]. Therefore, the concept replacement of tissues has been substituted with regeneration of tissues.

Second and third generation of biomaterials are called *bioactive glasses*.

Before discussing *bioactive glasses* in more details, the structure of bone and general issues related to orthopaedic applications are presented in the next section.

1.1.2. Bone structure

The match of the materials elastic properties with bone properties is difficult, since the structure of bone is quite complex [23], therefore it is important to understand its structure. Figure 1.1 shows the hierarchical structure of bone.

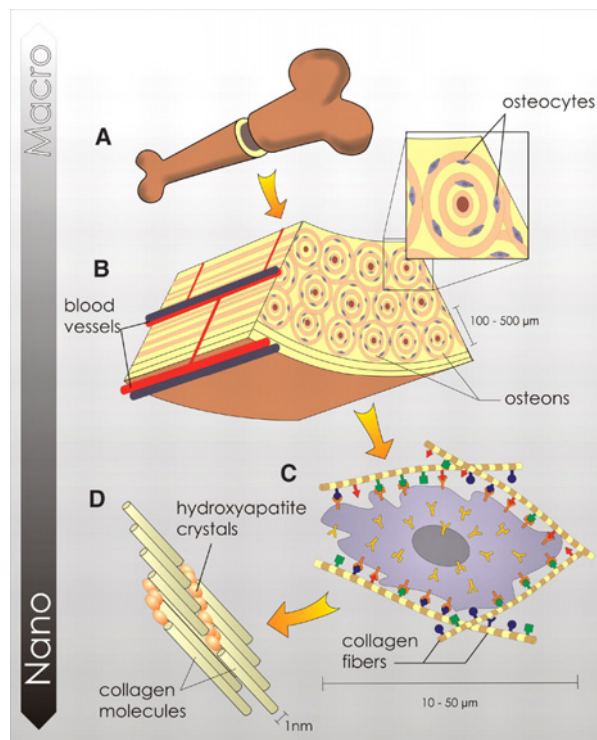


Figure 1.1. Hierarchical organization of bone [24].

Bone matrix is a natural composite of collagen (polymer) and bone mineral (ceramic). Collagen is a triple helix of protein chains that has high tensile and flexural strength. Bone mineral is a crystalline calcium phosphate ceramic (hydroxycarbonate apatite, HCA) that provides the stiffness and high compressive strength of bone (D). The most internal part of bone contains the *marrow*, where stem cells are, which can give rise to all types of blood cells. The resident cells are coated in a forest of cell membrane receptors that respond to specific binding sites (C) and the well-defined nanoarchitecture of the surrounding extracellular matrix. The two most important types of bone are cortical and cancellous bone. Cortical

bone also known as compact bone surrounds the marrow and is a dense structure with high mechanical strength (A). In compact bone, parallel rods of collagen and apatite are bundled together, arranged in circles around the *harvesian channels*, or *osteons* where blood vessels and nerves pass (B). Near the end of the bone, at the bonehead, a less dense type of bone is found, called *cancellous*, or *trabecular*, *spongy bone* [24, 25].

The process of bone regeneration (osteogenesis) involves two types of cells: *osteoblasts* and *osteoclasts*. The extracellular matrix of mineralizable collagen is laid down by osteoblasts (osteogenic cells), which develop (differentiate) from stem cells. They secrete collagen which then mineralizes to form an HCA-collagen structure. An osteoblast that becomes surrounded by concentric rings of mineralized tissue is called an *osteocyte* (Figure 1.1). Osteoclasts are cells that resorb old bone and bone that is not required (i.e. not under any load). Osteoporosis occurs as osteoblasts become less active, but bone is still removed by osteoclasts. An aim of regenerative medicine is to stimulate the body to reactivate osteogenic cells to re-create the natural three-dimensional architecture of bone.

Hench proposed a specific bioactivity classification for biomaterials intended to be used for orthopedic implants [11]. Materials belonging to “*class B*” are *osteoconductive* (ability of a material in contact with host bone to stimulate bone growth along the surface of it), and bond to hard tissue (bone). They resorb very slowly if at all in contact with newly forming bone. Examples of class B bioactive materials are synthetic hydroxyl apatite (HAp), tri-calcium phosphate ceramics (β -TCP) and HAp-coated porous titanium oxide (titania) [11]. Materials belonging to “*class A*” are not only *osteoconductive*, but they are also *osteoproduative* (ability of a material to stimulate new bone growth on their surface, even away from the glass/bone interface). They bond to both bone and soft connective tissues and resorb as new bone replaces it. Examples of class A bioactive materials are *bioactive glasses*.

1.1.3. Bioactive glasses

There are two types of bioactive glasses: melt-derived and sol-gel derived.

1.1.3.1. Melt-derived bioactive glasses

The study of bioactive materials began with the discovery that silicate glasses of a specific composition were able to bond to bone. The first bioactive glass studied was *Bioglass*[®] 45S5, introduced by Hench in 1971 [7]. *Bioglass*[®] 45S5 is produced by quenching, and its specific composition is 45% SiO₂, 24.5% CaO, 24.5% Na₂O, 6% P₂O₅ (expressed as weight %). The name ‘45S5’ refers to both the SiO₂ content (45% wt) and the Ca/P molar ratio (5).

Glasses with substantially lower molar ratios of Ca to P (in the form of CaO and P₂O₅) do not bond to bone [26]. However, substitutions in the 45S5 of 5 to 15 wt% B₂O₃ for SiO₂, or 12.5 wt% CaF₂ for CaO have no measurable effect on the ability of the material to form a bone bond [26]. Greenspan [27] showed that addition of as little as 3 wt% Al₂O₃ prevents bonding. Gross found that a bioactive glass-ceramic with small additions (0 to 5 wt%) of K₂O and MgO (*Ceravital*[®]) also bond to bone with a mechanically strong interface. They find that small additions of Al₂O₃, Ta₂O₅, TiO₂, Sb₂O₃, or ZrO₂ inhibit bone bonding [28].

The most rapid rates of bonding both to soft and hard connective tissue occurs within 5-10 days for bioactive glasses composed of SiO₂, CaO, Na₂O and P₂O₅ are obtained with SiO₂ contents of 40-52% weight [11, 29, 30]. Bioactive glasses or glass-ceramics containing 55-60% SiO₂ require a longer time to form a bond with bones, and do not bond to soft tissues. Glass compositions with more than 60% SiO₂ do not bond either to bone or to soft tissues, and elicit formation of a non-adherent fibrous interfacial capsule [31].

A two-phase silica-phosphate glass-ceramic composed of apatite (Ca₁₀(PO₄)₆(OH)F) and wollastonite (CaO·SiO₂) crystals plus a residual SiO₂ glassy matrix, termed A/W glass-ceramic (*Cerabone*[®]) with composition (wt%): 34.2% SiO₂, 44.9% CaO, 16.3% P₂O₅, 0.5% CaF₂, 4.6% MgO [32, 33] also bonds with bone [33]. Addition of Al₂O₃ or TiO₂ to the A/W glass-ceramic inhibits bone bonding.

The most bioactive melt-quench composition is *Bioglass*[®] 45S5 and is used in orthopaedic and dental fields [11, 30, 34, 35].

1.1.3.2. Sol-gel derived bioactive glasses

In the early 1990s, Li and colleagues proposed the sol-gel route for the synthesis of bioactive glasses [36]. The sol-gel route requires noticeably lower

temperatures than the melt quench method for obtaining bioactive glasses. Sol-gel derived bioactive glasses have been synthesized in the SiO₂-CaO-P₂O₅ [37, 38] or even the SiO₂-CaO binary system, containing up to 90% SiO₂ [39-41].

Sol-gel glasses tend to be more bioactive and resorb quicker than melt-derived glasses of similar compositions. This is because sol-gel glasses have a nanometer scale textural porosity, which increases the specific surface area by two orders of magnitude compared to a melt-derived glass of a similar composition [42, 43]. The textural porosity not only increases the surface area, but it also exposes many silanol groups to the solution, which act as nucleation sites for HCA (hydroxycarbonate apatite) layer deposition. In sol-gel glasses the surface and structural properties (such as surface area and porosity) can be tailored by modifying the synthesis parameters (*see section 1.2.*).

To improve some specific characteristics of glasses, such as mechanical properties and resorption capacity new network modifiers were added to obtain MgO-CaO-P₂O₅-SiO₂ [44-46] and ZnO-CaO-P₂O₅-SiO₂ [47-50] sol-gel glasses.

A further advantage of sol-gel route is that possible dopants, such as silver, can be incorporated [51, 52], thus giving antimicrobial properties to the material, without compromising its bioactivity.

By foaming sol-gel derived bioactive glasses, scaffolds with a hierarchical pore structure similar to that of trabecular bone, with interconnected macropores (modal diameter in excess of 100µm) and a textural porosity (diameters of 10-20 nm), have been obtained by Jones *et al.* [25, 52-55]. The scaffolds have been obtained in the 58S (60% SiO₂, 36% CaO, 4% P₂O₅), 70S30C (70% SiO₂, 30% CaO) and even 100S (100% SiO₂) systems (expressed as mole%). The obtained bioactive sol-gel scaffolds stimulated the formation of mineralized bone nodules within 2 weeks of in vitro culture of primary human osteoblast without the presence of supplementary growth factors in the medium, which is unique to bioactive glasses [25, 55].

Due to the fact that low temperatures are required in sol-gel process, polymers can be included in the bioactive glasses. Therefore, a new class of advanced bioactive glasses used in regenerative medicine has been developed: *organic-inorganic hybrid*, with improved mechanical strength, elasticity or a certain level of degradation. *Class I*, corresponding to hybrid systems in which weak

interactions (such as, van der Waals forces, hydrogen bonds) are created between organic and inorganic phases, were obtained [56]. Hybrids of this class mostly include poly(vinylalcohol) (PVA) [57-59] as the organic component. *Class II* corresponds to organic-inorganic hybrids where both organic and inorganic components are bonded through strong covalent chemical bonds by using a coupling agent (a functionalised precursor, *see section 1.2.*). Strong covalent links between the inorganic and organic chains are essential in obtaining a tough composite material that degrades as one material. This is the case of hybrids with silica and poly(methylmethacrylate) (PMMA) [60, 61], poly(ϵ -caprolactone) (PCL) [62, 63], gelatin [4, 64-66] or poly(γ -glutamic acid) (γ -PGA) [5, 6, 67, 68]. Their properties can be varied by changing the ratio of the inorganic and organic parts.

The bioactive foam scaffolds and the organic-inorganic hybrids are candidates for third-generation tissue-engineering applications [20] that can stimulate tissue growth, repair and regeneration.

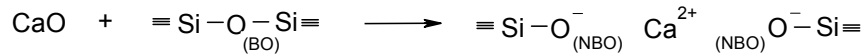
1.1.4. Glass structure and bioactivity

To better understand how bioactive glasses work when put in contact with body fluids, a few concepts concerning the partial dissolution of the silicate network and the reactivity of the glass surface will be given in the following section.

Most of the bioactive glasses are silica-based. In a crystalline solid made of silica (e.g. quartz), SiO_4 tetrahedra are organised in a well-defined crystalline network (Figure 1.2 a). In amorphous silica, SiO_4 tetrahedra are still linked together, but the angle between them is not constant, and the resulting structure is not completely organised, in contrast to the crystalline structure typical of all other solids. For this reason, glass structure is called *amorphous* (without a definite shape) (Figure 1.2. b).

SiO_2 is called a *network former*, since glass structure is mostly kept together by SiO_4 tetrahedra. Other oxides can be used as glass formers, such as P_2O_5 or B_2O_3 . Alkaline and alkaline-earth oxides are added to glass as *network modifiers*, in that they interrupt the network created by the glass former (Figure 1.2. c). The resulting structure is called a *random network*, and was first hypothesized by Zachariassen in 1932 [69].

In pure silica glass (Figure 1.2. a and b), all the SiO_4 tetrahedra are linked together. Every O atom is linked to 2 Si atoms. These O atoms are called *bridging oxygens* (BO). When a modifier is added to a glass composition, cations interrupt the silica network, and some O atoms are linked just to one Si atom. These O atoms are called *non-bridging oxygens* (NBO):



The bond between NBOs and cations is ionic and is less strong than the Si-O bond.

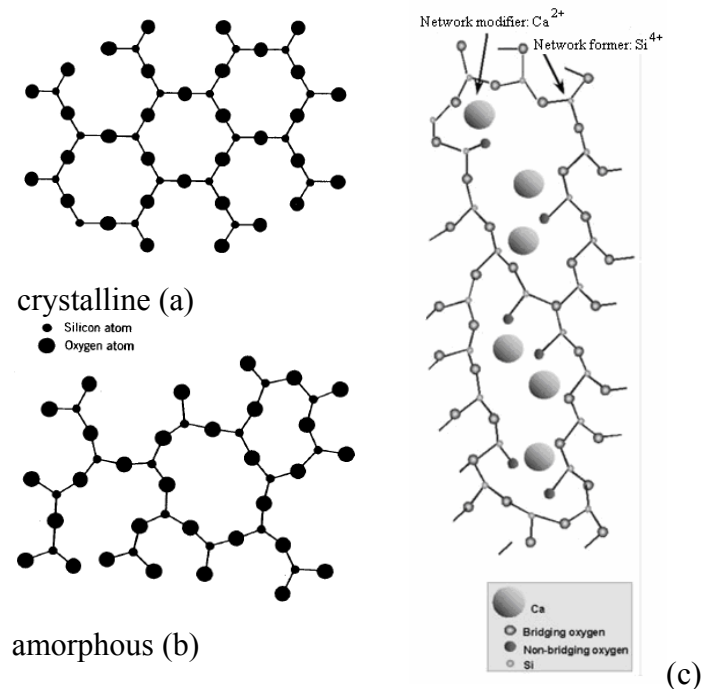


Figure 1.2. (a) Crystalline silica, (b) Amorphous silica, (c) Effect of introduction of Ca^{2+} cations in a silica network [70].

The *network connectivity* (NC), defined as the average number of BO atoms per glass-forming species, was introduced to describe the bioactivity [71-73]. By comparing the NC of glass compositions with different bioactivities (measured either as the rate of formation of the HA layer or as the bone-bonding ability), an empirical upper limit around $\text{NC}=3$ was proposed, separating bioactive ($\text{NC}<3$) from bioinactive ($\text{NC}>3$) glasses [71, 72]. Low NCs denote open and fragmented glass structures, whose rapid partial dissolution in an aqueous physiological environment will lead to HA formation and bone bonding in a shorter time, compared with glasses

with a more interconnected network. A classification based on the NC is not always accurate as was demonstrated by Hill, who considered a wider range of compositions [73]. He showed that even some glasses with $NC < 3$ were bio-inactive. The reason is that the NC estimated from the glass composition is based on the assumptions of regular coordination for all network-forming ions and of a homogeneous glass structure.

The importance of a *fast initial dissolution* of silicate fragments in the bioactive process was confirmed by Argos et al. [74]. Linear silicate chains have a higher mobility and can approach the glass–tissue interface faster, compared with more bulky features such as rings. When thermal treatment is used to promote the condensation of chains into rings of tetrahedra, the whole dissolution process is slowed down [75]. The migration, detachment and release of silicate units initially incorporated in a ring requires the breaking of a larger number of covalent Si–O bonds, compared with the release of a linear silicate chain. This is due to the fact that Si atoms incorporated in chains are, on average, less interconnected than Si atoms in rings. Moreover, the opening of stable (five- or six-membered) silica rings is energetically unfavoured, which further inhibits the release of soluble silica incorporated in ring-like structures.

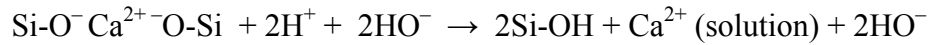
This disordered structure, enhanced by the presence of network modifiers, gives rise to the high reactivity of these glasses in aqueous environments.

1.1.5. Bioactive reaction mechanism of HCA layer deposition: Hench's hypothesis

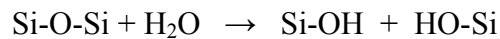
Even though the composition of bioactive glasses synthesized is quite different, it seems that the mechanism of HCA (hydroxycarbonate apatite) formation involves some specific steps that are analogous for all of them. It was hypothesized that a hydrated silica layer was formed on the surface of these glasses prior to the deposition of HCA, and that silanol groups could be specific sites of nucleation of apatite. Clark and Hench first proposed a well-detailed sequence of reactions occurring at the surface of silica-based bioactive glasses [29, 76, 77].

Bonding of bone to bioactive glasses involves 12 reaction stages:

1) Rapid exchange of network modifier ions (Na^+ and/or Ca^{2+}) in the glass with H^+ in solution:

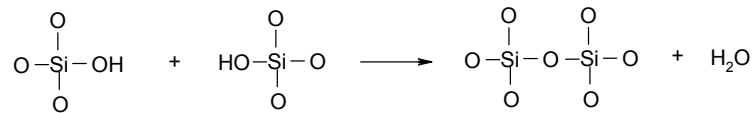


2) Loss of soluble silica as $\text{Si}(\text{OH})_4$ to the solution, resulting from breaking of Si-O-Si bridges and subsequent formation of surface silanol groups (Si-OH) in the process at the glass solution interface:



This stage is usually controlled by interfacial reaction.

3) Condensation and repolymerization of surface silanols to form a SiO_2 -rich layer on the surface depleted in alkalis and alkaline-earth cations:



4) Migration of Ca^{2+} and PO_4^{3-} groups to the surface through the silica-rich layer forming a CaO- P_2O_5 -rich film on the top of the SiO_2 -rich layer, followed by growth of the amorphous CaO- P_2O_5 -rich film by incorporation of soluble calcium and phosphates from solution.

5) Crystallisation of the amorphous CaO- P_2O_5 film by incorporation of HO^- , CO_3^{2-} or F^- anions from solution to form a mixed hydroxyl, carbonate, fluoroapatite layer.

- 6) Adsorption of biological moieties in the HCA layer
- 7) Action of macrophages
- 8) Attachment of stem cells
- 9) Differentiation of stem cells
- 10) Generation of matrix
- 11) Crystallisation of matrix
- 12) Proliferation and growth of bone

Following contact with a physiological fluid, the first five reaction stages lead to rapid release of soluble ionic species and formation of a high surface area hydrated

silica and polycrystalline HCA bi-layer on the glass surface. After these physical-chemical reactions occurred, biological moieties began to interact with the glass surface. Collagen molecules are incorporated in the HCA layer (stage 6) and influence the length of time macrophages are required to prepare the implant site for tissue repair (Stage 7) and the attachment (Stage 8) and synchronised proliferation and differentiation of osteoblasts (Stage 9). Mineralisation of the matrix (Stage 10) follows soon thereafter and mature osteocytes, encased in a collagen-HCA matrix, are the final product after 6–12 days *in vitro* and *in vivo*. Differences in the *in vivo* behavior of various glass compositions are due to the differences in the rate of stage 5, HCA formation. [7, 11, 29, 30, 76-78].

To understand the interaction of bioactive materials with cells, the importance of the cell cycle (Figure 1.3.) in bioactivity is presented. In order for new bone to form it is essential for osteoprogenitor cells to undergo *mitosis*. *Resting cells* are in the *G0* phase (Figure 1.3.).

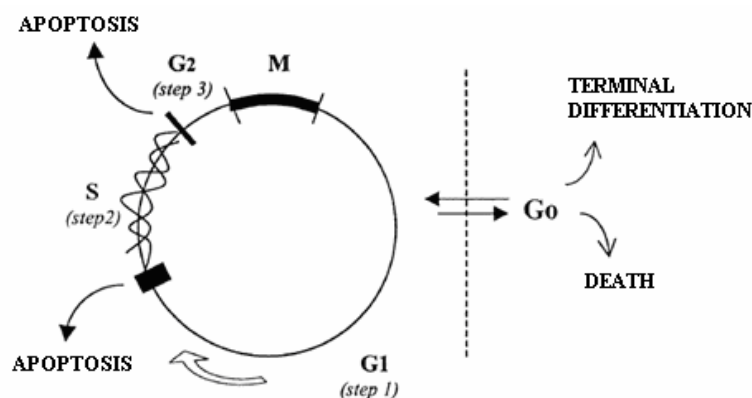


Figure 1.3. Schematic of osteoblast cell cycle [78, 79].

Every new cell cycle begins after a cell has completed the preceding mitosis. *If the local chemical environment is suitable*, and following a critical period of growth in the *G1 phase*, the cell enters the *S phase* when DNA synthesis begins. Next the cell is ready to undergo mitosis with a second phase of growth termed the *G2 phase* [78, 79, 80]. If the local chemical environment does not lead to completion of the *G1 phase* or the *G2 phase* then the cell proceeds to programmed cell death, *apoptosis*. Bio-inert materials or Class B bioactive materials do not produce the local

chemical environment to enable the few osteoprogenitor cells present to pass through these cell cycle checkpoints. This explains the slow rates of bone growth [81, 82] of the tissues grown in the presence of Class B bioactive materials. However, chemical substitution of silicon for calcium in synthetic HAp shows improved bone ingrowth *in vivo* over phase pure HAp granules [83]. For class A bioactive materials the rate of forming mineralised bone nodules *in vitro* [19, 80, 84, 85] is also similar to the kinetics of bone growth *in vivo* [86]. The *role of the bioactive glass* is primarily to release the critical concentrations of biologically active ions especially critical concentrations of soluble silica and calcia at the rate needed for *cell proliferation and differentiation* [18, 19, 79, 87]. Moreover, molecular biology studies conducted by Xynos [18, 19, 79, 87] indicate that the dissolution products of Class A bioactive glasses have been found to up-regulate seven families of genes in osteoblasts and to have an effect on the cell cycle.

1.2. Sol-gel method, a non-conventional route to obtain biomaterials

The sol-gel process has been known over 150 years, when the first metal alkoxide was prepared by Ebelmen [88] in 1846, from SiCl_4 and alcohol, and it was found that the compound gelled when exposed to the atmosphere. Sol-gel chemistry has been investigated extensively since the mid-1970s, when sol-gel reactions were used to produce a variety of inorganic networks i.e., monoliths, films, fibers, monosized powders from metal alkoxides [89-103].

1.2.1. Sol-gel hydrolysis and condensation reactions

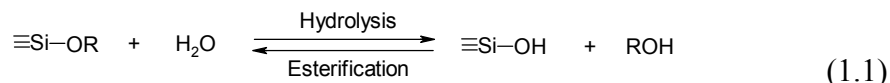
The sol-gel method involves the transition of a system from a liquid sol (a colloidal dispersion of particles in a liquid) into a solid gel phase (a continuous capillary solid framework encompassing a continuous liquid phase) [96, 100-102].

The sol-gel process can ordinarily be divided into the following steps:

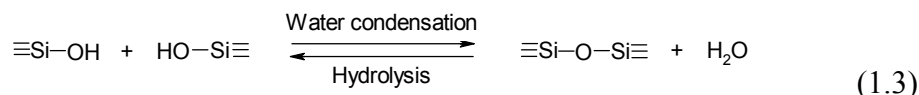
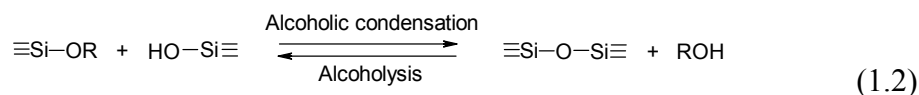
- forming a solution, or sol,
- gelation,
- aging,
- drying, and
- densification

In this process it is necessary to have a forming gel agent like silicon alkoxides that undergo:

- *hydrolysis* reactions where the alkoxide group Si-OR (R is an alkyl group) reacts with water giving Si-OH groups.



- *condensation* reactions forming Si-O-Si units, the residual products being alcohols and water.



Usually condensation reactions (eq. 1.2 and 1.3) start before hydrolysis (eq. 1.1) is complete. As water and alcoxysilanes are immiscible, a mutual solvent is normally used for complete homogenization. The alcohol is not simply a solvent; it can participate in esterification or alcoholysis reactions.

The parameters which naturally control these reactions, from the beginning to the end, will mainly control the sol to gel transition process. The several parameters which influence the sol-gel process, including the precursors' activity, water/alkoxide ratio, solution pH, steric and inductive effects, and the nature of the catalyst, solvent and additive (type of organic group(s) used as network modifier(s)) [96, 98, 103] will be very briefly considered first. Thus knowledge of the mechanisms and kinetics of these reactions should provide insight into the structures of gels and gel-derived glasses.

1.2.1.1. Precursors

Tetrafunctionalized silica alkoxides (with respect to hydrolysis reaction), and/or n-functionalized alkoxides (n<4), Figure 1.4 are generally used as precursors

in a sol-gel process. Here, n is representative of the number of organic radicals connected to the silicon molecule and f is representative of the number of reactive alkoxy groups connected to the silicon molecule.

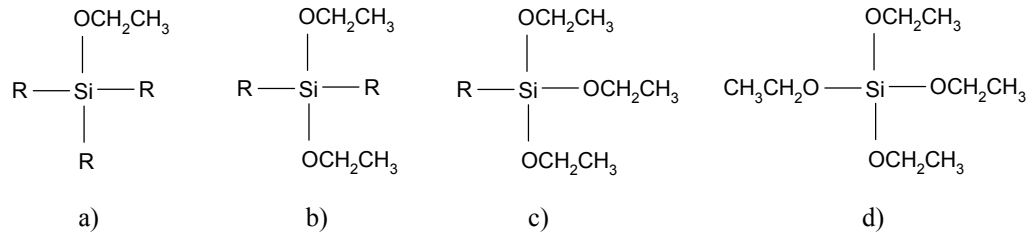


Figure 1.4. The $R'_nSi(OEt)_f$ functionality spectrum of a) monofunctional, b) difunctional, c) tri-functional and d) tetra-functional alkoxydes [59].

For a mono-functional silicon alkoxy ($f = 1$, $n = 3$), the monomer „terminates” the polymer chain since there is only a single reaction site on the molecule. A di-functional silicon alkoxy ($f = 2$, $n = 2$) behaves as a „bridging” agent, connecting molecules in a linear fashion. A tri-functional silicon alkoxy ($f = 3$, $n = 1$) behaves as an „crosslinker”, allowing for branching in the network. A tetra-functional silicon alkoxy ($f = 4$, $n = 0$) behaves as a „networking” agent, allowing for complete connectivity between all functional groups of the molecule.

Tetraethylorthosilicate (TEOS) was the main precursor in the sol-gel synthesis of the bioactive sol-gel samples studied in this thesis. Another two precursors have been used, a mono and a trifunctional precursor, trimethylethoxysilane (TMES) and 3-glycidoxypropyltrimethoxysilane (GPTMS), respectively.

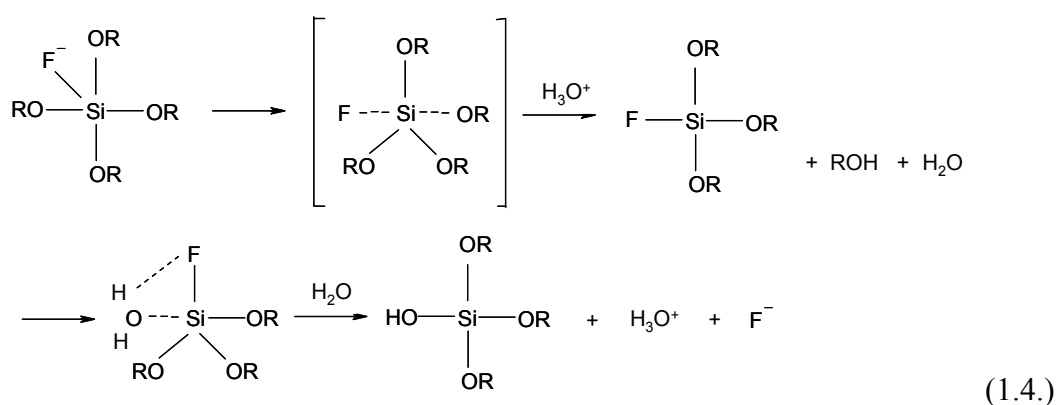
1.2.1.2. Water-to-alkoxide ratio (R)

The hydrolysis ratio R , allows control of the extent of hydrolysis. R can vary from <1 to over 25 depending on the desired polysilicate product, for example, fibers, bulk gels or colloidal particles. By increasing the value of R , the hydrolysis reaction is accelerated. However when R is increased while maintaining a constant solvent:silicate ratio, the silicate concentration is reduced [96, 98].

1.2.1.3. Effect of catalysts

Hydrolysis is most rapid and complete when catalysts are employed. Although mineral acids or ammonia are most generally used in sol-gel processing,

other known catalysts are acetic acid, KOH, amines and KF [96]. An interesting behaviour is showed by HF. F^- is about the same size as HO^- and has the ability to increase the coordination of silicon above four, for example in SiF_6^{2-} . Many of the properties of HF catalysed gels are similar to those of base catalysed gels, which suggests that the roles of HO^- and F^- are similar. Andrianov [104] proposes that the catalytic effect of F^- involves the displacement of an RO^- via a bimolecular nucleophilic displacement reactions (SN_2-Si) mechanism followed by preferential hydrolysis of the Si-F bond:



Although *the condensation* of silanols can proceed thermally without involving catalysts, their use especially in organosilanes is often necessary.

The use of catalysts drastically lowers the gelation times. The catalysts used in the synthesis of the bioactive samples were HNO_3 , HCl and HF .

1.2.1.4. Steric and inductive effects

Steric factors exert the greatest effect on the hydrolytic stability of organoxysilanes. According to Voronkov [105], any complication of the alkoxy group retards the hydrolysis of alkoxy silanes, but the hydrolysis rate is lowered the most by branched alkoxy groups.

Substitution of alkyl groups for alkoxy groups increases the electron providing effect of the ligand, conversely hydrolysis (substitution of OH for OR) or condensation (substitution of OSi for OR or OH) increases the electron withdrawing effect (Figure 1.5). Alkyl substitution and hydroxyl substitution should therefore increase the stability of positively and negatively charged transition states, respectively.

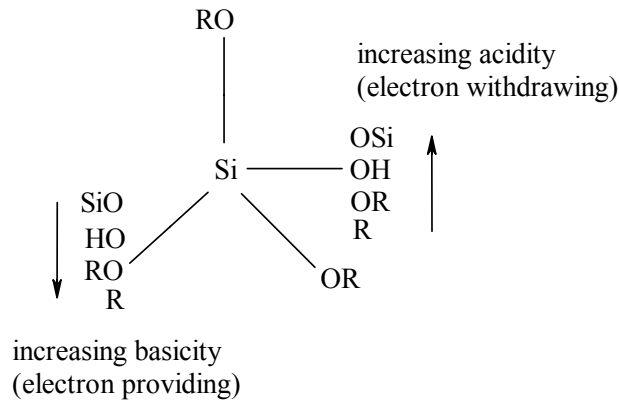


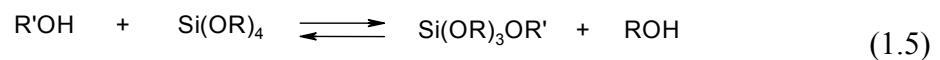
Figure 1.5. Inductive effects of substituents attached to silicon, R, OR, OH, or OSi.

1.2.1.5. Solvent effects

The solvents are added mainly to prevent liquid-liquid phase separation during the initial stages of the hydrolysis reaction and to control the concentrations of silicate and water that influence the gelation kinetics. Two important characteristics of solvents are: (1) polarity, which largely determines the solvating ability for polar or non-polar species, and (2) the availability of labile protons. The latter characteristic determines whether anions or cations are solvated more strongly and whether or not the solvent can participate in dissociative reactions such as alcoholysis of hydrolysis (reverse of eqs. (1.2) and (1.3)). More polar solvents (water (protic) and dimethylsulfoxide (aprotic)) were used in the sample preparation in this thesis to solvate polar, tetrafunctional and/or trifunctional silicate species used in sol-gel processing.

1.2.1.6. Transesterification, reesterification, and hydrolysis

The hydrolysis reaction (eq. (1.1)) may proceed in the reverse direction, *reesterification*, in which an alcohol (or a protonated alcohol or alkoxide anion under acidic and basic conditions, respectively) displaces a hydroxyl group to produce a water molecule [96]. Transesterification is the reaction in which an alcohol displaces an alkoxide group to produce an alcohol molecule:

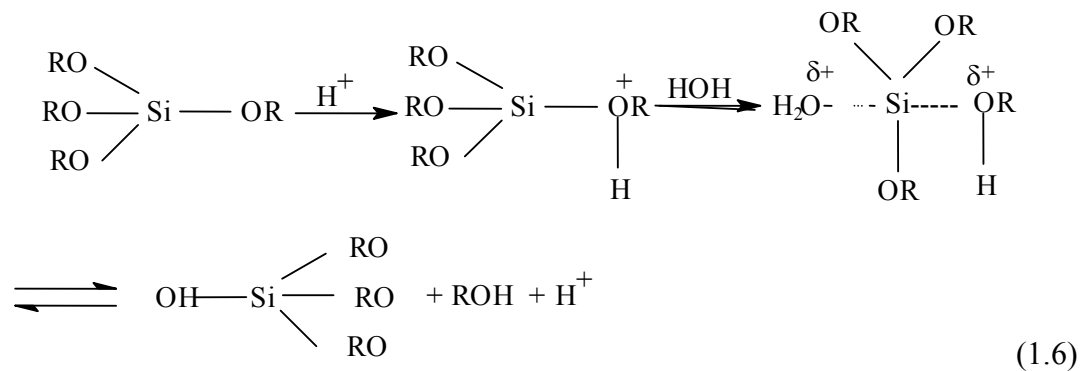


In sol-gel processing transesterification often occurs when alkoxides are hydrolysed in alcohols containing different alkyl groups. Transesterification is an important reaction in multicomponent systems which employ several alkoxides with differing alkoxide substituents

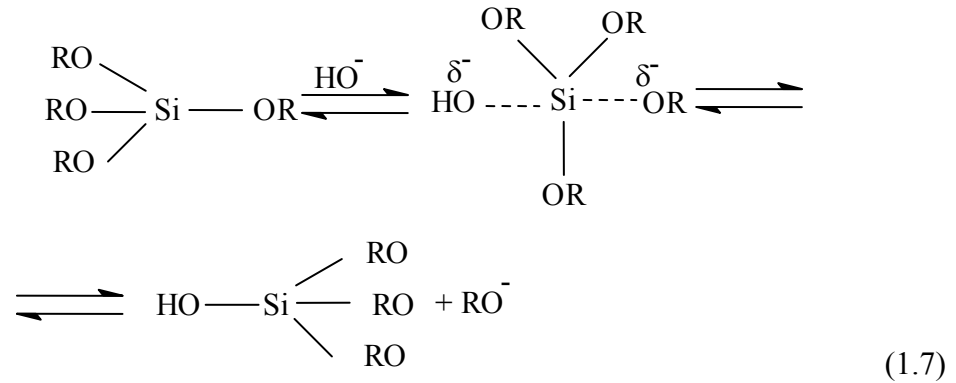
1.2.2. Mechanism of reactions

It is generally argued that hydrolysis proceeds by bimolecular nucleophilic displacement reactions (S_N2 -Si reactions) involving pentacoordinate intermediates.

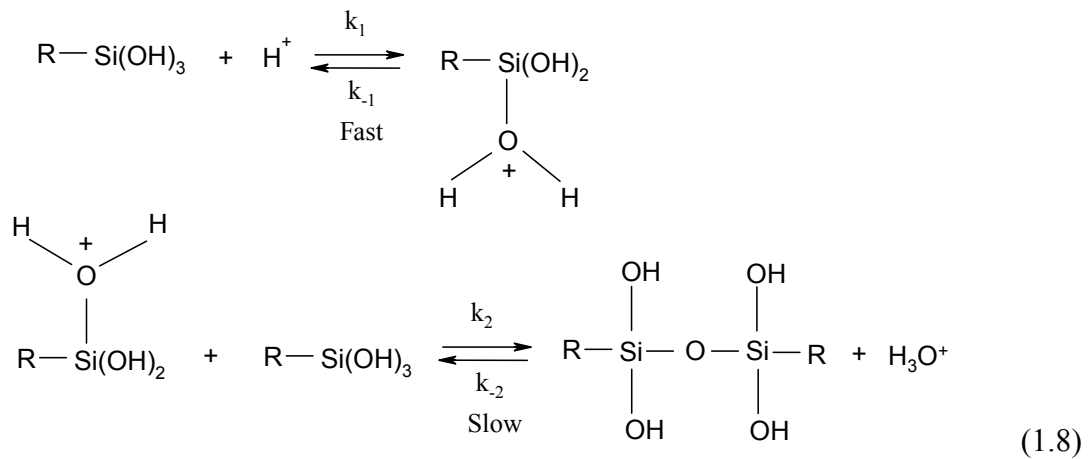
Under acidic conditions, an alkoxide group is protonated in a rapid first step. Electron density is withdrawn from silicon making it more electrophilic and thus more susceptible to attack by water. The water molecule attacks from the rear and acquires a partial positive charge. The positive charge of the protonated alkoxide is correspondingly reduced making alcohol a better leaving group. The transition state decays by displacement of alcohol accompanied by the inversion of the silicon tetrahedron [96]:



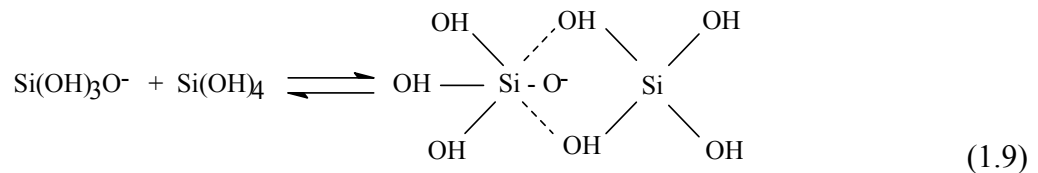
Under basic conditions, it is likely that water dissociates to produce hydroxyl anions in a rapid first step. The hydroxyl anion then attacks the silicon atom. Again, an S_N2 -type mechanism has been proposed in which the HO^- displaces RO^- with inversion of the silicon tetrahedron:



The *acid-catalysed condensation* take place by protonation of the most basic silanol species (silanol contained in monomers or weakly branched oligomers), where k_1 and k_2 represent the reaction constants:



The *base-catalysed condensation* reaction takes place by the attack of a nucleophilic deprotonated silanol on a neutral silicate species [96]:



It is generally believed that both acid- and base-catalysed condensation mechanisms involve penta- or hexa-coordinated silicon transition states.

1.2.3. Structural evolution

On the shortest length scale, the nearest neighbor of silicon may be an alkoxide group (OR), a hydroxyl group (OH), or a bridging oxygen (OSi). On intermediate length scales, oligomeric species (dimers, trimers, cyclic trimer, cyclic tetramers, etc.) may be linear, branched or cyclic. On a length scale large with respect to the monomer and small with respect to the polymer, structures may be dense with well defined solid-liquid interfaces, uniformly porous, or tenuous networks [59, 96, 106]. The gel point is considered to be the moment when the sol suddenly loses its fluidity and takes on the appearance of an elastic solid.

It can generally be said that sol-gel derived silicon oxide networks, under acid-catalysed conditions, yield primarily linear or randomly branched polymers which entangle and form additional branches resulting in gelation (Figure 1.6) [96, 107, 108]:

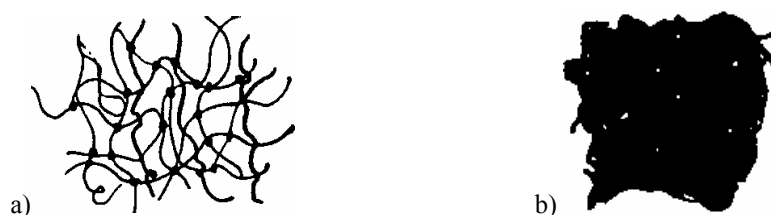


Figure 1.6. Scheme of acid-catalyzed gel (a), desiccated xerogel (b).

On the other hand, silicon oxide networks derived under base-catalysed conditions yield more highly branched clusters which do not interpenetrate prior to gelation and thus behave as discrete clusters (Figure 1.7) [96, 107, 108]:



Figure 1.7. Scheme of base-catalyzed gel (a), desiccated xerogel (b).

Under acidic conditions, hydrolysis occurs at a faster rate than condensation and the resulting gel is weakly branched. Under basic conditions, the reverse is true and the resulting gel is highly branched and contains colloidal aggregates. Furthermore, acid-catalysed gels contain higher concentrations of adsorbed water, silanol groups, and unreacted alkoxy groups than base-catalysed ones. These differences in microstructure and surface functionality result in different responses to heat treatment. Acid- and base-catalysed gels yield micro- (pore width less than 2 nm) and meso-porous (2–50 nm) materials, respectively, upon heating [96]. Clearly an acid-catalysed gel which is weakly branched and contains surface functionalities that promote further condensation collapses to give micropores. Therefore, a crucial point can be highlighted: *the initial microstructure and surface functionality of a gel dictates the properties of the heat-treated products.*

1.3. Characterisation methodology

In order to probe the atomic and nano-scale structural and textural properties of a complex porous amorphous material a range of genuinely complementary techniques should be applied as part of an overall methodology. A strong collaboration between the University of Warwick, Imperial College London, the University of Kent and the Eastman Dental Institute, London has been involved developing an advanced characterisation methodology for bioactive materials. Methods such as solid-state NMR, diffraction, microscopy, nitrogen adsorption, differential thermal analysis (DTA), thermogravimetric analysis (TGA), X-ray micro-computed tomography, Inductive Coupled Plasma (ICP) analysis, Fourier transform infra red (FT-IR), ultraviolet visible (UV-VIS), X-ray absorption (EXAFS-extended X-ray absorption fine structure, XANES-X-ray absorption near edge structure) and Raman techniques have been employed. Figure 1.8 shows the relationship between the various methods for investigating the structure, texture and bioactivity of sol-gel derived bioactive materials. While by this collaboration, the structural, textural and bioactive properties are examined and improved by using multiple techniques, the present thesis has been focused on characterisation of the sol-gel derived bioactive scaffolds and nanocomposites from the solid state NMR point of view.

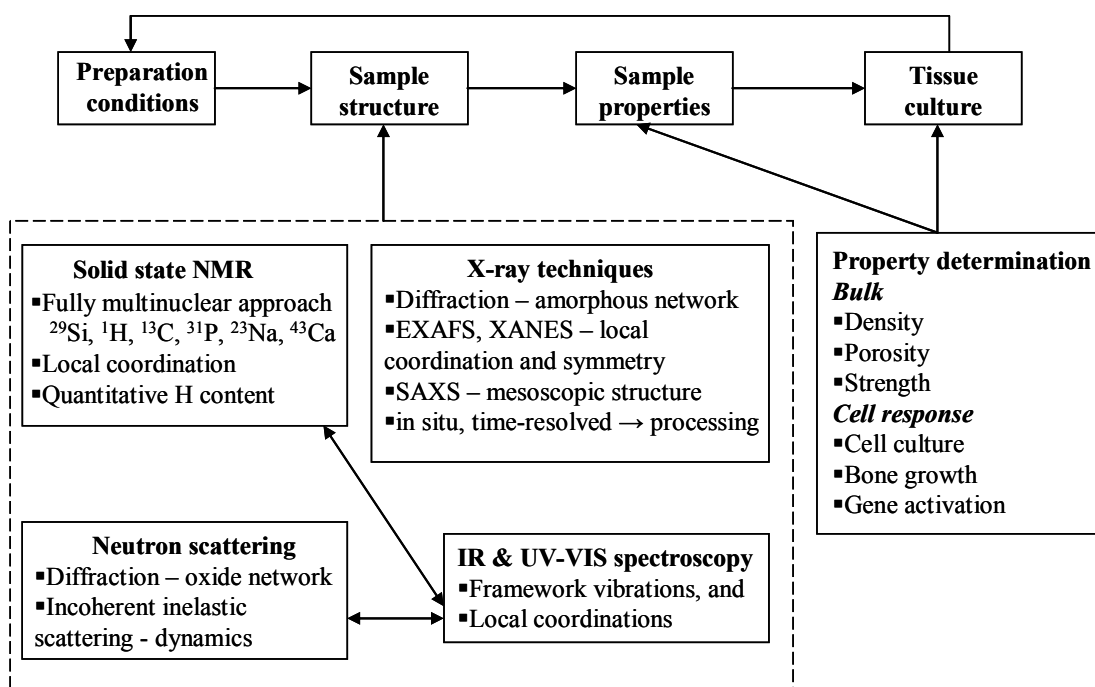


Figure 1.8. Summary of the various methods for investigating the structure, texture and bioactivity of sol-gel derived bioactive materials [109].

The specific contributions this thesis has made to the large scale collaborative activity can be divided into 6 specific studies:

1. Examining the nanostructure evolution with temperature, as well as characterising the inhomogeneity of $\text{SiO}_2\text{-CaO}$ sol-gel bioactive glasses.
2. Explore the mechanism of nanopore enlargement on the glasses after drying and prior to stabilisation, to verify the trimethylsilylation reaction mechanisms.
3. Examine the role of phosphorous in sol-gel bioactive glasses in the $\text{SiO}_2\text{-CaO-P}_2\text{O}_5$ ternary system.
4. Test the hypothesis of bonding of functionalised polymer to the inorganic network in the case of organic-inorganic hybrid scaffolds.
5. Test Hench's hypothesis of the mechanism of HCA layer deposition on bioactive glasses.
6. Examine the inhibitive effect of serum proteins in the mechanism of apatite growth on both melt-quench (*Bioglass*[®]) and sol-gel (*TheraGlass*[®]) derived bioactive glasses.

Solid state NMR is a powerful tool for investigating structural and dynamic disorder in sol-gel derived glasses [96, 109-112]. The great utility of NMR lies in the fact that it is element-selective, since only the local environment of the particular nucleus under study is probed. Also it is a non-destructive technique and requires a relatively small amount of sample. Combinations of multinuclear experiments can then provide complementary information about various aspects of the structural problem under study.

Six nuclei will be looked at in this study: ^{29}Si , ^1H , ^{13}C , ^{31}P , ^{23}Na and ^{43}Ca . ^{29}Si NMR is performed for three reasons: to determine the role of the calcium as network modifier in the silicate network, to investigate the structural changes on the silicate network as it is subjected to heat treatment and to verify the bonding between organic and inorganic networks in the hybrid systems. ^1H and ^{13}C NMR are very useful in determining the organic content remaining from the organic precursors for the thermally treated samples, as well as to examine the change in the state of the bonding between the organic (polymer) and the inorganic (silicate) components for hybrid samples. ^{31}P is a very sensitive nucleus and even thin, amorphous surface layers can be observed as they are deposited from simulated body fluid. Also it gives us information about the role of phosphorous in bioactive glasses. ^{23}Na NMR is very useful in providing unique information about the local bonding environment of the sodium. ^{43}Ca NMR provides new and unique information about the local coordination of calcium.

The remaining work of this thesis has been divided into seven other chapters. In Chapter 2 the theory of NMR will be outlined including the properties of the nuclei that are examined in this thesis, while in Chapter 3 the experimental aspects of the studies will be presented. Chapter 4 will discuss the nanostructure evolution of binary $\text{SiO}_2\text{-CaO}$ (70S30C) sol-gel derived bioactive glasses and nanostructure inhomogeneity of monoliths is investigated. The trimethylsilylation reaction mechanisms used to tailor the nanoporosity will be examined. In Chapter 5 the addition of P_2O_5 in the silica-calcium oxide system will be studied for sol-gel samples and compared for the two synthesis routes: inorganic and alkoxide. Chapter 6 will be focused on the study of the organic-inorganic hybrid systems. First, class II hybrids of compositions of 30 and 60 wt % gelatin with different mole ratio of coupling agent/gelatin will be analysed and compared with class I hybrids. Secondly

the poly(γ -glutamic acid)/ silica hybrid material with composition 40 wt% organic and 60 wt% inorganic (composition 70 mol% SiO₂ and 30 mol% CaO) will be analysed. The influence of coupling agents and the gelling conditions, as well as the addition of calcium ions in the form of inorganic or organic salt on the hybrid network will be examined. Chapter 7 will be focused on comparison studies performed to determine the inhibitive effects of serum proteins against apatite growth on both melt-quench (*Bioglass*[®]) and sol-gel (*TheraGlass*[®]) derived bioactive glasses. Eventually, overall conclusions of the thesis, along with future directions for this work will be presented in Chapter 8.

2.

NMR THEORETICAL BACKGROUND

2.1. Introduction

Nuclear magnetic resonance (NMR) spectroscopy, first observed in 1946 by Purcell [113] and Bloch [114] in condensed matter, has grown tremendously from its initial stage, spreading its influence to a wide range of disciplines such as chemistry, physics, biology, geology and medicine. This chapter will provide some of the most important aspects of the background theory of NMR based on books and articles written by MacKenzie and Smith [109], Levitt [115], Duer [116], Harris [117] and Eckert [111].

2.2. The NMR Hamiltonian

Any nuclei containing an odd number of either protons or neutrons, or both, possesses angular momentum, \mathbf{I} , and consequently a magnetic moment $\boldsymbol{\mu}$:

$$\boldsymbol{\mu} = \gamma \hbar \mathbf{I} \quad (2.1)$$

where γ is the gyromagnetic ratio of the nucleus, and \hbar is Planck's constant divided by 2π .

The quantisation laws for angular momentum predict that any nucleus with nuclear spin-quantum number I has $2I + 1$ states. In the absence of an external field or other internal interactions, all of the energy levels in a system are degenerate. In the presence of an externally applied magnetic field of magnitude B_0 these states become non-degenerate due to the Zeeman interaction,

$$\hat{H}_z = \boldsymbol{\mu} \cdot \mathbf{B}_0 \cdot \hat{I}_z \quad (2.2)$$

where \mathbf{B}_0 is taken along the z-axis. H_z is often referred to as the *Zeeman Hamiltonian*. This then results in discrete energy levels:

$$E_m = -m\gamma\hbar B, \quad (2.3)$$

where m is the magnetic quantum number and ranges in unit steps from $+I$ to $-I$, and \mathbf{B} is the magnetic field experienced by the nuclei, consisting of the external field \mathbf{B}_0 and internal components \mathbf{B}_{int} (usually $\ll \mathbf{B}_0$), which arise from *internal interactions* of the nuclei with their surrounding environment:

$$\mathbf{B} = \mathbf{B}_0 + \mathbf{B}_{int} \quad (2.4)$$

A transition energy level diagram of a spin number $I = 1/2$ as a function of externally applied magnetic field \mathbf{B} is shown in Figure 2.1.

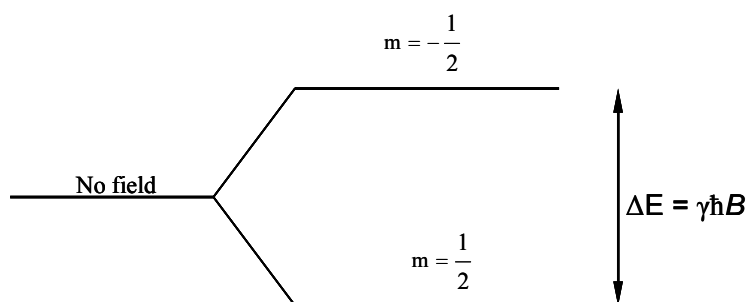


Figure 2.1. Energy level diagram for $I = 1/2$.
 $\gamma > 0$ was assumed [109].

Since these internal fields (\mathbf{B}_{int}) are intimately related to the structure of the material, their evaluation is of central interest in NMR spectroscopy. To measure the energy differences between the magnetic spin states (and therefore \mathbf{B}_{int}), a second oscillating magnetic field, \mathbf{B}_1 , is introduced by a radio-frequency (*r.f.*) pulse, in a direction perpendicular to \mathbf{B}_0 . The amplitude of \mathbf{B}_1 oscillates at an *angular frequency*, ω_0 (rad/s), the frequency at which transitions between the energy states occur. At resonance the condition:

$$\omega_0 = -\gamma B \quad (2.5)$$

holds. Here $\omega_0 = 2\pi\nu_0$, and ν_0 (Hz), also known as '*Larmor frequency*', is the frequency of the electromagnetic radiation at which absorption occurs.

2.3. Internal interaction mechanisms

In general, the internal interactions B_{int} arise from the composite effect of a number of physically distinct mechanisms. These interactions are tensors with both a *spatial part and a spin part* [118]. The spatial part expresses the dependence of the interaction on the molecular orientations, keeping the spin polarisations and the static magnetic field fixed. The spin part expresses the dependence of the interaction on the spin orientations, keeping the molecular orientation and the static magnetic field fixed.

The most important interactions in diamagnetic insulating materials are chemical shielding (CS), magnetic dipole-dipole coupling (D), J coupling (J) and for nuclei with spin quantum number $>1/2$, nuclear electric quadrupole coupling (Q).

The total Hamiltonian is the sum of all of the Hamiltonians for each interaction:

$$\hat{H}_{\text{total}} = \hat{H}_Z + \hat{H}_{rf} + \hat{H}_{CS} + \hat{H}_D + \hat{H}_J + \hat{H}_Q \quad (2.6)$$

\hat{H}_{rf} describes the interaction of the spins with the periodically fluctuating magnetic component of the radiofrequency field and does not need to be considered when describing the internal mechanisms. \hat{H}_z and \hat{H}_{rf} are external Hamiltonians.

The Zeeman interaction is normally the largest interaction present in nuclear spin systems in the presence of strong magnetic fields. This interaction has been discussed previously in *section 1.2*. The effects of \hat{H}_{CS} , \hat{H}_D , \hat{H}_J (and sometimes \hat{H}_Q if present, where generally $\hat{H}_Q \gg \hat{H}_{CS}$, \hat{H}_D , \hat{H}_J) upon the Zeeman energy levels are assumed to be minor compared to that of \hat{H}_z (termed the high field limit), therefore the other interactions usually are treated as perturbations to the Zeeman energy levels. All of the above interactions are anisotropic. In the following sub-sections, the physical nature of these internal interactions will be discussed in more detail.

2.3.1. The chemical shift interaction

The chemical shift interaction is a response by the electrons surrounding a nucleus to the applied magnetic field. The electrons are charged particles, and when they are subjected to a magnetic field, they tend to respond in a manner such that they create an induced magnetic field that opposes the applied magnetic field (B_0).

As a result, the electrons shield the nucleus from the applied field. A nucleus thus feels a local magnetic field:

$$\mathbf{B} = \mathbf{B}_0(1 - \sigma) \quad (2.7)$$

The chemical shift Hamiltonian acting on spin \mathbf{I} can be written as [109]:

$$\hat{H}_{CS} = -\gamma \hat{\mathbf{I}} \cdot (1 - \sigma) \cdot \mathbf{B}_0 \quad (2.8)$$

where σ is a rank 2 orientation-dependent tensor denoting the *chemical shielding*. The magnitude of the shielding effects is proportional to the applied field.

In a suitably chosen frame of reference (the PAS-principal axis system), the chemical shielding tensor, σ , is diagonal, leaving three nonzero parameters. These tensor values along the diagonal are called *the principal values*, and they are denoted with numeric subscripts (σ_{xx} , σ_{yy} , and σ_{zz}). The principal components are assigned [119] such that:

$$|\sigma_{11} - \sigma_{iso}| \leq |\sigma_{22} - \sigma_{iso}| \leq |\sigma_{33} - \sigma_{iso}| \quad (2.9)$$

where σ_{iso} , the isotropic chemical shielding value is the arithmetic mean of the principal values:

$$\sigma_{iso} = \frac{\sigma_{11} + \sigma_{22} + \sigma_{33}}{3} \quad (2.10)$$

Although the interaction is chemical shielding, what is normally measured in an experiment is a frequency that is related to the chemical shielding, *the chemical shift* (δ):

$$\delta = \frac{\sigma_{ref} - \sigma_{sample}}{1 - \sigma_{ref}} \quad (2.11)$$

The isotropic chemical shift, δ_{iso} , is usually reported in units of parts per million (ppm):

$$\delta_{iso} = \frac{\nu_{iso} - \nu_{ref}}{\nu_{ref}} (\times 10^6) \quad (2.12)$$

where ν_{ref} is the frequency of a suitable reference compound for the nucleus under investigation. The principal values components can be written as:

$$\delta_{iso} = \frac{\delta_{11} + \delta_{22} + \delta_{33}}{3} \quad (2.13)$$

with $|\delta_{11} - \delta_{iso}| \geq |\delta_{22} - \delta_{iso}| \geq |\delta_{33} - \delta_{iso}|$ [119].

Therefore, the chemical shift values are essentially the experimental measurements of the chemical shielding tensor. A useful consequence of definition of the chemical shift is that the same ppm value will be measured for δ_{iso} regardless of the magnetic field employed.

To describe the NMR lineshape two parameters are used: Ω and κ

$$\Omega = \sigma_{33} - \sigma_{11} = \delta_{11} - \delta_{33} > 0 \quad (2.14)$$

$$\kappa = \frac{3(\sigma_{iso} - \sigma_{22})}{\sigma_{33} - \sigma_{11}} = \frac{3(\delta_{22} - \delta_{iso})}{\delta_{11} - \delta_{33}} \quad (2.15)$$

where Ω , the span, defines the actual width of the powder pattern, while κ , the skew, which varies from -1 to 1 , defines the asymmetry of the powder pattern.

The chemical shift tensor components can provide valuable qualitative information about local symmetry [111, 116]. Powder patterns arise from samples where there are many crystallites randomly oriented, so that all possible molecular orientations are present with a random distribution. For spherically symmetric (cubic) environments, all tensor components are equal, and only one sharp, unstructured signal is observed (Figure 2.2 a).

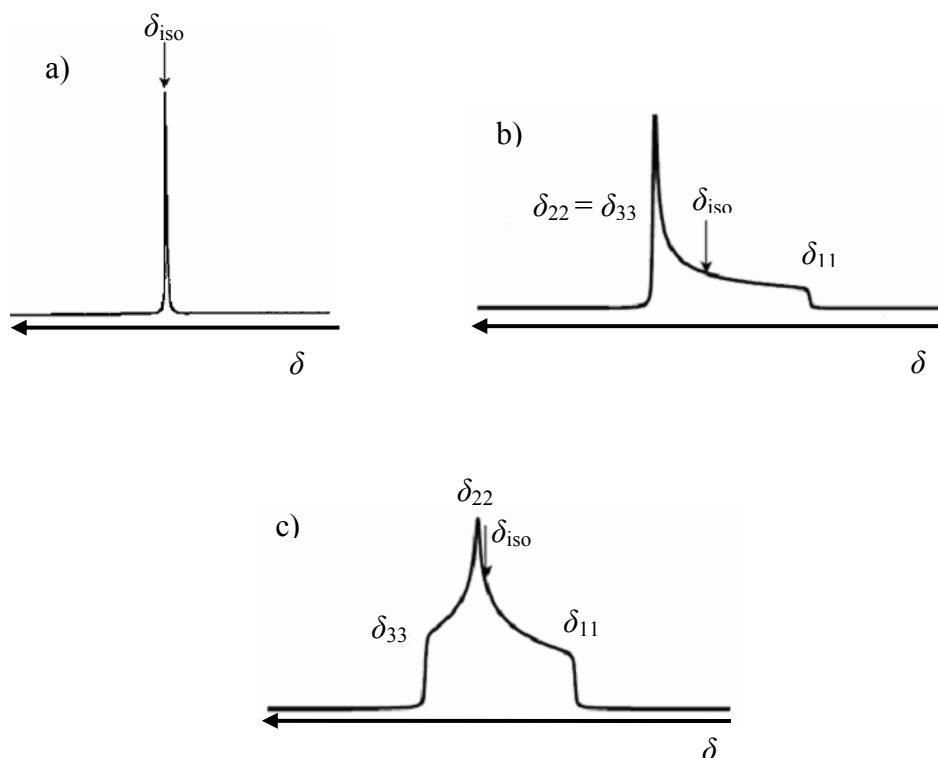


Figure 2.2. Typical chemical shift-dominated NMR powder patterns: (a) spherically symmetric chemical shift tensor, (b) axially symmetric chemical shift tensor, and (c) asymmetric chemical shift tensor [111, 116].

For the axially symmetric case, the powder pattern is represented in Figure 2.2 b. Nuclei in non-axially symmetric environments have lineshapes such as shown in Figure 2.2 c.

2.3.2. Dipole-dipole coupling

The magnetic dipole-dipole interaction is a two spin interaction which describes the effect of the local magnetic fields associated with the magnetic moments of surrounding nuclei. Two nuclei with nonzero spin quantum numbers can be viewed as little magnets. Their projection along the \mathbf{B}_0 field is given by the m_z quantum number. The local field that one spin “sees”, depends on the alignment of the second spin with respect to the \mathbf{B}_0 field. If the second spin is aligned with the field, then the local field at the first spin will be larger, and the opposite is true if the second spin is aligned against the field. The dipole-dipole coupling (sometimes called the direct dipole-dipole coupling) depends on the orientation of the vector connecting two spins with respect to the magnetic field and the distance between the

spins, $\propto (3\cos^2\theta - 1)/(r^3)$, where θ is the angle between the internuclear vector, \mathbf{r} , and the magnetic field; and r is the distance between spin I and spin S . Therefore, the corresponding Hamiltonian describing the interaction between two spins, with gyromagnetic ratios γ_I and γ_S and internuclear distance r , is given by [116]:

$$\hat{H}_D = -\left(\frac{\mu_0}{4\pi}\right) \cdot \frac{\gamma_I \gamma_S \hbar}{r^3} \{A + B + C + D + E + F\} \quad (2.16)$$

where

$$\begin{aligned} A &= \hat{I}_z \hat{S}_z (3\cos^2\theta - 1) \\ B &= -\frac{1}{4} [\hat{I}_+ \hat{S}_- + \hat{I}_- \hat{S}_+] (3\cos^2\theta - 1) \\ C &= \frac{3}{2} [\hat{I}_z \hat{S}_{++} + \hat{I}_+ \hat{S}_z] (\sin\theta \cos\theta) e^{-i\varphi} \\ D &= \frac{3}{2} [\hat{I}_z \hat{S}_{--} + \hat{I}_- \hat{S}_z] (\sin\theta \cos\theta) e^{+i\varphi} \\ E &= \frac{3}{4} [\hat{I}_+ \hat{S}_+] \sin^2\theta e^{-2i\varphi} \\ F &= \frac{3}{4} [\hat{I}_- \hat{S}_-] \sin^2\theta e^{+2i\varphi} \end{aligned} \quad (2.17)$$

Terms A to F represent the so-called ‘‘dipolar alphabet’’. Only terms A and B commute with \hat{I}_z and represent the secular part of \hat{H}_D which is independent of time. Terms C to F are called the non-secular part of the \hat{H}_D and are time-dependent. Therefore terms C to F are non-energy conserving and are negligible compared to the energy conserving terms A and B, hence the Hamiltonian is often reduced leaving only the secular terms A and B (provided the spins are the same). Term A describes the classical interaction of the two magnetic moments whereas B is the quantum-mechanical term associated with coupled transitions between different spin states of two coupled spins (‘‘flip-flop’’-term, i.e. $\hat{I}_+ \hat{S}_-$). As for heteronuclear nuclei the term B is not secular, this term is energy-conserving only if the interaction is homogeneous in the presence of strong homonuclear couplings.

The powder lineshape for a dipole-dipole coupling is symmetric about 0, and it is called a *Pake pattern* [120]. For heteronuclear dipolar couplings, the splitting

between the “horns” (the two highest intensity peaks) of the Pake pattern is equal to the dipolar coupling. The horns for two homonuclear dipole-dipole coupled spins are separated by $\frac{3}{2}d$, where d is given by [115]:

$$d = -\left(\frac{\mu_0}{4\pi}\right) \cdot \frac{\gamma_I \gamma_S \hbar}{r^3} \quad (2.18)$$

and is known as *dipolar-coupling constant* (in units of $\text{rad}\cdot\text{s}^{-1}$), where μ_0 is the permeability of free space.

An example of a Pake pattern lineshape for a pair of through space dipole-dipole coupled spin 1/2 nuclei is shown in Figure 2.3, where the homo (d^{H}) and hetero (d^{IS}) dipolar coupling constants (in units of Hz) are inserted.

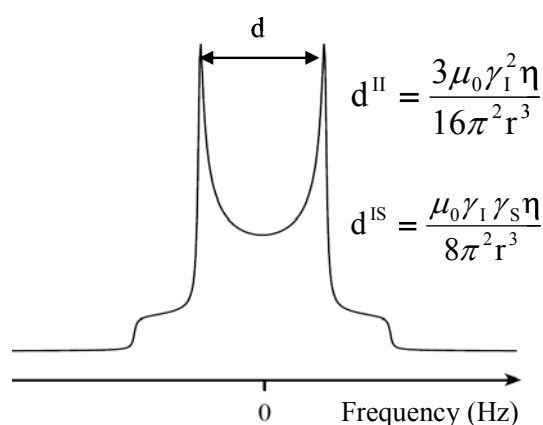


Figure 2.3. Powder pattern lineshape for a pair of through space dipole-dipole coupled spin 1/2 nuclei [111].

In this thesis homonuclear ^1H - ^1H dipolar couplings as well as heteronuclear couplings (^{13}C - ^1H , ^{31}P - ^1H , ^{29}Si - ^1H) have been considered in describing the sol-gel derived bioactive glasses.

2.3.3. The J-coupling

The J-coupling, or indirect spin-spin coupling, is a two spin interaction, just as the direct dipole-dipole coupling, however, instead of a through-space interaction, the J coupling is a through-bond interaction, mediated through the bonding electrons.

J couplings usually are smaller than dipolar couplings. The dipolar coupling is averaged to normally zero in liquids due to rapid tumbling of the molecules which allows them to sample all orientations with respect to B_0 resulting in a zero time-averaged coupling. For NMR spectra in solids, the effect of J-coupling is typically small compared to the dipolar coupling and is ignored for the nuclei studied in this thesis. In the literature, however, the measurement of J-couplings for $^{29}\text{Si-O-}^{29}\text{Si}$ [121, 122], $^{29}\text{Si-O-}^{31}\text{P}$ [123], $^{13}\text{C-}^1\text{H}$ [124], $^{43}\text{Ca-O-}^{13}\text{C}$ [125] has been performed in systems similar with the ones studied in this thesis.

2.3.4. The nuclear electric quadrupole interaction

This interaction arises from the interaction of non-spherically symmetric nuclear electrical charge distributions with the electric field gradient (EFG) generated by an asymmetric electrical charge distribution in molecules. This interaction affects only nuclei with $I > 1/2$ in non-cubic environments. The quadrupolar interaction is, in general, substantially larger than the dipole-dipole couplings, chemical shielding, and J coupling interactions. Although the quadrupolar interaction can be large, in most cases it is still smaller than the Zeeman interaction and its effect is typically described as a perturbation to the Zeeman energy levels.

The Hamiltonian characterising this interaction can be written as [116]:

$$\hat{H}_Q = \frac{e^2 q Q}{4I(2I-1)h} \left[3\hat{I}_z^2 - \hat{I}^2 + \frac{1}{2}\eta_Q \left(\hat{I}_x^2 - \hat{I}_y^2 \right) \right] \quad (2.19)$$

The EFG can be described as a tensor, and is defined by three components (V_{11} , V_{22} and V_{33}) in its principal axis system. The quadrupolar interaction is characterised by two parameters, C_Q and η_Q . The magnitude of the interaction experienced by a nucleus is given by the quadrupolar coupling constant (in units of Hz) [109]:

$$C = \frac{e^2 q Q}{h} \quad (2.20)$$

where e is the elementary charge, h is the Planck constant, Q is the quadrupole moment, which expresses how much the nuclear electrical charge distribution

deviates from spherical symmetry; eq (V_{33}) is the major component of the EFG in the PAS. The quadrupolar splitting parameter (quadrupole frequency) (in Hz) can be defined as:

$$\nu = \frac{3C}{4I(2I - 1)} \tag{2.21}$$

The deviation from axial symmetry of the EFG tensor is expressed using the asymmetry parameter, η_Q ($0 \leq \eta_Q \leq 1$):

$$\eta_Q = \frac{V_{11} - V_{22}}{V_{33}} \tag{2.22}$$

The principal values are chosen such that $|V_{33}| \geq |V_{22}| \geq |V_{11}|$ and $V_{11} + V_{22} + V_{33} = 0$ (Laplace equation).

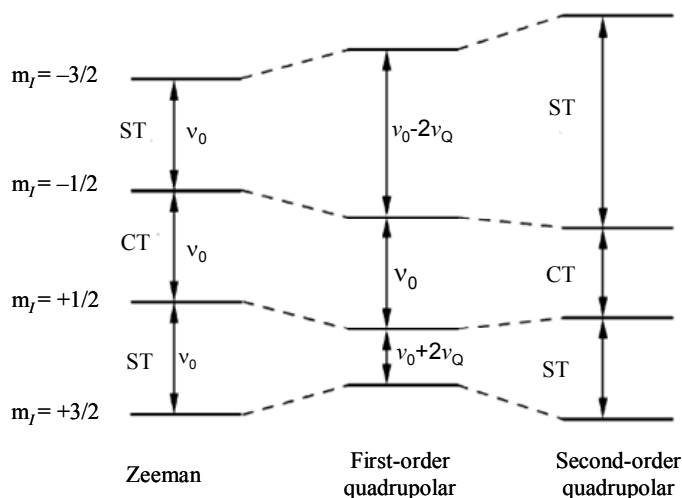


Figure 2.4. Schematic energy level diagram for a spin $I = 3/2$ nucleus showing the effect of the Zeeman, first-order and second-order quadrupolar interactions upon the four energy levels [127]. The central transition (CT) is unaffected by the first order quadrupolar interaction whereas the satellite transitions (ST) show a significant perturbation. All transitions are affected by the second-order quadrupolar interaction.

Although the quadrupole interaction is an electrical interaction it depends on the orientation of the nuclear spins and therefore affects the nuclear energy level

splittings [126]. Figure 2.4 shows the perturbation of the four Zeeman energy levels for a spin $I = 3/2$ nucleus by the quadrupolar interaction.

Under the first-order quadrupolar interaction it can be observed two distinct types of transitions: (i) an unaffected central transition (CT) (with $m_I = +1/2 \leftrightarrow m_I = -1/2$), at ν_0 (Larmor frequency); and (ii) two satellite transitions (ST) (with $m_I = -3/2 \leftrightarrow m_I = -1/2$ and $m_I = +1/2 \leftrightarrow m_I = +3/2$), with frequencies of $\nu_0 + 2\nu_Q$ and $\nu_0 - 2\nu_Q$, respectively. The quadrupolar frequency, ν_Q (Hz), is given by:

$$\nu = \frac{3C}{4I(2I-1)} (3\cos^2\theta - 1) \left(m_I - \frac{1}{2} \right) \quad (2.23)$$

where θ is the angle between PAS of the EFG and the magnetic field in the laboratory frame along the z axis (for simplicity, axial symmetry (i.e., $\eta_Q = 0$) has been assumed).

For a powdered sample many different crystallite orientations are present and a large anisotropic broadening of the satellite transitions is observed. The central transition, unaffected by the quadrupolar interaction to first-order, remains sharp and narrow (Figure 2.5.), and is usually the only transition observed experimentally.

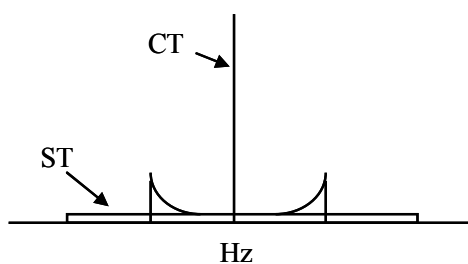


Figure 2.5. The effect of the first-order quadrupolar interaction to the NMR lineshape for a nucleus with spin $I = 3/2$ [111].

The quadrupolar interaction is often of sufficient magnitude that the first-order perturbation theory employed to describe its effect on the Zeeman energy levels is no longer sufficient and higher-order terms have to be considered.

As shown in Figure 2.4., all transitions are affected by the second-order quadrupolar interaction, with the correction to the frequency given by (for simplicity $\eta_Q = 0$):

$$\begin{aligned}
\nu_{1/2,-1/2}^{(2)} &= -\frac{1}{8\nu_0} \left[\frac{3C}{4I(2I-1)} \right]^2 \left[I(I+1) - \frac{3}{4} \right] (1 - \cos^2 \theta) (9 \cos^2 \theta - 1) \quad (2.24) \\
&= -\frac{1}{8} \frac{\nu^2}{\nu_0} \left[I(I+1) - \frac{3}{4} \right] (1 - \cos^2 \theta) (9 \cos^2 \theta - 1)
\end{aligned}$$

As can be observed in equation 2.24, the second-order quadrupolar interaction has rank 4 components, in addition to rank 2 and rank 0 tensors [109]. The second-order interaction is typically an order of magnitude smaller than the first-order interaction, as it is proportional to $\frac{\nu^2}{\nu_0}$. The effect of the second-order quadrupolar interaction upon the central-transition NMR spectrum in static regime can be seen in Figure 2.7.a (see section 2.4), where an anisotropically broadened powder-pattern lineshape is shown.

2.4. Magic angle spinning (MAS)

Magic angle spinning (MAS) is a technique, which allows high-resolution NMR spectra to be obtained from solid materials [128, 129]. MAS is used routinely to remove the effects of chemical shift anisotropy and to assist in the removal of homo and heteronuclear dipolar coupling effects. When the sample is spun about an axis, the spatial tensors become time dependent. This technique involves rotating the solid specimen about an axis inclined at the angle $54^\circ 44' 8''$ to the direction of the magnetic field of the NMR magnet. Every crystallite orientation has acquired a modulation factor $1/2(3\cos^2\theta_m - 1)$ ($=P_2(\cos\theta_m)$, the second-order Legendre polynomial). θ_m is the angle between the spinning axis and the magnetic field. If $P_2(\cos\theta_m) = 0$, then $\theta_m = \arccos(1/\sqrt{3})$. Several of the above interactions contain the term $(3\cos^2\theta - 1)$ where θ is the angle between the applied field and a direction which depends on the interaction (see Figure 2.6). This is strictly true if only first-order broadening effects are present. If the sample is rotated about an axis inclined at the angle θ_m to the applied magnetic field, then θ varies with time as the molecule rotates with the sample. The average of the orientation dependence is:

$$\langle 3 \cos^2 \theta - 1 \rangle = \frac{1}{2} (3 \cos^2 \theta_m - 1) (3 \cos^2 \beta - 1) = 0 \quad (2.25)$$

and therefore for $\theta_m = \arccos(1/\sqrt{3})$ this average value will be 0. The angle β is between the principal z-axis of the interaction tensor and the spinning axis (Figure 2.6).

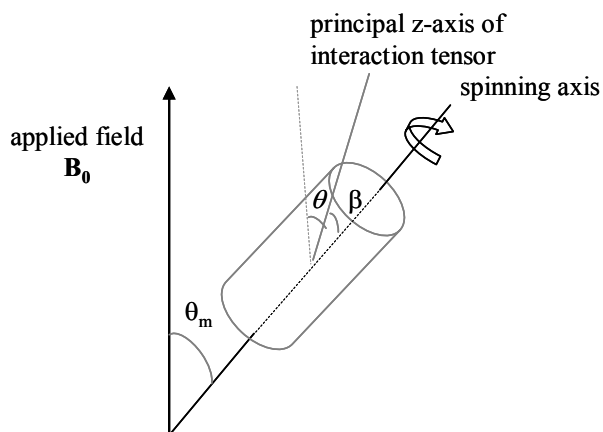


Figure 2.6. Schematic representation of the MAS experiment [116].

For a spin $I = 1/2$ nucleus, sufficiently rapid rotation about this particular axis removes most broadening interactions from the NMR spectrum leaving only fine structure and resolution which approaches that found in NMR spectra of liquids. If the detection is not rotor-synchronised, then the Hamiltonian will be time-dependent, leading to a more complicated spectrum. The spectrum will contain spinning sidebands (provided the interaction is larger than the modulation frequency) [130]. The spinning sidebands are signals separated from the isotropic line by integer multiples of the spinning frequency, ν_r .

The situation for MAS averaging of quadrupolar broadened lines is more complicated. As was shown in section 2.3 (see eq. 2.24), quadrupolar nuclei characterised by larger C_Q values and requiring treatment to second-order need to be described by rank 4 tensors. MAS and rotor-synchronized data acquisition removes only rank 2 tensors contribution thus the maximum expected narrowing of a quadrupolar dominated line is $\sim 30\%$ of the original static linewidth (see Figure 2.7).

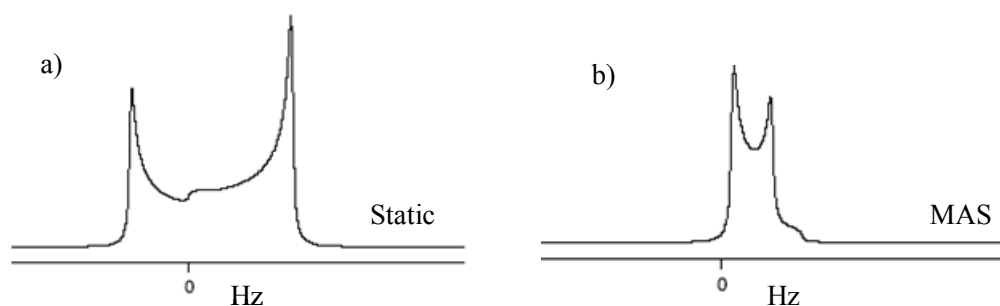


Figure 2.7. The effect of the second-order quadrupolar interaction under static (a) and MAS (b) conditions on the NMR lineshape for a nucleus with spin $I=3/2$ [127].

The maximum broadening is expected for a $\eta_Q = 0$ lineshape and the overall line narrowing reduces to a factor of 0.75 as η_Q approaches a value of 1.

2.5. Combined rotation and multiple-pulse spectroscopy

Although in principle sample spinning at the magic angle can eliminate the direct dipolar anisotropy, in many cases this is not practical for nuclei with high gyromagnetic ratios (such as ^1H) which have correspondingly large dipolar coupling constants. When these coupling constants are of greater magnitude than the technically achievable MAS rotation rates, MAS alone cannot fully average out the dipolar anisotropy. To eliminate dipolar coupling effects in such cases, radio-frequency (r.f.) spin irradiation can be used in decoupling sequences. This is the technique known as *Combined Rotation and Multiple-Pulse Spectroscopy* (CRAMPS) [131-134]. Radio-frequency pulsing makes the components of the spin angular momentum operators (\hat{I}_x , \hat{I}_y , \hat{I}_z) time-dependent. Therefore the CRAMPS technique uses rotations in both “spin space” and in the real space of the laboratory frame [134].

In CRAMPS, MAS at moderate speeds averages the chemical shift anisotropy whereas the application of a homonuclear *r.f.* decoupling sequence averages out the homonuclear dipolar coupling. This is accomplished by rotating the magnetisation with $\pi/2$ pulses along the x and y directions with phase cycling. The result is that the magnetisation vector spends an equal amount of time along each of the x, y and z axes; hence, the time-averaged magnetisation lies along the diagonal of a cube, which is oriented at the magic angle with respect to the applied magnetic field. The $(3\cos^2\theta_m - 1)/2$ factor that scales the dipolar interaction is thus zero; the pulse

sequence produces the same result as MAS, but without the requirement for fast sample spinning.

Among the various multiple-pulse schemes that are normally employed, the Lee-Goldburg (LG) [135], the Frequency-Switched Lee-Goldburg (FSLG) [136-138], the Phase-Modulated Lee-Goldburg (PMLG) [139], and the Decoupling Under Mind Boggling Optimisation (DUMBO) [140-143] sequences are most widely used for several years.

In this thesis CRAMPS using DUMBO sequences have been used in Chapter 6 in both single and double quantum dimensions to remove ^1H - ^1H homonuclear dipolar couplings in organic-inorganic hybrid systems.

2.6. Cross-polarisation

Even with the line-narrowing techniques described in *sections 2.4 and 2.5.*, NMR experiments on solids with spin -1/2 nuclei with low gyromagnetic ratio are still difficult to perform due to their lack of sensitivity and their long spin-lattice relaxation time. These problems can be overcome by using the cross-polarisation (CP) technique in solids [144-146] where both abundant (*I*) and dilute (*S*) nuclei coexist. Also it can be used to obtain information on which spins are close in space. Cross-polarisation (Figure 2.8.) transfer is mediated by the heteronuclear dipolar interaction between *I* and *S* spins.

The pulse sequence has three main steps (Figure 2.8 a) which in terms of the spin thermodynamics are [118]:

- Cooling down the abundant spin system
- Contact between the *I* and *S* spins to allow polarisation transfer
- Observation of the dilute spins.

First, the *I*-spins are converted into a non-equilibrium state: a 90° preparation pulse followed by a strong \mathbf{B}_I field in phase with the transverse magnetisation which then forces the *I*-spins to stay parallel to the \mathbf{B}_I direction (“spin-locking”). In the spin-locking frame, immediately after the 90° pulse, the *I*-magnetisation is still \mathbf{M}_I with the same degree of order, but the energy levels are now much closer (i.e. $\gamma\hbar B_I$ as opposed to $\gamma\hbar B_0$). With the new field B_I the system can now be assigned with an effective spin temperature T_{pI} defined by:

$$M_I = \frac{N_I \gamma_I^2 \hbar^2 I(I+1) B_0}{T_L} = \frac{N_I \gamma_I^2 \hbar^2 I(I+1) B_{II}}{T_{pl}} \quad (2.26)$$

where T_L is the thermodynamic lattice temperature.

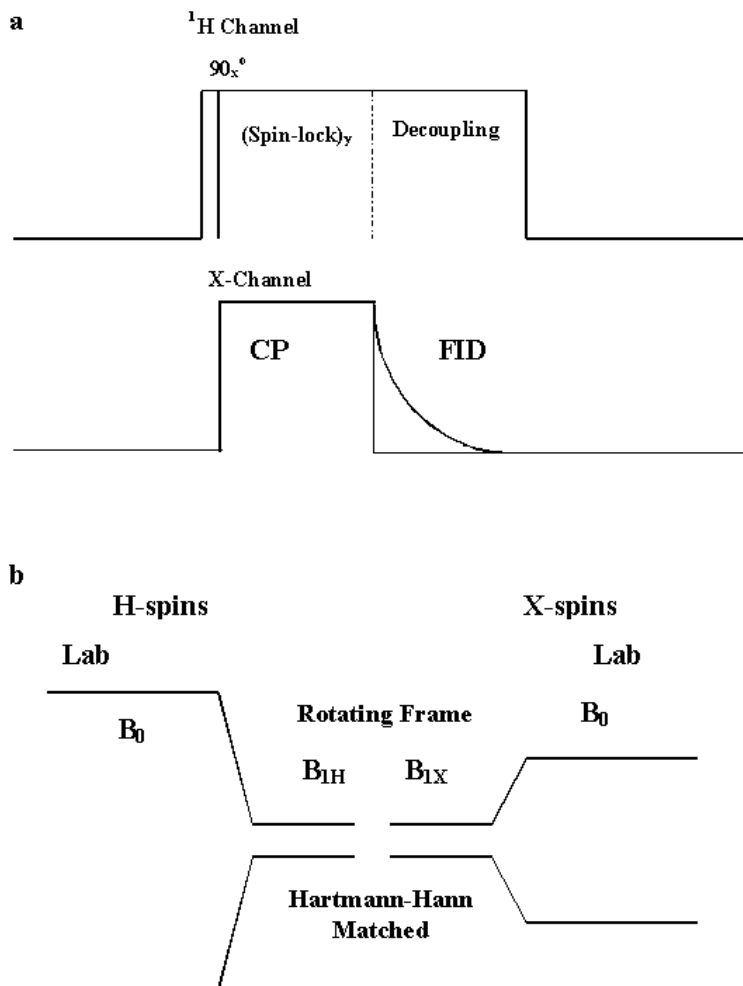


Figure 2.8. (a) Schematic representation of the CP sequence for $^1\text{H} \rightarrow \text{X}$. (b) The changes of the energy levels from the laboratory frame and in the rotating frame showing the Hartmann-Hahn condition [109].

As $B_{II} \ll B_0$ and the degree of order amongst the spins remains the same (i.e. M_I is constant) it follows that:

$$T_{pl} = \frac{B_{II} T_L}{B_0} \quad (2.27)$$

Hence the I -spins are effectively very cold. In contrast, the S -spins starts off with no transverse magnetisation, so in terms of thermodynamics, are very hot. However, the spin systems have to be allowed to communicate efficiently and this is achieved by applying a second B_I field, this time to the S -spins. If the two spins to be brought in contact are spin $\frac{1}{2}$ then the condition the two fields must meet is the Hartmann-Hahn condition [144] given for the static case by (Figure 2.6 b):

$$\gamma_I B_{II} = \gamma_S B_{IS} \quad (2. 28)$$

When this term is present the dipole-dipole flip-flop terms ($\hat{I}_+ \hat{S}_-$) are energy conserving therefore order can be transferred between the I and S spins. Thermodynamics means that the transfer of order occurs, tending to give the two systems a common spin temperature T_{p2} given by:

$$T_{p2} = T_{p1} \left[\frac{N_S}{N_I} + 1 \right] \quad (2. 29)$$

The implication of this equation is that the spin temperature for the I -spin system changes very little, so that I -magnetisation essentially remains unchanged as a result of the contact, while the S spins gain transverse magnetisation proportional with $|\frac{\gamma_I}{\gamma_S}|$ [109].

It was shown [118] that for many CP experiments where there are many more I spins than S , and when T_{IS} (contact time between spins I and S) $\ll T_{I\rho}^S$ (the relaxation time of the spin-locked S-magnetisation in the rotating frame) the following dynamics approximately hold:

$$M^{CP}(t) = M_0^{CP} \left[\frac{\exp\left(-\frac{t}{T_{I\rho}}\right) - \exp\left(-\frac{t}{T_{IS}}\right)}{1 - \frac{T_{IS}}{T_{I\rho}}} \right] \quad (2. 30)$$

In the above equation T_{IS} determines rate of transfer of magnetisation from I nuclei by dipolar interactions to S nuclei and hence the build up of signal, while $T_{I\rho}$, the relaxation time of the spin-locked I -magnetisation in the rotating frame, determines the time scale of the decay of magnetisation. The stronger the dipole coupling, the shorter contact time is.

In this thesis CP was applied to ^{13}C , ^{29}Si and ^{31}P to enhance the signal and to obtain information on which species are closed in space.

2.7. Two-dimensional methods

The methods described until now are one-dimensional methods, but even more can be learned if the information is spread into two dimensions. In this section the basic aspects of the two-dimensional (2D) spectroscopy will be presented. A detailed description of the pulse sequences of the different 2D techniques used to analyse the sol-gel bioactive glasses will be given in Chapter 3. 2D spectroscopy first proposed in 1971 by Jeener [147] and after performed by Aue *et al.* [148], has widespread use in sciences as physics, chemistry, biology and medicine. In a two-dimensional NMR experiments the pulse sequences can typically be described by four stages (Figure 2.9) [149]:

- a) a preparation period in which the pulses are applied to place the spin system in the desired initial non-equilibrium state,
- b) an evolution or frequency-labelling period (t_1). During the evolution period t_1 (this variable is important because whatever modulation that takes place in this period is going to be “carried over” to further periods of evolution) the system is allowed to evolve under suitably tailored Hamiltonians.
- c) a mixing period during which the spins may be subjected to further interactions and the system is interrogated by applying a pulse that creates observable magnetisation,
- d) a detection period (t_2) during which the signal is acquired.

To obtain a two-dimensional data set an array of one-dimensional spectra is collected with the evolution period (t_1 time) incremented from experiment to experiment.

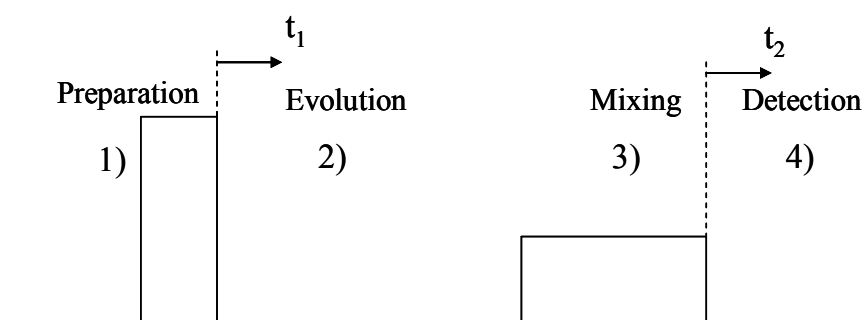


Figure 2.9. Time intervals in a basic two-dimensional experiment [109].

These data can then be Fourier transformed along each time dimension to obtain a two-dimensional spectrum which is a function of the frequencies ω_1 and ω_2 that characterise each time period. Thus the double transformation may formally be expressed as [115-117, 149-151]:

$$S(t_1, t_2) \xrightarrow{\text{FT over } t_2} S(t_1, f_2) \xrightarrow{\text{FT over } t_1} S(f_1, f_2) \quad (2.31)$$

2D correlation spectroscopy is based on the transfer of coherence from one transition to another and allows one to visualize the structure of the spin system. The term coherence can be understood as a relation between the m eigenstates of the nuclei in the system, where the order of the coherence is given by Δm [115].

In this thesis, for spin 1/2 nuclei, single-quantum (SQ)/double-quantum (DQ) homonuclear [152-156] and single-quantum (SQ)/single-quantum (SQ) heteronuclear (HETCOR) [157-160] MAS two-dimensional correlation spectroscopy (Figure 2.10) has been applied in the study of sol-gel derived bioactive glasses. In the case of SQ/SQ heteronuclear correlation the I and S spins are of different species. A peak on the spectrum correlates the I and S SQ frequencies. In HETCOR, the coherence transfer leads to an enhancement of sensitivity as well, by means of indirect detection, as will be shown in Chapter 7. In double-quantum (DQ)/single-quantum (SQ) correlation, spins I and S are of the same isotopic species. Thus, the DQ frequency, given in the indirect dimension, is the sum of SQ frequencies for a spin pair. A resonance peak due to double quantum coherence (DQC) between nuclei of the same SQ chemical shift (S - S) appears along the diagonal of the spectrum,

whereas peaks due to DQCs of nuclei with different SQ frequencies (I - S) appear equidistant from the diagonal. The lack of a peak at I - I indicates that no DQC exists between two spins of SQ frequency, ω_I .

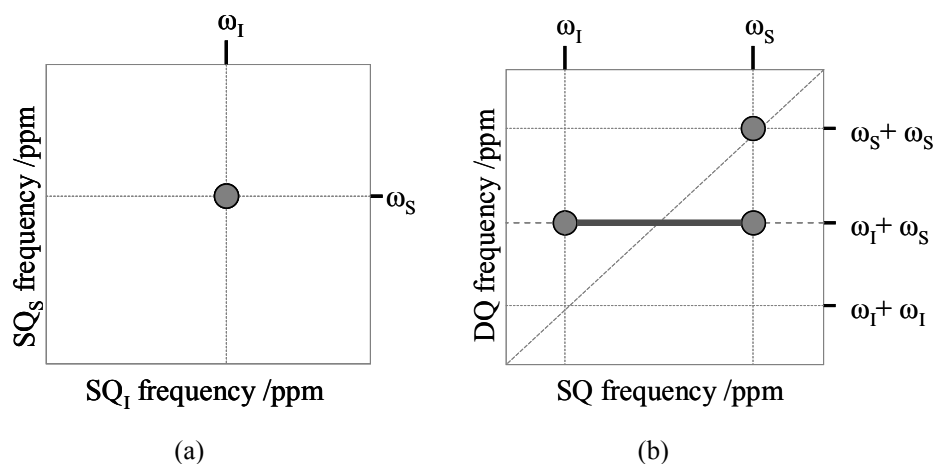


Figure 2.10. Schematic 2D (a) SQ-SQ and (b) DQ-SQ correlation spectra [156].

DQC in the above example can be described as a concerted evolution of coupled spins, which can be excited and detected under the irradiation of carefully designed *r.f.* pulse sequence, as it will be shown in Chapter 3.

For quadrupolar nuclei, to improve the resolution of spectra, multiple-quantum MAS (MQMAS) experiments have been performed in Chapter 7 for a spin $3/2$ nucleus. In 1995, Frydman *et al.* introduced the MQMAS technique for removing the second-order quadrupolar broadening [161, 162]. A combination of symmetric multiple-quantum and single-quantum coherences is used in half-integer spins to remove the anisotropic fourth-rank terms of the second-order quadrupolar interaction. A two-dimensional data set is obtained that correlates the multiple-quantum coherences (MQCs) ($m/2, -m/2$) in the indirect dimension, ν_1 , with single-quantum coherences ($1/2, -1/2$) in the direct dimension, ν_2 [163]. All coherences are assumed to be symmetric coherences ($m/2, -m/2$) as the effects of the first-order quadrupolar interaction can be neglected during periods of free evolution.

2.8. Relaxation mechanism

Relaxation is the aspect of the NMR that describes the dynamical processes in a system of spins. The magnetic moment of the sample changes from zero to \mathbf{M}_0 ,

the equilibrium value, in a magnetic field \mathbf{B}_0 . Bloch assumed that the components of \mathbf{M} decay to \mathbf{M}_0 exponentially, but he allowed the components of \mathbf{M} parallel and perpendicular to \mathbf{M}_0 to decay with different time constants T_1 and T_2 . With the z axis chosen along \mathbf{B}_0 the decay of magnetisation can be written as:

$$\frac{dM_z}{dt} = \frac{M_0 - M_z}{T_1} \quad (2.32)$$

$$\frac{dM_x}{dt} = \frac{-M_x}{T_2} \quad (2.33)$$

$$\frac{dM_y}{dt} = \frac{-M_y}{T_2} \quad (2.34)$$

The return to thermal equilibrium is known as relaxation where T_1 and T_2 are the relaxation times. The decay of the longitudinal component (\mathbf{M}_z) may differ from the decay of the transverse components (\mathbf{M}_x and \mathbf{M}_y) because the energy of the spin system depends on \mathbf{M}_z . Any change in \mathbf{M}_z is accompanied by an energy flow between the nuclear spin system and the other degrees of freedom of the system (lattice). The relaxation time T_1 which describes this flow is usually known as the *spin-lattice or longitudinal relaxation time*. T_2 is known as *the transverse or spin-spin relaxation time* as direct interactions between the spins of different nuclei can cause relaxation of \mathbf{M}_x and \mathbf{M}_y without energy transfer to the lattice.

The longitudinal magnetisation along the direction of the magnetic field \mathbf{B}_0 builds up as:

$$M_z(t) = M_0 \left(1 - \exp\left(\frac{-t}{T_1}\right)\right) \quad (2.35)$$

The component of magnetisation precessing in the x - y plane decays exponentially as the individual spins dephase, with relaxation time constant T_2 :

$$M_x(t) = M_{x,t=0} \exp\left(\frac{-t}{T_2}\right) \quad (2.36)$$

Hence any magnetization in xy - plane decays exponentially to zero. The transverse relaxation time is a result of the dephasing of the magnetization in the xy - plane of the magnetic moments precessing about B_0 . The moments do not experience the same magnetic field due to interactions and inhomogeneities in the static magnetic field B_0 . The T_2^* seen through the decay of the magnetization can be written as:

$$\frac{1}{T_2^*} = \frac{1}{T_2} + \frac{1}{T_2'} \quad (2.37)$$

where T_2 is the decay of the magnetization due to the interactions, and T_2' is due to the effect of inhomogeneities in the field. T_2 can provide information about the interactions and the nature of the motion that modulates the interactions and causes relaxation.

T_1 and T_2 relaxation are caused by local fluctuations in the magnetic or electric field at the nucleus [115]. T_1 and T_2 relaxation can also be induced through the quadrupolar, dipole-dipole and chemical shift anisotropy interaction mechanisms presented in section 2.3. The dipole-dipole and chemical shift anisotropy relaxations are smaller compared to quadrupolar one. The presence of paramagnetic species with unpaired electrons aids the relaxation mechanism.

3.

EXPERIMENTAL ASPECTS

3.1. Introduction

This chapter reviews the experimental aspects of the techniques used in this study. The first part of the chapter introduces the main equipment needed to perform an NMR experiment, introducing the standard detection and processing methods of the NMR signal, notably Fourier Transform spectroscopy. This is followed by the pulse sequences used to record the solid-state NMR spectra under Magic Angle Spinning (MAS) such that structural information for bioactive glasses can be observed. The relevant physical properties of NMR nuclei under study are also presented. Finally, the method of preparing the samples is discussed.

3.2. NMR experimental setup

The most important components of a pulsed Fourier Transform (FT) NMR spectrometer are shown schematically in Figure 3.1 a. A *waveform source* produces a continuous voltage oscillating sinusoidally at the desired frequency. This output is chopped into pulses by a *gate* opened and closed by a *pulse generator*, which is controlled by the *spectrometer computer*. The pulses are amplified and sent to the *NMR probe* which is placed at the centre of a high static magnetic field. The probe holds and spins the sample, couples the radiofrequency field to the spins, and picks up the NMR signal. Its crucial component is a coil of wire or foil placed around the sample, to which the transmitter pulses are applied. The alternating current in the coil generates a magnetic field with the same frequency and phase as the *transmitter*. The precessing nuclear magnetisation excited by this radiofrequency field induces in the coil an oscillating voltage, the NMR signal, which is passed to the *receiver*. After amplification, the NMR signal from the probe is mixed with a reference voltage, usually of the same frequency as the pulses used to excite the spins. This mixing subtracts the reference frequency from the NMR signal to produce an audio-frequency voltage (up to a few kHz), which is *amplified* further, *digitised* by an

analogue-to-digital converter (ADC) and *processed* in the computer where it can be manipulated and converted into a spectrum [164]. This difference in frequency is expressed as [115]:

$$\Omega = \omega_0 - \omega_{rf} \quad (3.1.)$$

where Ω is known as the *resonance offset frequency* of the observed nucleus, and describes the oscillation frequency with respect to the carrier frequency of the *r.f.* pulse.

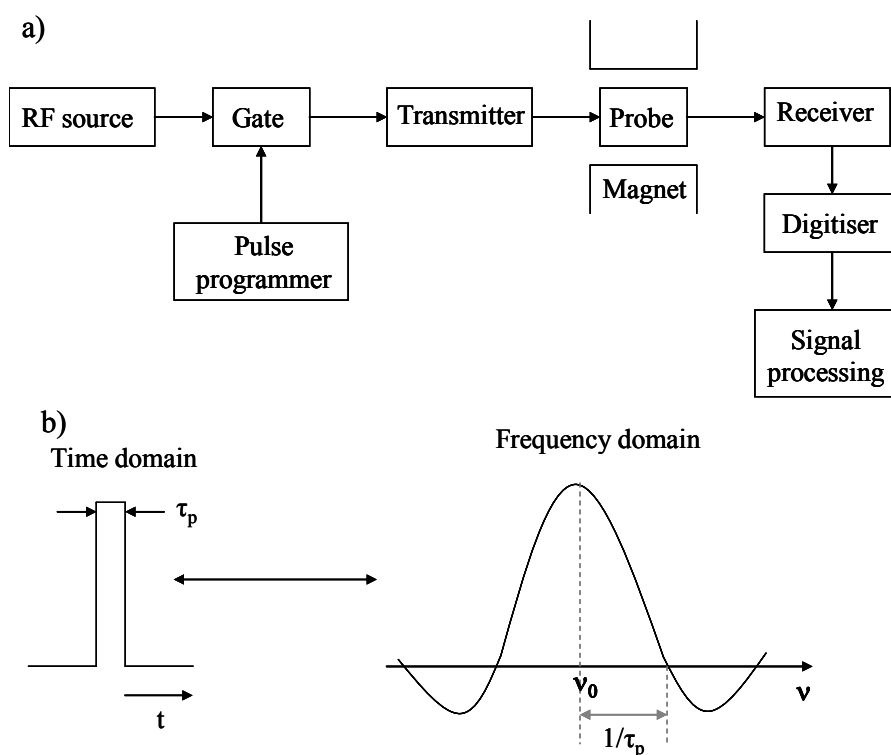


Figure 3.1. a) The basic components of a pulsed FT NMR spectrometer and b) The relationship between the time and frequency domains of an r.f. pulse of frequency ν_0 (Hz) and duration τ_p [109].

Spinning the sample at a precisely defined speed and angle places further design requirements on a solid-state NMR instrument. A critical component is the MAS speed controller which supplies the spinning gases, as well as monitors and controls the spinning speed. MAS involves the application of two separate gas streams: bearing gas to support the sample, and drive gas to spin it [165].

The most frequently used transform for NMR data processing is the Fourier transform (FT) that transforms time-domain data into frequency domain data. The NMR signal is often referred to as a Free Induction Decay (FID). Ordinarily, the FT takes in a FID and returns a spectrum. The Fourier transform for an angular frequency in units of rad/s, ω , can be defined as [115, 149, 151]:

$$S(\omega) = \int_0^{+\infty} s(t) \exp(-i\omega t) dt \quad (3.2)$$

where $\omega = 2\pi\nu$.

The distribution of *r.f.* magnetic field amplitudes, which represents the FT of a rectangular pulse of duration τ_p , takes the form [117]:

$$A(\nu) = \frac{\sin \pi \tau_p (\nu_0 - \nu)}{\pi (\nu_0 - \nu) \tau_p} \quad (3.3)$$

The carrier frequency is chosen to be close to resonance of the nucleus of interest, that $B_{\text{eff}} \sim B_1$. This distribution is illustrated in Figure 3.1.b, which shows the *frequency domain* equivalent, $S(\nu)$ of a short pulse in the *time domain*, $s(t)$.

The FID is detected using two orthogonal detection channels which are 90° out-of-phase with each other, where one analog-to-digital converter (ADC) gives the real part and the other gives the imaginary part [117, 149]. This is known as *quadrature detection*. The advantage of quadrature detection is the ability to determine sign information, enabling the transmitter frequency to be placed in the middle of the spectral window [166]. This technique also leads to further performance advantages, e.g., signal-to-noise improvements of $2^{1/2}$ [167].

Two-dimensional Fourier transformation, which plays a central role in 2D spectroscopy, is a straightforward generalisation of the one-dimensional Fourier transformation discussed above. A schematic 2D experiment has been shown in Figure 2.9. The preparation *r.f.* pulses are used to generate spin coherences which are detected during the t_1 period, and mixing pulses create the final detectable coherences, measured in t_2 , which must be of the order $p = -1$ to induce an NMR signal in the receiver coil.

2D spectra can be phase or amplitude-modulated. These expressions refer to the t_1 -dependence of the signal $s(t_1, t_2)$ which becomes particularly obvious after 1D-Fourier transformation with respect to t_2 : depending on the type of 2D experiment the spectrum $s(t_1, \omega_2)$ may appear modulated either in amplitude or in phase as a function of t_1 . Phase-modulated 2D spectra give rise to unwanted phase twist peaks, a mixture of absorption and dispersion mode one-dimensional Lorentzians, with dispersion in the middle and absorption at the edges. Pure phase 2D spectra can be obtained for amplitude modulation [150, 168]. The amplitude-modulated time-domain signal may be converted into a pure 2D spectrum by a 2D Fourier transformation that is real with respect to t_1 and complex with respect to t_2 [149]. Four signal components are distinguished in such a way that real and imaginary parts can be combined independently in both dimensions, by introducing a hypercomplex 2D Fourier transformation [149]. For amplitude modulated 2D spectra the signal can be recorded according to the States [169], time-proportional phase increments (TPPI) [170] or combined States-TPPI [171] methods.

The States technique [169] acquires two complementary amplitude-modulated signals for each Δt_1 increment of the two-dimensional experiment, where the second phase of the preparation pulse is shifted by $\pi/2|p|$, where $|p|$ is the order of coherence in the evolution period. In the TPPI [170] method only one FID is recorded for each Δt_1 increment. The increment in t_1 is halved to $1/2sw_1$ (sw_1 represents the spectral width of the indirect dimension), and the phase of the preparation pulse is shifted for each successive t_1 increment by $\pi/2|p|$.

The States method [169] in the HETCOR and MQMAS experiments or the combined States-TPPI [171] method in SQ-DQ correlation experiments have been used in this work. The States-TPPI technique combines the principles of both methods, such that, two FID signals are recorded $\pi/2$ out of phase with one another as in the States method, and the phase of the preparation pulse is inverted by a phase change of π .

3.3. Pulse sequences

The different pulse sequences used to investigate the bioactive sol-gel samples are presented in the next sections.

3.3.1. Single pulse experiment

A simple, single pulse experiment is presented in Figure 3.2. The magnetisation is tipped through the flip angle $\phi_1 = -\gamma B_1 \tau_p$ and the FID is measured using a four step phase cycle sequence, CYCLOPS (CYCLically Ordered Phase Sequence) [172], with phases of the *r.f.* being successively shifted by 90° . Usually ϕ_1 is $\pi/2$ radians. For example, a $\pi/2$ pulse of a $2.5 \mu\text{s}$ width corresponds to 100 kHz *r.f.* field. The FID is not acquired immediately after the pulse as the electronics take a finite time to switch the amplifiers off, and get the receiver ready for acquisition. This time is known as *deadtime*.

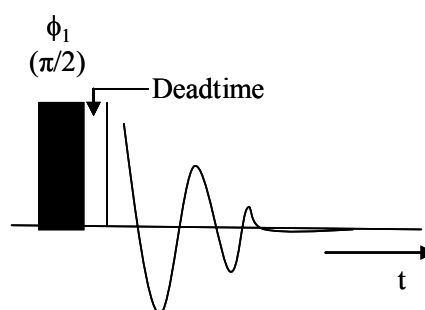


Figure 3.2. A single pulse sequence.

Another effect contributing to the *deadtime* is probe coil ringdown. When the B_1 pulse is applied to the coil, immediately, it is subjected to a force between the oscillating current in the coil and the static B_0 field. This causes it to oscillate at the Larmor frequency ω_0 , and when the pulse is turned off, its continued oscillation within B_0 can cause a voltage to be induced in it. The receiver can detect this effect and the time taken for the signal to decay is dependent on the diameter of the coil, the frequency of the pulse and the material the coil is made of [109].

If the T_1 relaxation time for the sample is long, different tip angles can be used to overcome the problem of the time between repeating the experiment. Since silicon can suffer from a long relaxation time, 30° and 45° tip angles were used for the ^{29}Si measurements.

For the quadrupolar nuclei, the 90° pulselength is usually measured for a solution reference. Since the angle through which the magnetisation of the quadrupolar nucleus is tipped depends on the quadrupolar coupling constant (C_Q) the

nucleus experiences, as well as the length of the pulse, typically a small tip angle ($\leq \pi/6$ on a solution) is used [173]. If the quadrupolar interaction is much larger than the applied *r.f.* field, the optimum pulse lengths for selective NMR excitation of any single-quantum transition for quadrupolar nuclei in the solid state are given by [174]:

$$\tau_p = \frac{\pi}{2\omega_1 \sqrt{I(I+1) - m(m+1)}} \quad (3.4)$$

For selective excitation of the central transition, as $m = -1/2$, equation 3.4 simplifies to:

$$\tau_p = \frac{\pi}{2\omega_1 \left(I + \frac{1}{2}\right)} \quad (3.5)$$

For a powder sample, this does not mean that only the central transition is excited since, for certain orientations, the satellite transitions will be in the same spectral range as the central transition. Thus, for powder samples, the term of “partly selective” pulses is often used [165]. Therefore quantitative analysis can be performed on spectra of quadrupolar nuclei if a small tip angle is employed.

3.3.2. Pulsed echo experiment

The echo pulse sequence [175] is shown in Figure 3.3. In this experiment, the magnetisation is first tipped by a ϕ_1 pulse (usually 90°) and allowed to evolve for a time τ . It is then tipped by a pulse twice as long (180°), and after another time τ an echo is created. The first pulse tips the magnetisation about the y-axis from lying on the z-axis onto the x-axis. These spins then dephase in the x-y plane since some spins will precess faster than the rotating frame precession, and some spins will precess slower. This causes the FID signal to decay to zero. After a time τ , the magnetisation is flipped 180° about the y-axis, so the dephased spins still lie in the x-y plane, but are a mirror image of themselves. The spins now precess in the opposite direction at the same speed as they dephased at, so a time τ after the second pulse, all the spins recombine to create an echo.

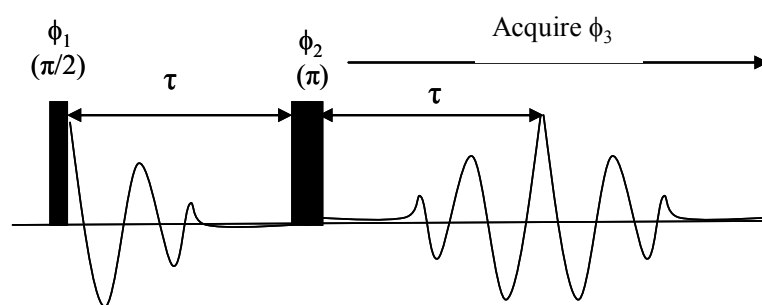


Figure 3.3. A pulse echo sequence.

Under MAS, τ needs to be an integer number of rotor cycles.

3.3.3. Cross polarisation and heteronuclear decoupling

Cross polarisation (CP) is a two channel technique which transfers magnetisation from the high- γ spins, I, to the low- γ spins, S.

The pulse sequence (see Figure 2.8.) starts with a 90° pulse on the I channel which effectively moves the I nuclear magnetisation onto the x-y plane in the rotating frame picture. This is followed by a contact pulse on both channels. When the Hartmann-Hahn condition is met ($\gamma_I B_{1I} = \gamma_S B_{1S}$), then both I and S nuclei will precess at the same rate. The magnetic energy level splittings for the two species are then equal, so transverse magnetisation from the I nuclei induced by the earlier 90° pulse which is then spin-locked into the x-y plane can then exchange energy with nearby S nuclei. When the contact pulse is turned off, a normal FID can then be measured from the S channel nuclei since S magnetisation is now effectively precessing in the x-y plane. A decoupling field is usually applied to the I nuclei whilst S signal is acquired, which effectively causes a continual precession of the I spins so that any dipolar coupling between I and S nuclei is averaged out and increases the resolution of the S resonances. Under MAS, the match condition given in Eq. 2.28 is modified to:

$$\gamma_I B_{1I} = \gamma_S B_{1S} \pm n\omega_r \quad (3.6)$$

where $n = 1, 2$ and ω_r (in rad/s) is the rotation frequency of the rotor [146]. Magic angle spinning averages out dipolar couplings where the degree of averaging

increases with ν_r ($\omega_r/2\pi$, in kHz) and therefore reduces cross-polarisation efficiency. CP is observed to be more efficient under fast MAS when a pulse of ramped amplitude [176-178] is applied on one of the channels to broaden the matching conditions for the spin system (see Fig. 3.4). In Figure 3.4 the ramp amplitude was applied to I channel, as it was used in this study.

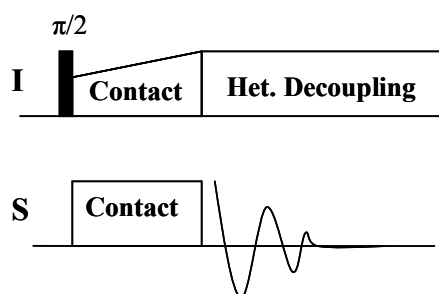


Figure 3.4. Cross polarisation (CP) pulse sequence used to enhance the sensitivity of a dilute spin, S, in the presence of an abundant spin, I.

Contrary to direct excitation of the S nuclei, the necessary delay between acquisitions is determined by the relatively short spin-lattice relaxation time, T_{1I} , of the I nuclei and not by the long relaxation time, T_{1S} of the S nuclei, which is a further advantage of CP. Therefore many measurements of the FID can be acquired over a shorter experimental time period. Because dipole-dipole interactions decay with the third power of the distance (see equation 2.18), this technique will only excite resonances of S nuclei that are close enough to the I nuclei to exchange magnetisation efficiently during the contact period. The heteronuclear decoupling scheme used in this work, is the SPINAL-64 (*small phase incremental alternation*, with 64 steps) [179] sequences, which is generally applied at ν_1 (^1H) = 100 kHz and for MAS spinning frequencies, $\nu_r = 12.5$ kHz. The two basic elements Q and \bar{Q} of the SPINAL-64 sequences are constructed in the following way:

$$Q: \phi_p - \Delta\phi_p \quad -\phi_p + \Delta\phi_p \quad \phi_p \quad -\phi_p \quad \phi_p + \Delta\phi_p \quad -\phi_p - \Delta\phi_p \quad \phi_p \quad -\phi_p$$

$$\bar{Q}: -\phi_p + \Delta\phi_p \quad \phi_p - \Delta\phi_p \quad -\phi_p \quad \phi_p \quad -\phi_p - \Delta\phi_p \quad \phi_p + \Delta\phi_p \quad -\phi_p \quad \phi_p$$

These elements are then combined into SPINAL-64 supercycle sequences:

$$\text{SPINAL-64} = \overline{Q}\overline{Q}\overline{Q}\overline{Q}\overline{Q}\overline{Q}\overline{Q}\overline{Q}$$

Here ϕ_p and $\Delta\phi_p$, the phase of the pulse and the phase difference between pulses, are 15° and 5° , respectively. Each pulse duration corresponds to a flip angle of slightly less than 180° ($5 \mu\text{s}$ for $\nu_1 = 100 \text{ kHz}$).

This technique is applied in this thesis for $I = {}^1\text{H}$, $S = {}^{13}\text{C}$, ${}^{29}\text{Si}$ and ${}^{31}\text{P}$. As the S magnetisation is derived via a transfer process that depends on the heteronuclear dipolar coupling, the CP technique is a semi-quantitative method determined by the relative I-S proximities, as well as the effect of any motional processes.

3.3.4. Homonuclear decoupling

In organic molecules due to strong homonuclear dipole-dipole interactions (*see section 2.3.2.*), the signal of ${}^1\text{H}$ nuclei is poorly resolved, which lead to a broadening of the spectra. While the effect of these broadening mechanisms is reduced as ν_r increases, even at fast spinning speeds, adequately resolved ${}^1\text{H}$ spectra in such systems are still difficult to obtain. Therefore by using the *CRAMPS method* (*see section 2.5.*) efficient line-narrowing in ${}^1\text{H}$ spectra of molecules with strong dipole-dipole couplings can be achieved [141, 143, 156, 180, 181].

In this work homonuclear decoupling sequences from the DUMBO family [140-143], namely window DUMBO-1 [140, 141] and eDUMBO-1₂₂ [142], have been used to obtain high resolution ${}^1\text{H}$ spectra. DUMBO families are robust and efficient on-resonance homonuclear decoupling sequences based on continuous modulation of the phase of *r.f.* field [140-143]. This allows numerical optimization of decoupling performance using computer models of the behaviour of the spin system [140]. The phase function of the DUMBO-1 sequence was generated as a Fourier series. The length of the basic cycle (cycle time, τ_c) corresponds to a 6π *r.f.* pulse, (3 complete rotations about the effective field B_{eff}).

The original DUMBO-1 scheme [140] was developed in a “quasi-static” regime which assumes that the spinning speed is slow compared to the cycle time, τ_c , of the pulse sequence [131, 134]. Later it was experimentally optimised for ${}^1\text{H}$ spectra under MAS, at $\nu_r = 22 \text{ kHz}$ and 12.5 kHz , leading to the eDUMBO-1₂₂ and eDUMBO-1_{12.5} schemes [142], respectively. It was shown that eDUMBO-1₂₂

homonuclear decoupling sequences lead to high-resolution ^1H spectra up to spinning rates of $\nu_r = 65$ kHz [143].

It was suggested [141] that the window DUMBO-1 be used for direct ^1H detection whereas the eDUMBO-1₂₂ is preferred for indirect time-evolution periods.

Figure 3.5 shows the pulse sequences used to perform the 1D CRAMPS experiments, where window DUMBO-1 [140, 141] homonuclear decoupling scheme has been employed.

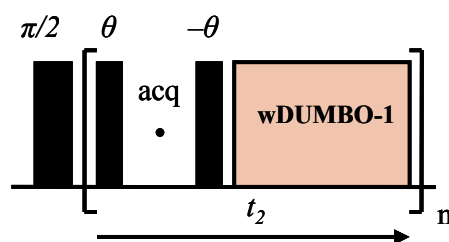


Figure 3.5. Pulse sequence of continuous 1D windowed homonuclear decoupling for obtaining a directly detected high-resolution ^1H spectrum.

A decoupling amplitude of $\nu_l = 100$ kHz, corresponding to a DUMBO-1 cycle time (6π) of $30 \mu\text{s}$ was used. The best duration that was found was $24 \mu\text{s}$ for DUMBO-1, the phase being switched across 320 steps. Each cycle is surrounded, before and after, by a short prepulse, such that the spin magnetisation spends the same amount of time along each of the x, y and z axes during one cycle of the decoupling block. These prepulses are given by the flip angle θ , with a duration typically between $0.5\text{-}1 \mu\text{s}$. The initial phase of the DUMBO-1 pulse is usually $160\text{-}230^\circ$. The duration of the prepulse and initial phase of the DUMBO-1 pulse are optimised to give the smallest central frequency artefact in the decoupled ^1H spectrum. The chemical shift axis is also scaled by the homonuclear decoupling sequence. The scaling factor has been determined for each sample by a superposition of the spectra performed under CRAMPS and non-decoupled MAS.

3.3.5. Two-dimensional NMR techniques

3.3.5.1. Homonuclear correlation

The techniques described until now have been focussed upon the averaging or removal of dipolar interactions in the solid-state by MAS or CRAMPS in order to

obtain high-resolution spectra. As the magnitude of the dipolar coupling between a pair of nuclei, (given by d , see Eq. 2.18) is related to the internuclear separation of the two spins, a controlled reintroduction of the dipolar interaction under MAS NMR (dipolar *recoupling* [182, 183]) can provide spectra containing information about interatomic proximities in solids. As the dipolar coupling is completely averaged to zero over each period of MAS rotation, the application of r.f. pulses specifically synchronised with the rotor period, τ_r (and applied at intervals of less than τ_r) reintroduce the effect into the spin system [183].

The ^1H - ^1H proximities have been studied in this thesis in Chapter 6 for the organic-inorganic hybrid systems by the generation of ^1H - ^1H double-quantum coherences (DQC) between coupled spin pairs [156].

Symmetry based recoupling CN_n^v sequences, introduced by Levitt *et al.* [183, 184] are an efficient set of schemes for spin-interaction recoupling, where N , n and v , the symmetry numbers, are integers. The symbol CN_n^v refers to a set of rotor synchronized *r.f.* pulse cycles, with the following properties [184]:

- Each *r.f.* cycle has a duration $\tau_c = n\tau_r/N$, where $\tau_r = 2\pi/\omega_r$ is the rotation period, and ω_r is the sample rotation frequency. This implies that N *r.f.* cycles are timed to coincide with n sample rotation periods.
- Each *r.f.* cycle is designed to provide no net evolution of the nuclear spin states, when only the *r.f.* field is taken into account.
- The *r.f.* phase of consecutive cycles differs by $2\pi v/N$. The phase (ϕ) of the p^{th} cycle is therefore given by $\phi_p = \phi_0 + 2\pi vp/N$, with $p = 0, 1, 2, \dots$. Here ϕ_0 is the initial phase of the whole block.

The duration of an entire CN_n^v sequence is denoted $T = N \cdot \tau_c$. The symmetry numbers n and v represent the spatial sample rotation and the phase rotations of the r.f. fields, respectively. A complete sequence consists of n complete sample rotations and v complete r.f. phase rotations. The sample rotation is continuous, while the pulse phase rotations are performed in N discrete steps. In the general case, each element C_ϕ may itself consist of pulses with different phase [184]. The $C7_2^1$ sequence recouples homonuclear dipole-dipole coupling terms. This symmetry generates a double-quantum recoupling sequence.

The Permutationally Offset Stabilized C7 (POST-C7) [185] sequence, is given in Figure 3.6, where the C_ϕ elements are divided into component pulses of *flip angle*, θ , and *overall phase*, ϕ , in degrees. In the POST-C7 method, the phase ϕ is incremented by $(2\pi/7)$ radians between successive elements.

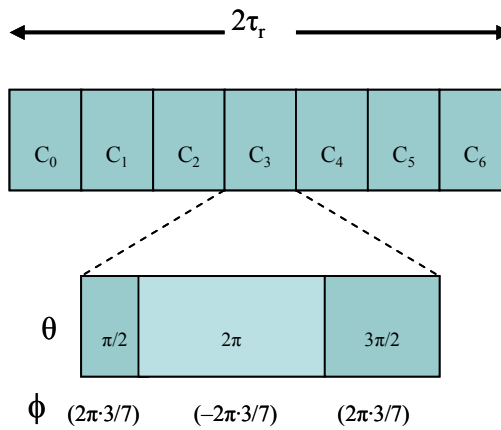


Figure 3.6. Pulse sequences for the symmetry-based POST-C7 sequence [185].

The POST-C7 dipolar recoupling sequence is used in this thesis in the two-dimensional DQ-SQ CRAMPS experiment shown in Figure 3.7.

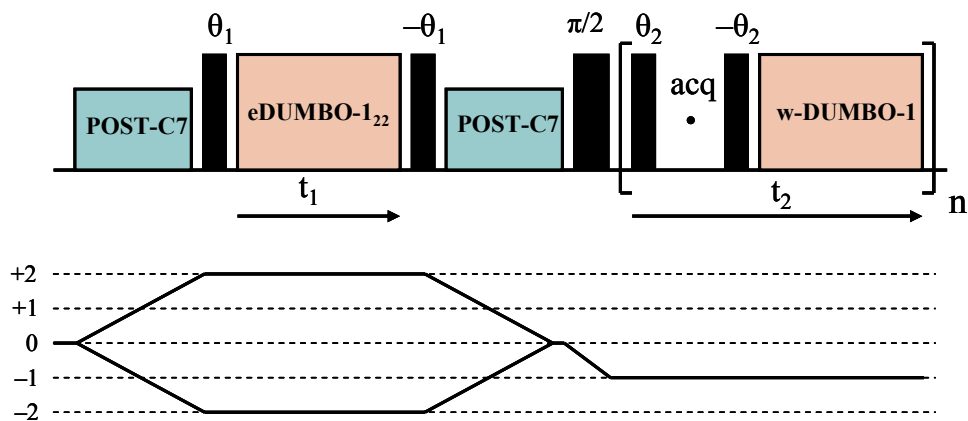


Figure 3.7. Pulse sequence and coherence transfer pathway diagram for the ^1H DQ CRAMPS experiment [155]. eDUMBO-1₂₂ [142.] and windowed DUMBO-1 [140, 141] homonuclear decoupling are applied in t_1 and t_2 , while DQ excitation and reconversion is achieved using the POST-C7 recoupling sequence [185].

High-resolution ^1H spectra are obtained by the use of two phase-modulated homonuclear decoupling schemes, the windowless eDUMBO-1₂₂ [141] and windowed-DUMBO-1 [140, 141] (see section 3.3.4.), applied in the t_1 and t_2 dimensions, respectively. The length, together with the phases (relative to that of the eDUMBO scheme) of the prepulses θ_1 , was carefully calibrated to minimize the artifact in $f1$. The pulse θ_1 before t_1 ensures that there is no magnetisation component along the effective field of the eDUMBO-1₂₂ sequence [141]. A second pulse θ_1 after t_1 rotates the magnetisation back in preparation for the application of the DQ reconversion sequence. In addition, prepulses θ_2 were inserted before and after each detection window to minimize quadrature images in the direct dimension. POST-C7 was chosen for the excitation and reconversion of DQ coherences. The C7 and POSTC7 sequences have a phase dependence upon the rotor phase, resulting in increased DQ efficiency and negating the need for rotor-synchronised 2D experiments [184].

As a result of the $C7_2^1$ symmetry condition, the nutation frequency of the DQ irradiation is given by $\omega_{1C7} = 7\omega_r$. The *r.f.* amplitude applied is typically 100 kHz. The experiments were performed at $\nu_r = 12.5$ kHz, corresponding to a recoupling amplitude of $\nu_1 = 87.5$ kHz. A Bruker 4 mm probe has been used in these experiments.

The number of C_ϕ elements used for excitation and reconversion, optimised in general to 3 elements (the recoupling time, $\tau_{\text{rec}} = 68.6$ μs , corresponding to a spinning speed of 12.5 kHz [155]) was found to give maximum DQ intensity.

It has been shown [156] that pairs of ^1H - ^1H DQ peaks are generally observed in such 2D spectra for internuclear ^1H distances of approximately $<3.5\text{\AA}$.

3.3.5.2. Heteronuclear correlation

The most basic type of single-quantum (SQ)/single-quantum (SQ) heteronuclear correlation (HETCOR) experiment in solids is simply a two-dimensional extension of cross-polarisation experiment in which the pulse that generates the initial transverse magnetisation is separated from the Hartmann-Hahn matching pulses by a time period t_1 [157]. The pulse sequence and the coherence transfer pathway diagram for the heteronuclear correlation experiments used in this thesis are shown in Figure 3.8.

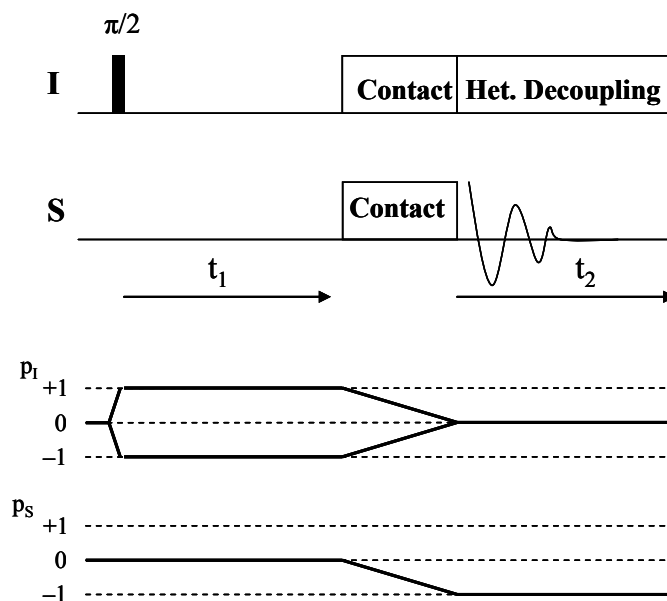


Figure 3.8. Pulse sequence and coherence transfer pathway diagram for the SQ-SQ HETCOR experiments. p_I and p_S represent the coherence order of I and S nuclei, respectively.

In this work, the mixing sequence used in heteronuclear correlation experiments to promote transfer of magnetisation between heteronuclei is a cross-polarisation step, with a properly adjusted contact pulse being applied to each nucleus. The CP pulse sequence was discussed in *section 3.3.3*. The experiment begins by exciting single-quantum coherence (transverse magnetisation) on spins I and allows it to evolve in t_1 . Contact pulses applied to both spins at the end of t_1 result in cross-polarisation from spin I to spin S , after which the resulting S spin transverse magnetisation is observed in t_2 . The SPINAL-64 [179] sequences (see *section 3.3.3*) have been used during the heteronuclear decoupling schemes. In the experiments the t_1 increment was set as an integer number of the rotor period ω_r . The resulting two-dimensional spectrum will then correlate specific sites in the MAS spectrum of the first nucleus with the sites of the second nucleus that are near enough for polarisation transfer to occur between them. The peak intensities are typically not quantitative, but HETCOR experiments can provide qualitative information about spatial proximity. In this work, experiments are typically carried out at $\nu_r = 12.5$ kHz, using a Bruker 4 mm probe and have been applied to ^{29}Si and ^{31}P in Chapter 7.

3.3.5.3. Multiple-quantum MAS (MQMAS)

The principle of a MQMAS experiment is that the $\langle m, -m \rangle$ multiple quantum transition is correlated to the $\langle 1/2, -1/2 \rangle$ transition [161, 162]. The MQMAS experiment is used to achieve high resolution spectra for half integer quadrupolar nuclei, in this thesis being applied to ^{23}Na throughout Chapter 7. The resolution enhancement stems from the fact that the quadrupole frequencies for both transitions are correlated. The frequency of a $\langle m, -m \rangle$ transition, in Hz, is given by:

$$\nu_p = C_0(p)\nu_0^Q - \frac{7}{18}C_4(p)\nu_4^Q(\theta, \phi) \quad (3.7)$$

where $p = 2m$ is the order of the coherence, $p = 1$ for the $\langle 1/2, -1/2 \rangle$ transition, $p = 3$ for the $\langle 3/2, -3/2 \rangle$ transition. ν_0^Q and $\nu_4^Q(\theta, \phi)$ represent the isotropic and the anisotropic part of the quadrupole frequency. The coefficients are defined as:

$$C_0(p) = p \left(I(I+1) - \frac{3}{4}p^2 \right) \quad (3.8)$$

$$C_4(p) = p \left(18I(I+1) - \frac{17}{2}p^2 - 5 \right) \quad (3.9)$$

Table 3.1 gives a list of the values of the coefficients for the various coherences for a spin $I = 3/2$ quadrupolar nucleus.

Table 3.1. NMR parameters for different transitions of a quadrupolar nucleus with $I = 3/2$.

I	m_z	$p = \Delta m_z$	$C_0(p)$	$C_4(p)$	$C_4(p)/C_4(1)$ QA
3/2	1/2	1	3	54	
	3/2	3	-9	-42	-7/9

The ratio of the rank 4 anisotropic broadening between triple- and single-quantum coherences is referred to as the quadrupole anisotropy (QA). For spin $I = 3/2$ it equals $-7/9$.

In order to select symmetrical coherence-transfer pathways ($0, \pm 3, 0, -1$) and to avoid distortions of the spectra, a sequence of three *r.f.* pulses (Figure 3.9), including a z-filter pulse (zero-quantum filter), ϕ_3 , [186] has been used.

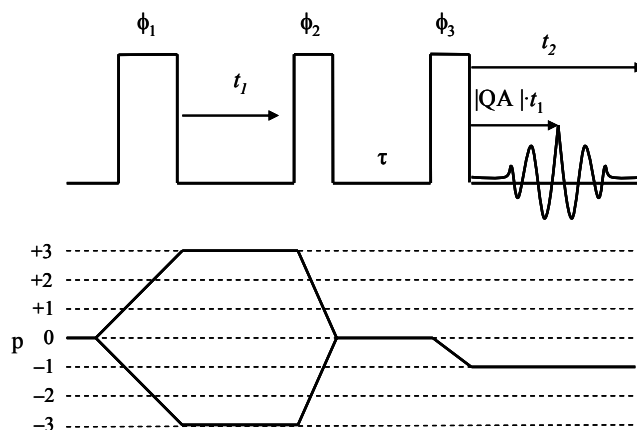


Figure 3.9. MQMAS pulse sequence and the coherence pathways.

The first pulse ϕ_1 is a 180° pulse and creates the maximum amount of ± 3 quantum symmetrical coherences. Both coherences evolve during t_1 period. During the 3Q evolution, the second-order quadrupolar interaction is averaged as the experiment is conducted under MAS. The second pulse ϕ_2 is approximately a 60° pulse and converts the 3Q coherences to zero quantum coherence, which evolves for a period τ . The first two pulses use a strong *r.f.* field in order to maximize excitation and conversion efficiencies. By applying phase cycling only populations of $\pm 1/2$ levels are not negligible after the second pulse and the z-filter (ϕ_3). The z-filter transforms both these populations into an observable signal of coherence $p=-1$, which is observed during t_2 . The signal is then acquired immediately after the third pulse and the echo will form at a time $t_2 = |QA| \cdot t_1$, where QA is given in Table 3.1. The last pulse is a selective 90° pulse of moderate *r.f.* field. The pulses have been optimized independently by using the first spectrum ($t_1=0$). The States method [169] has been used for sign discrimination.

In this work, the *r.f.* amplitudes for the first two pulses were ~ 160 kHz, corresponding to pulse lengths of $3 \mu\text{s}$ and $1 \mu\text{s}$, respectively. The z-filter is a soft pulse of a length of $17 \mu\text{s}$, corresponding to a *r.f.* field of ~ 15 kHz.

The time delay τ needs to be long enough to change the phase and amplitude for the selective 90° pulse. This is due to the fact that the delay acts to remove other unwanted coherences, which can appear because of incomplete relaxation between cycles and so inefficient removal of unwanted coherences by phase cycling. τ is set as $n\tau_r$, where $\tau_r = 2\pi/\omega_r$ is the rotor period, and n is an integer. Here $\tau = 20 \mu\text{s}$. Fourier-transformation results in a two-dimensional frequency spectrum in which the f_1 dimension exhibits an isotropic spectrum and the f_2 dimension, the anisotropic powder patterns associated with the central transition (corresponding to a single quantum coherence which evolves during t_2) of the different sites. The MQMAS spectra in this work have been performed using a Bruker 3.2 mm probe at 20 kHz spinning speed.

3.4. Experimental parameters of NMR nuclei

In comparing nuclei, a first consideration is the sensitivity which is given by the receptivity of a nucleus. The receptivity is a measure of the amount of signal expected to be obtained for a nucleus, and it is defined as [117, 173]:

$$\gamma^3 C I(I+1) \quad (3.10)$$

where C is the natural abundance of the isotope under investigation.

One of the most important factors the signal depends on is the applied magnetic field, with the signal being proportional with B_0^2 , also depends on the T_1 spin-lattice relaxation time of the nucleus, which differs between different systems and nuclei. Some of the relevant properties of the nuclei studied during this work are presented in Table 3.2.

Table 3.2. Physical properties of the NMR nuclei studied in this thesis [109, 117].

Isotope	Spin	C (%)	$\gamma / 10^7$ (rad T ⁻¹ s ⁻¹)	Q (10 ²⁸ Q/m ²)	Quadrupole broadening	Receptivity relative to ¹³ C
¹ H	1/2	99.985	26.75	-	-	5.67×10^3
¹³ C	1/2	1.108	6.73	-	-	1.00
²⁹ Si	1/2	4.70	-5.32	-	-	2.10
³¹ P	1/2	100	10.84	-	-	3.77×10^2
²³ Na	3/2	100	7.08	0.1	2.47	5.26×10^2
⁴³ Ca	7/2	0.145	-1.80	-4.08×10^{-2}	1.39×10^{-1}	4.92×10^{-2}

The quadrupole broadening provides the second-order quadrupolar broadening factor, normalised to ^{27}Al , which is proportional to [173]:

$$\frac{Q^2}{\gamma} \frac{(a - \frac{3}{4})}{(2I(2I-1))^2} \quad (3.11)$$

where $a = I(I+1)$. γ and Q represent the magnetogyric ratio of the nucleus and the quadrupolar moment for quadrupolar nuclei, respectively.

^1H is a spin $\frac{1}{2}$ nucleus that is very abundant (99.985%). Due to its high sensitivity and natural abundance, the proton constitutes an attractive nucleus to probe the structure of powdered materials by solid-state NMR. In this study, it is used to follow the hydrogen content and speciation, which appear strongly connected to bioactivity and the loss of hydroxyls and organic groups directly. It has been known that ^1H MAS NMR of glasses can distinguish different proton species in glasses at relatively modest MAS rates [187] due to the relatively low proton density and hence weak dipolar coupling. However, in organic-inorganic systems, the dipole-dipole interactions are strong and higher MAS speed or CPMAS was used in this study in Chapter 6, either to determine the speciation of these systems in 1D or to probe ^1H - ^1H proximities in SQ-DQ homonuclear correlation.

^{13}C is a spin $\frac{1}{2}$ nucleus that has a low natural abundance of 1.1%. Due to its low sensitivity, ^{13}C signal is routinely enhanced by the use of ^1H - ^{13}C CP. In this study, ^{13}C CP NMR is used to determine or confirm the structures of residual (unhydrolysed/uncondensed) alkoxy groups of the sol-gel starting materials and to follow the loss of organic fragments groups directly with the temperature. Also it was used to examine the bonding between the organic (polymer) and the inorganic (silicate) components for hybrid samples.

^{29}Si is a spin $\frac{1}{2}$ nucleus that has a low natural abundance of 4.7% and is usually characterised by long spin-lattice relaxation times, T_1 [109]. The ^{29}Si chemical shift is usually used to identify the type and the network connectivity of silicate species, which is related to bioactivity (*see Chapter 1*). The connectivity of network structure may be expressed by the distribution of silicon Q^n species, i.e., SiO_4 tetrahedra linked with n other SiO_4 tetrahedra ($n = 0$ to 4) where n designates the number of bridging

oxygens (Figure 3.10). In silicates, the largest effect of structure on chemical shift is that of coordination number. Thus, δ for SiO_6 groups is in the range of about -180 to -220 ppm relative to tetramethylsilane (TMS), and is in nearly all cases between about -65 and -120 ppm for SiO_4 groups. The second most important effect is that of the number and identity of first cation neighbors. If bridging oxygens are considered as those shared with tetrahedral Si or neighbors, and non-bridging oxygens to be those shared with larger and/or lower charged M cations (i.e. Na^+ , Ca^{2+}), SiO_4 tetrahedra are in perfect analogy to those in Figure 3.10 and they will be terminated by O^- . For a fixed M cation type, decreasing n by one tends to increase δ by about 10 ppm to less negative, higher frequencies. Each Q^n species thus has a distinct, but somewhat overlapping range of δ .

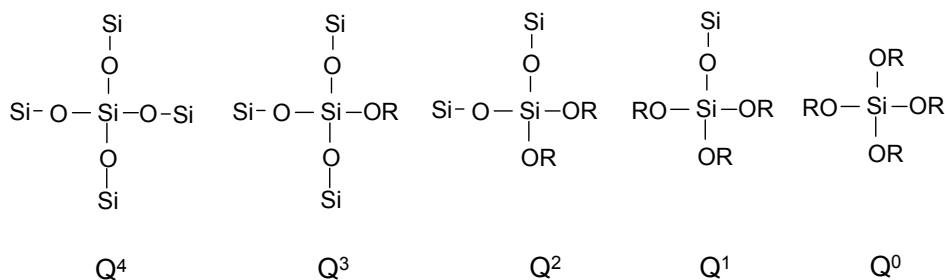


Figure 3.10. Q^n species in sol-gel silicate glasses, where $\text{OR} = \text{OR}, \text{OH}, \text{O}^-$, with R being an organic radical [109].

Another effect in the silicon chemical shift is the substitution of bridging oxygens by Si-C bonds. Besides Q^n , it can be distinguished mono-(M), di-(D) and tri-(T) functional silicon atoms in siloxane, where a bridging oxygen is substituted by 1, 2 or 3 Si-C bonds, respectively.

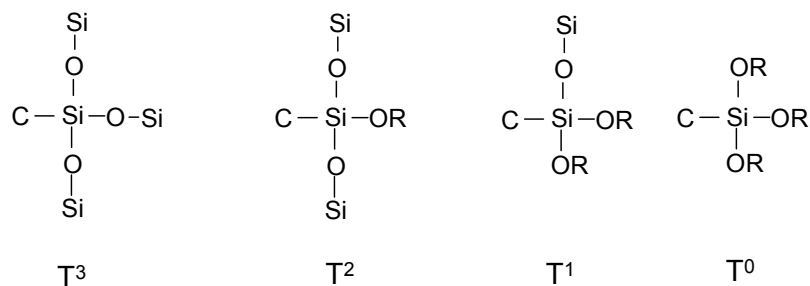


Figure 3.11. T^n species in silicate glasses obtained by sol-gel process, where $\text{OR} = \text{OR}, \text{OH}, \text{O}^-$, R is an organic radical.

As an example in Figure 3.11, the trifunctional silicon atoms are presented. They exhibit very characteristic sharp and non-overlapping shift ranges that are useful for both qualitative and quantitative analysis of polysiloxane mixtures, as it will be shown throughout this work.

^{31}P is a spin 1/2 nucleus with 100% natural abundance and a high resonance frequency, make it readily observable. The quantitative P^n speciation, where n denotes the number of P-O-P bridges, (Figure 3.12) is of intrinsic interest for an understanding of phosphate glasses.

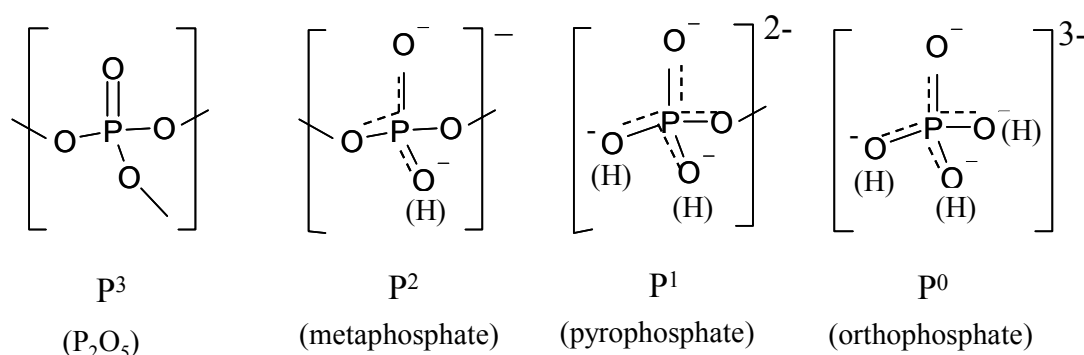


Figure 3.12. Phosphate tetrahedral sites that can exist in phosphate glasses [188, 189].

^{31}P MAS NMR has been used in this study to probe the local structure of phosphate glasses and the formation of apatite-like layers in glasses immersed in simulated body fluid.

^{23}Na is a quadrupolar nucleus with a non-integer spin ($I=3/2$) and is subject to the quadrupolar interaction which plays an important role in the lineshape and peak position [109]. The quadrupolar interactions are dominated by the charge distribution around the sodium ions, *i.e.* preferably by the effective charge and geometrical arrangements of the atoms in the first coordination sphere of the sodium cation [190], thus valuable information on sodium local bonding may be derived from the ^{23}Na NMR.

^{43}Ca is a spin 7/2 quadrupolar nucleus with a very low natural abundance ($\sim 0.14\%$) and small gyromagnetic ratio γ_{Ca} [109, 125, 191-197], making it experimentally difficult. ^{43}Ca NMR studies on biomaterials are few in literature [125, 191-206] and most of them have been performed by our group [125, 191-193, 196-

201]. Natural abundance ^{43}Ca NMR performed in sol-gel derived glasses in SiO_2 - CaO system [192] shows that disorder cause enough chemical shift dispersion to broaden the resonance significantly and no signal has been obtained for stabilised samples. The first natural abundance ^{43}Ca NMR evidence of the two crystallographically-distinct Ca species in hydroxyapatite were resolved at 18.8 T [198]. By enrichment of hydroxyapatite with ^{43}Ca the first experiment to unambiguously resolve of the two calcium sites using triple-quantum MAS has also been performed [199]. These results indicate new opportunities for the study of biomaterials. Calcium has a sensitive chemical shift range that should reveal the local bonding, when calcium is bonded to different organic species [193]. In this study ^{43}Ca NMR has been used to determine the changes in calcium environment, when different calcium precursors as calcium source have been used in the synthesis of organic-inorganic hybrids.

Listed in Table 3.3 are the primary and secondary references used to determine the reference of the chemical shift scale for the isotopes studied in this work.

Table 3.3. Primary reference compounds for the isotopes studied.
The secondary references used have been listed as well as the frequency and magnetic fields [109, 117].

Isotope	Field (T)	Frequency (MHz)	Reference Compound	Secondary Reference	Secondary Shift (ppm)
^1H	8.45	360.13	TMS	Adamantane $\text{C}_{10}\text{H}_{16}$	1.8
	11.75	500.10	$\text{Si}(\text{OCH}_3)_4$	Alanine,	1.0, 3.5 and 8.35
^{13}C	7.05	75.50	TMS	Adamantane	38.56 and 29.5
	11.75	125.8		Alanine, $\text{C}_3\text{H}_7\text{O}_2\text{N}$	20.5, 51.0 and 177.8
^{29}Si	7.05	59.62	TMS	Kaolinite,	-92
	14.1	119.24		$\text{Al}_2\text{Si}_2\text{O}_5(\text{OH})_4$	
^{31}P	7.05	121.49	H_3PO_4 87%	Ammonium	0.9
	11.75	202.48		dihydrogen phosphate	
	14.1	242.98		$\text{NH}_4\text{H}_2\text{PO}_4$	
^{23}Na	14.1	158.7	NaCl solution 1M	NaCl powder	7.2
^{43}Ca	14.1	40.46	CaCl ₂ solution 1M		0

Four magnetic fields of 7.05, 8.45, 11.75 and 14.1 T, which correspond to proton resonance frequencies of 300, 360, 500 and 600 MHz, respectively, were used to obtain the NMR data in this thesis. The details of each experiment will be given to the corresponding chapter.

3.5. Synthesis of sol-gel derived biomaterials

Nanostructured calcium silicates glasses and organic-inorganic hybrid scaffolds studied in this thesis have been synthesised using the sol-gel procedure. This involved the use of alkoxides as precursors which has the advantage that homogeneous, high purity, sol-gel products can be obtained at low temperature and the structural and textural properties can be tailored by manipulating the sol-gel parameters (*see Chapter 1*). The samples have been synthesised by Dr Julian R. Jones' group at Imperial College London. The nanostructured sol-gel silicate glasses have been obtained with different nominal compositions: 100S (100 mol% SiO₂), 70S30C (70 mol% SiO₂, 30 mol% CaO) and 58S (60 mol% SiO₂, 36 mol% CaO, 4 mol% P₂O₅). Different calcium oxide sources have been used: calcium nitrate tetrahydrate (Ca(NO₃)₂·4H₂O), calcium chloride (CaCl₂) as inorganic sources and calcium methoxyethoxyde (CME-Ca(OCH₂CH₂OCH₃)₂) as an alkoxide source. Class I and Class II hybrid samples were synthesised, where in the former only weak Van der Waal's forces, hydrogen bonding and/or ionic bonding exist and in the latter strong covalent bonding is present due to the use of the organosilane GPTMS as a coupling agent. The polymers used as organic networks are gelatin and poly(γ -glutamic acid) (γ -PGA). The structure of alkoxides used in the sol-gel process is shown in Figure 3.13.

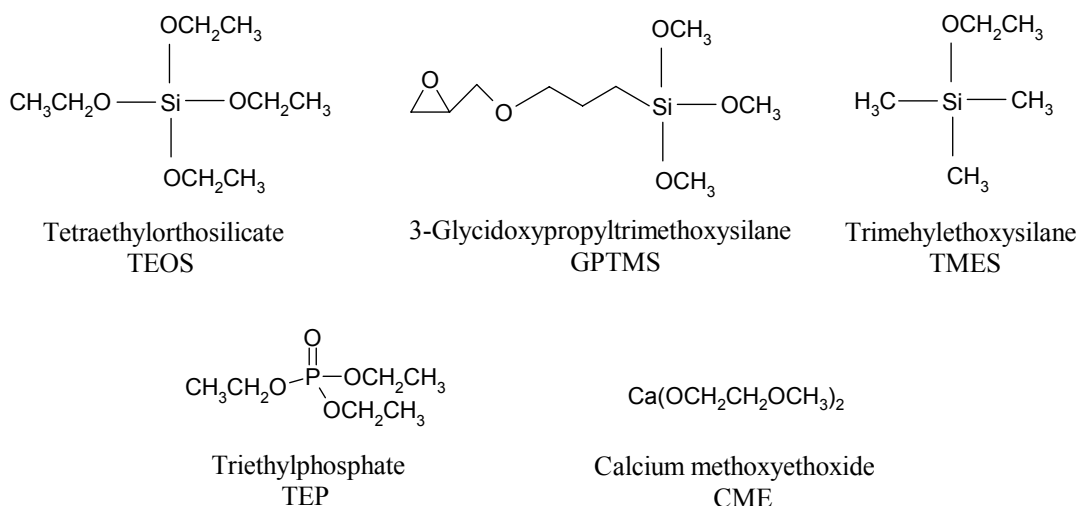


Figure 3.13. The structure of alkoxides used in the sol-gel synthesis.

3.5.1. Sol-gel synthesis of 70S30C bioactive glasses

Synthesis of traditional 70S30C consists of five stages: mixing, casting, ageing, drying and stabilisation. During the mixing stage TEOS was hydrolysed in a 0.2mol/l nitric acid (HNO₃) for 1 h. The mole ratio H₂O/TEOS=12 and volume ratio H₂O/HNO₃=6. Calcium nitrate, Ca(NO₃)₂·4H₂O was added to the solution in a proportion to obtain the composition 70 mol% SiO₂, 30 mol% CaO on the final product. The sol was then cast in 60 ml polymethyl pentene (PMP) moulds. The sol was left in the mould for 72 h at room temperature, when the poly-condensation reaction start to progress. Gelation and ageing of the gels took place at 60 °C for 72 h using a heating rate of 5 °C/min. The drying of the gels was carried out by loosening the mould lids and heating with a three-stage schedule: to 60 °C at 0.1 °C/min and holding for 20 h; heating to 90 °C at 0.1 °C /min and holding for 24 h; heating to 130 °C at 0.1 °C/min and holding for 40 h. The dried gels were cooled to room temperature at 0.1 °C/min and then transferred into an alumina crucible for stabilisation, which followed a three-stage schedule: heating to 300 °C from room temperature at 1 °C/min and holding for 2 h; heating to 600 °C at 1 °C/min and holding for 5 h; furnace cooling to room temperature. The process flow chart is presented in Figure 3.14.

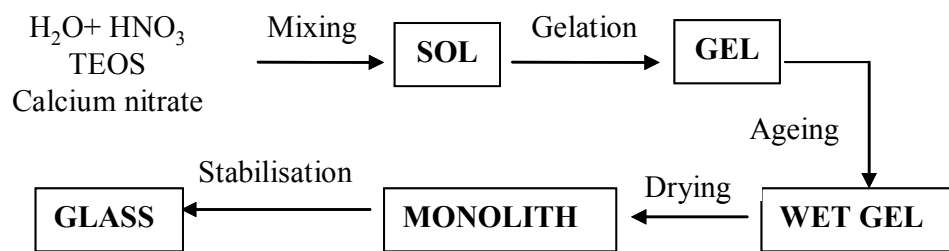


Figure 3.14. Process flow chart for the synthesis of 70S30C sol-gel derived glasses.

New materials were synthesised by adding trimethylethoxysilane (TMES) at different stages of the process. Two groups of samples modified with TMES (TMS-70S30C) were synthesised: TMS-A series, where the TMES was added to the sol early in the process, soon after hydrolysis completed and before casting. In TMS-B samples, the TMES was added 3 days after casting the sol after some condensation had taken place, but prior to complete gelation. For both TMS-A and TMS-B,

specific amounts of TMES was added to 35 ml of traditional 70S30C sol (T-70S30C, 70S30C without TMES) and vigorously agitated for 1 h. Sub-groups within the TMS-A and TMS-B samples were divided according to the TMES amounts added, which determined the TMES:TEOS ratio (TT ratio). Details are shown in Table 3.4.

Table 3.4. The dosage of trimethylethoxysilane per 35 ml of normal 70S30C of TMS-A and TMS-B sub-groups (TT represents the mole ratio of TMES/TEOS).

Samples	Time point of addition	TMES per 35 ml sol	TT Ratio
TMS-A4	Before casting	4 ml	1:4
TMS-B1	After casting	1 ml	1:16
TMS-B2	After casting	2 ml	1:8
TMS-B3	After casting	3 ml	3:16
TMS-B4	After casting	4 ml	1:4

TMS-A samples were found to have separated into two components, termed upper and lower components. TMS-B glasses were more homogeneous.

3.5.2. Sol-gel synthesis of 58S bioactive glasses

Glasses composed of 60 mol% SiO₂, 36 mol% CaO, 4 mol% P₂O₅ were prepared by the sol-gel method employing two different pathways: via an inorganic route and via an alkoxide route. Calcium nitrate and calcium methoxyethoxide (CME) have been used as the calcium sources in the inorganic and alkoxide routes, respectively. TEOS and triethylphosphate (TEP) have been used as precursors for the SiO₂ and P₂O₅. The inorganic route has been similar with the synthesis procedure described for the S70C30 glasses in the *section 3.5.1*. First, the sol preparation from TEOS, TEP and Ca(NO₃)₂•4H₂O in acidified water took place. The precursors have been mixed in proportion for glass composition required when the hydrolysis of alkoxides takes place. After the sol was cast in the moulds for completion of gelation, was followed by aging at 60°C for 3 days and drying of the gel at 130°C. Thermal stabilisation took place at 700°C. High temperature samples were achieved by sintering at 800 °C, after stabilisation stage.

CME is an alkoxide which was synthesised by reacting calcium metal with 2-methoxyethanol under an argon atmosphere at 80°C for 24 h. The ratio of the reaction was 1 g calcium metal to 24 ml 2-methoxyethanol. The resultant solution was centrifuged to remove unreacted calcium metal and the CME solution was obtained with a concentration of 0.001 mol/ml.

The glass synthesis with CME started with mixing TEOS and CME under nitrogen atmosphere. After 1h of being stirred, the sol was hydrolysed by introducing it inside a hermetic container together with water and gelling at 25 °C for 3 days. The gel obtained was aged and dried at 60 °C. The samples were taken through the full sol-gel heat treatment (dried at 60~130 °C, stabilised at 700 °C, sintered at 800 °C after stabilisation) to compare with conventional sol-gel glasses prepared via the inorganic route.

A portion from the sol was poured into polymethyl propylene moulds and gelled by hydrofluoric acid (HF). The ratio of HF (0.5 %) to sol is 1.5 ml to 50 ml.

All the samples were grind into particles of sizes between 38-90 µm before characterisation. The names of the samples were represented by 58S “calcium precursor” followed by the temperature, e. g. 58S Nitrate (CME) 700. Where HF has been used as catalyst was specified after the temperature (58S Nitrate 700 HF).

3.5.3. Organic-inorganic nanocomposite scaffolds

3.5.3.1. Silica-gelatin hybrid scaffolds

Class I and class II silica-gelatin have been synthesized. Gelatin (Bovine) was dissolved in 10 mM hydrochloric acid (HCl) at a concentration of 50 mg/ml. This solution was functionalised by addition of an appropriate amount of GPTMS as a coupling agent to covalently link gelatin to silica, to give C-factors (the mole ratio of GPTMS/gelatin) ranging between 0-2000. The functionalised gelatin solution was left to mix for 14 h before being added as a sol-gel precursor. TEOS, the sol-gel precursor for silica, was hydrolysed separately by adding in the following order: deionised water, HCl (1 N) and tetraethyl orthosilicate (TEOS). The mole ratio of H₂O/TEOS was 4 and HCl was added to catalyse TEOS hydrolysis at a volume ratio (water/HCl) of 3. The solution was stirred for 1 hour to allow hydrolysis of TEOS, resulting in a colloidal solution (a sol) of Si(OH)₄ (*see eq. 1.1*) before adding the functionalised gelatin solution, which was mixed for a further 1h.

At higher C-factors, the total organic content is increased substantially due to the organic contribution from GPTMS. Two volume ratios (functionalised gelatin/hydrolysed TEOS) were used in this study: 60/40 and 85/15 referred to as 30 wt% and 60 wt% respectively, representing the final weight percentages of gelatin in the 0 C-factor materials. Once the functionalised gelatin solution has mixed for 1

hour in the sol, hydrofluoric acid (HF, 5 vol%) was added to the sol at sol/HF volume ratio of 100/1 to catalyse the inorganic condensation reaction. Sols were cast into moulds, where they gelled as monoliths and were aged for 1 week to allow for further condensation and then dried at 60 °C for 120 h.

3.5.3.2. Silica-calcium oxide- (γ -PGA) organic-inorganic hybrids

Silica-calcium oxide-poly(γ -glutamic acid) (γ -PGA) organic-inorganic hybrids were synthesised starting from different calcium precursors: calcium chloride, CaCl_2 and the calcium salt form of γ -PGA. In all samples, the mole ratio of Si/Ca was 70/30 to obtain the inorganic part in the same composition as the 70S30C (70 mol% SiO_2 , 30 mol% CaO) bioactive glasses. Calcium nitrate has not been used in the synthesis of the hybrids, as the removal of toxic nitrate by-products takes place over 400°C [1]. At this temperature the polymer can be removed from the system.

Figure 3.15 shows the schematic reactions of the hybrid synthesis using CaCl_2 as calcium precursor.

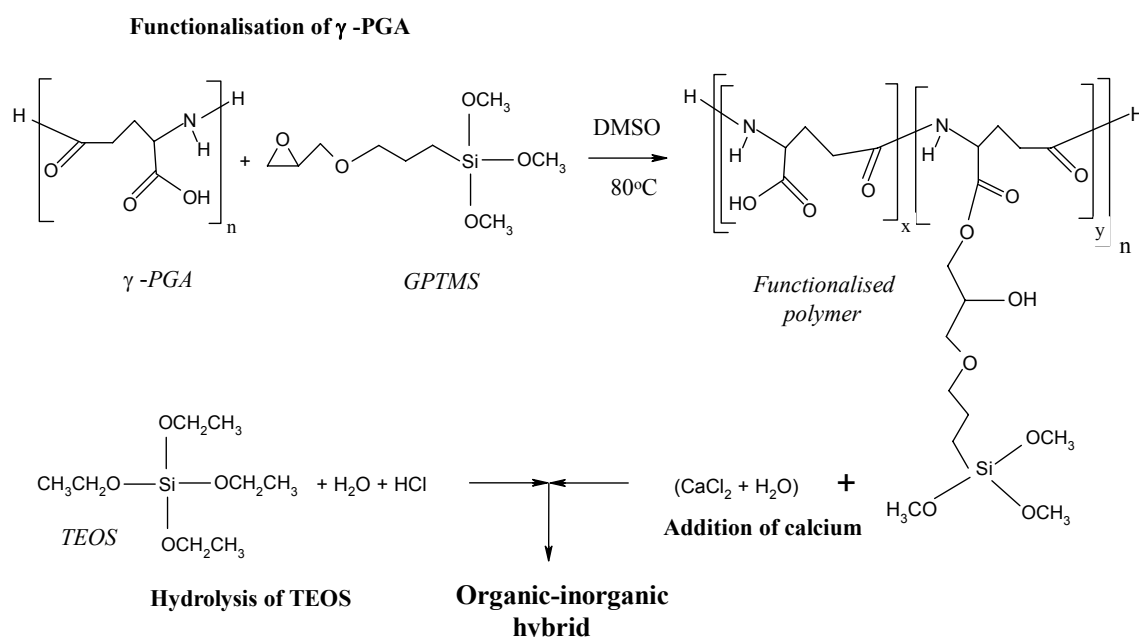


Figure 3.15. Schematic of the reactions for the hybrid synthesis.

γ -PGA was first functionalised with the organosilane GPTMS in dimethyl sulfoxide (DMSO) at 80 °C for 12 h in a dry N_2 atmosphere, where the carboxylic acid group of the polymer was reacted with the epoxy group on the GPTMS by ring opening

esterification. During the functionalisation process the inorganic functional group trimethoxysilane on GPTMS had hydrolysed and partially condensed to other GPTMS molecules forming Si-O-Si bridging oxygens. Part of DMSO was removed by rotary vacuum evaporation. The second step in the synthesis of the hybrid was the addition of CaCl₂ solution to the functionalised polymer (Figure 3.15). The solution was stirred for 5 minutes. The inorganic sol was prepared by the hydrolysis of the silica precursor, TEOS, in acidic conditions, using a solution of 1N HCl as catalyst, in a separate beaker and mixed for 1 h. The hydrolysis ratio H₂O/TEOS (R) was 6. The two solutions were added together to create the hybrid sol (Figure 3.15). A portion from the hybrid sol (10 ml) was poured into polymethyl propylene moulds and gelled by HF (0.6 ml, 5 vol%). The gelled hybrids were sealed and aged at 60 °C for 3 days and dried at 60 °C for 4 days. The wt% ratio of inorganic/organic constituents was 60/40 and the glutamic acid:GPTMS mole ratio (X_{EC}) was in the range 1 to 100. SiO₂- (γ-PGA) hybrids corresponding to X_{EC} of 2 and 50 have been synthesised following the same procedure, but without adding the CaCl₂.

The synthesis of organic-inorganic hybrids starting from the calcium salt form of γ-PGA (Figure 3.16) instead of CaCl₂, has been performed following the same procedure as above (Figure 3.15).

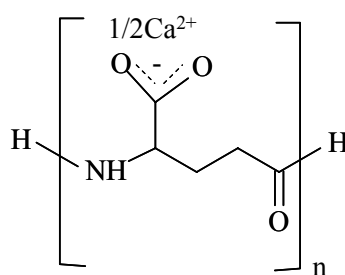


Figure 3.16. Calcium salt form of γ-PGA.

1 mol of GPTMS was added for every 2 moles of polymer with 40% polymer in the inorganic matrix.

3.6. Bioactive media used to test in-vitro bioactivity

To study the protein effects on apatite growth, serum complemented SBF was used to compare with pure SBF. TheraGlass[®] (TG, sol-gel derived 70 mol% SiO₂, 30

mol% CaO, stabilised at 700 °C) and Bioglass[®] (BG, melt-derived 46.1 mol% SiO₂, 26.9 mol% CaO, 24.5 mol% Na₂O and 2.5 mol% P₂O₅), which are provided by NovaThera Ltd. (a wholly owned subsidiary of MedCell BioSciences Ltd), were used as glass particles to conduct bioactivity tests. All the glass samples were ground by ball miller and sieved by 38 µm sieves. Simulated body fluid, SBF, was prepared following the previous method initially proposed by Kokubo [15]. The ion concentrations of SBF and human plasma are shown in Table 3.5.

Table 3.5. Concentration (mM) and pH of SBF and human plasma [207].

Ion	SBF (mM concentration)	Plasma (mM concentration)
Na ⁺	142	142
K ⁺	5.0	5.0
Mg ²⁺	1.5	1.5
Ca ²⁺	2.5	2.5
Cl ⁻	147.8	103.0
HCO ₃ ⁻	4.2	4.2
HPO ₄ ²⁻	1.0	1.0
SO ₄ ²⁻	0.5	0.5
pH	7.25	7.20-7.40

Foetal bovine serum (FBS) was purchased from Invitrogen[™] UK. Two bioactive media were used for the bioactivity tests, including pure SBF (pSBF) and SBF complemented with 10% FBS (sSBF).

Previous protocols were followed to conduct the bioactivity tests [208]. 75 mg of glass powders (BG and TG) were immersed in 50 ml of pSBF (or sSBF) at 37 °C in incubator with an agitation of 120 rpm. The samples were filtered after a series times (2 h, 1 d and 7 d) and the glass powders were reserved for further solid-state NMR analysis. The briefs of the samples were represented by pSBF/sSBF “immersing time” BG/TG, e. g. pSBF 2h BG.

4.

SOL-GEL 70S30C BIOACTIVE GLASSES

4.1. Introduction

Bioactive glasses bond to bone and are osteogenic [7], which is thought to be due to genetic stimulation of genes in osteoblasts by their dissolution products [18]. Sol-gel derived porous glasses exhibit a better bioactive behaviour than normal bulk, melt-quenched glasses of the same composition, due to the porosity of the former that results in a very high surface area to volume ratio [42, 43]. The 70S30C (70 mol% SiO₂ and 30 mol% CaO) composition is thought to be suitable for bone repair [209]. However, strong compositional inhomogeneity is found within 70S30C monolith samples by using traditional synthesis protocols [41]. It is therefore important to understand the modifications that alkaline earth modifiers, such as CaO, engender in silica glass structure.

The structure of glasses and melts in the metal oxide-silica systems can be described as a network of interconnected SiO₄ tetrahedra, partially interrupted by the presence of metal oxides (network-modifiers). The connectivity of the network structure may be expressed by the distribution of silicon Qⁿ species, i.e., SiO₄ tetrahedra linked with *n* other SiO₄ tetrahedra (where *n* = 0 ~ 4) [109]. Solid-state NMR spectroscopy is a powerful method to characterize the chemical structure of glasses that are derived from the sol-gel method [109-111, 210, 211]. ²⁹Si-NMR is useful in distinguishing and quantifying the Qⁿ speciation [109]. Unfortunately, the differences in chemical shifts that are caused by the exchange of a silanol group by an alkoxy group are too small to be detected in a solid-state ²⁹Si NMR spectrum [212]. Maciel and co-workers showed that surface Qⁿ species of silica gels could be determined, quantitatively, by ²⁹Si CP MAS NMR [213-215].

From the perspective of oxygen environments, three types of sites can be distinguished: (1) bridging oxygen (BO), oxygen that bridges two neighboring SiO₄ tetrahedra within the network structure; (2) non-bridging oxygen (NBO), oxygen that is coordinated to only one Si and to one or more metal cations (M), and thus

terminates the network structure, and (3) free oxygen, oxygen that is only coordinated to M cations and is thus not part of the network structure [216].

In this chapter the solid state ^1H , ^{13}C and ^{29}Si MAS NMR spectroscopy of sol-gel derived bioactive glasses in the $\text{SiO}_2\text{-CaO}$ system containing 30 mol% CaO was carried out. Aims of the present study were the identification of the proton content, the network connectivity and the carbon backbone in the xerogels and the evolution of the structures with the stabilisation process. The inhomogeneity of 70S30C samples made by the traditional method [41] has also been studied. The last part of this chapter was focussed on the study of the hypothesis that condensation inhibitors added before the stabilisation stage could tune the nanopore sizes. Trimethylethoxysilane (TMES) is a potent condensation inhibitor due to its mono-functional-group chemical structure. It can also act as a cap on the surface of the silica nanoparticles formed during condensation and inhibit further condensation reactions between the surface OH groups of the structural units. TMES was used previously to decrease surface hydrophilicity of the MCM series of materials and stabilise surface OH groups from water molecules and hydrolysis [217].

4.2. Experiment details

Synthesis of 70S30C sol-gel derived bioactive glasses has been described in Chapter 3.

The ^1H MAS NMR spectra were recorded using Varian-Chemagnetics CMX 360 MHz (8.45 T) or Bruker 500 MHz (11.7 T) spectrometers operating at 360.13 MHz and 500.1 MHz respectively. MAS spectra were recorded with a Varian 4 mm MAS probe spinning at 12 kHz, using a 20 s recycle delay and a $2.0\ \mu\text{s}$ (90° tip angle) pulse, with 128 acquisitions added together or a Bruker 4 mm probe at 12.5 kHz, using a 5 s recycle delay and a $2.50\ \mu\text{s}$ (90° tip angle) pulse for measurements performed at 8.45 and 11.7 T, respectively. The chemical shift was referenced externally to adamantane ($\text{C}_{10}\text{H}_{16}$) at 1.8 ppm. To determine the proton content each sample was weighed. The integrated signal was normalised to take into account the amount of sample so that the absolute level of protons can be deduced. ^{29}Si MAS NMR spectra were collected on a Varian InfinityPlus 300 MHz spectrometer operating at 59.62 MHz. A 20 s recycle delay and a $5\ \mu\text{s}$ (45° tip angle) were used which produced relaxed spectra. ^{29}Si spectra were referenced to TMS at 0 ppm. ^{29}Si

CP MAS NMR spectra were collected on a Field-Sweep Chemagnetics Infinity 300 MHz spectrometer operating at 59.47 MHz. A 5 ms contact pulse was used and a 10 s recycle delay collected under ^1H decoupling. The spectra were referenced to kaolinite at -92 ppm. ^{13}C CP-MAS NMR spectra were collected on a Varian InfinityPlus 300 spectrometer (7.05 T) operating at 75.47 MHz. A Bruker 4 mm MAS probe was used with the sample spinning at 7 kHz. A 5 ms contact pulse was used and a 10 s recycle delay, under ^1H decoupling. The spectra were referenced externally to adamantane as a secondary shift reference, with its more intense peak set to 38.56 ppm.

4.3. Results and discussion

4.3.1. Nanostructure evolution of 70S30C sol-gel bioactive glasses

^1H MAS NMR was used to investigate the nature of the sol-gel glass surfaces through its various proton environments present as SiOH groups and adsorbed water. The surface silanols play a decisive role for glass bioactivity because they act as nucleation sites for HCA formation [7, 11]. ^1H MAS NMR of glasses can distinguish different proton species in glasses at relatively modest MAS rates [187] due to the relatively low proton density and hence correspondingly relatively weak dipolar coupling.

^1H MAS NMR results at 8.45 T of a silica sample, 100S, and a 30% calcium oxide containing silica sample, 70S30C, both not stabilised and stabilised are shown in Figure 4.1.

The integrated intensities of the ^1H MAS NMR spectra were calculated directly using the spectrometer software (Table 4.1). The normalisation was carried out by weighing each sample and comparing the result with the integrated intensity of the reference adamantane spectrum.

In dried, non-stabilised xerogels, the tall peak centred at approximately 5 ppm is due to physisorbed water at the silica surface [218]. The peak from around 1 ppm can be attributed to residues from alkoxide chains [219] and the shoulder around 3 ppm to weakly hydrogen-bonded silanols [220]. As can be observed the intensity of the peak around 1 ppm is higher for the sample containing calcium, suggesting that this sample contains more alkoxide residues from TEOS molecules.

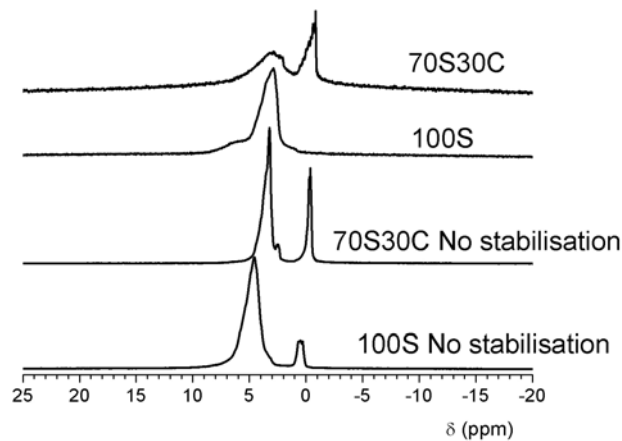


Figure 4.1. ^1H MAS NMR spectra of 100S no stabilisation, 70S no stabilisation, 100S (x4) and 70S30C (x8).

Table 4.1. Amount of hydrogen in mol/g of samples as determined by ^1H NMR.

Sample	Hydrogen content (mol/g)
100S No stabilisation	$(1.8 \pm 0.06) \times 10^{-2}$
70S30C No stabilisation	$(2.0 \pm 0.1) \times 10^{-2}$
100S	$(5.8 \pm 0.2) \times 10^{-3}$
70S30C	$(9.3 \pm 0.3) \times 10^{-3}$

After stabilisation, there is an important difference between the silica and silica-calcium oxide samples. In the thermally treated silica matrix sample the spectrum is dominated by a resonance at 2.9 ppm with a shoulder at 6.3 ppm. There is a significant loss of total proton signal of $\sim 68\%$. The peak at 2.9 ppm can be attributed to internal silanols, while the shoulder can be due to relatively strongly hydrogen bonded siloxanes [221, 222]. For the 70S30C sample, in the ^1H MAS NMR spectrum are 2 resonances at 2.9 ppm and -0.8 ppm and the hydrogen signal is reduced by $\sim 54\%$. The peak at -0.8 ppm can be assigned to the hydrogen atom connected to Ca-O groups [223]. The peaks corresponding to residues from the alkoxide are not present, suggesting that they have been removed by thermal treatment.

For the pure silica sample, heat treatment leads to the removal of more hydrogen content than for sample containing calcium. This can be due to the removal of adsorbed water and residual organics from precursors and further condensation of

OH groups on the surface. Also the 70S30C sample having calcium it adsorbs more water compared with the pure silica matrix.

The results obtained from ^{29}Si MAS NMR spectroscopy provide a better understanding of the effect of calcium on the connectivity of silica network. ^{29}Si MAS NMR spectra of the 100S and 70S30C samples, both not stabilised and stabilised samples are shown in Figure 4.2.

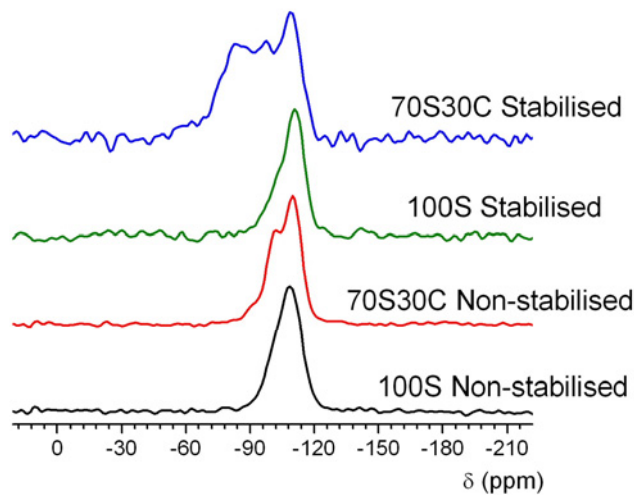


Figure 4.2. ^{29}Si MAS NMR spectra of 100S, and 70S30C, respectively, not stabilised and stabilised samples.

To quantify the Q^n distribution the ^{29}Si MAS NMR spectra were deconvolved by Gaussian fitting using DMFIT software [224]. Q^n species are silicon atoms in the glass network that are connected to other silicon atoms by n bridging oxygens (oxygen atoms covalently bond to two silicon atoms Si-O-Si) bonds corresponds to the structures of $\text{Si}(\text{OSi})_n(\text{OR})_{4-n}$, where OR is OH, $\text{CH}_3\text{CH}_2\text{O}$ or O^- , i.e. a non-bridging oxygen [109, 214, 221, 225]. Therefore, the $\text{Si}(\text{OSi})_n(\text{OH})_{4-n}$ are denoted as $Q^n(\text{H})$, while $\text{Si}(\text{OSi})_n(\text{O}^-)_{4-n}$ with NBOs are labelled as $Q^n(\text{Ca})$. In looking at the range of samples five signals could be distinguished, with typical shifts of -72 , -81 , -91 , -100 and -108 ppm which correspond to $Q^0(\text{H})$ ($Q^1(\text{Ca})$), $Q^1(\text{H})$ ($Q^2(\text{Ca})$), $Q^2(\text{H})$ ($Q^3(\text{Ca})$), $Q^3(\text{H})$ and Q^4 , respectively [109]. Such $Q^n(\text{Ca})$ environments have been reported in the literature for CaO-SiO₂ glasses [226, 227].

Table 4.2. ^{29}Si MAS NMR data for measured samples, giving the spectral deconvolution into different Q^n species.

Sample	$\text{Q}^1(\text{Ca})$			$\text{Q}^2(\text{Ca})$			$\text{Q}^2(\text{H}), \text{Q}^3(\text{Ca})$			$\text{Q}^3(\text{H})$			Q^4		
	δ (ppm)	FWHM (ppm)	I (%)	δ (ppm)	FWHM (ppm)	I (%)	δ (ppm)	FWHM (ppm)	I (%)	δ (ppm)	FWHM (ppm)	I (%)	δ (ppm)	FWHM (ppm)	I (%)
100S Non-stabilised	-	-	-	-	-	-	-91.4	8.6	8	-100.8	8.0	34	-110.1	9.3	58
70S30 Non-stabilised	-	-	-	-	-	-	-93.8	7.1	4	-102.1	9.7	27	-111.3	9.7	69
100S Stabilised	-	-	-	-	-	-	-92.2	7.7	4	-100.1	9.0	17	-109.1	11.9	79
70S30C Stabilised	-73.9	10.1	8	-81.4	8.8	17	-88.5	8.8	16	-97.3	10.1	23	-109.5	11.5	36

Table 4.3. ^{29}Si CP MAS NMR data at a contact time of 5 ms of $\text{SiO}_2\text{-CaO}$ sol-gel samples (xerogels and thermal treated samples).

Sample	$\text{Q}^2(\text{H}), \text{Q}^3(\text{Ca})$			$\text{Q}^3(\text{H})$			Q^4		
	δ (ppm)	FWHM (ppm)	I (%)	δ (ppm)	FWHM (ppm)	I (%)	δ (ppm)	FWHM (ppm)	I (%)
100S Non-stabilised	-92.0	5.4	18	-96.1	7.4	66	-105.7	8.6	16
70S30 Non-stabilised	-89.4	7.5	9	-98.9	8.7	58	-108.6	9.9	33
100S Stabilised	-94.4	8.4	9	-104.3	10.5	73	-114.4	6.7	18
70S30C Stabilised	-88.3	14.6	23	-101.1	18.3	61	-115.36	14.6	17

FWHM, δ and I represent the linewidth full-width half-maximum, ^{29}Si chemical shift and relative intensity, respectively. Errors associated with measurements are — FWHM ± 1 ppm, $\delta \pm 2$ ppm and Integral $\pm 2\%$.

For non-stabilised samples R is an OH, as shown from an ^{17}O NMR study in literature [210], NBOs are not present at this temperature. In the case of a 70S30C stabilised sample, R can be either an OH or an O^- .

An example of a simulation is presented for the 100S no stabilisation sample in Figure 4.3 which shows three different Q^n species.

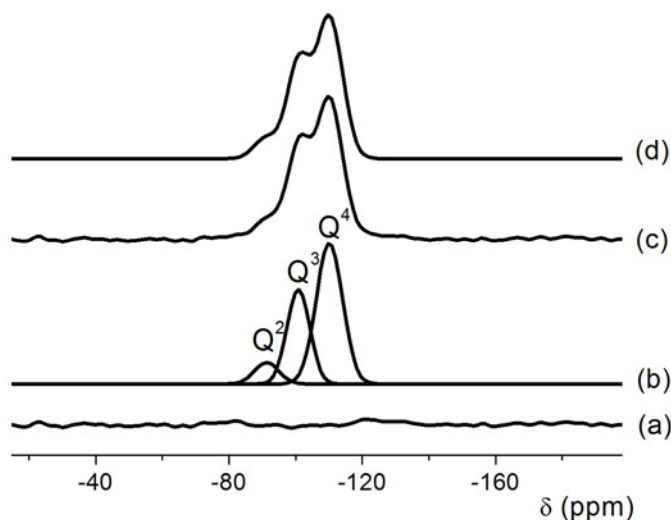


Figure 4.3. Fit of the 100S Non-stabilised: (a) difference between spectrum and simulation, (b) deconvolution in 3 peaks, (c) spectrum and (d) the simulation.

The results of the Gaussian fitting of all of the ^{29}Si MAS NMR spectra are summarised in Table 4.2.

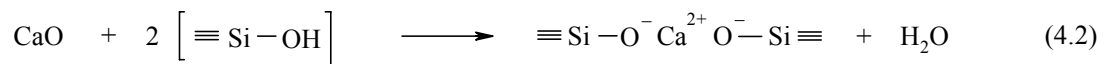
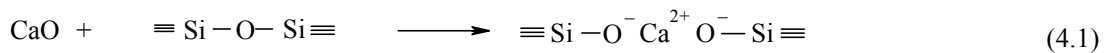
For the non-stabilised 100S and 70S30C xerogels, it can be observed that calcium cations from calcium nitrate appear to allow the formation of a more polymerised silica network at this stage. This could be due to the ionic nature of the calcium nitrate, although not yet part of the silica network having some effect on the gelation of the TEOS. Lin *et al.* showed by ^{43}Ca NMR that calcium at this stage is present as calcium nitrate [192].

This behaviour can be understood from the factors governing the sol-gel process. The existence of a non-bridging oxygen attached to an Si atom is highly unlikely at the initial stage of gel formation involving hydrolysis and polycondensation as given by reactions (1.1)-(1.3) (see section 1.2) [96]. After the hydrolysis (reaction 1.1) and condensation reactions (reactions 1.2 and 1.3) have

been induced, alcohol (reaction 1.2) and water (reaction 1.3) as by products are released in the reaction medium. The water content (hydrolysis ratio) is higher and together with the calcium nitrate present in the system could lead to a significant increase in the polymerisation of the silica network. Hydrolysis and condensation of TEOS results in the formation of primary particles of silica which aggregate to form colloidal particles (namely secondary particles) in the sol. The further polycondensation and aggregation of silica secondary particles leads to gelling of the solution. Aging and drying the gel at low temperature promotes more condensation and the secondary particles coalesce to form the tertiary particles [1].

On increasing the temperature to 600 °C the formation of Si-O⁻, Si-OH and/or Si-O-Ca units occurs, which is reflected on ²⁹Si MAS NMR spectra of the 70S30C sample, where a more complete range of Qⁿ species is now present, and significantly differs from the spectrum of pure silica sample heat treated to 600°C where the proportion of Q⁴ species has significantly increased (Figure 4.2, Table 4.2), as well as the network connectivity. Incorporation of Ca²⁺ cations into silica, a large network modifier, clearly leads to the breaking of Si-O-Si bonds that formed during the early stages of the reaction and the formation of a much more disordered silicate network and a decrease of the concentration of Q³ (H) and Q⁴ species.

When the calcium ions are added to the silica, it is assumed that the Ca²⁺ ions might be combined with the O⁻ ions bonded to the SiO₄ groups. After completion of the polycondensation reaction, higher-temperature heat treatment of the gel promotes the depolymerisation reaction (4.1) or the reaction between silanols and calcium ions (4.2):



This breakup leads to primarily ionic bonding between the calcium cations and the non-bridging oxygen. This fact explains the peaks broadening of the ²⁹Si MAS NMR spectra for S70C30 stabilised sample containing Ca²⁺ ions. This is believed to be due to calcium incorporation into the silica network during the high-temperature heat

treatment in the stabilisation stage, as the silica network connectivity decreases rather than an expected increase as in the case of pure silica matrix.

In the case of S70C30 stabilised sample, there is a competing role of Ca^{2+} and H^+ on the charge compensation of NBOs [109]. To verify which Q^n species are close to H^+ or Ca^{2+} , ^{29}Si CP MAS NMR have been performed. Because dipole-dipole interactions decay with the third power of the distance, only those nuclei in the proximity of protons are detected by CP [109]. ^{29}Si CP MAS NMR spectra for the 100S and 70S30C, on both non-stabilised and stabilised samples are shown in Figure 4.4.

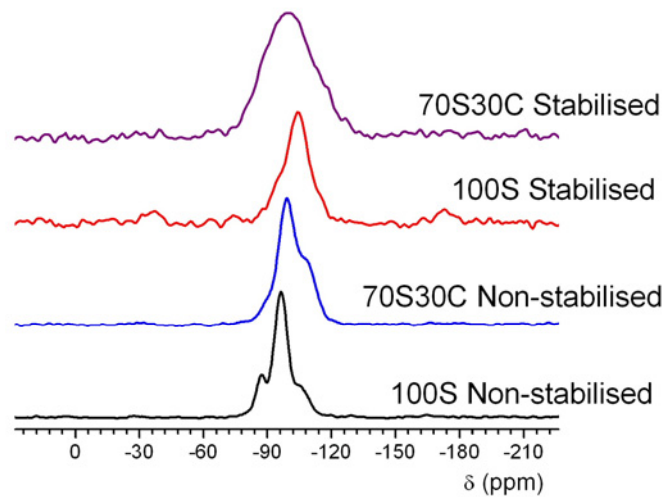


Figure 4.4. ^{29}Si CP MAS NMR spectra of 100S, and 70S30C, respectively, non stabilised and stabilised samples, at a contact time of 5 ms.

Q^4 silicons far away from protons are not detected with CP. Q^4 species bonded to a $\text{Q}^2(\text{H})$ silicon will be easier to cross-polarize than a Q^4 surrounded by four other fully condensed Q^4 silicon centres. The dipole-dipole interactions between protons and silicon nuclei are stronger for $\text{Q}^2(\text{H})$ silicons than for Q^4 silicons.

CP spectra show for all samples the presence of Q^n species with $n=2-4$ (Table 4.3). The inefficient CP of Q^4 is illustrated in Figure 4.4. The peak intensity of Q^3 is higher than that of Q^2 and Q^4 in the CP spectrum obtained with a contact time of 5 ms. The differences in the CP behaviour of the different Q^n silicon nuclei suggest

that there could be differences in CP parameters for a Q^n species belonging to different silica samples.

For non-stabilised samples in the ^{29}Si CP MAS NMR spectra (Figure 4.4) the intensity of the Q^4 peak of 70S30C no stabilisation sample is almost double compared with the 100S no stabilisation sample. This can be observed also from Table 4.3 where the number of Q^4 silicons in this sample is double. This can be attributed to the fact that Q^4 silicons in the system 70S30C no stabilisation are much easier to excite by CP than the Q^4 silicons in the 100S no stabilisation sample. This could be due to differences in local proton densities (number of silanol groups, residual organic groups and water content), and differences in all dynamic processes (proton exchange, mobilities of residual organic groups, physically adsorbed water and siloxane structures) which is higher in 70S30C no stabilisation than in the 100S no stabilisation sample.

For stabilised samples the intensity of the Q^4 species is almost the same for the two samples. For the 70S30C sample in the CP spectrum the signals around -70 and -80 ppm corresponding to $Q^1(\text{Ca})$ and $Q^2(\text{Ca})$ species, respectively, do not appear, which can indicate that the SiO_4 groups are bonded to Ca^{2+} ions through siloxane bridges rather than to protons as an OH. For all samples, the most intense signal appears for $Q^3(\text{H})$ species suggesting that the OH species are preferentially being attached to these sites in the structure. As can be observed from Figure 4.4 and Table 4.3 all three types of silicon sites in 70S30C stabilised sample have larger linewidth than those in the stabilised pure silica matrix spectrum. This greater linewidth probably relates to the greater dispersion of local surface geometries in the surface of this sample.

The increased relative intensities of the $Q^2(\text{H})$ ($Q^3(\text{Ca})$) and $Q^3(\text{H})$ peaks, relative to the Q^4 peak, in the CP-MAS spectra of the samples (Figure 4.4), in comparison with the relative peak intensities in the corresponding MAS NMR spectra (Figure 4.2), reflect the preferential selection of sites with a more direct association with the protons by the ^1H - ^{29}Si CP process [228].

The data from CPMAS experiments at a single contact time should be regarded as qualitative rather than quantitative. Excitation by cross-polarization was not used for quantitative analysis, because the CP parameters could differ for

different samples and because some of the Q⁴ nuclei could not be detected by this method.

¹³C CP MAS NMR spectra at 7.05 T of silica matrix, 100S, and 30% calcium oxide containing silica matrix, 70S30C, both not stabilised samples are shown in Figure 4.5. ¹³C CP-MAS NMR showed the presence of the ethoxy groups (CH₃CH₂O) in the non-stabilised samples (Figure 4.5). The stabilised samples did not give a signal.

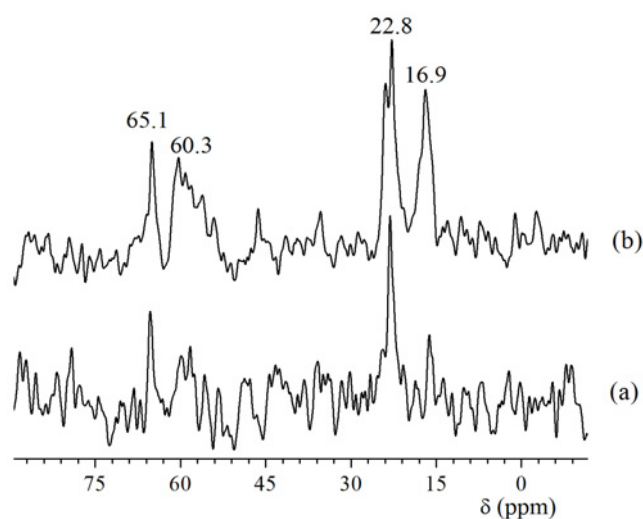


Figure 4.5. ¹³C CP MAS NMR spectra of 100S (a), and 70S30C (b), respectively, not stabilised samples, at a contact time of 5 ms.

The carbon of the methyl group was found close to 17 ppm and the carbon bonded to oxygen had a chemical shift around 60 ppm [229]. The origin of the observed unhydrolysed ethoxy groups is from TEOS molecules [229]. This implies that several percent of the ethoxy groups do not leave the TEOS molecules. At this stage the hydrolysis reaction (reaction 1.1) is complete [96]. The peaks at 22.8 and 65.1 ppm are from ethoxy groups in different environments, and can be due to free ethoxy groups [229] which are formed from the polycondensation reactions (reaction 1.2) which take place between two siloxanes [96] and can be trapped in pores.

The peaks are more intense for the calcium-containing sample. The ¹³C CP MAS NMR supports the ¹H NMR data, where the residues from TEOS alkoxide were found in higher concentration for the sample containing calcium. For S100 no stabilisation sample, the low intensity of the peaks at 17 and 60 ppm could indicate

that the $\text{SiOCH}_2\text{CH}_3$ groups were hydrolysed and an increased number of silanol groups ($\text{Si}(\text{OCH}_2\text{CH}_3)_4 \rightarrow \text{Si}(\text{OH})_4$) formed that could cause Si–O–Si bonds due to subsequent condensation compared with the calcium-containing silica sample (S70C30 no stabilisation). These findings are not accompanied by a substantial increase in Q^4 species for S70C30 no stabilisation sample as the ^{29}Si MAS NMR spectra revealed. However the Q^3 and Q^2 concentration is lower for 70S30C non-stabilised sample, which can imply that ethoxy groups are attached to these species in the silica network.

From solid state NMR, the evolution of the calcium distribution can be schematically illustrated as in Figure 4.6.

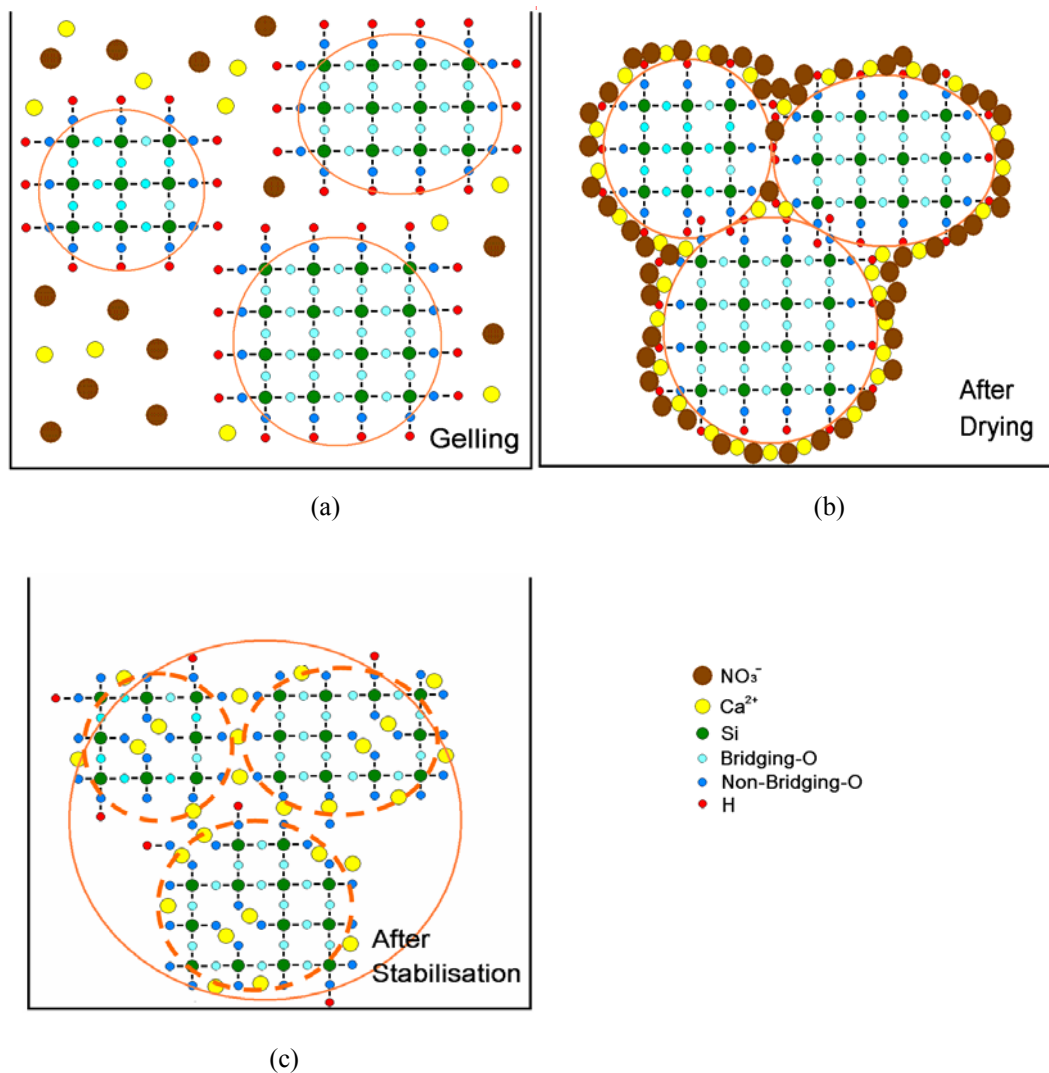


Figure 4.6. Schematic illustration of evolution of calcium distribution during the gelling stage (a), after the drying stage (b) and the stabilisation stage (c) following the sol-gel process.

Before drying, calcium nitrate is dissolved in the sol before gelation point and in the pore liquor after gelation point as shown in Figure 4.6 a. Calcium nitrate deposits onto the silica secondary particles during drying as shown in Figure 4.6 b. During stabilisation, as shown in Figure 4.6 c, nitrate decomposed and part of the calcium incorporated into the network of silica secondary particles as network modifiers. The oxygen in the Si-O-Ca bonds as was confirmed by neutron diffraction [230] and ^{17}O NMR [210] is a non-bridging oxygen. This is also in agreement with our ^{29}Si MAS NMR results.

4.3.2. Inhomogeneity characterisation in 70S30C sol-gel bioactive glasses

The compositional inhomogeneity found in 70S30C monolith samples by traditional protocols [41] was characterised here using ^1H and ^{29}Si MAS NMR. Figure 4.7 shows the separation of 70S30C monoliths after stabilisation into distinct components, a central translucent part surrounded by an opaque part.

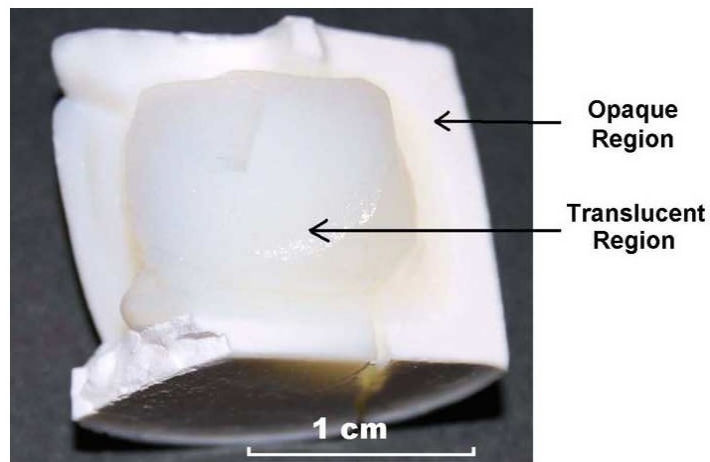


Figure 4.7. Cross-section of a 70S30C monolith made with the traditional method [2].

Hench and West [100] proposed that OH groups remained on the glass surface (products of hydrolysis reactions during the mixture stage and cannot be completely removed during the stabilisation stage) and hydrogen-bonded water (the concentration of which is determined by OH groups) could absorb light. The transparency difference between in the two regions could thus be due to the difference of surface OH group density in the two parts. Therefore, NMR is a powerful tool to verify the effects of the OH groups.

^1H MAS NMR results of the opaque and translucent parts which have been physically separated are shown in Figure 4.8.

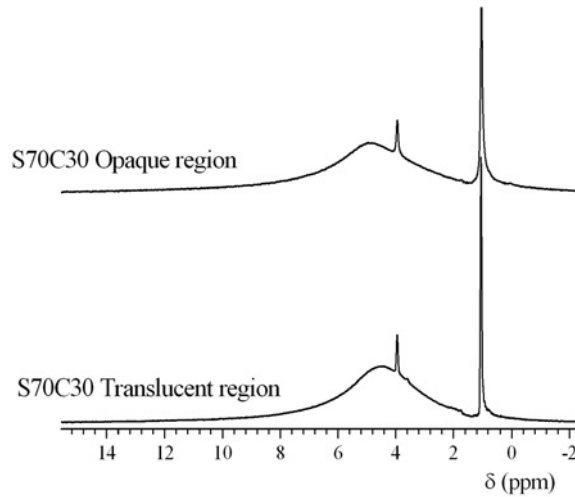


Figure 4.8. ^1H MAS NMR spectra of samples taken from the translucent and opaque regions of traditional 70S30C monoliths.

The broad component at 5 ppm on both samples corresponds to adsorbed water at the silica surface [218]. The two sharp peaks at approximately 4 ppm and 1 ppm can be attributed to water-like fluid [231] and isolated hydroxyls coordinated to calcium ions which are not part of the silicate network [216], respectively. Cations of relatively large field strength (defined as Z/R^2 , Z : charge and R : M-O bond length), as Ca^{2+} are capable of forming “free hydroxyls” [216] only linked to the calcium cation and not part of the silicate network. They are produced by adsorbed water dissolution of non-bridging oxygens (NBOs), when bridging oxygens (BOs) are obtained:



The peak corresponding to isolated hydroxyls is taller in the translucent region. Also the peak corresponding to adsorbed water has a higher intensity for the translucent region, as the translucent region being in the centre of the bulk can retain more water compared with the opaque region. This could explain the higher concentration of OH coordinated to calcium, as more SiOCa can react with H_2O . The

translucent region presents another two small peaks at 1.9 and 3.6 ppm from isolated and weakly hydrogen bonded silanols, respectively. The hydrogen contents in the two regions are shown in Table 4.4, which shows that the hydrogen content in opaque part is only approximately 50% of that in the translucent one.

Table 4.4. Hydrogen content in mol/g calculated from ^1H MAS NMR spectra.

Sample	Hydrogen content (mol/g)
S70C30 Translucent region	$(6.6 \pm 0.2) \times 10^{-3}$
S70C30 Opaque region	$(3.0 \pm 0.1) \times 10^{-3}$

This indicates that the surface OH groups and hydrogen-bonded water do not contribute to the transparency difference between the two parts. The lower hydrogen contents in the opaque parts could be due to the higher concentration of calcium that replaces the OH groups on the glass surface. This could also explain the lack of the resonances from SiOH in the opaque region compared with the translucent one.

^{29}Si MAS NMR spectroscopy could further confirm the calcium distribution in the translucent and the opaque regions by quantifying individual Si species in the silicate matrix. The ^{29}Si MAS NMR spectra are shown in Figure 4.9 for the translucent and opaque regions.

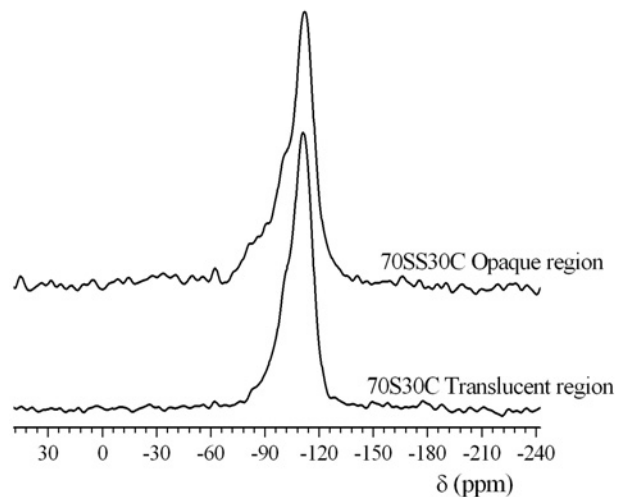


Figure 4.9. ^{29}Si MAS NMR spectra of samples in the translucent and opaque regions of traditional 70S30C monoliths.

Table 4.5. ^{29}Si MAS NMR data of 70S30C bioactive glass (traditional method), giving the spectral deconvolution into different Q^n species.

Sample	$Q^1(\text{Ca})$			$Q^2(\text{Ca})$			$Q^2(\text{H}), Q^3(\text{Ca})$			$Q^3(\text{H})$			Q^4		
	δ (ppm)	FWHM (ppm)	I (%)	δ (ppm)	FWHM (ppm)	I (%)	δ (ppm)	FWHM (ppm)	I (%)	δ (ppm)	FWHM (ppm)	I (%)	δ (ppm)	FWHM (ppm)	I (%)
70S30C Translucent region	-	-	-	-83.2	6.0	2	-91.9	10.0	8	-101.1	9.4	21	-111.6	11.3	69
70S30C Opaque region	-73.5	5.4	1	-81.7	8.4	6	-90.4	8.6	9	-100.2	9.7	20	-112.2	11.9	64

Table 4.6. ^{29}Si MAS NMR data for measured samples, giving the spectral deconvolution into different Q^n species.

Samples	$\text{HO-Si}(\text{CH}_3)_3$		$-\text{Si-O-Si}(\text{CH}_3)_3$		$Q^1(\text{Ca}), Q^0(\text{H})$		$Q^2(\text{Ca}), Q^1(\text{H})$		$Q^3(\text{Ca}), Q^2(\text{H})$		$Q^3(\text{H})$		Q^4		NC
	δ (ppm)	I (%)	δ (ppm)	I (%)	δ (ppm)	I (%)	δ (ppm)	I (%)	δ (ppm)	I (%)	δ (ppm)	I (%)	δ (ppm)	I (%)	
TMS-A4 non-stabilised upper component	17.4	1	12.9	10	-	-	-	-	-93.1	2	-102.1	18	-111.4	69	3.44
TMS-A4 non-stabilised lower component	17.0	4	12.2	40	-	-	-	-	-91.1	1	-100.4	17	-108.4	38	2.45
TMS-B1 non-stabilised	17.7	2	13.5	6	-	-	-	-	-94.6	3	-102.4	22	-111.5	67	3.46
TMS-B2 non-stabilised	18.9	2	14.2	17	-	-	-	-	-92.3	2	-100.3	21	-109.0	58	3.16
TMS-B3 non-stabilised	17.0	5	12.2	23	-	-	-	-	-93.1	2	-101.8	20	-110.1	50	2.87
TMS-B4 non-stabilised	16.5	4	11.8	29	-	-	-	-	-93.5	2	-101.7	17	-110.1	48	2.76
T-70S30C non-stabilised	-	-	-	-	-	-	-	-	-93.8	4	-102.1	27	-111.3	69	3.65
TMS-A4 stabilised upper component*	-	-	-	-	-77.1	5	-83.9	5	-91.8	5	-101.7	26	-110.8	59	-
TMS-B2 stabilised*	-	-	-	-	-	-	-80.5	4	-91.4	7	-99.6	19	-109.1	70	-
T-70S30C stabilised*	-	-	-	-	-73.9	8	-81.4	17	-88.5	16	-97.3	23	-109.5	36	-

FWHM, δ and I represent the linewidth full-width half-maximum, ^{29}Si chemical shift and relative intensity, respectively.

Errors associated with measurements are — FWHM \pm 1 ppm, $\delta \pm$ 2 ppm and Integral \pm 2%

*For stabilised samples the network connectivity has not been calculated because of the competing role of H^+ and Ca^{2+} in charge compensation of the NBO.

The results of deconvolution of the ^{29}Si MAS NMR spectra are shown in Table 4.3. As was shown above, calcium ions act as a network modifier leading to a less-connected silica network, increasing the number of non-bridging oxygen bonds, which open up the network [1]. As clearly shown in Table 4.5 the concentrations of Si species associated with calcium ions ($\text{Q}^3(\text{Ca})$, $\text{Q}^2(\text{Ca})$, $\text{Q}^1(\text{Ca})$) are higher in the opaque region than those in the translucent region. The difference in calcium distribution in the two regions can be understood from the evolution of the glass structure when calcium nitrate is used as the calcium precursor in the sol-gel synthesis. Calcium nitrate dissolves in the pore liquid (the by-products of polycondensation – alcohol and water) during the gelation and ageing stages. Due to the shrinkage of the gels during the ageing stage, much of the pore liquid and calcium nitrate are expelled out of the gels [1, 232]. During the stabilization stage, calcium diffuses into the gel but the diffusion path is very long for calcium to reach the inner part of the monoliths. Therefore, the outer regions (the opaque region) of the monoliths have higher calcium content than the centre (the translucent region).

4.3.3. Tailoring the nanoporosity of 70S30C sol-gel derived bioactive glasses by using trimethylethoxysilane

The two series made with TMES (collectively termed TMS-70S30C), TMS-A and TMS-B will be analysed, and compared to traditionally synthesised sol-gel glass (T-70S30C) described in section 4.3.1. The two TMS-A components of TMS-A samples were found to have separated into are named upper and lower components. The separation of components in TMS-A was hypothesised to be due to a heterogeneous TMES distribution, since a lower liquid component (a thin liquid layer beneath the sol) was observed after mixing the TMES with the sol. The lower liquid component might be due to separation of excess unreacted TMES (including hydrolysis products $(\text{CH}_3)_3\text{Si-OH}$ and self-condensation products $(\text{CH}_3)_3\text{Si-O-Si}(\text{CH}_3)_3$) from the sol. MAS NMR was used to confirm this hypothesis. TMS-B4 and TMS-A4 were made with the same TT (TMES:TEOS) ratio (1:4) and were used to determine how the point of TMES addition affects the process and the glass structure. The ^{29}Si MAS NMR spectra of dried, but not stabilised TMS-B4, and both upper and lower components of TMS-A4 are shown in Figure 4.10.

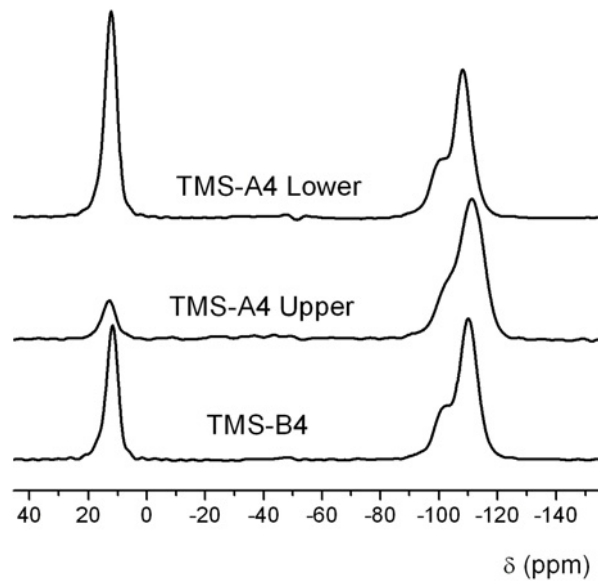


Figure 4.10. ^{29}Si MAS NMR spectra of non-stabilised TMS-B4 and the two components (upper and lower) observed in non-stabilised TMS-A4.

Unstabilised samples were used as they would still contain organic components from the TMES. Relative proportions of the different Q^n species and network connectivities (from NMR) are given in Table 4.6. The network connectivity, which is defined as the mean number of bridging Si-O-Si bonds per silicon atom, was calculated according to the amount of each of the different silicate species present in the glass. Network connectivity was calculated according to the equation:

$$\text{NC} = (4 \times Q^4\% + 3 \times Q^3\% + 2 \times Q^2\% + Q^1\% + \text{Si-O-Si}(\text{CH}_3)_3) / 100. \quad (4.4)$$

Figure 4.10 and Table 4.6 shows that more $-\text{Si-O-Si}(\text{CH}_3)_3$ bonds were found in the lower component of TMS-A4 compared with the upper component. The Q^4 species concentration in the lower component (38%) was also much lower than the upper component (69%) as shown in Table 4.6. The mean silicate network connectivity of the lower component (2.45) was significantly lower than that of the upper component (3.44). TMS-B4 and TMS-A4 have the same TT ratio; however, both the $-\text{Si-O-Si}(\text{CH}_3)_3$ bond content (29%) and the network connectivity (2.76) of TMS-B4 were between the values of the upper and lower components in TMS-A4.

^1H MAS NMR shown in Figure 4.11 supports the above hypothesis. The broad peak around 0 ppm in all samples is due to hydrogen from $\text{Si}(\text{CH}_3)$ group. As can be observed in the non-stabilised TMS-A4 upper component, the concentration of $\text{Si}(\text{CH}_3)$ groups are lower compared with the non-stabilised TMS-B4 and TMS-A4 lower component. This is in agreement with the ^{29}Si MAS NMR results.

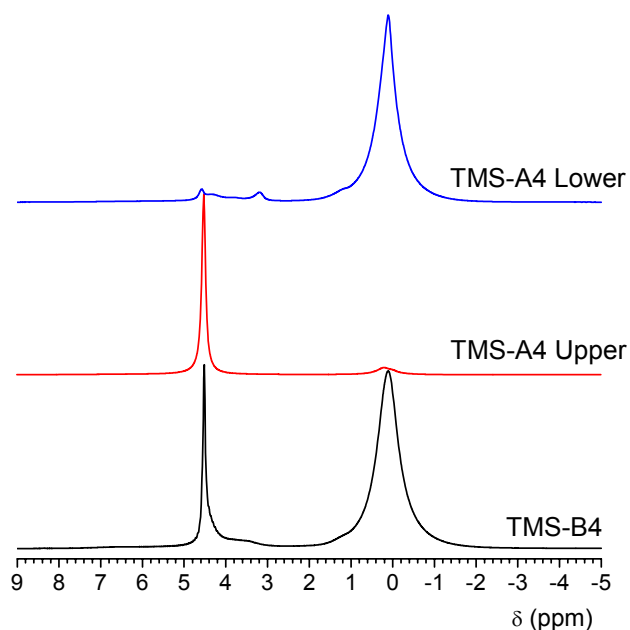


Figure 4.11. ^1H MAS NMR spectra of non-stabilised TMS-B4 and the two components (upper and lower) observed in non-stabilised TMS-A4.

All samples present a sharp peak around 4.6 ppm due to water molecules. The broad resonances at 1.3 and 4.2 ppm of TMS-B4 and TMS-A4 lower component are from CH_3 and CH_2O residual alkoxide from TEOS [219]. This finding also supports the initial hypothesis of the separation of the two TMS-A4 components. TMS-B4 and TMS-A4 lower component present a broad resonance around 3.2-3.5 ppm due to weakly bonded SiOH [233]. The linewidth of the 3.5 ppm peak for the TMS-B4 sample can be due to an inhomogeneous broadening associated with a variety of hydrogen-bonded silanols [221]. The hydrogen content is shown in Table 4.7. The TMS-A4 non-stabilised upper component shows a lower hydrogen content compared with the other two samples. This is due to the lower concentration of unreacted

TMES from the sol and further confirms our ^{29}Si NMR results and therefore the initial hypothesis.

Table 4.7. The H contents of non-stabilised and stabilised TMS-70S30C and T-70S30C calculated from ^1H NMR spectra.

Samples	H contents mol/g
TMS-A4 non-stabilised upper component	$(1.5 \pm 0.05) \times 10^{-2}$
TMS-A4 non-stabilised lower component	$(5.2 \pm 0.2) \times 10^{-2}$
TMS-B1 non-stabilised	$(0.7 \pm 0.02) \times 10^{-2}$
TMS-B2 non-stabilised	$(1.3 \pm 0.04) \times 10^{-2}$
TMS-B3 non-stabilised	$(2.0 \pm 0.6) \times 10^{-2}$
TMS-B4 non-stabilised	$(3.0 \pm 0.1) \times 10^{-2}$
TMS-A4 stabilised upper component	$(6.0 \pm 0.2) \times 10^{-3}$
TMS-B2 stabilised	$(3.0 \pm 0.1) \times 10^{-3}$
T-70S30C stabilised	$(9.3 \pm 0.3) \times 10^{-3}$

The ^1H MAS NMR spectra of non-stabilised TMS-B samples with different TT ratios present similar peaks (Figure 4.12) and the hydrogen content increase with increasing the TT ratio is due to the increasing of residual organics from TMES molecules. The peak positions are the same as for TMS-B4 and TMS-A4 lower and upper components.

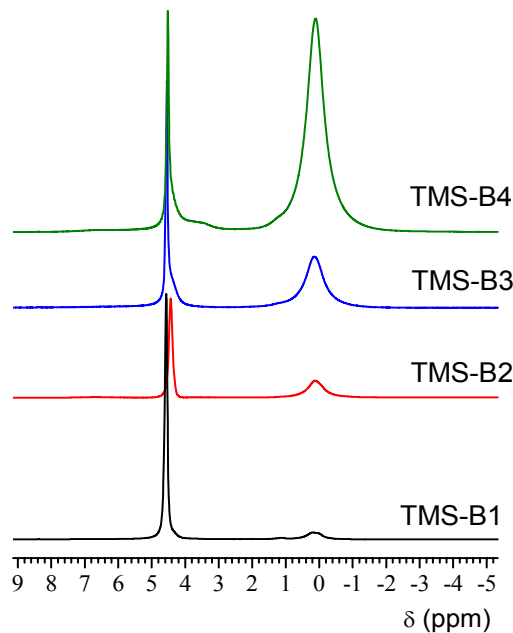


Figure 4.12. ^1H MAS NMR spectra of non-stabilised TMS-B samples with different TT ratio

To explore the mechanism of nanopore enlargement and verify the trimethylsilylation reaction mechanisms, ^{29}Si MAS NMR was conducted on the glasses after drying and prior to stabilisation. ^{29}Si MAS NMR spectra of the TMS-B series samples are shown in Figure 4.13.

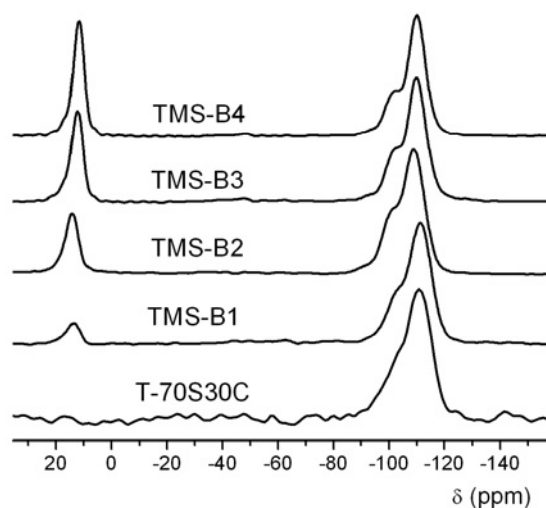


Figure 4.13. ^{29}Si MAS NMR spectra of non-stabilised T-70S30C and TMS-B series samples with various TT ratio.

The chemical shifts and relative intensities of the Si species and mean network connectivities are shown in Table 4.6. Organic siloxane bonds $-\text{Si}-\text{O}-\text{Si}(\text{CH}_3)_3$ were identified in the TMS-B samples by the peak at approximately 13 ppm chemical shift. The intensities associated with these bonds increased as the TT ratio increased and the intensity of peaks associated with the Q^3 and Q^4 species decreased (Table 4.6). The network connectivity decreased as the TT ratio increased, verifying the original hypothesis: trimethylsilylation reactions occurred during the sol-gel processes of TMS-70S30C samples, decreasing the network connectivity of the glass by replacing the silanol groups ($\text{Si}-\text{OH}$) with $-\text{Si}-\text{O}-\text{Si}(\text{CH}_3)_3$ groups and inhibiting the condensation reactions between the OH groups on the secondary particle surfaces. The large volume and the hydrophobicity of $-\text{O}-\text{Si}(\text{CH}_3)_3$ groups acted as barriers and retarded the fusion between the particles. The inhibition effects were enhanced as the TMES concentration increased. The use of TMES inhibits the fusion between the secondary particles via the trimethylsilylation reactions. The difference

between TMS-A and TMS-B samples can be explained by the different reaction kinetics of TMES at different time points during the sol–gel process, which can also explain the homogeneity difference between TMS-A and TMS-B samples.

The secondary particles formed during the mixing stage, after hydrolysis of the TEOS and the start of the condensation reactions [1]. The particles were highly reactive to TMES before casting due to the high OH group density on their surfaces. The addition of TMES at this point (TMS-A series) enhanced the trimethylsilylation reactions and inhibited further condensation between the secondary particles. For TMS-B series, as TMES was added after casting and prior the gelation, the secondary particles became considerably less reactive to TMES since further condensation reactions occurred and decreased the OH group density on the secondary particles and increased the particle size (TMS-B series). The trimethylsilylation reactions were thus relatively less effective in TMS-B series, compared to TMS-A4, and the fusion between the secondary particles was then not noticeably retarded.

The upper component of TMS-A4 (TT ratio 1:4) was used for further analysis, as the lower component of TMS-A has excessive unreacted TMES and shows no nanoporosity [3]. From the TMS-B series, the TMS-B2 (TT ratio 1:8) was used for further analysis, since it showed a significant increase in nanopore size [3].

It is important that the glasses made with TMES can still contain calcium and be bioactive. Therefore the calcium incorporation into the TMS samples can be monitored by comparing the network connectivity before and after the stabilisation stage. In order to test the calcium incorporation in TMS-70S30C samples, ^1H and ^{29}Si MAS NMR of stabilised TMS-A4, TMS-B2 and T-70S30C were conducted. The ^1H MAS NMR spectra of stabilised TMS-A4 (upper component), TMS-B2 and T-70S30C are shown in Figure 4.14.

The broad resonance at 4.2–4.7 ppm for TMS-B2 and TMS-A4 stabilised samples can be assigned to H-bonded H_2O molecules with surface Si-OH groups [233]. The sharp peak around 1.5 ppm is due to isolated internal silanols [220, 221]. By removing water by thermal treatment, some of the hydrogen bonded silanols which were bonded just to water, detected in unstabilised samples become isolated SiOH at higher temperatures by progressive removal of SiOH via condensation/dehydroxylation. Also the isolated silanols in interstices between

particles because of steric hindrance have little chance to be accessible to water molecules. This could explain the absence of this peak for TMS-A4 sample, where now strongly hydrogen bonded silanols are still present as an additional broad resonance of low intensity centered around 7.2 ppm [221, 222]. The difference in peak positions can be due to different water content in the samples. For TMS-A4 and TMS-B2 compared with 70S30C stabilised samples there is no evidence of H atoms connected to Ca-O groups.

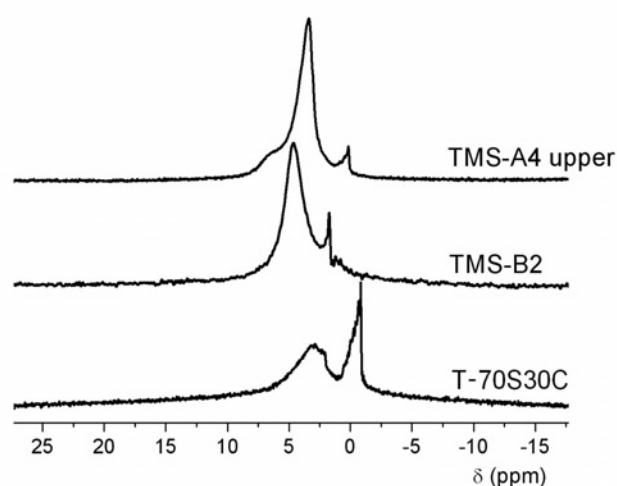


Figure 4.14. ^1H MAS NMR spectra of stabilised TMS-A4 upper, TMS-B2 and T-70S30C samples.

The H contents of the samples (Table 4.7) were determined. The results show that the H contents in TMS-A4 ($(6.0 \pm 0.2) \times 10^{-3}$ mol/g) and TMS-B2 ($(3.0 \pm 0.1) \times 10^{-3}$ mol/g) were lower than that in T-70S30C ($(9.3 \pm 0.3) \times 10^{-3}$ mol/g). This is due to replacement of the surface OH groups by O-Si(CH₃)₃ groups during the trimethylsilylation reactions. The oxidation of -Si(CH₃)₃ groups during the stabilisation stage converted the methyl groups into CO₂ and H₂O. The exothermic reactions might enhance further condensation reactions between the existing OH groups, which were not replaced by O-Si(CH₃)₃ groups. Comparing non-stabilised samples (Table 4.7), the hydrogen content is reduced almost by one order of magnitude, as by stabilisation the organics are removed from the system, as shown above. However, TMS-A4 compared with TMS-B2 sample still presents a small amount of Si(CH₃) species with a resonance around 0 ppm as a sharp component,

suggesting a relative mobility of these species (rotating CH₃ around Si-C bond) on the surface of the silica particles.

The ²⁹Si MAS NMR spectra of the stabilised TMS-A4 (upper component), TMS-B2 and T-70S30C are compared in Figure 4.15.

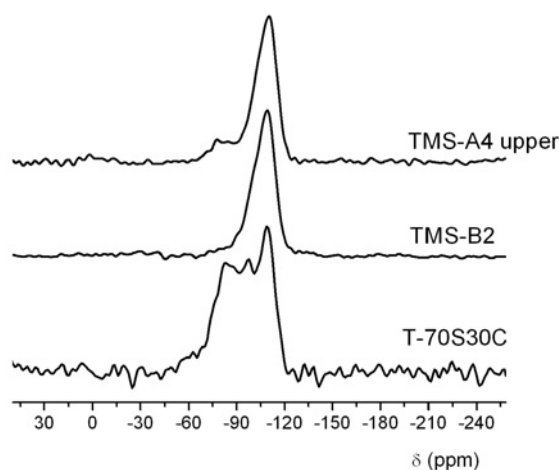


Figure 4.15. ²⁹Si MAS NMR spectra of stabilised TMS-A4 upper, TMS-B2 and T-70S30C samples.

The composition of various silicate species and the TMES content are shown in Table 4.6. The organic content from TMES was removed from the samples by the heat treatment during the stabilisation stage (600 °C), as the signals corresponding to -Si-O-Si(CH₃)₃ group were absent in the spectra of the stabilised TMS-A4 and TMS-B2. For TMS-A4 these species have to be in very low concentration and have not been detected in the ²⁹Si NMR spectrum compared with ¹H NMR spectrum. After the stabilisation stage, the concentration of Q³(H) and Q⁴ of TMS-B2 increased, whereas the same species for both TMS-A4 and T-70S30C decreased. In TMS-A4 and T-70S30C, the calcium is incorporated into the silica network during the stabilisation stage which results in the decrease of the network connectivity. The unexpected increase in the concentration of Q³(H) and Q⁴ species of TMS-B2 could be due to two possible reasons. Since inorganic calcium nitrate (calcium precursor) could be repelled from the organic content in the unstabilised samples, the calcium incorporation during the stabilisation stage was thus inhibited in TMS-A4 and TMS-B2. This could decrease its degradation rate and bioactivity. Table 4.6 shows that the organic content was higher in non-stabilised TMS-B2 (-Si-O-Si(CH₃)₃ groups 17%

and HO-Si(CH₃)₃ groups 2%) than that in TMS-A4 (-Si-O-Si(CH₃)₃ groups 10% and HO-Si(CH₃)₃ groups 1%, upper component), which resulted in lower calcium incorporation in TMS-B2 compared with TMS-A4. Although the calcium incorporation in TMS-A4 was better than that in TMS-B2, the organic content in TMS-A4 still inhibited the calcium incorporation compared with T-70S30C. This is confirmed by the concentration of Qⁿ species associated with Ca²⁺, which is lower for stabilised TMS-A4 compared with the stabilised T-70S30C. Therefore, the sequence of the extent of calcium incorporation into the silicate network is T-70S30C > TMS-A4 > TMS-B2. Compared with T-70S30C, more calcium in TMS-70S30C might stay on the surface of silicate particles after the thermal decomposition of nitrate instead of being incorporated into the silica network. The other possible reason for the concentration of Q³(H) and Q⁴ increase in TMS-B2 after stabilisation could be attributed to the oxidation of -Si(CH₃)₃ groups of the TMES nano-clusters in this sample during the stabilisation stage and the reactions could cause condensation between the -Si(CH₃)₃ groups within the clusters. This could contribute in the increased silicate connectivity in TMS-B2 compared with TMS-A4.

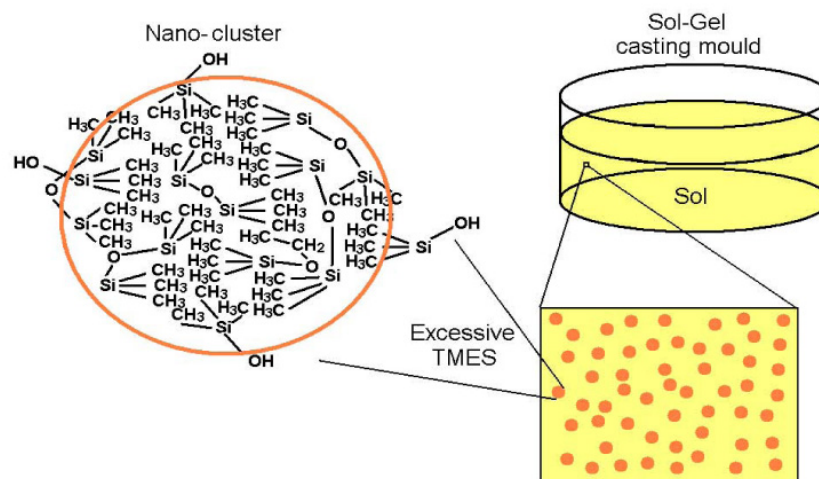


Figure 4.16. Schematic illustration of “nano-cluster” formed by excessive TMES in the sol of TMS-B2 [3].

This can be understood from the evolution of the TMS-B2 sample. The organic components from excess TMES (including hydrolysis products (CH₃)₃Si-OH

and self-condensation products $(\text{CH}_3)_3\text{Si-O-Si}(\text{CH}_3)_3$) can constitute “nano-clusters” which were dispersed within TMS-B2. Figure 4.16 schematically illustrates the “nano-clusters”. When the viscosity of the sol increased during the casting stage, the vigorous agitation after the TMES addition caused excess TMES aggregation into “nano-clusters” via hydrophobic interactions, which were “trapped” within the sol of TMS-B2. The dispersed nano-clusters act as an organic template, which burns off during the stabilisation stage leaving the enlarged nanopores. During the stabilisation stage, the excess TMES might incorporate into the primary silicate network via oxidation and condensation reactions between the $\text{Si}(\text{CH}_3)_3$ groups. If more TMES was added, the “nano-cluster” templates are likely to become more numerous and larger. Excess TMES is clearly not soluble in the sol, but when the viscosity is high, clusters of it become trapped (TMS-B series), but when viscosity is low, it separates (TMS-A series).

4.4. Conclusions

Solid state NMR of sol-gel derived bioactive glasses (70 mol% SiO_2 and 30 mol% CaO) shows that the stabilisation process produces a loss of residual organic fragments and structural hydroxyls. From ^1H MAS NMR clearly different proton species can be detected, with some that must be associated with the calcium. ^{29}Si MAS NMR indicates that on decomposition of the nitrate Ca^{2+} enters the silicate network during the stabilisation stage increasing the range of Q^n species present and hence the disorder of the silicate network. The experimental results demonstrate that quantitatively reliable results about all the Q^n species, including Q^4 , can only be obtained with direct excitation of the silicon nuclei. ^{13}C CP MAS NMR spectra show that several percent of the ethoxy groups of the TEOS monomers are not hydrolysed and end up inside the silica matrix at the xerogel stage.

Sol-gel derived 70S30C glass monoliths produced using the traditional method present a heterogeneous calcium distribution which results in the large scale nanostructural inhomogeneity of the glasses, with translucent regions towards the centre of the monolith and thick opaque regions around the outside. The opaque region had a higher concentration of calcium than the translucent one. The heterogeneous calcium distribution within the monoliths probably resulted from the diffusion difficulties of the calcium during the drying stage.

Two series of samples using TMES as a condensation inhibitor were analysed by solid state NMR and compared with a traditional 70S30C sol-gel derived bioactive glass. ^1H and ^{29}Si NMR supported the hypothesis of the inhomogeneity between the two series as TMES was added at different time in the process. TMES residues were present in the xerogel stage, for the TMS-B series their concentration being between the two components TMS-A separates into. The hydrogen content and the concentration of organic siloxane bonds $\text{Si-O-Si}(\text{CH}_3)_3$ were found to increase with TMES which acted as a condensation inhibitor due to a trimethylsilylation mechanism. In the mechanism of trimethylsilylation reactions in TMS-A and TMS-B samples, the OH groups on the surface of silicate nanoparticles (secondary particles) before the stabilisation stage were replaced by $\text{O-Si}(\text{CH}_3)_3$ groups, which acted as barriers and inhibited the fusion of secondary particles into tertiary particles. Compared with TMS-B samples, since TMES was added before the casting stage for TMS-A samples, TMES covered the secondary particles effectively and blocked their fusion into tertiary particles. The excess TMES in the TMS-B samples dispersed into the viscous sol as nanoclusters and the clusters, which burned off after the stabilisation stage, acted as templates in the TMS-B samples. By adjusting the dosage of the TMES as a quencher, the distribution of calcium is affected and the over-all network connectivity. The incorporation of calcium in the silicate network was sacrificed in the TMS-B samples, even if the homogeneity was improved.

5.

SOL-GEL 58S (SiO₂-CaO-P₂O₅) DERIVED BIOACTIVE GLASSES

5.1. Introduction

The SiO₂-CaO-P₂O₅ system is one of the most widely studied in the field of bioactive sol-gel glasses [37, 38, 234-237] with the 58S (60 mol% SiO₂, 36 mol% CaO, 4 mol% P₂O₅) composition being the most bioactive one [238]. The relation between bioactivity and the phosphorus content has been explored in the sol-gel derived glasses [234-237]. It was shown that although not strictly necessary for bioactivity, the introduction of small amounts of P₂O₅ in the glass enhances the apatite crystallisation [234-237, 239].

One of the advantages of sol-gel process is that it is possible to use inorganic salts or alkoxides as calcium source reagents via inorganic or alkoxide routes to obtain bioactive glasses [240]. The use of calcium alkoxides, comparing calcium nitrates has the advantage that high temperatures are not required for the removing of toxic nitrates as by-products [1]. The use of high temperatures can alter the structural and textural properties of the bioactive glasses [241, 242]. Glasses exhibit better structural and textural properties with a thicker and compact homogeneously distributed apatite-like layer formed in simulated body fluid [240] when calcium methoxyethoxide (CME) was used.

Solid state NMR studies of phosphate sol-gel derived bioactive glasses have been recently reported in literature [243-246]. It was shown that in the 58S composition, phosphorus is present as separate nanometer-sized clusters of amorphous calcium orthophosphate, dispersed over the pore walls [245].

The aim of this chapter is to follow the nanostructure evolution with temperature by solid-state NMR spectroscopy in 58S derived sol-gel bioactive glasses synthesised via inorganic and alkoxide routes.

5.2. Experimental details

The syntheses of the samples by inorganic and alkoxide routes have been described in Chapter 3. The ¹H MAS NMR spectra were recorded using a Bruker 500 MHz (11.7 T) spectrometer operating at 500.1 MHz. MAS spectra were recorded with a Bruker 4 mm probe at 12.5 kHz, using 5 s recycle delay and a 2.50 μs (90° tip angle) pulse. The chemical shift was referenced externally to adamantane (C₁₀H₁₆) at 1.8 ppm. The hydrogen content determination has been described in Chapter 4. ³¹P MAS NMR and ³¹P CP MAS NMR spectra were measured on a Bruker 500 MHz system, operating at 202.48 MHz using a Bruker 4 mm probe, at a spinning speed of 12.5 kHz. For MAS NMR spectra 3.0 μs (90° tip angle) pulse and 3 s pulse delays have been used. For the CP MAS NMR spectra, a 3 ms contact pulse was used, along with a 3 s recycle delay and collected under ¹H decoupling. Ammonium dihydrogen phosphate, NH₄H₂PO₄, has been used as external reference at 0.9 ppm. ²⁹Si MAS NMR spectra were collected on a Varian InfinityPlus 300 MHz spectrometer operating at 59.62 MHz. A 30 s recycle delay and a 3 μs (30° tip angle) were used which produced relaxed spectra. ²⁹Si spectra were referenced to TMS at 0 ppm. ¹³C CP MAS NMR spectra have been recorded on a Bruker 500 MHz system with a 4 mm Bruker probe spinning at 8 kHz. A contact time of 1 ms and 5 s pulse delay have been used. SPINAL 64 heteronuclear decoupling was applied. Alanine has been used as external reference at 20.5 ppm.

5.3. Results and discussion

The ¹H NMR spectra of samples synthesised from calcium nitrate and calcium methoxyethoxide as calcium precursors, are shown in Figures 5.1 and 5.2 a and b, respectively. In figure 5.2 a, for the 58S CME 130 and 58S CME 500 samples an insert to magnify the corresponding region is shown. The hydrogen content as obtained from the integrated intensity of the spectra and the peaks position are shown in Table 5.1.

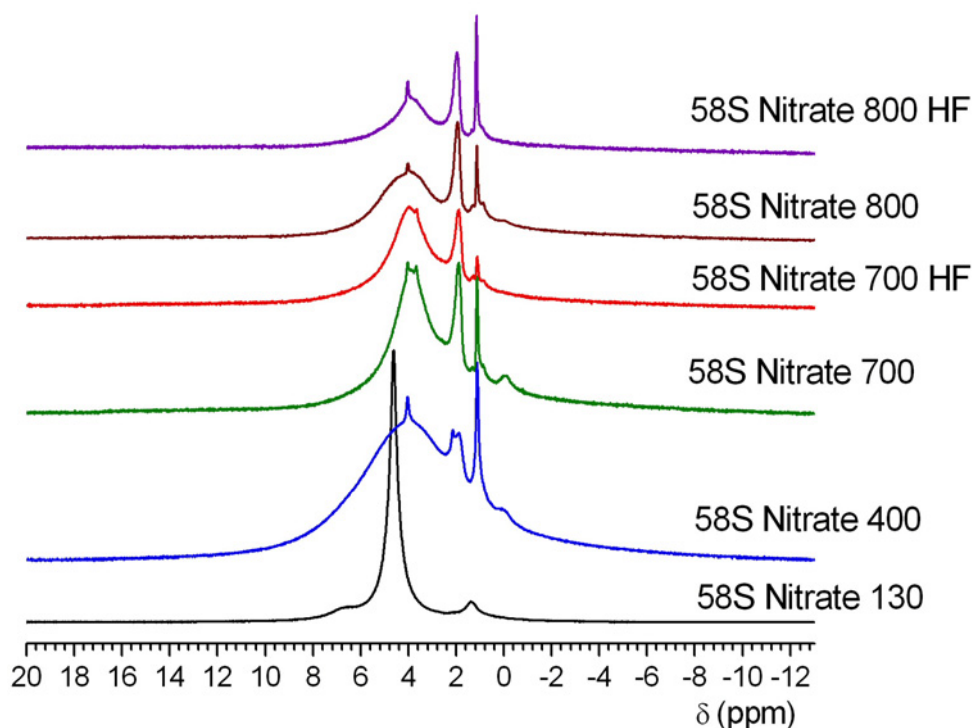
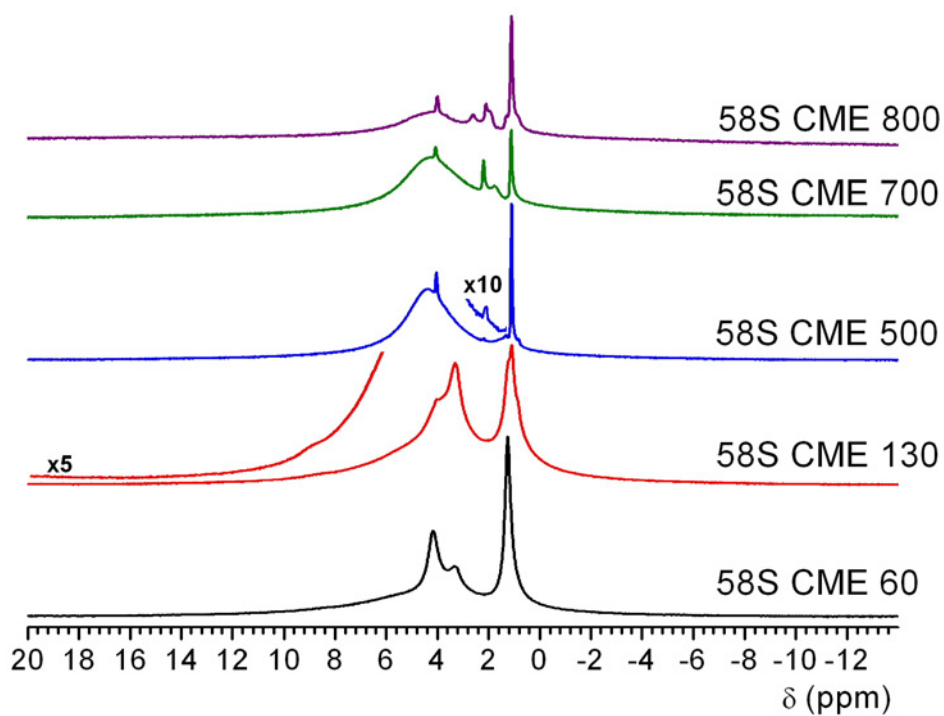


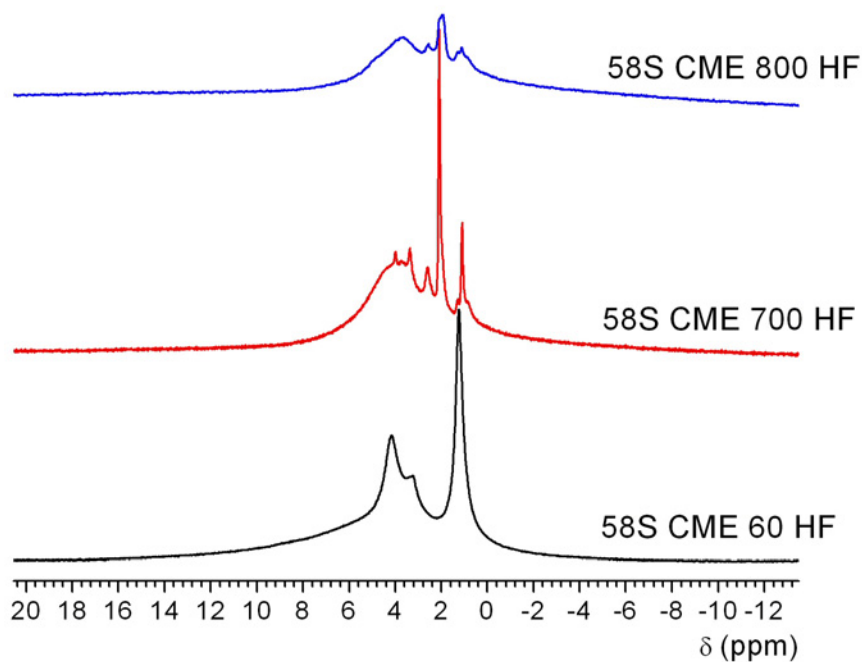
Figure 5.1. ^1H MAS NMR spectra of 58S samples synthesised via inorganic route.

Table 5.1. The hydrogen content and peak position as determined from ^1H NMR spectra.

Sample	Hydrogen content (mol/g)	Peak position (ppm) ± 0.1 ppm accuracy.
Inorganic route		
58S Nitrate 130	$(2.31 \pm 0.76) \cdot 10^{-2}$	6.8, 4.6, 1.3
58S Nitrate 400	$(6.76 \pm 2.23) \cdot 10^{-3}$	4.4, 4.0, 2.1, 1.9, 1.1, 0.0
58S Nitrate 700	$(2.08 \pm 0.69) \cdot 10^{-3}$	4.0, 3.8, 3.7, 1.9, 1.3, 1.1, 0.9, 0.0
58S Nitrate 700 HF	$(2.86 \pm 0.94) \cdot 10^{-3}$	4.0, 3.7, 1.9, 1.3, 1.1, 0.9,
58S Nitrate 800	$(1.32 \pm 0.43) \cdot 10^{-3}$	4.3, 4.0, 1.9, 1.3, 1.1, 0.9, 0.0
58S Nitrate 800 HF	$(9.50 \pm 3.13) \cdot 10^{-4}$	4.0, 3.7, 2.0, 1.3, 1.1, 0.9
Alkoxide route		
58S CME 60	$(1.71 \pm 0.56) \cdot 10^{-2}$	6.5, 4.1, 3.3, 1.2
58S CME 60 HF	$(1.90 \pm 0.63) \cdot 10^{-2}$	5.6, 4.2, 3.2, 1.2
58S CME 130	$(2.86 \pm 0.94) \cdot 10^{-2}$	8.7, 5.8, 4.1, 3.3, 1.2, 1.1, 0.8
58S CME 500	$(1.38 \pm 0.46) \cdot 10^{-2}$	4.4, 4.0, 2.2, 1.3, 1.1, 0.8
58S CME 700	$(5.75 \pm 1.90) \cdot 10^{-3}$	4.3, 4.1, 2.2, 1.8, 1.1
58S CME 700 HF	$(1.26 \pm 0.42) \cdot 10^{-3}$	4.3, 4.0, 3.4, 2.6, 2.1, 1.3, 1.1, 0.8
58S CME 800	$(5.11 \pm 1.69) \cdot 10^{-4}$	4.5, 4.0, 2.6, 2.1, 1.3, 1.1, 0.9
58S CME 800 HF	$(3.42 \pm 1.13) \cdot 10^{-4}$	3.7, 2.6, 2.0, 1.3, 1.1, 0.9



(a)



(b)

Figure 5.2. ^1H MAS NMR spectra of 58S samples synthesised via alkoxide route (a and b).

At low temperature for both nitrate (58S Nitrate 130) and CME (58S CME 60, 60HF and 130) samples the residues from the alkoxide chains can be detected in

the ¹H MAS NMR spectra. In samples synthesised by alkoxide route, beside the peaks from TEOS and TEP residues at 1.2-1.3 ppm and 4.0 ppm [219] for methyl hydrogens (CH₃) and methylene hydrogens from -CH₂O- groups, respectively, another resonance at 3.2-3.3 ppm appears. This is due to hydrogens from methoxymethyl (CH₃O) group from CME precursor. -CH₂O- groups from CME have the same chemical shift as the ones from TEP and TEOS at 4.1 ppm. These peaks are broad due to homonuclear coupling. The peak at 4.6 ppm in the nitrate sample is due to physisorbed water. This can hinder the observation of the peak for CH₂O which appear at 4.0 ppm in alkoxide residues [219]. In this sample the peaks from alkoxide residues are small in intensity, suggesting that most of them have been removed from the system. Beside the peaks from alkoxide chains, other resonances as very broad signals can be detected in the spectra of these samples in the 5.6-8.7 ppm region (Table 5.1). These peaks suggest a moderately strong hydrogen bonded OH, either SiOH [220-222, 233, 247] or POH [248], with O-H...O distances (d_{O-H...O}) of 2.88, 2.87, 2.84, 2.83, 2.76 Å for resonances at 5.6, 5.8, 6.5, 6.8 and 8.7 ppm, respectively, calculated with the formula [249]:

$$\delta_{\text{iso}} (\text{ppm}) = 79.05 - 0.255d_{\text{O-H}\cdots\text{O}} (\text{pm}) \quad (5.1)$$

There is no difference between the 60°C CME samples when HF was used as catalyst in the sol-gel synthesis (58S CME 60 and 58S CME 60 HF) as is shown in the Figure 5.2. a and b and in Table 5.1, where the hydrogen content for the two samples is similar ((1.71±0.56)·10⁻² and (1.90±0.63)·10⁻², respectively). Also on increasing the temperature to 150°C for the CME sample the peak from CH₂O at 4 ppm is much smaller in intensity compared to peaks corresponding to CH₃ and CH₂O at 1.3 and 3.3 ppm, and now CH₃ and CH₂O are comparable in intensity. This suggests that CH₃ and CH₂O are removed from the system in a higher concentration comparing CH₃O, which mean that the residues from TEOS and/or TEP are less than the ones from CME. The peak at 1.3 ppm has now three components at 1.3, 1.1 and 0.9 ppm, probably due to some incomplete oxidation residues. Similar components have been attributed in the literature to organic surface contamination for melt-derived glasses [231], but in our case are residues from alkoxide chains. CME hydrolysis and condensation is faster compared with TEP and TEOS, therefore the

hydrolysis product of CME, methoxyethanol (CH₃OCH₂CH₂OH) can be trapped in the pores during the shrinking of the gel with increasing the temperature to 130 °C and this explains the higher concentration of these species. An interesting effect of this sample is the increased hydrogen content comparing samples at 60°C, probably due to adsorbed water on the surface as an effect of the presence of highly reactive calcium ions.

With increasing the temperature to 400 and 500 °C for nitrate and CME samples, respectively, the well defined peaks corresponding to the alkoxide chain do not appear in the spectrum suggesting that they have been removed by thermal treatment. This is also supported by the hydrogen content decrease as shown in Table 5.1. The resonances at 1.3 and 0.8 ppm from organic residues appear as very small components in the spectra suggesting that most of the alkoxide residues have been eliminated from the system. The peak at 1.1 ppm for both samples is within the range from organic residues from methyl hydrogens, but for 58S CME 500 it is very intense and sharp. Therefore, it is possible that this peak to be assigned to “free hydroxyls” coordinated to calcium cations, CaOH and not part of the silicate network. [216], produced by adsorbed water dissolution of non-bridging oxygens (NBOs), when bridging oxygens (BOs) are obtained (*see eq. 4.3*). The sharpness of the peak suggests that these hydroxyls coordinated to calcium are non-hydrogen bonded.

For 58S Nitrate 400 sample the peak is broader comparing 58S CME 500 sample, possibly due to a higher contribution from the organic residues and a lower mobility.

The sharp peaks at 1.9 and 2.1 ppm are probably due to isolated internal silanols [220, 221, 233, 247]. For nitrate samples two types of OH can be detected, while for CME samples, the peak corresponding to isolated OH is very low in intensity. The physisorbed water on both samples appears at 4.6 ppm. The peak at 4.1 ppm in the same region with the resonance from CH₂O but it is very sharp, similar to those found in liquids. Consequently, it can be attributed to the fluid-like water inclusions [231]. Similar peaks have been detected in the literature [231, 249]. At this temperature further condensation between silanols take place and water as a condensation product can be trapped in pores. Also, due to the high concentration of

calcium ions, the adsorbed water can form a layer like water which condenses to form liquid water phase in the pores.

The peak at 0.0 ppm in the 58S Nitrate 400 sample corresponds to the structural OH found in hydroxyl apatite (HAp) [250-252], suggesting the formation of structures similar to HAp at this temperature for samples synthesized via the inorganic route. The peak is absent in the spectrum of CME samples.

The spectra of samples synthesised by inorganic route and thermally treated to 700 and 800 °C present similar behaviour. The 58S Nitrate 700 sample has two sharp peaks in the water region, probably the sharp peak at 3.7 ppm is also a water inclusion in a different environment compared with the 4.0 ppm peak. All four samples present just one type of isolated silanol at 1.9-2.0 ppm. The spectra of the samples with fluoride ions in composition (58S Nitrate 700 HF and 58S Nitrate 800 HF) do not show the peak at 0.0 ppm. This can be due to the fact that either the HAp-like structure is not formed or the HO⁻ ions in the apatite structure have been substituted by F⁻ ions. For the 700 °C sample containing fluoride ions, the concentration of free hydroxyls at 1.1 ppm is very low probably due to the low concentration of adsorbed water on the surface, therefore the calcium ions' ability to coordinate to water is reduced.

For samples synthesised by the alkoxide route and thermally treated to 700 and 800 °C, the spectra are slightly different compared with the inorganic route. Beside the peaks corresponding to isolated internal silanols, another resonance appears at 2.6 ppm attributed to external silanols bridged to each other and not with water molecules [220]. For the 58S CME 700 HF sample two types of water inclusions are observed and the concentration of internal silanols is high, as the peak corresponding to these species is the highest in the spectrum and is very sharp. This suggests that new SiOH are formed in the system by reaction 4.3, and are on the interior of the particles inaccessible to water molecules. By increasing the temperature to 800 °C they condense to form new Si-O-Si BOs. This explains the lower intensity of the peak for the 58S CME 800 HF sample. In all CME spectra the peak at 0.0 ppm is absent, either hidden in the background or the HAp is not formed in the system.

All samples made via inorganic or alkoxide routes present the small peaks at 1.3 and 0.8 ppm, as some organic fragments from alkoxide chains remain in the

system even at 800°C, probably trapped in pores. Also with increasing the temperature the hydrogen content decreases, as organic fragments and water are eliminated. The position of the fluid-like water inclusions and physisorbed water depend on the water content of each sample.

To further analyse the loss of organics with the temperature ^{13}C CP MAS NMR has been performed. The spectra of the sample synthesised by inorganic and alkoxide routes are presented in Figures 5.3. and 5.4. a and b, respectively.

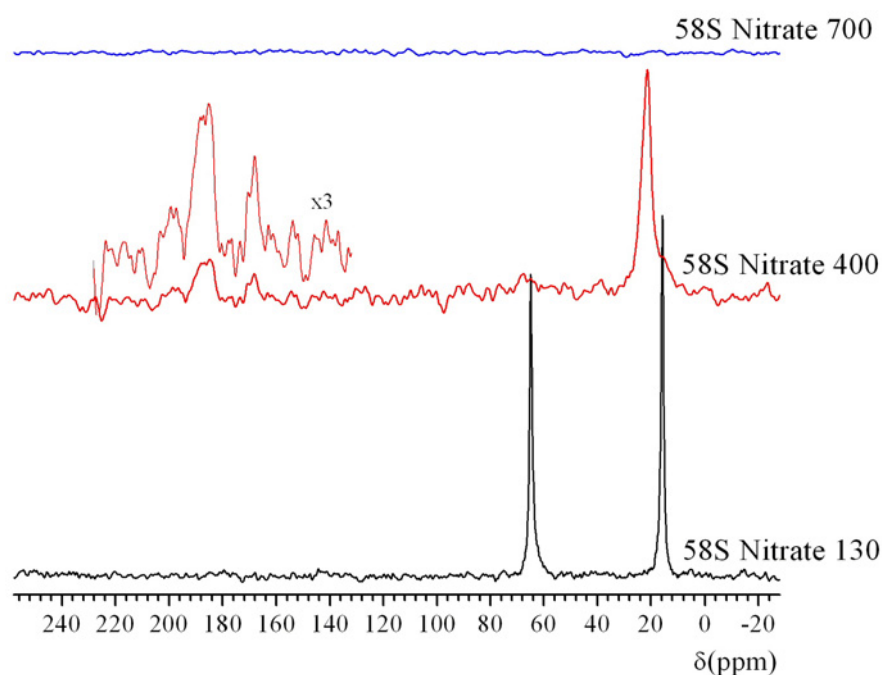
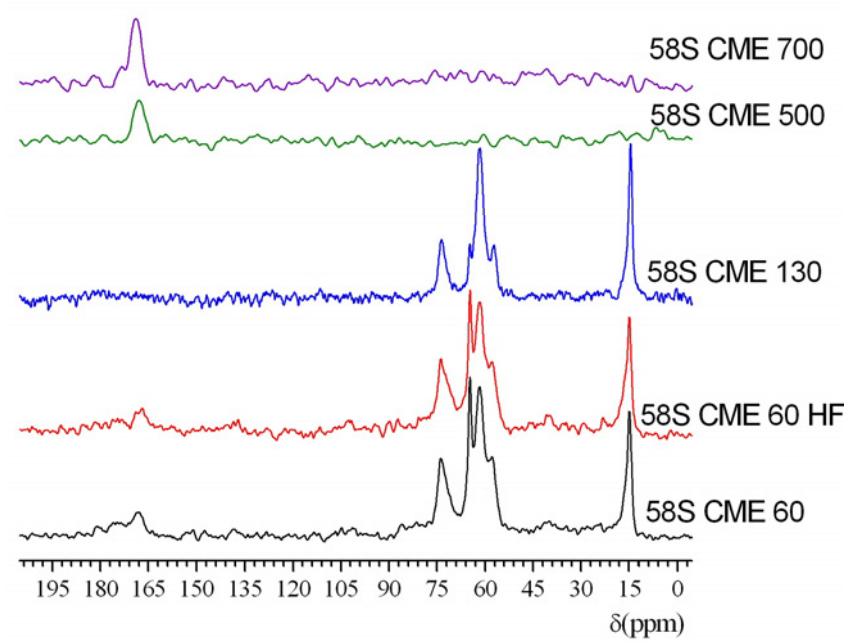
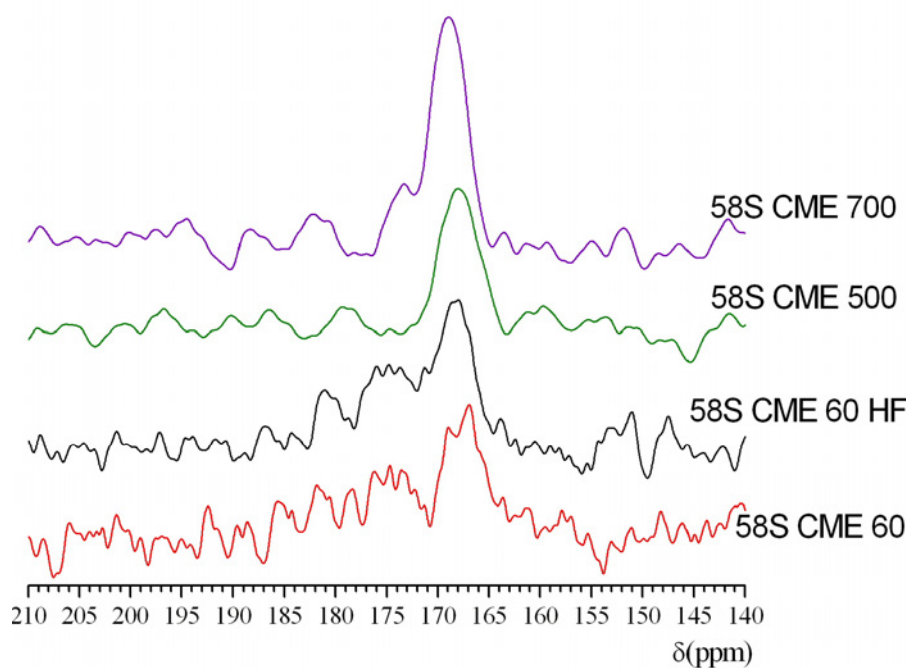


Figure 5.3. ^{13}C CP MAS NMR spectra of 58S samples synthesised from nitrate as calcium precursor, with an insert for 58S Nitrate 400 sample showing the carbonate region.

In the 58S Nitrate 130 sample the peaks at 15.7 and 64.9 ppm correspond to CH_3 and OCH_2 from residual alkoxide chains from TEOS and TEP [253]. Increasing the temperature to 400 °C, the peak from methyl is still present at 21.5 ppm, with a very small contribution of OCH_2 at 67.8 ppm, suggesting that by increasing the temperature more organics have been removed. This is consistent with the ^1H NMR data where the resonances from organic fragments are reduced in intensity. Also other peaks appear as can be seen in table 5.2. The peaks at 168.5 and 170.8 ppm can be attributed to carbonates that form on the surface.



(a)



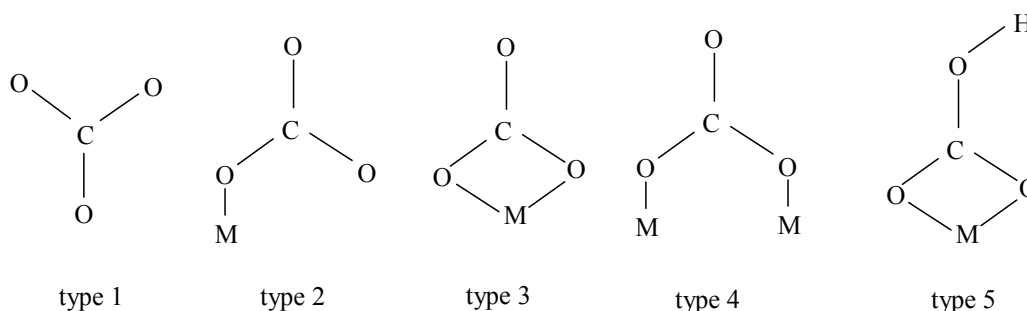
(b)

Figure 5.4. ^{13}C CP MAS NMR spectra of 58S samples synthesised from CME as calcium precursor (a) and the carbonate region (b).

Table 5.2. Peak position from ¹³C CP MAS NMR spectra.

Sample	Peak position (ppm) ± 0.1 ppm accuracy
Inorganic route	
58S Nitrate 130	15.7, 64.9
58S Nitrate 400	21.5, 67.8, 168.5, 170.8, 184.5, 186.7
58S Nitrate 700	-
Alkoxide route	
58S CME 60	14.9, 57.9, 61.7, 64.7, 73.8, 165.8, 166.9, 168.9, 173.3, 174.7, 176.2
58S CME 60 HF	15.0, 57.8, 61.7, 64.7, 74.0, 167.9, 168.7, 171.3, 173.6, 174.7, 175.9, 180.1
58S CME 130	14.6, 57.1, 61.5, 64.8, 73.6
58S CME 500	168.5, 169.6
58S CME 700	168.9, 173.3

It was shown that different types of carbonates can be form by the adsorption of CO₂ on metal oxides [254]. In Figure 5.5 some of the most representative species are presented.

**Figure 5.5.** Possible surface carbonate-like species [254]. Double bonds and charges are omitted for simplicity.

The CO₃²⁻ ion consists of a central sp² hybridized C atom, with three O atoms at the corners of an equilateral triangle [255] (type 1, Figure 5.5.). Type 1 is a symmetrical, ionic carbonate-type ion, whereas types 2-5 are coordinated-type carbonates: monodentate (type 2), bidentate (type 3), bridged or “organic like type” (type 4) and bicarbonate (type 5), respectively.

It was shown [256] that the mechanism of formation of carbonates on the surface of 58S samples synthesised from calcium nitrate as the CaO precursor, involves a reaction of CO₂ with the water present on the surface of these samples to give carbonate ions:



Calcium ions present on the silica surface can form NBOs with two silanols. The calcium ions in these NBOs are very reactive and can interact with carbonate ions to form ionic carbonates (type 1 in Figure 5.5.) as shown by the ¹³C CP NMR results. As was shown [256], on the 58S surface of the sample made from nitrate there are no O²⁻ species sufficiently basic to lead to the formation of the coordinative carbonates (type 2-5 in Figure 5.5) at this temperature.

In literature, the reported chemical shifts for synthesised crystalline calcium carbonates are [257, 258]: calcite (168.7 ppm), monohydrocalcite (171.7 ppm), vaterite (170.7 and 169.6 ppm), aragonite (171.0 ppm). Amorphous calcium carbonates are characterized by a very broad symmetric peak at 169.0 ppm [257, 258]. Other authors [259] found an amorphous-like carbonate peak at 168.4 ppm. Amorphous carbonate phosphate was found to 168.2 ppm [259].

For substituted apatites the peak positions have been reported as follow:

-type A substituted apatites (Ca₁₀(PO₄)₆CO₃) at 166.5 ppm [259] as a well defined narrow peak. This would not give signal in the CP spectrum as CO₃²⁻ replaces HO⁻, the main proton source for the polarisation transfer;

-type B substituted apatites (Ca₉(PO₄)₄(CO₃OH)₂) at 170.2 ppm [259] as an asymmetric signal. Other authors [260] found the peak at 166.4 or 166.8 ppm as a narrow resonance;

-type AB substituted apatites showed a combination of peaks from type A and type B substituted apatites [259, 261]. The same behaviour was found for hydroxyl carbonate apatite [261].

Therefore we can attribute the peaks at 168.7 and 170.8 ppm to calcite and aragonite, respectively, formed on the surface. The peak at 170.8 ppm can have also contribution from type B substituted apatite, as in ¹H NMR spectrum of this sample we detect the signal corresponding to apatites. These peaks are broader compared with the ones in crystalline compounds, as they are more disordered.

The peaks at 184.5 and 186.7 ppm can be due to CO gas [262] that resulted from incomplete oxidation of organic radicals and can be trapped in pores. No evidence of CO₂ was found at 125 ppm [262].

Further increasing the temperature to 700 °C leads to the removal of organics and carbonates. The absence of the carbonates with increasing temperature suggests that these species are either mobile or decompose with temperature and not all of

them occupy defined sites in the apatite structure. Thus the type B carbonate apatite contribution, if present, is small. This can be due also to the fact that the phosphate concentration in the 58S samples is low (corresponds to a calculated 4% P₂O₅) as well. Also the molecular CO was removed from the system.

For the CME samples thermally treated at 60°C without and with HF as catalyst, 58S CME 60 and 58S CME 60 HF, respectively, besides the peaks from TEOS and TEP alkoxides at ~15 and ~65 ppm, the peaks corresponding to methoxyethoxide are present. The resonances for methoxymethyl (CH₃O), methylene carbon adjacent to the methoxy group (-CH₂O-) and methylene carbon attached to the ethoxide oxygen (-OCH₂-) can be distinguished at around 57.8, 74.0 and 61.7 ppm, respectively. The peaks from carbonates are also present in both samples and for the fluorine containing sample, 58S CME 60 HF, a small contribution from CO can be observed. The formation of the surface carbonates at this temperature is due to the high reactivity of calcium ions present in the system, due to the high reactivity of CME as alkoxide. In both samples the presence of calcite can be observed at 168.7 and 168.9 ppm. Garcia *et al.* [263] has found calcite by XRD and IR in CaO-SiO₂ fresh gels prepared by alkoxide route, which were stable up to 600°C.

Beside the peaks from ionic carbonates, type 1, Figure 5.5, the samples present another 3 peaks in the 173-176 ppm region. These peaks do not appear in the 58S Nitrate 400 sample, suggesting that they are of a different nature. Similar to CO₂, CME has been shown to have a dual-functional Lewis base-acid character [264], thus the presence of sufficiently basic O²⁻ species can lead to coordinated carbonate-like species (Type 2-5, Figure 5.5.), which are not stable at temperature. It was shown [262] that there seems to be a correlation between the IR and ¹³C NMR data consisting in the magnitude of the splitting of the ν₃ carbonates band and both the chemical shift (related to the ionicity of the C-O bonds) and the difference in the chemical shift of the ¹³C carbonate resonance (a measure of the range of the carbonate environments). In the 58S CME 60 and 58S CME 60 HF samples there seems to be at least two types of coordinated carbonates. Calcium monodentate carbonates showed in the IR spectra a splitting of 100 cm⁻¹, while for bidentate carbonates the splitting was 240 cm⁻¹ [265]. In the ¹³C CP NMR spectra of the 58S CME 60 sample we can observe a difference between chemical shifts of 1.4 and 2.9

ppm, thus it is possible that both monodentate and bidentate coordinative calcium carbonates to be formed. Similar trend is observed for sample synthesized with HF, where the difference in chemical shifts is 1.2 and 2.4 ppm.

These carbonate species are absent at 130 °C, as the spectrum of 58S CME 130 shows, consequently they are either decomposed or are highly mobile on the surface and cannot be detected by CP. The peak at 64.7 ppm has a smaller intensity compared with the 60°C sample, as more of the methylene carbons from TEOS and TEP are removed with increasing temperature. These findings support the ¹H NMR data, where the residues from TEOS and TEP have smaller intensity compared with those from CME. Also the peak corresponding to methylene carbon adjacent to the methoxy group decreases in intensity, probably some of them are decomposed or are highly mobile on the surface and are not detected.

With increasing the temperature to 500°C and 700 °C it is possible that some of the carbonates enter the silica matrix and their mobility becomes restricted. This would explain the appearance of the carbonates again at these temperatures. They are more disordered compared to at 60°C. As can be seen from the ¹³C CP MAS NMR spectra now the peaks are expanded over the range of the carbonates obtained at 60°C. The peaks corresponding to carbonates at 500°C and 700°C originate probably from amorphous like carbonate species or very disordered calcite in different environments, due to a distortion of the planar structure with changing in the bond lengths between carbon and oxygen in the carbonate anions by immobilization in the silicate network. This would explain the splitting observed for the peaks. The resonances corresponding to organic residues from alkoxides are absent as they are eliminated from the system and the remaining ones are mobile and are not detected, as in the ¹H NMR of these samples (58S CME 500 and 58S CME 700) some of the alkoxide residues were still present in low concentration.

The lability of the carbonate layer is more pronounced for the nitrate samples compared to the CME ones, as the carbonates in nitrate do not enter the silicate network to restrict their mobility, as they are absent in the spectrum of samples thermally treated at 700 °C. Also from nitrate samples just ionic carbonate like species are formed while from CME monodentate and bidentate coordinative carbonates can be formed.

^{31}P MAS NMR spectra of the 58S samples synthesised via the inorganic route are shown in Figure 5.6. The deconvolution of the spectra using DMFIT software [224] is presented in Table 5.3.

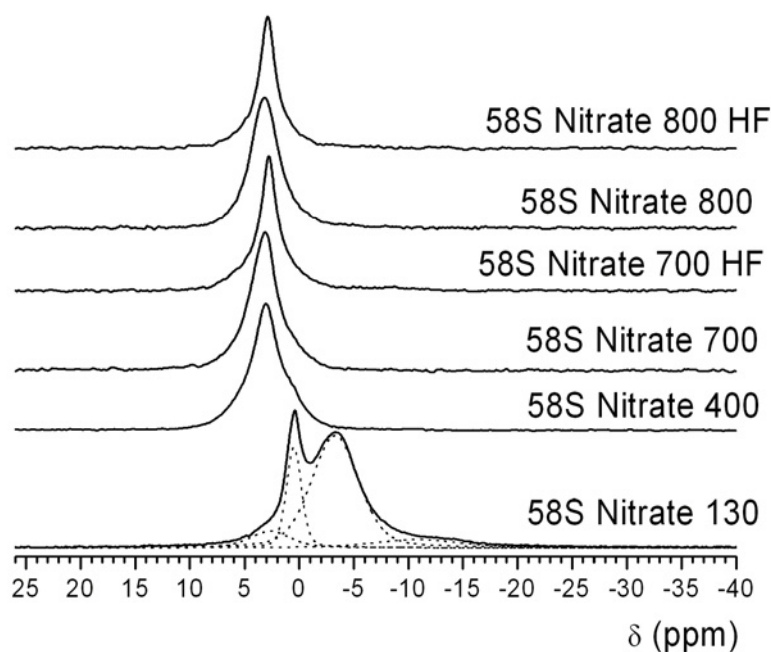


Figure 5.6. ^{31}P MAS NMR spectra of 58S Nitrate samples.

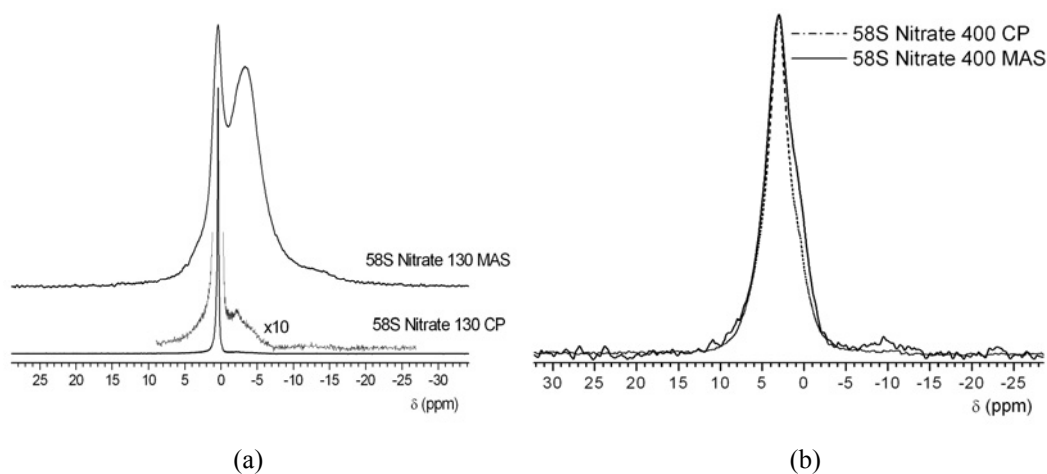


Figure 5.7. A comparison between ^{31}P MAS and ^{31}P CP MAS spectra of 58S Nitrate 130 (a) and 58S Nitrate 400 (b) samples, respectively.

Table 5.3. ³¹P MAS NMR data for measured samples, giving the spectral deconvolution into different species.

Sample	δ (ppm)	FWHM (ppm)	I (%)												
INORGANIC ROUTE															
58S Nitrate 130				2.7	4.4	8	0.5	1.6	19	-3.3	5.1	65	-10.8	9.3	8
58S Nitrate 400	5.6	3.4	11	3.1	3.0	64	0.5	2.6	19	-	-	-	-9.3	7.0	6
S58 Nitrate 700	5.2	3.0	22	3.1	2.3	63	0.6	2.9	15	-	-	-	-	-	-
S58 Nitrate 700 HF	5.1	3.3	18	2.8	1.7	58	0.8	3.3	17	-	-	-	-7.8	7.1	7
S58 Nitrate 800	6.2	2.8	6	3.2	2.9	84	0.1	2.6	10	-	-	-	-	-	-
S58 Nitrate 800 HF	4.6	3.3	22	2.9	1.6	63	0.8	3.7	15	-	-	-	-	-	-
ALKOXIDE ROUTE															
58S CME 60	-	-	-	-	-	-	-	-	-	-2.4	4.6	93	-6.7	3.4	7
58S CME 60 HF	-	-	-	3.4	5.8	12	-	-	-	-2.0	4.8	69	-6.5	9.4	19
58S CME 130	-	-	-	-	-	-	-	-	-	-2.3	4.8	92	-6.5	3.6	8
58S CME 500	-	-	-	3.6	5.6	91	-	-	-	-2.1	5.3	4	-7.3	9.4	5
58S CME 700	-	-	-	3.1	6.6	91	-	-	-	-2.4	4.2	3	-6.0	7.0	6
58S CME 700 HF	-	-	-	3.0	7.1	89	-	-	-	-2.4	3.8	5	-7.1	6.5	6
58S CME 800	-	-	-	2.7	7.5	88	-	-	-	-	-	-	-6.8	9.3	12
58S CME 800 HF	-	-	-	3.8	4.5	93	-	-	-	-	-	-	-6.1	7.7	7

FWHM, δ and I represent the linewidth full-width half-maximum, ³¹P chemical shift and relative intensity, respectively. Errors associated with measurements are — FWHM ± 1 ppm, δ ± 1 ppm and Integral ±2%.

For the 58S Nitrate 130 sample, phosphorus was found in 4 different environments, corresponding to chemical shifts presented in the Table 5.3. The peak at 0.5 ppm is very narrow. This peak can be assigned to phosphorus atoms in O=P(OH or OCH₂CH₃)₃ which correspond to hydrolysed or unhydrolysed monomers from the TEP. Similar species have been found by ³¹P NMR on phosphosilicate glasses made from TEP and TEOS [266, 267]. TEP hydrolysis is slower than TEOS [253, 268] and some phosphorus monomers similar to those in the starting material (TEP) are trapped in the pores when the pores shrink during the heat treatment. The chemical shifts for O=P(OCH₂CH₃)₃ and OP(OH)₃ have been reported to be -1.5 ppm [266, 269] and 0 ppm [269], respectively. The peak at 2.7 ppm is due to calcium orthophosphate [270, 271]. The peak at -10.8 ppm can be assigned to dimeric pyrophosphate units ((P₂O₇)⁴⁻) [109, 271], where the phosphate tetrahedron connects with another phosphate tetrahedron and are charge balanced by calcium ions.

The peak at -3.3 ppm is not straightforward to be assigned. It can be due either to H_nPO₄⁽³⁻ⁿ⁾⁻ units or to P-O-P units which is likely to originate from different environments comparing P-O-P units at -10.8 ppm. The -3.3 ppm peak can be due to P-O-P units, where phosphorus sites are connected with water molecules by hydrogen bonding. This would explain the signal appearance for this resonance in the CP spectrum compared with the -10.8 ppm resonance (Figure 5.7 a). For H_nPO₄⁽³⁻ⁿ⁾⁻ the reported chemical shift is between -1.5 and 1.7 ppm for HPO₄²⁻ (monetite, CaHPO₄, at -1.5 and 0 ppm, brushite, CaHPO₄·2H₂O, at 1.7 ppm), while H₂PO₄⁻ have been reported between -4.6 and 0.5 ppm (Ca(H₂PO₄)₂ at 0 and -1.5 ppm, Ca(H₂PO₄)₂·H₂O at -0.1 and -4.6 ppm) [109, 270-272]. However the ¹H NMR spectra showed a resonance just at 6.7 ppm while the acid protons for these species appear above 8 ppm [109, 250]. It is possible that the high concentration of organics and water at this temperature lead to a broadening of these resonances which will hide the peaks. Also strong hydrogen bonding between the acid protons and organic fragments or the silanols cannot be excluded and helps the acid proton mobility which can explain the peak position in ¹H spectra [273], since proton chemical shifts depend directly on the degree of hydrogen bonding (and therefore, proton acidity) [249].

Dynamic processes with water molecules or the solvents formed from the alkoxide residues can take place. In the ³¹P CP MAS spectra of 58S Nitrate 130

sample (Figure 5.7 a) the signal, if from P-OH is very weak. All these factors together with strong ¹H-¹H dipolar couplings between acid proton and oxygen can lead to a broadening of the resonances in ¹H NMR spectra and might not be detected or could be around 6 ppm. However, this resonance in the ³¹P NMR spectrum is possible to have a contribution from both species, P₂O₇⁴⁻ and H_nPO₄⁻³⁺ⁿ which could explain the peak position. Also the acid proton and water presence as a result of hydrogen bond formation and probably proton exchange can lead to a redistribution of the electron density to the phosphorus nucleus [274].

In the CP spectrum of this sample (Figure 5.7. a), the main component is at 0.5 ppm and the peaks corresponding to orthophosphate at 2.7 ppm and pyrophosphates at -10.8 ppm are absent suggesting that it corresponds to ³¹P sites far from hydrogen. The sharpness of the peak at 0.5 ppm suggests that the phosphorus sites are ordered, but the efficiency of the CP suggests that they are protonated and strongly dipolar coupled to protons, while the phosphorus sites corresponding to the peak at -3.3 ppm is unprotonated or the proton is mobile but dipolar coupled. This confirms the assumption that the peak at 0.5 ppm is due to hydrolysed monomers from TEP, while the peak at -3.3 ppm is due to the H_nPO₄⁽³⁻ⁿ⁾⁻ and/or P₂O₇⁴⁻ which are close to water molecules and can be involved in intramolecular or intermolecular hydrogen bonding.

In the literature a peak around 0.0 ppm has been attributed to β-tricalcium phosphate (β-TCP) [275, 276], and calcium phosphate [274] as well. These species would have to cross-polarise from more distant hydrogens, such as water, or OH. The strong CP suggests that the highest contribution of the 0.5 ppm peak is not due to β-TCP or calcium phosphate, such that the initial assumption seems to be correct.

Increasing the temperature to 400 °C the peak at -3.3 ppm disappears with the formation of calcium orthophosphate (Figure 5.6) due to either opening of the P-O-P bridges and/or loss of the acid proton of these species (eq. 5.3):



This is supported from the ³¹P MAS NMR data in table 5.3 where the concentration of orthophosphates at 3.1 ppm increases to 64%. The peak from crystalline HAp was reported to be 2.8 ppm [270, 277], whereas a peak at 3.16 ppm

was reported for a carbonate type B substituted apatite [260] synthesised from monetite. For poorly crystallised HAp the peak was reported to be at 3.3 ppm [273]. Thus in our spectra the peak position at 3.1 ppm and the linewidths can suggest the formation of a poorly crystallised HAp with a contribution from type B carbonate substituted apatite, especially since the ¹³C CP NMR data show evidence of carbonates. The lack of ¹³C CP signal of apatite at this temperature can be due to the fact that the contribution from type B apatite is low and was not detected. The peak at 5.6 ppm is also characteristic of orthophosphate environments. As is shown in Figure 5.7 b for this sample the CP and MAS spectra are very similar. Some of the species at 0.5 ppm do not cross-polarise, are far from hydrogen and are not accessible, as the intensity of the peak is smaller than in MAS, these species cannot originate from TEP precursor, therefore the contribution of this peak is from orthophosphate environments. In the literature [275, 276] β-TCP showed the highest peaks around 0.5 and 5-6 ppm. Therefore the formation of this phase at this temperature beside apatite cannot be excluded. β-TCP was found to be formed in the synthesis of HAp from TEP and calcium nitrate by the sol-gel method [278]. A small amount of pyrophosphates is still present at -9.3 ppm.

At 700 and 800 °C the contribution from pyrophosphates cannot be observed, as the P-O-P bridges are opened to form orthophosphate. The orthophosphate phases around 0 and 5 ppm are still present. The orthophosphates in the apatite structure have a slightly increased local ordering at 700 °C as the linewidth of this phase is narrower (Table 5.3). The concentration of the apatite phase seems to increase at 800 °C. For samples containing fluorine it can be observed both at 700 and 800 °C that the peak at 2.8-2.9 ppm is very sharp and the position is similar with crystalline apatites [270]. From ¹H NMR, no signal at 0.0 ppm was detected in these samples, probably fluoride ions substitute OH in the apatite structure to form fluoroapatite. For fluorine substituted apatite the peak position in ³¹P NMR spectra has been reported at 2.8 ppm [270]. The apatitic phase in these samples form in lower concentration (Table 5.3) and has an increased local ordering (FWHM of 1.6 ppm) compared with samples without fluorine.

³¹P NMR spectra of samples synthesised via the alkoxide route and thermally treated at different temperatures are shown in Figure 5.8.

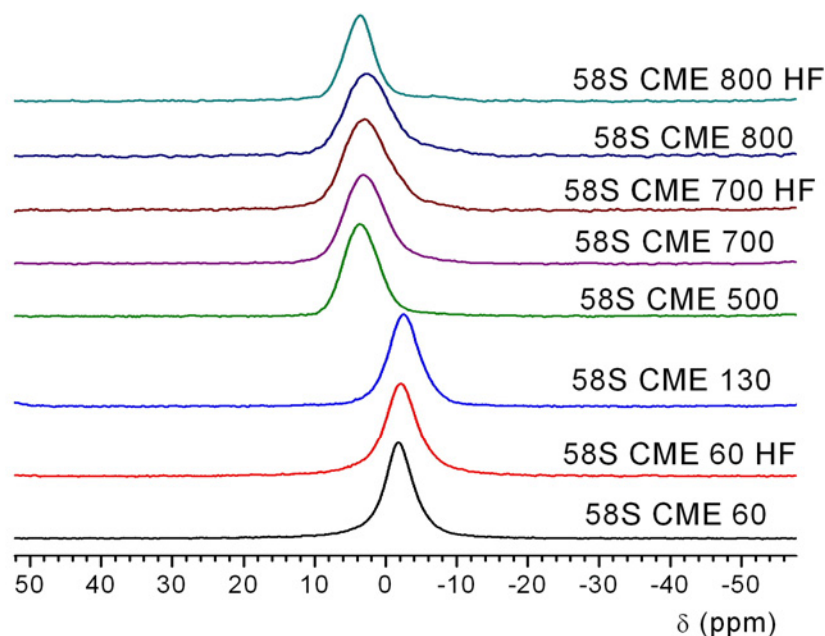


Figure 5.8. The ³¹P MAS NMR spectra of samples synthesised via alkoxide route.

For samples thermally treated at 60 and 130 °C (Figure 5.8, Table 5.3), the peak around -2.0 ppm can be due to HPO₄²⁻, where the absence of the acid proton in ¹H NMR spectra is due to the same factors as for S58 Nitrate 130 sample. The presence of pyrophosphate is evident at -6.5 ppm. The peak corresponding to free TEP monomers is absent. In the sample made with HF as catalyst, the concentration of the HPO₄²⁻ phase is lower compared with the sample without HF at the same temperature (58S CME 60 HF and 58S CME 60), as they can either condense to form P-O-P (eq. 5.4.), or lose the acid proton to form orthophosphate (eq. 5.3.) with a resonance at 3.4 ppm:



This can be explained by the effect of HF as catalyst, when the condensation reactions are favoured, where now the concentration of P-O-P is higher (19% for 58S CME 60 HF compared to 7% for 58S CME 60, Table 5.3).

However in the ¹H NMR spectra of the 130 °C thermally treated sample, a broad peak at 8.7 ppm was detected, which can confirm the hypothesis of HPO₄²⁻ phase formation in the samples synthesized via the alkoxide route.

Increasing the temperature to 500 °C, the formation of orthophosphates takes place (ec. 5.3), with a chemical shift at 3.6 ppm, with calcium as the charge-balancing cation. The HPO₄²⁻ phase is still present, but in low concentration (4%). The pyrophosphates are still present in the system, in low concentration, as some of the P-O-P bridges have been opened with the formation of orthophosphate.

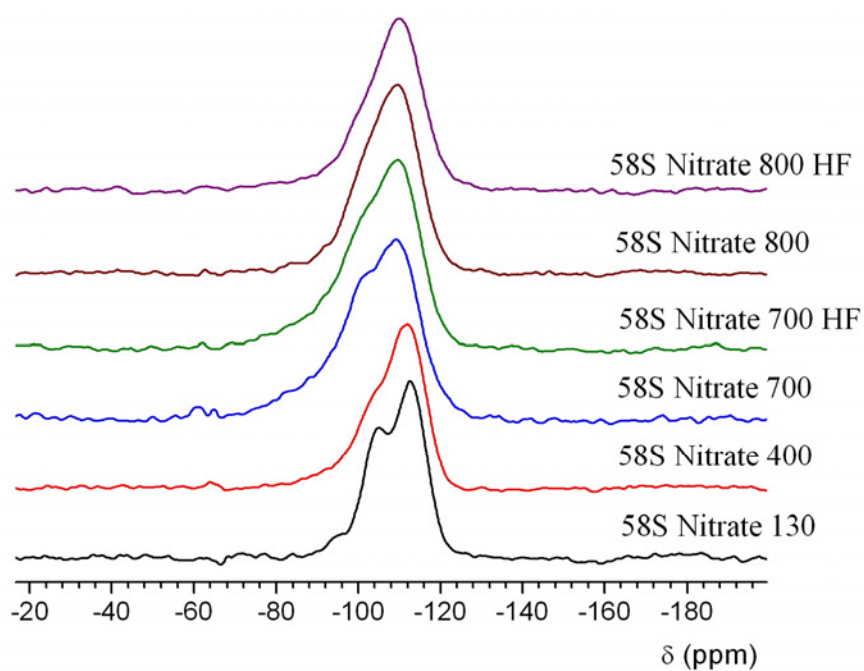
Further increase of the temperature to 700 and 800 °C lead to the condensation of the remaining HPO₄²⁻, which do not appear at 800 °C, with an increase of P-O-P bridges for the 58S CME 800 sample, where the concentration of pyrophosphates units is slightly higher compared with sample containing fluoride ions at the same temperature.

For samples synthesised via the alkoxide route, xerogels and thermally treated samples the linewidths are broader compared with samples synthesised via the inorganic route at corresponding temperatures, suggested a more disordered orthophosphate environment. In the alkoxide series when the temperature is increased from 500 to 800 °C a disorder of the orthophosphate phase occurs as is evident from Table 5.3, where an increase in the linewidths can be observed. The 58S CME 800 HF sample presents a slightly increased local ordering as the linewidth is 4.5 ppm (Table 5.3).

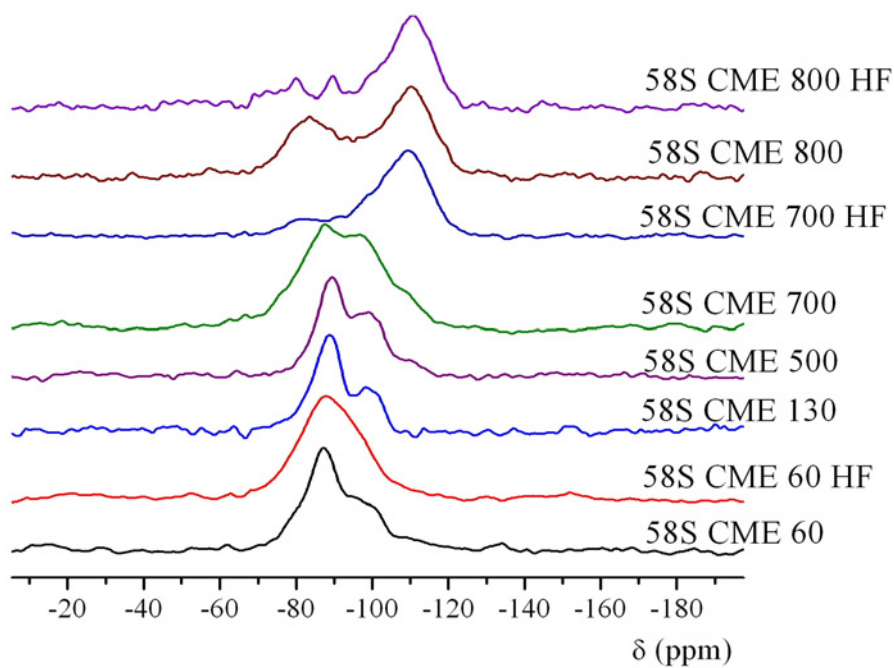
The results obtained from ²⁹Si MAS NMR spectroscopy provide a better understanding of the effect of calcium and phosphorus on the connectivity of silica network by the distribution of silicon Qⁿ species. Qⁿ(H) and Qⁿ(Ca) species have been defined in Chapter 4.

²⁹Si MAS NMR spectra of samples synthesised by inorganic and alkoxide routes and thermal treated at different temperatures are shown in Figure 5.9 a and b. To quantify the Qⁿ distribution the ²⁹Si MAS NMR spectra were deconvolved by Gaussian fitting using DMFIT software [224]. The results of deconvolution are shown in Table 5.4.

The 58S sample synthesised from nitrate and thermally treated at 130°C (58S Nitrate 130) shows a well polymerized silica network at this stage as is illustrated by the concentration of Q⁴ (62%) and Q³(H) (31%) in Table 5.4. This can be explained by the fact that at this stage calcium is not yet part of the silicate network. At this temperature calcium nitrate is not yet decomposed [1] and is on the surface of the particles.



(a)



(b)

Figure 5.9. ^{29}Si MAS NMR spectra of 58S samples synthesised by inorganic (a) and alkoxide (b) routes.

Table 5.4. ²⁹Si MAS NMR data for measured samples, giving the spectral deconvolution into different Qⁿ species.

Sample	Q ¹ (Ca)			Q ² (Ca)			Q ² (H), Q ³ (Ca)			Q ³ (H)			Q ⁴		
	δ (ppm)	FWHM (ppm)	I (%)	δ (ppm)	FWHM (ppm)	I (%)	δ (ppm)	FWHM (ppm)	I (%)	δ (ppm)	FWHM (ppm)	I (%)	δ (ppm)	FWHM (ppm)	I (%)
INORGANIC ROUTE															
58S Nitrate 130	-	-	-	-	-	-	-95.4	7.3	7	-104.0	6.9	31	-112.7	9.0	62
58S Nitrate 400	-	-	-	-85.9	6.1	2	-93.4	8.7	6	-102.8	9.2	27	-112.1	10.0	65
58S Nitrate 700	-76.2	6.7	2	-82.5	7.0	4	-91.9	10.9	14	-100.3	8.9	24	-109.8	11.8	56
58S Nitrate 700 HF	-76.9	6.2	2	-84.1	7.1	4	-90.9	7.6	6	-99.6	10.9	29	-110.0	12.1	59
58S Nitrate 800	-	-	-	-84.6	6.4	2	-91.3	5.0	2	-100.1	9.8	24	-109.8	12.2	72
58S Nitrate 800 HF	-	-	-	-79.6	10.7	3	-91.0	11.1	6	-100.3	9.7	17	-110.3	12.5	74
ALKOXIDE ROUTE															
58S CME 60	-71.2	6.5	2	-79.1	7.8	13	-87.1	8.6	47	-97.6	11.6	32	-111.4	11.6	7
58S CME 60 HF	-	-	-	-77.7	12.5	15	-87.2	11.6	50	-96.4	11.4	28	-108.5	13.0	7
58S CME 130	-73.5	9.7	6	-80.6	7.9	11	-88.4	8.7	55	-99.6	9.3	28	-	-	-
58S CME 500	-	-	-	-81.5	5.9	6	-88.9	7.7	46	-98.9	10.4	42	-110.4	7.0	6
58S CME 700	-66.8	7.9	3	-77.2	9.1	11	-86.7	10.4	36	-97.5	12.0	40	-108.8	9.5	10
58S CME 700 HF	-	-	-	-82.0	13.4	14	-90.6	5.5	3	-99.2	10.5	19	-109.9 -120.1	12.8 9.8	62 2
58S CME 800	-72.4	7.3	4	-79.4 -83.7 ^a	6.6 4.4	13 6	-88.1	6.7	11	-96.9	10.9	15	-110.1	13.3	51
58S CME 800 HF	-72.9 -80.0 ^c	8.3 4.3	7 8	-84.1 -89.5 ^b	4.6 4.0	2 6	-	-	-	-100.0	9.0	14	-110.6 -117.7	11.0 7.0	60 3

FWHM, δ and I represent the linewidth full-width half-maximum, ²⁹Si chemical shift and relative intensity, respectively.

Errors associated with measurements are — FWHM ± 1 ppm, δ ± 2 ppm and Integral ±2%.

^a Q²(Ca) in three-ring silicate ions in α-CaSiO₃ (pseudo-wollastonite)

^b Q²(Ca) in chain silicate ions in β-CaSiO₃ (wollastonite)

^c Q¹(Ca) in cuspidine, Ca₄Si₂O₇F₂.

With increasing the temperature to 400 °C, a small increase in the Q⁴ species is observed with the appearance of a peak at -85.9 ppm. This peak can be attributed to Q²(Ca), as Q¹(H) is unlikely to be formed in the system. This can also be supported by the fact that calcium ions interact with two silanols (see eq. 4.2.) and increase the rigidity of the network. As the silicate network becomes more rigid, the bridging and non-bridging oxygens become more covalent. As a consequence the silicon nucleus becomes more shielded and the chemical shift moves towards more negative values. As the concentration of Q⁴ is not decreased, calcium ions do not enter in silica network at this temperature and the NBOs are formed on the surface, rather than in the silicate network. This is consistent with the ¹³C NMR spectra where the formation of calcium carbonates has been observed. This reaction of calcium with silanols can generate new sites capable of water adsorption and diminishes the total number of surface hydroxyls, as was shown in Table 5.4, where a decrease in Q³(H) and Q²(H) was observed. This is also supported by our ¹H NMR spectra where the signal from water is increased at 400 °C (Figure 5.1).

By stabilisation of the sample at 700 °C, more calcium ions as a network modifiers, are incorporated into silica network and break siloxane bonds with a decrease of Q⁴ and Q³(H) species to 56% and 24%, respectively (Table 5.4). A small amount of Q¹(Ca) is formed and the concentration of Q²(Ca) is increased as calcium is incorporated in the silicate network. This also explains the peak broadening in this sample. Some of calcium ions are involved in charge-balancing the formed orthophosphate as ³¹P NMR data revealed, the remaining calcium will depolymerise the silicate network. We can consider of Ca/P ratio between 1.5 and 1.67 corresponding to Ca/P ratios of Ca₃(PO₄)₂ and HAp, respectively. For samples synthesised using HF as catalyst and stabilised at 700 °C (58S Nitrate 700 HF) the concentration of Q⁴ and Q³(H) is slightly increased while the concentration of Q²(H)(Q³(Ca)) is decreased compared with 58S Nitrate 700 sample. As was shown, F⁻ ions have a high affinity for calcium modifier cations [279, 280] and removes them from the silicate network, with the effect of increasing the connectivity of the silica. This can be due to the fact that during the stabilisation process CaF₂ is formed. The formation of CaF₂ has been observed in gels synthesised by using HF as catalyst [5]. The two samples present just a slight difference, as most of the F⁻ ions are

involved in the formation of the apatitic phase and the remaining fluoride ions are in very low concentration, if still present.

Further increasing the temperature to 800 °C leads to an increase in the Q⁴ concentration to 72%. Q¹(Ca) species are absent and the concentration of Q²(Ca) and Q²(H) (or Q³(Ca)) species decrease with increasing the temperature. Q³(H) species seem to remain the same as for the 700 °C thermally treated sample. This behaviour can be explained by the fact that the glass transition temperature (T_g) was reported to be around 800 °C for 58S composition [75]. Structural densification starts as the glass approaches T_g. Consequently, viscous flow occurs between 700 and 800 °C and the start of structural densification near T_g causes breaking and reforming of bonds in the silicate network [96]. Also the material moves by the viscous flow or diffusion in such a way that part of the calcium ions are removed from the silicate network and migrate to the surface of the particles. The composition is an intermediate between a sol-gel glass and a fully densified glass which has a behaviour similar to the corresponding melt-derived composition.

For the 58S Nitrate 800 HF sample, the concentration of Q³(H) is lower and Q⁴ is slightly increased compared with the sample 58S Nitrate 800 where no F⁻ ions are involved. Probably during the structural densification the two samples behave differently, as HF catalysed gels have a similar structure with the base catalysed ones [96] and during the sintering they have a reduced concentration of hydroxyl groups on the surface as is reflected by a smaller concentration of Q³ species (17% compared with 24%, Table 5.4).

For samples synthesised by the alkoxide route, starting from CME as calcium precursor, as both CME and TEOS are alkoxides, condensation reactions between (OC₂H₅)₃SiOH and HOCa(OCH₂CH₂OCH₃) obtained from the alkoxides hydrolysis reactions, take place in the early steps of the gel formation and form SiO⁻ Ca²⁺ OSi non-bridging oxygens (NBOs). This explains the low concentration of Q⁴ species even at 60 °C, when calcium is incorporated in the silicate matrix at this temperature. At this stage there seems to be a very small difference between samples synthesised using HNO₃ and HF as catalysts. However, when HF was used as catalyst (58S CME 60 HF sample), Q¹(Ca) are not formed at this stage, probably due to the F⁻ ions present in the system when the condensation reaction between two SiOH groups can take place before the hydrolysis reaction is complete [96] and less calcium ions are

incorporated in the silicate matrix. The absence of Q⁴ species in the sample thermally treated at 130 °C can be explained by the fact that by increasing the temperature, further interactions between silanols and calcium ions occur and when the gel shrinks it incorporates calcium in the silicate network. This is supported by the presence of a higher concentration of Q¹(Ca) species in the system.

Increasing the temperature to 500°C, formation of new siloxanes bridges takes place (Table 5.4, Figure 5.8 b), where now a small amount of Q⁴ species are formed and the concentrations of Q³(H) and Q²(H) increase. Also at this temperature Q¹(Ca) is absent from the system. As the ³¹P NMR data (Table 5.3, Figure 5.6) showed at this temperature the main component was phosphorus in an orthophosphate environment. Therefore some calcium ions are involved in charge-balancing orthophosphate species and they are removed from their network-modifying role in the silicate. In response, the silicate network repolymerises with the formation of new Si-O-Si bridges. Thus, phosphorus acts as a scavenger and removes calcium from the silicate network, and the effect is to increase the polymerisation of the silicate network. Similar results have been reported in literature [245, 281, 282] for glasses with low concentrations of phosphorus. New silanols are also formed as the concentration of Q³(H) is increased. This can be due to an interaction between calcium ions and the adsorbed water present at the surface when some Si-O⁻Ca²⁺ bridges are open with the formation of new Si-OH [216, 283] bonds (eq. 4.3). This supports our ¹H NMR data where free hydroxyls coordinated to calcium ions took place at 500 °C.

The condensation of surface silanols at 500 °C leads to the formation of new siloxane bridges, with a decrease of the concentration of Q³(H) and Q²(H) and an increase of Q⁴ species on increasing the temperature to 700 °C. Some of the Q²(H) units lead to the formation of new Q²(Ca) species. Probably some of the calcium ions involved in the interaction with adsorbed water react with the SiOH to form Qⁿ(Ca), namely Q¹(Ca) and Q²(Ca). This is also supported from ¹H NMR spectra where the hydrogen content is decreased, as most of the organics and some of the water was eliminated from the system. When F⁻ ions are present in the system (58S CME 700 HF sample) the concentration of Q⁴ species is increased substantially to 62%. Also the concentration of the silicon tetrahedra of lower connectivity (Q³(H) and Q²(H) and/or Q³(Ca)) is decreased to 19% and 3% respectively (Table 5.4, Figure 5.8 b).

This can be due to the fact that the presence of fluorine may influence the T_g of the glass and the structural densification to occur earlier with the reformation of the silicate network having similar effect as for nitrate samples thermally treated to 800 °C. Also the increase in connectivity of the silicate network when fluorine is present can be due to the high affinity for calcium modifier cations as was described for similar samples obtained via inorganic route (58S Nitrate 700 HF). However in this sample the concentration of the available fluoride ions is higher, therefore the concentration of CaF₂ is higher compared with the nitrate one as they were not found to be involved in the formation of apatitic structures. Another role of fluorine in this system is to enhance the P-Si interactions, with the formation of Si-O-P bonds as can be observed in Table 5.4, where a small fraction of Q⁴ with a resonance at -120.1 ppm can be detected. This resonance has been assigned to a four-coordinated silicon tetrahedron with three phosphorus and one silicon [266]. Due to the low concentration of F⁻, these species are formed in a small amount.

The differences observed between 700 °C thermally treated sample synthesised by inorganic and alkoxide routes using HF as catalyst, 58S Nitrate 700 HF and 58S CME 700 HF, respectively, can be due to the fact that in the nitrate sample most of the fluorine ions are on the surface of the silica particle and/or have been involved in the formation of fluoroapatite phase as the ³¹P data suggested, while in the CME sample they are incorporated in the silicate network. Also the calcium concentration in the silicate network is higher for samples from CME compared with nitrate as shown above in the concentration of Q⁴ and Q³(H) species (Table 5.4).

By increasing the temperature to 800 °C, when the viscous flow occurs and the structural densification starts, the effect is similar as for 58S Nitrate 800 sample, with an increase of the Q⁴ concentration to 51% and a decrease of the Q³(H) to 15% for 58S CME 800 sample. Also the concentration of Q²(H) (or Q³(Ca)) decreases to 11%, with an increase in the concentration of Q²(Ca). This suggests that some of the Q²(H) units are either involved in the formation of siloxane bridges or in the formation of new Q²(Ca). As can be observed from the Figure 5.8 b the spectrum of the 58S CME 800 sample contains a narrow peak on top of the broad line. Q²(Ca) species in this sample exist in two environments. The Q²(Ca) in three ring silicate ions in α -Ca₃Si₃O₉ (pseudo-wollastonite) and the chain configuration in β -Ca₃Si₃O₉ (wollastonite) have recorded shifts of -83.5 and -89.0 ppm, respectively [225, 284].

The chemical shift at -83.7 ppm with a FWHM of 4.4 ppm in Table 5.4 is then assigned to $Q^2(\text{Ca})$ environments in $\alpha\text{-Ca}_3\text{Si}_3\text{O}_9$ ring metasilicate phase which separate from silicate network.

For the 58S CME 800 HF sample, in Fig. 5.8 b two sharp peaks at -80.0 and -89.0 ppm are observed with FWHM of 4.0 and 4.3 ppm, respectively (Table 5.4). The peak at -89.0 ppm can be assigned to the chain configuration in $\beta\text{-Ca}_3\text{Si}_3\text{O}_9$ (wollastonite) phase [284]. This phase is probably separated from the silicate network. It seems that when fluorine is involved, a chain configuration of $\text{CaO}\cdot\text{SiO}_2$ is preferred comparing the sample without fluorine where rings were found. The peak at -80.0 ppm can be assigned to silicon tetrahedra in $Q^1(\text{Ca})$ configuration in cuspidine ($\text{Ca}_4\text{Si}_2\text{O}_7\text{F}_2$) which can be formed at this temperature due to the affinity of fluorine for calcium ions and to possible formation of CaF_2 . This species has a reported chemical shift of -79.9 ppm [284]. As fluoride ions are relatively in low concentration the amount of this phase is small (8%). This phase has been also detected in the literature in the melt-quench synthesised samples containing CaF_2 [280]. On increasing the temperature to 800 °C, as the concentration of Q^4 is not visibly changed, the formation of $Q^n(\text{Ca})$ of lower connectivity as shown in Table 5.4 is probably due to $Q^3(\text{H})$ species interacting with calcium ions. The Si-O-P bridges are still present at -117.7 ppm.

In nitrate samples containing fluoride ions thermally treated at 700 and 800 °C (58S Nitrate 700 HF and 58S Nitrate 800 HF), the Si-O-P bonds are absent from ^{29}Si NMR spectra, suggesting that P does not copolymerise with the silicate network, and just P-O-P bonds are formed at 700 °C, as the ^{31}P NMR data suggests. Also the phase separation other than calcium orthophosphate and HAp from the silicate network in the samples synthesised by inorganic route has not been observed as in the case of samples obtained via alkoxide route.

5.4. Conclusions

In this chapter bioactive glasses with 58S composition synthesised via inorganic and alkoxide sol-gel routes and thermally treated at different temperatures have been analysed using multinuclear solid state NMR. ^1H and ^{13}C CP MAS NMR showed that residual organic fragments from alkoxides are eliminated by increasing the temperature, but a small fraction remain in pores even at 800 °C. ^1H MAS

revealed surface associated and fluid-like water molecules as well as different types of hydroxyls, SiOH and POH isolated or involved in hydrogen bonding and free hydroxyls coordinated to calcium ions. ¹³C CP MAS NMR showed the formation of different types of carbonate. For samples obtained via the alkoxide route the formation of carbonates took place even at low temperatures and their stability is high compared with samples synthesised via the inorganic route. ³¹P MAS and CP MAS NMR revealed different phosphorus environments at lower temperatures. By increasing the temperature, the orthophosphate in different environments separate from the silicate network. For nitrate samples the formation of HAp or fluoroapatite when fluorine was present and β-TCP was observed, while for CME samples just disordered orthophosphates are formed in the system. As ²⁹Si NMR data revealed, calcium was incorporated at low temperatures when the alkoxide route was employed while for the inorganic route, higher temperatures were needed for calcium incorporation. When the glasses approach the glass transition temperature structural densification starts, for both routes, a reorganisation of silicate network was observed with the separation of calcium silicate crystalline phases and cuspidine when fluorine was involved, for the samples obtained via the alkoxide route.

6.

ORGANIC-INORGANIC NANOCOMPOSITE SCAFFOLDS

6.1. Introduction

The sol-gel method allows the preparation of tailor-made hybrid nanocomposites with various compositions and structures. Organic-inorganic hybrids were shown to be an excellent class of bioactive materials [57, 58, 60-66]. To obtain stronger interactions between organic and inorganic networks functionalised silanes as crosslinkers are used. The coupling agent 3-glycidoxypropyltrimethoxysilane (GPTMS) is one of the most common precursors used in the synthesis of hybrids in the sol-gel process [124, 285-290]. Combining biocompatible and biodegradable polymers such as gelatin [4, 64, 65, 291, 292] or poly(γ -glutamic) acid [5, 6, 67, 68] with brittle bioactive ceramics using a crosslinking agent, could produce biodegradable and bioactive organic-inorganic scaffolds for tissue engineering with improved mechanical properties. An ideal scaffold for bone tissue engineering should fulfill several criteria [25]: to be biocompatible, to resorb into the body at controlled rates as the bone regenerates, to have an interconnected porous network and act as a guide and stimulus for tissue growth in three dimensions, its mechanical properties should match that of the bone.

Solid state NMR offers a unique perspective in the characterization of the sol-gel derived hybrids. The aim of the present study was the identification of the organic-inorganic structures of hybrids in SiO₂-gelatin and SiO₂-CaO-(γ -PGA) systems when GPTMS has been used as a crosslinking agent and in particular the kind of bonds between the organic and the inorganic components of the system from ²⁹Si, ¹H, ¹³C and ⁴³Ca solid-state NMR. For example strong ¹H-¹H dipolar interactions can be used to probe the ¹H-¹H spatial proximities from ¹H DQ MAS either at fast MAS [124, 156, 293] or CRAMPS [156, 294, 295]. In this study ¹H DQ CRAMPS using DUMBO [140-143] ¹H decoupling and POST-C7 [185] recoupling techniques have been employed. ¹H and ¹³C NMR were used to gain information on

the formation and growth of organic network, the GPTMS epoxy ring opening by gelatin and γ -PGA and to identify the amino acids residues. ^{29}Si NMR experiments are of prime importance in estimating the extent of condensation and the degree of crosslinking of the silica network. ^{43}Ca NMR has been performed to identify the calcium environments when different calcium sources have been used in the synthesis of the scaffolds.

6.2. Experiment details

The syntheses of organic-inorganic hybrids in both gelatin-silica and poly(γ -glutamic) acid-silica-calcium oxide systems have been described in Chapter 3.

The ^1H MAS NMR spectra were recorded using a Bruker 500 MHz (11.7 T) spectrometer operating at 500.1 MHz. MAS and fast MAS spectra were recorded with Bruker 4 mm and 2.5 mm probes at 12.5 and 30 kHz, respectively, using 5 s recycle delay and a 2.50 μs (90° tip angle) pulse. ^1H CRAMPS both 1D and DQ spectra of silica-gelatin hybrids have been performed at an MAS frequency of 12.5 kHz and a ^1H Larmor frequency of 500 MHz, with pulse sequences shown in Figures 3.5 and 3.7, respectively. The chemical shift for all ^1H NMR experiments was referenced externally to alanine at 1.0 ppm. The scaling factors for $F2$ and $F1$ have been calculated for each sample using the following formula:

$$(\delta_{\text{last peak}}^{\text{CRAMPS}} - \delta_{\text{first peak}}^{\text{CRAMPS}}) / (\delta_{\text{last peak}}^{\text{MAS}} - \delta_{\text{first peak}}^{\text{MAS}})$$

The scale factors have been found close to 0.6 and 0.3 for $F2$ and $F1$ dimensions respectively. In 2D SQ-DQ spectra, for each of the 256 t_1 slices, 32 transients were coadded with a recycle delay of 5 s corresponding to a total time of 11.4 h.

^{29}Si MAS NMR spectra were collected on a Varian InfinityPlus 300 MHz spectrometer operating at 59.62 MHz. 20 and 30 s recycle delays were used for gelatin-silica and PGA-silica-calcium oxide systems, respectively, with a 5 μs (45° tip angle) pulse width. ^{29}Si spectra were referenced to TMS at 0 ppm.

^{13}C CP MAS NMR spectra have been recorded on a Bruker 500 MHz magnet with a 4 mm Bruker probe spinning at 12.5 kHz. A contact time of 1 ms and 5 s pulse delay have been used under ^1H decoupling. Alanine has been used as external

reference at 20.5 ppm. ^{43}Ca MAS NMR spectra have been performed on a Varian 600 MHz spectrometer operating at 40.36 MHz with a 9.5 mm Chemagnetics MAS probe spinning at 3.5 kHz. A large rotor volume has been used to increase the signal-to-noise. Spectra were acquired using an echo pulse MAS experiment with a pulse width of 3 μs (90°), a τ of 0.29 ms and a recycle delay of 0.5 s. The total time of experiment was around 72 h. Spectra were externally referenced to 1M saturated CaCl_2 solution at 0 ppm.

6.3. Results and discussion

6.3.1. Class I and class II of organic-inorganic hybrid nanocomposites in the SiO_2 -gelatin systems

Solid state ^{29}Si NMR was performed on the hybrid samples to first check the bonding of the functionalised polymer to the inorganic network in the hybrid and secondly to quantify the proportions of the condensed silicate species. The ^{29}Si MAS NMR can determine relative concentrations of Q^n and T^n species in class I (silica-gelatin) and class II (silica-GPTMS-gelatin) organic-inorganic hybrids. The ^{29}Si NMR spectra of class I hybrids when just TEOS and gelatin without GPTMS as crosslinking agent have been used, are shown in Figure 6.1 with the corresponding deconvolution [224] into Q^n silicate species in Table 6.1.

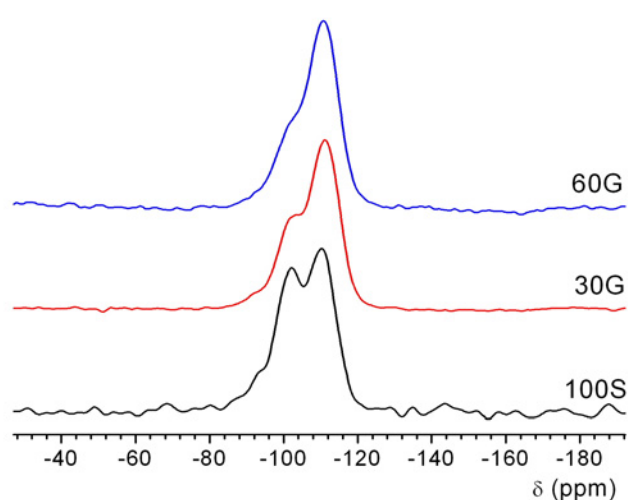


Figure 6.1. ^{29}Si MAS NMR spectra of silica-gelatin, class I hybrids.

Table 6.1. ^{29}Si MAS NMR data of class I and class II organic-inorganic hybrids, giving the spectral deconvolution into different T^n and Q^n species.

Sample	T^1			T^2			T^3			Q^2			Q^3			Q^4			D_c (%)
	δ (ppm)	FWHM (ppm)	I (%)																
Silica-gelatin organic-inorganic hybrids, class I																			
100S	-	-	-	-	-	-	-	-	-	-92.9	6.7	8	-101.3	7.9	40	-110.5	8.7	52	86.0
30G	-	-	-	-	-	-	-	-	-	-92.8	8.2	6	-101.6	7.8	27	-111.2	9.3	67	90.0
60G	-	-	-	-	-	-	-	-	-	-93.3	8.9	5	-101.4	8.4	24	-110.9	9.5	71	91.5
Silica-gelatin organic-inorganic hybrids, class II																			
100II 30G	-	-	-	-61.2	5.4	1	-66.0	3.2	1	-91.9	8.7	5	-100.9	8.0	32	-110.3	8.6	61	88.5
250II 30G	-50.5	5.1	1	-55.7	5.6	1	-63.9	10.9	7	-92.6	8.2	6	-101.6	7.6	28	-111.0	8.7	57	89.0
500II 30G	-50.1	6.0	1	-56.2	5.6	3	-64.0	8.7	10	-92.3	7.3	5	-101.2	7.4	30	-110.6	8.8	51	88.3
1000II 30G	-51.6	3.8	2	-57.6	7.9	8	-65.4	9.0	18	-91.0	6.5	2	-101.7	9.1	27	-111.4	8.2	43	92.8
1500II 30G	-53.6	3.1	1	-57.1	5.0	5	-64.8	9.0	26	-93.8	4.3	1	-101.8	7.6	21	-111.0	8.5	46	91.9
2000II 30G	-50.3	9.2	4	-58.3	8.8	11	-66.3	8.5	30	-92.6	8.7	2	-101.9	8.4	17	-110.9	8.1	36	88.4
100II 60G	-55.4	7.0	3	-62.0	6.2	4	-68.0	10.2	10	-94.8	4.6	2	-102.0	7.7	19	-111.4	9.3	62	90.9
500II 60G	-52.7	5.5	3	-58.1	6.4	5	-65.9	9.7	29	-92.3	4.8	2	-101.6	8.0	19	-110.9	8.2	42	90.6
1500II 60G	-45.6	4.6	2	-55.2	8.7	17	-63.6	7.3	51	-	-	-	-99.1	5.4	5	-108.4	7.3	25	91.8

FWHM, δ and I represent the linewidth full-width half-maximum, ^{29}Si chemical shift and relative intensity, respectively.

Errors associated with measurements are — FWHM \pm 1 ppm, $\delta \pm$ 2 ppm and Integral \pm 2%.

^{29}Si MAS NMR indicates that on increasing the gelatin concentration to 60% in the silica matrix, the Q^4 species concentration (Figure 6.1, Table 6.1) increases as well, with the decrease in concentration of Q^3 species, indicating an increase in the connectivity of the silica network. Gelatin contains amino groups which produce a basic nature and an increase in the pH of the system can occur with an increase in its concentration. This leads to an acceleration of the condensation reactions of the silanol groups [96] and an increase in the degree of crosslinking, D_c (Table 6.1). Also the peaks are broader for 60G compared with 30G sample, due to a more extensive crosslinking.

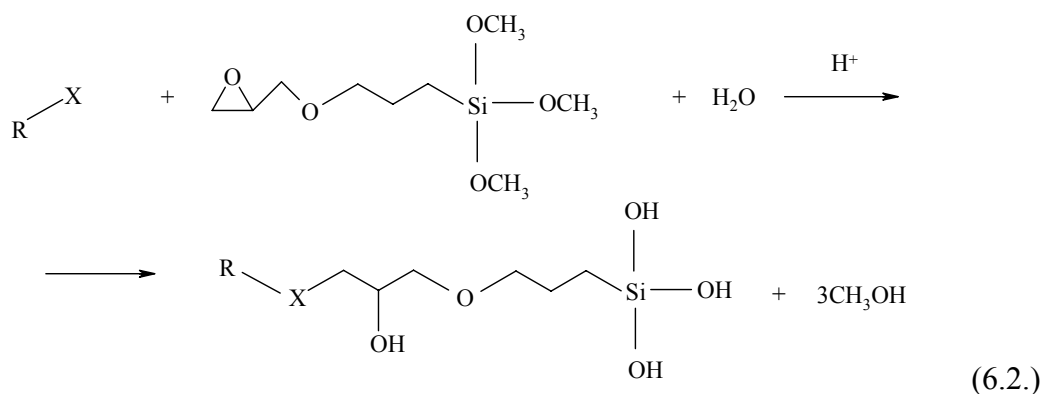
The degree of condensation of GPTMS and TEOS can be obtained from the proportion of T^n and Q^n species according to the following formula:

$$D_c(\%) = \left(\frac{1\text{T}^1 + 2\text{T}^2 + 3\text{T}^3}{3} + \frac{2\text{Q}^2 + 3\text{Q}^3 + 4\text{Q}^4}{4} \right) / 100 \quad (6.1)$$

For class I hybrids just Q^n species are obtained and the interactions between inorganic and organic networks are of a physical nature.

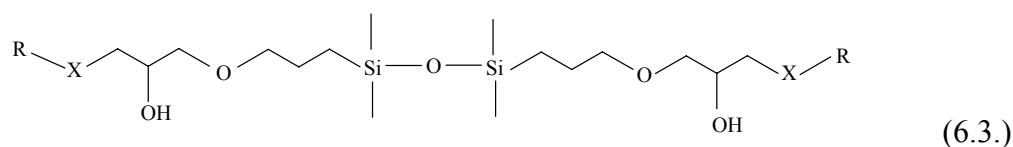
When GPTMS is used as a coupling agent to link organic and inorganic networks of gelatin and silica (class II hybrids) the systems behave differently compared with class I hybrids.

In the GPTMS reaction with gelatin, the cleavage of the C-O bond of the epoxy ring takes place through the attack of nucleophilic groups like COOH and NH_2 from amino acids constituents of gelatin molecules [64], as shown in eq. 6.2, where X represent a nucleophilic group:

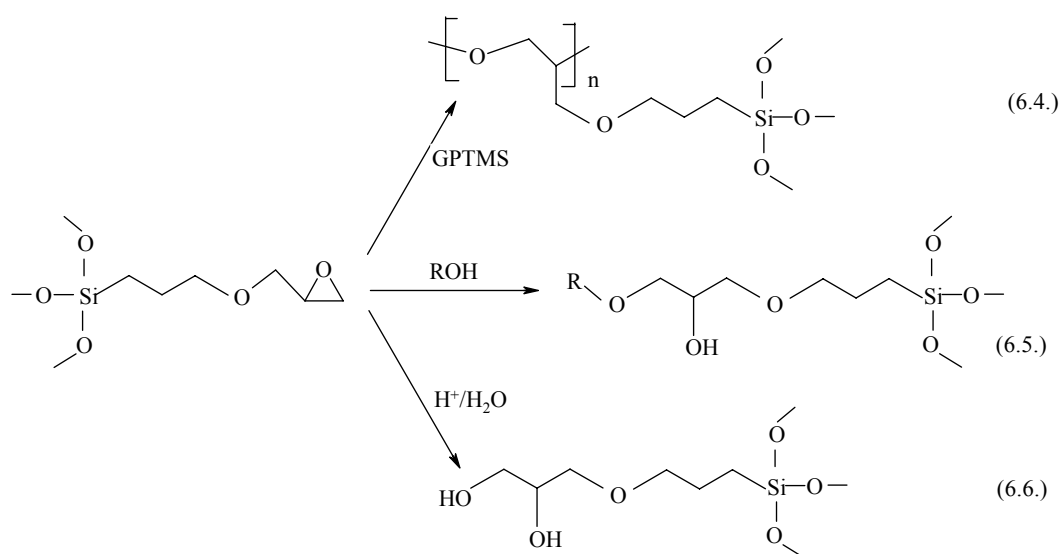


Simultaneously, the hydrolysis of SiOCH_3 groups in GPTMS occurs with the formation of silanol groups as shown above. In the meantime, hydrolysis and condensation reactions of TEOS take place (see eq. 1.1-1.3) with the formation of siloxane bonds.

The hydrolysis and condensation of the GPTMS and TEOS with the ring-opening reactions of the epoxy groups lead to a silica network covalently crosslinked to the gelatin [64] as shown in equation 6.3.

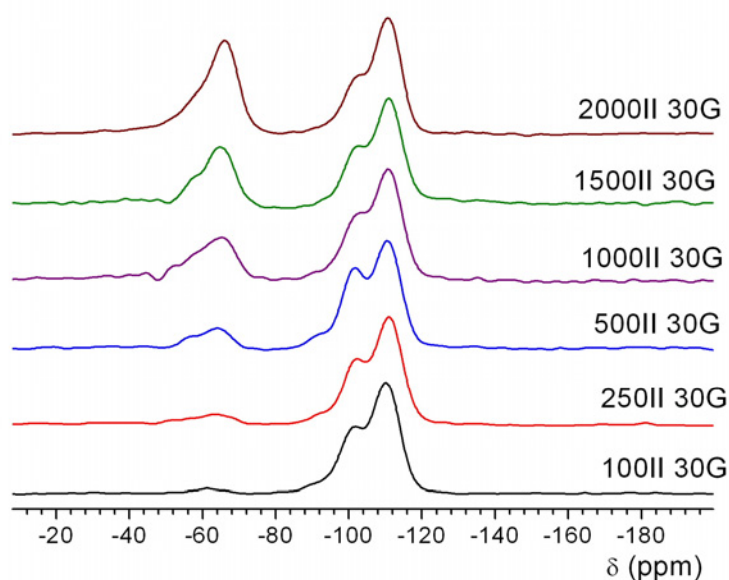


Other possible reactions can be involved in opening the epoxy ring of GPTMS molecules. It can proceed by self-polymerisation to form oligo or poly(ethylene oxide) (PEO) chains (Scheme 6.1, eq. 6.4) [124, 285-290]. It was shown [285] that the cleavage of epoxy ring can even take place by water in acid medium (Scheme 6.1, eq. 6.6) or by action of an alcohol (Scheme 6.1, eq. 6.5) to form diols and alkyl ether terminal groups, respectively. As ethanol and methanol (ROH) are forming as by-products in the system, their action on the epoxy ring cannot be excluded. These reactions are summarised in Scheme 6.1., equations 6.4-6.6.

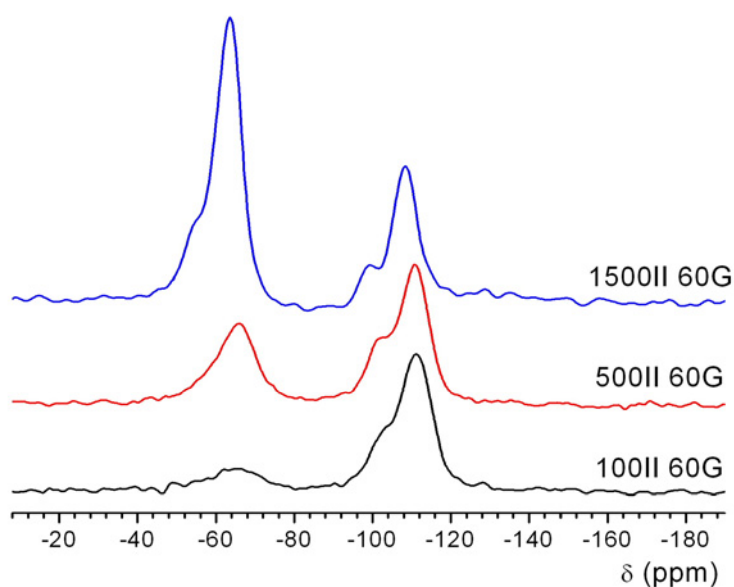


Scheme 6.1. The possibilities for the reactions of the epoxide group.

The ^{29}Si MAS NMR spectra of class II hybrids with 30 and 60% gelatin in the silica matrix for different C factors (molar ratio GPTMS:gelatin) are presented in Figure 6.2 a and b, with their deconvolution in T^n and Q^n species shown in Table 6.1. The degree of condensation (D_c) for the hybrids has also been calculated.



(a)



(b)

Figure 6.2. ^{29}Si MAS NMR spectra of class II silica-gelatin hybrids with 30% (a) and 60% (b) of gelatin for different C factors.

When GPTMS has been used as a crosslinking agent, the Q^4 species concentration decreased from 61 to 36% as the C factor increased from 100 to 2000 for 30% compositions (Figure 6.2 a and Table 6.1) and from 62 to 25% as the C factor increased from 100 to 1500 for 60% compositions (Figure 6.2 b and Table 6.1).

By increasing the C factor for both compositions, the concentration of T^3 species increases indicating an increase in organic-inorganic coupling, and for the compositions with the highest C factors (2000 for 30G and 1500 for 60G) T^3 and Q^4 species are dominant compared with species of lower connectivity (Q^3 , Q^2 and T^2 , T^1). This indicates that GPTMS provides a covalent link from the gelatin to silica inorganic network. For the same C factor, the concentration of T^3 species is higher and Q^4 species is lower for the 60% gelatin in silica matrix. The concentration of GPTMS is proportional to the gelatin concentration and consequently 60% compositions for the same C factor have a higher concentration of GPTMS.

However the network connectivity and the degree of crosslinking seems to experience a slight decrease for both compositions at lower C factors (up to 500) compared with the compositions without GPTMS with C factors 0 (30G and 60G). This may imply that the formation of the inorganic network can be affected by the extent of formation of the organic network from GPTMS, probably due to steric hindrance as the organic network grows limiting the extent of the inorganic network. As C factors increased over 500 for both compositions the D_c increased, except for the composition with 30% gelatin and a C factor of 2000. T^0 , Q^0 and Q^1 species are absent from the spectra and T^1 where present, are low in concentration, suggesting that condensation reactions between silanols from both TEOS and GPTMS alkoxides proceed almost to completion.

The ^{13}C CP MAS NMR spectra for silica-gelatin organic-inorganic hybrids, class I are presented in Figure 6.3.

The assignment of resonances of amino acid residues in gelatin have been made on the basis of ^{13}C chemical shifts for amino acids reported in the literature [296-301] and are numbered from 1 to 14 in Figure 6.3. The corresponding chemical shifts (ppm) of the amino acids residues are as follow: 17.5 (Ala β), 20.2 (Leu δ , Val γ , γ' , Thr γ), 25.5 (Pro γ , Glu β , Leu δ), 30.3 (Pro β , Arg β , Lys β), 38.1 (Hyp β , Asp β , Lyse, Leu β , Phe β , Ile β), 42.9 (Gly α , Arg δ), 48.3 (Pro δ), 55.6 (Ala α), 60.1 (Pro α ,

Hyp α , Lys α , Phe α), 62.4 (Ser β , Val α , Thr α , Ile α), 67.9 (Thr β), 71.2 (Hyp γ), 128.9 (Phe δ,ϵ), 157.7 (Arg ϵ). The carbonyl region from 165 to 183 ppm corresponds to the carbonyl and carboxylic carbons of amino acids residues.

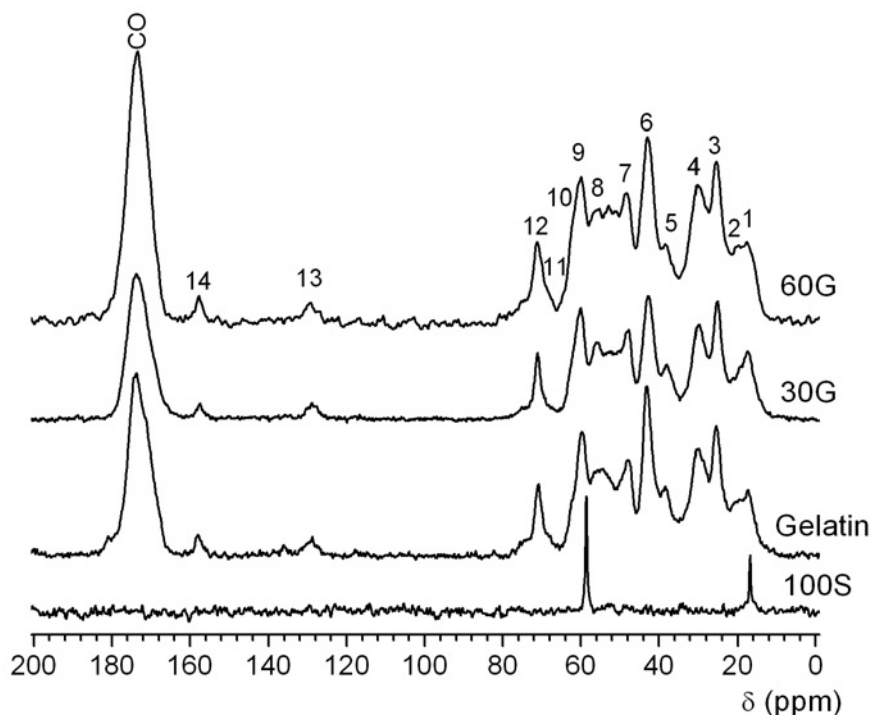


Figure 6.3. ^{13}C CP MAS NMR spectra of class I hybrids.

The structures of the most representative amino acids present in the gelatin structure are presented in Figure 6.4.

^{13}C CP MAS NMR spectra of silica matrix (100S) shows the residual carbon from TEOS backbone corresponding to $-\text{CH}_2\text{O}$ and $-\text{CH}_3$ at ~ 60 and ~ 18 ppm (Figure 6.3). Increasing the concentration of gelatin from 30% to 60% in the inorganic silica matrix, these peaks overlap with those of aliphatic region from amino acids, whose signals are dominant. For comparison the spectrum of gelatin is also shown. For the 60G sample, the peaks from the amino acids show a slightly broadening compared with the 30G sample, probably as the amino acids of gelatin network experience a restricted mobility due to the growth of the silicate inorganic network. This also supports the observations in the ^{29}Si MAS NMR spectra as the D_c and linewidths of Q^4 species increased with gelatin concentration.

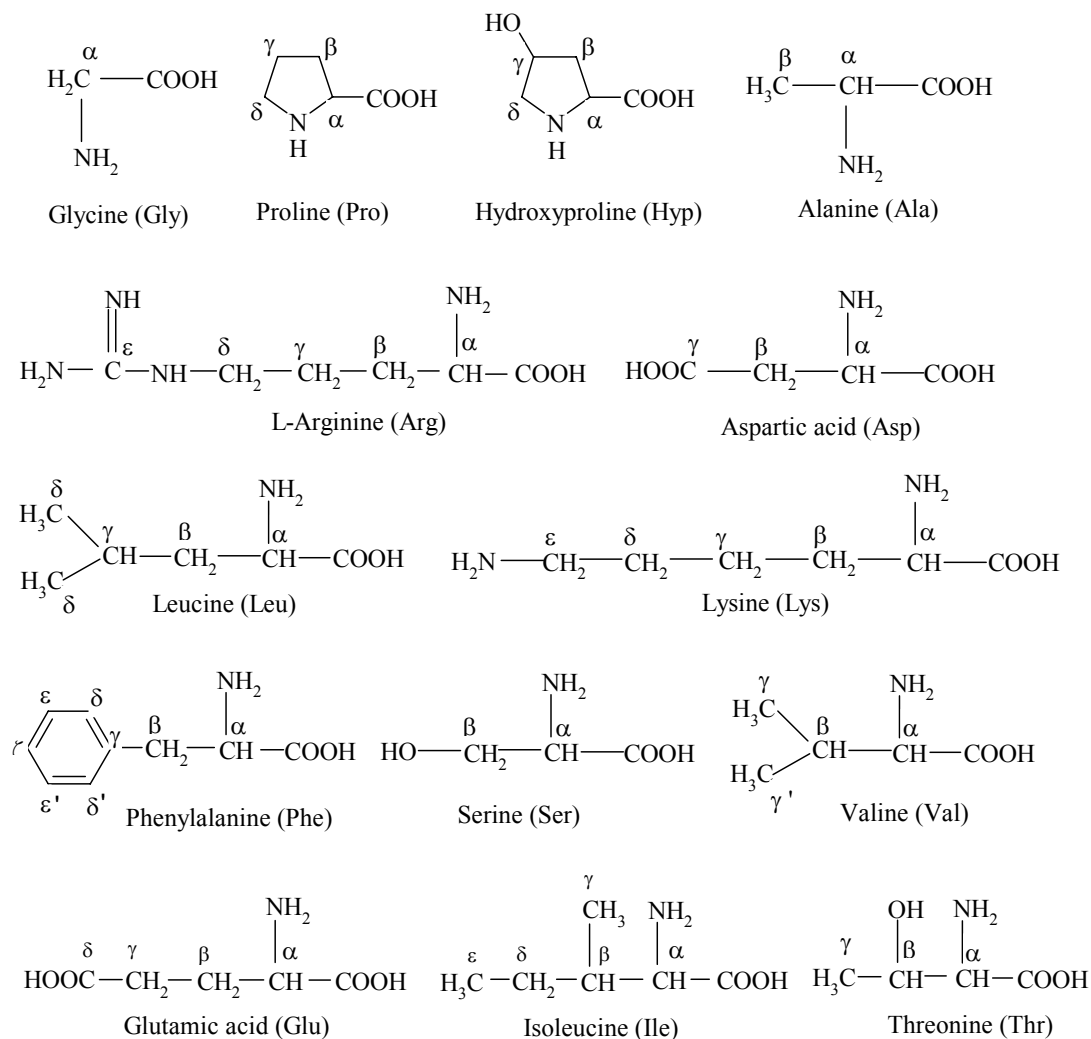


Figure 6.4. The structures of the most representative amino acids in the gelatin molecules

The ^{13}C CP MAS NMR spectra of class II hybrid nanocomposites with 30 and 60% of gelatin in the silica matrix having different C factors are presented in Figures 6.5 and 6.6.

On increasing the C factor to 2000 (Figure 6.5) and to 1500 (Figure 6.6) for 30% and 60% gelatin in silica matrix sample, respectively, the intensity of the peaks corresponding to amino acids in gelatin decreased, suggesting that amino acids were incorporated in the hybrid and provided a bridging link between the inorganic and organic networks. Also the broadening of peaks indicates a restricted mobility probably due to the growth of inorganic and organic networks.

As can be observed in the spectra of these samples besides the peaks from gelatin other peaks can be identified.

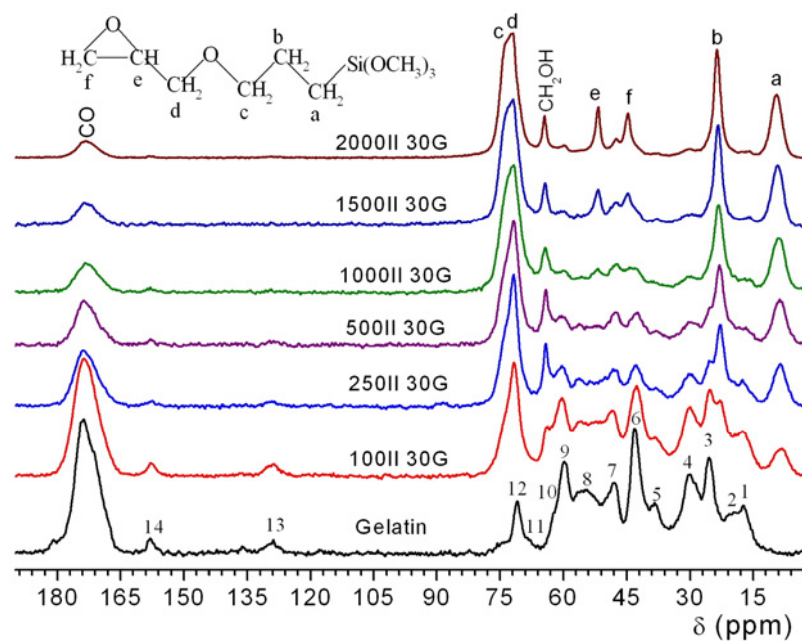


Figure 6.5. ^{13}C CP MAS NMR spectra of class II organic-inorganic hybrids containing 30% gelatin in silica matrix for different C factors. GPTMS structure is inserted.

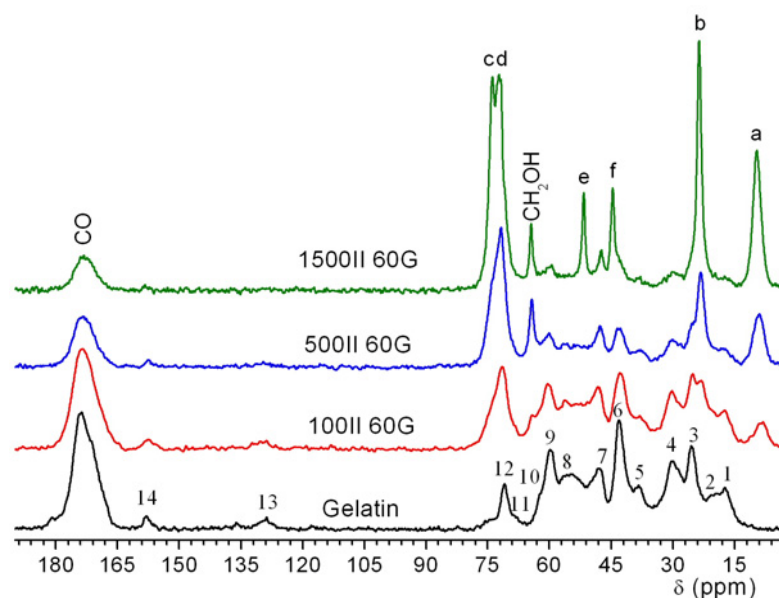


Figure 6.6. ^{13}C CP MAS NMR spectra of class II hybrid nanocomposites containing 60% gelatin in silica matrix for different C factors.

The GPTMS molecule has 6 carbon atoms (labelled a to f in the insert in the Figure 6.5.) with the corresponding resonances (in ppm) as follows [124, 285-290]: 9.7 (first carbon atom from the silicon (a)), 23.6 (second carbon atom from the

silicon (b)), 73.9 (carbon in the ether bridge of GPTMS (c)), 72.1 (carbon in the ether bridge of GPTMS (d)), 51.7 (carbon in the epoxy ring (e)), 44.7 (carbon in the epoxy ring (f)). No evidence of carbon from methoxy groups (SiOCH_3) in GPTMS molecules at 50 ppm [124] has been found in the ^{13}C spectra, suggesting that they have been hydrolysed to silanols. The peak at 64 ppm is due to the terminal carbon in the diol (CH_2OH) group formed by the ring opening reaction of GPTMS as shown in Scheme 6.1, equation 6.6. The resonances corresponding to C-atoms in the ethylether group ($\text{CH}_3\text{CH}_2\text{O}$, Scheme 6.1 equation 6.5.) around 15 and 67 ppm [302] are absent from the spectra, suggesting that if this reaction took place it is only minor. The peak at 48 ppm (labeled 7) by comparing with the other peaks corresponding to amino acids fragments decreases just slightly in intensity with increasing C factor indicating that it can also have a contribution from Si-O-C formed by the condensation reaction of diol with silanols [288], especially given that terminal diol has been found in the spectra. The peak around 70-75 ppm can have contributions from the carbons in oligo or PEO chains ($-\text{O}-\text{CH}_2-[-\text{CH}_2-\text{CH}_2]_n-\text{O}-$) as shown in eq. 6.4 in Scheme 6.1, and is an overlap of polymerised and unpolymerised species. This is evident from the appearance of a shoulder around 76 ppm at C factors up to 500 for both compositions (30 and 60% of gelatin, Figures 6.5 and 6.6, respectively) and the broadness of this peak for C factors 1000-2000 for the 30G composition. This is also supported by the fact that the peaks corresponding to carbons in a and b positions close to silicon atoms are broader at lower C factors (up to 500) compared with higher C factors, indicating that they are sensitive to organic polymerisation and due to an increase in organic network rigidity with the formation of PEO in these samples leads to a restricted mobility. This is correlated with ^{29}Si results where a slight decrease in the degree of crosslinking was found in these samples, due to the growth of the organic network.

As evidenced in Figures 6.5 and 6.6 for both compositions (30G and 60G) at C factors up to 500 the peaks corresponding to epoxide rings (labeled e and f) are absent from the spectra, indicating total completion of the ring-opening reaction by gelatin molecules. This supports the fact that on the organic network gelatin serves as a nucleophile for the epoxy-ring opening reaction. With increasing the C factor to 1500 for 60G (Figure 6.6) and to 1000-2000 for 30G (Figure 6.5) the signal from the carbons e and f appears in the spectra and for G30 composition seem to increase in

intensity with C factor. At higher concentrations of GPTMS, the amino acids from gelatin have been incorporated in the hybrid network, consequently some epoxy rings in GPTMS are not attacked and remain intact. The peak around 70-75 ppm is still broad for the 30G composition (Figure 6.5) even if does not present the shoulder, probably just shorter oligomers in poly(ethylene oxide) are formed and this could explain the sharpness for the carbons in the epoxide ring with increasing C factor to 2000, probably due to residual mobility of the glycidyl groups. The sharpness of the peaks for the 60G composition with C factor 1500 (1500II 60G, Figure 6.6) suggest that the carbon atoms have very little chemical dispersion and are in a well-defined sites and in a mobile chain, possibly due to a less extensive organic network and short PEO chains are mobile. As was shown by ^{29}Si NMR this sample presents a high degree of crosslinking for inorganic network with the highest concentration for T^3 species. This suggests that the organic network grows slower compared with the inorganic network and as gelatin is also incorporated, the organic chains cannot find enough space to grow, their length is reduced.

^1H NMR is a powerful tool for studying organic-inorganic hybrids due to solid-state NMR developments such as fast MAS and CRAMPS, allowing an increase in the resolution in ^1H spectra [124, 293-295].

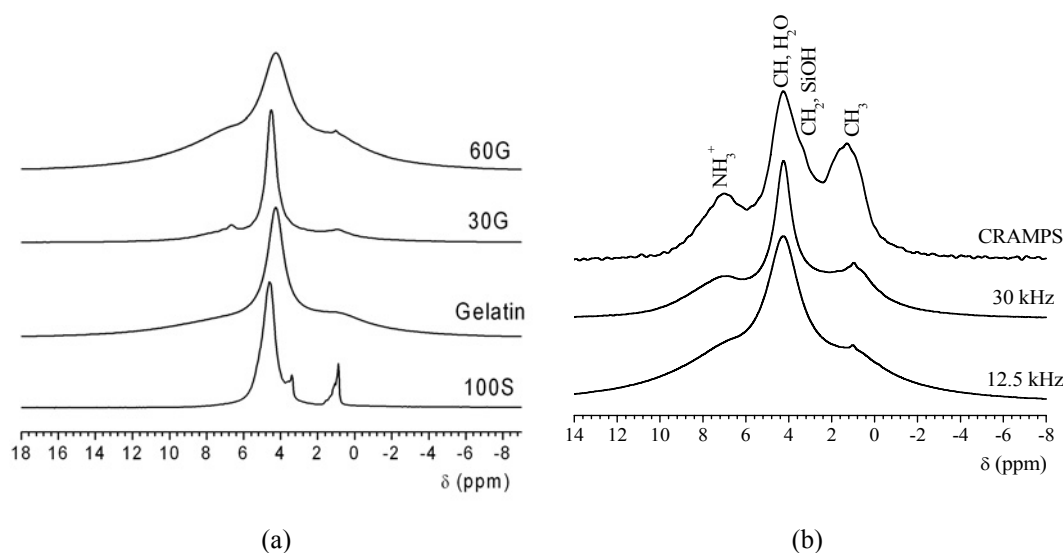


Figure 6.7. (a) ^1H MAS NMR spectra at 12.5 kHz of silica-gelatin class I hybrids. For comparison the gelatin spectrum is shown. (b) A comparison between spectra obtained at 12.5 kHz, 30 kHz and CRAMPS for the 60G sample.

The ^1H MAS NMR spectra of class I hybrids are shown in Figure 6.7 a, where the gelatin spectrum is also shown for comparison.

In a pure silica matrix (100S) spectrum recorded at 12.5 kHz the ^1H peaks at 1.2, 3.5 and 5 ppm correspond to CH_3 from TEOS residues, SiOH and water respectively. When gelatin is used the spectra become broader and featureless. Another resonance appears between 6-8 ppm due to NH_3^+ and NH amide groups of amino acids. The linewidths of the ^1H MAS NMR spectra increased as the concentration of the polymer in the silica matrix increased from 30 to 60% because of broadening due to stronger ^1H - ^1H dipolar coupling interactions (Figure 6.7 a). To increase the resolution of spectra fast MAS at 30 kHz and CRAMPS using windowed DUMBO-1 as a decoupling sequence have been performed. A comparison between MAS at 12.5, 30 kHz and CRAMPS is presented in Figure 6.7 b for silica-gelatin sample having 60% gelatin (60G). For this concentration of gelatin in silica a matrix, the CRAMPS gave the highest resolution of the spectra due to the high concentration of gelatin in the silica matrix and strong dipolar couplings.

The homonuclear decoupled spectra for 60% gelatin in a silica matrix for different C factors are presented in Figure 6.8.

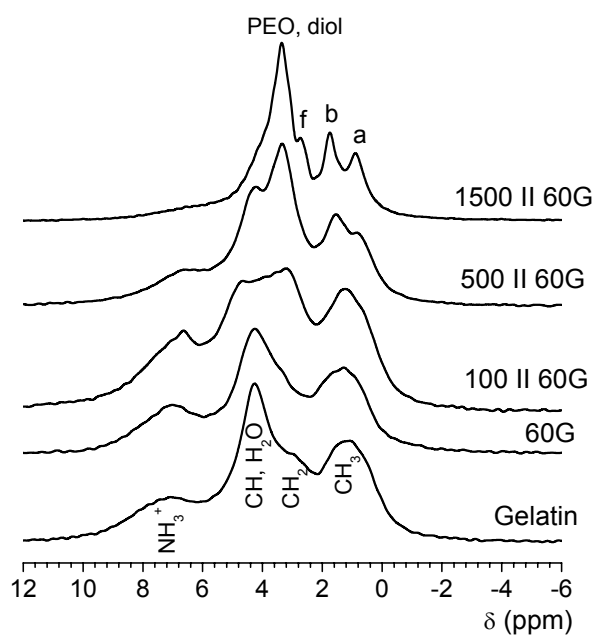


Figure 6.8. Homonuclear decoupled spectra using DUMBO-1 for 60% gelatin in a silica network for C factors from 0 (60G) to 1500 (1500 II 60G). The gelatin spectrum is also shown.

For 30% gelatin in a silica network with C factors from 0 to 2000 good resolution has been obtained even at 30 kHz (Figure 6.9 a), but using homonuclear decoupling (Figure 6.9 b) the peaks corresponding to the protons attached to C_a and C_b in GPTMS residues at 0.8 and 1.5 ppm have been resolved, suggesting stronger dipolar coupling interactions for these species.

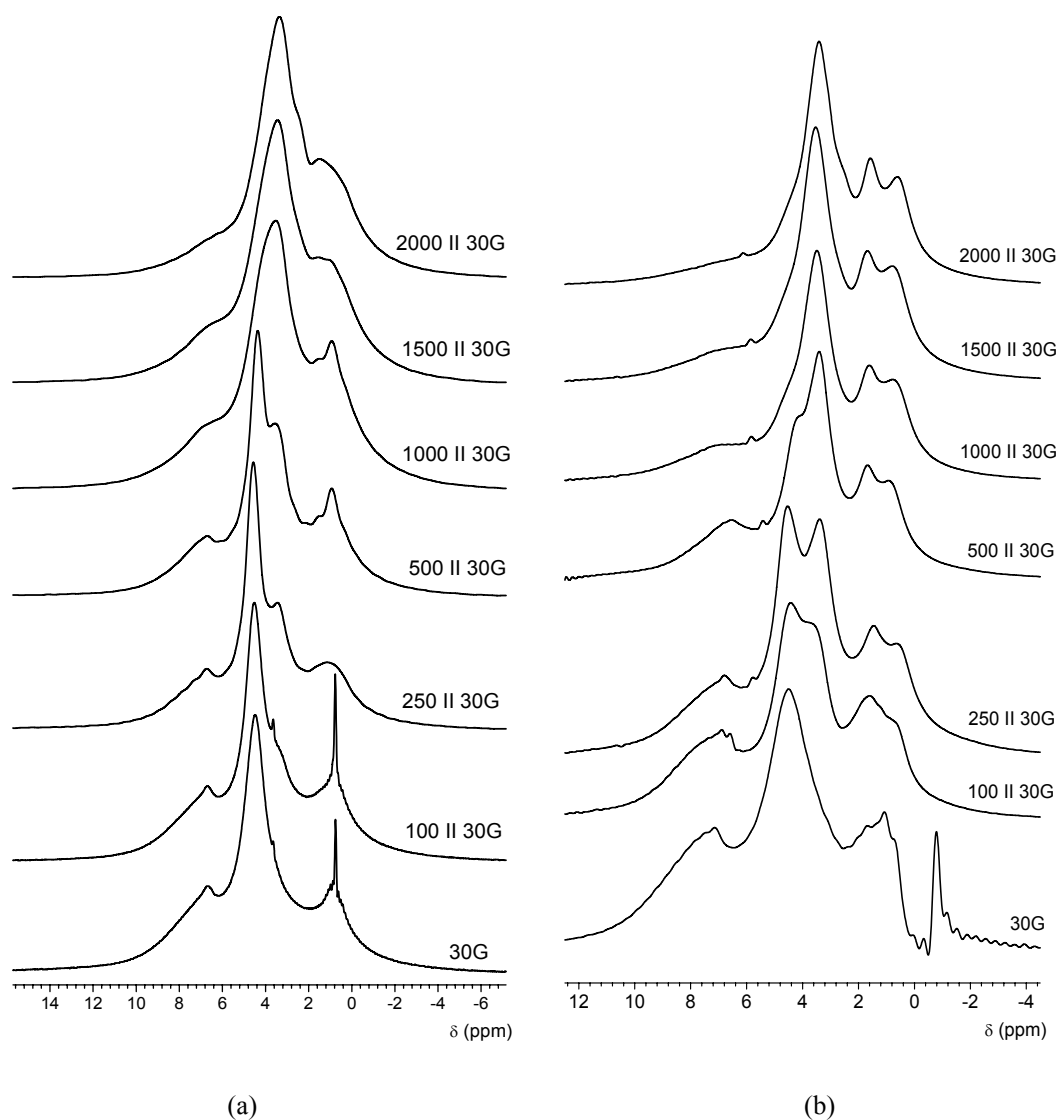


Figure 6.9. ¹H MAS NMR spectra recorded at 30 kHz (a) and homonuclear-decoupled spectra using windowed DUMBO-1 at 12.5 kHz (b) of hybrids with 30% gelatin in a silica matrix for C factors ranging from 0 (30G) to 2000 (2000 II 30G).

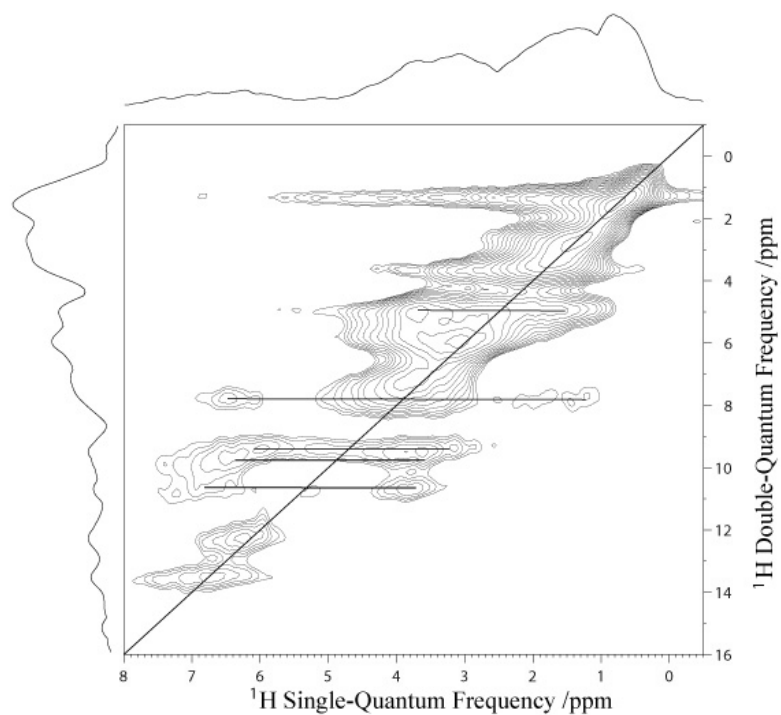
The ¹H spectra of 30G (Figure 6.9 a and b) and 60G (Figures 6.8) samples (C factors 0) are similar to that of gelatin and present mainly the resonances from gelatin molecules at 0.8, 3.5, 4.5 and 6.7 ppm corresponding to CH₃, CH₂, CH (H₂O)

and protonated NH_3^+ respectively. The resonances at 0.8 and 3.5 ppm can have contributions from TEOS residues and SiOH as well. For the 30G sample recorded with fast MAS (Figure 6.9 a) the peak at 0.8 ppm is sharp probably due to mobility of these species, while for the 60G sample they are more rigid due to higher concentration of gelatin.

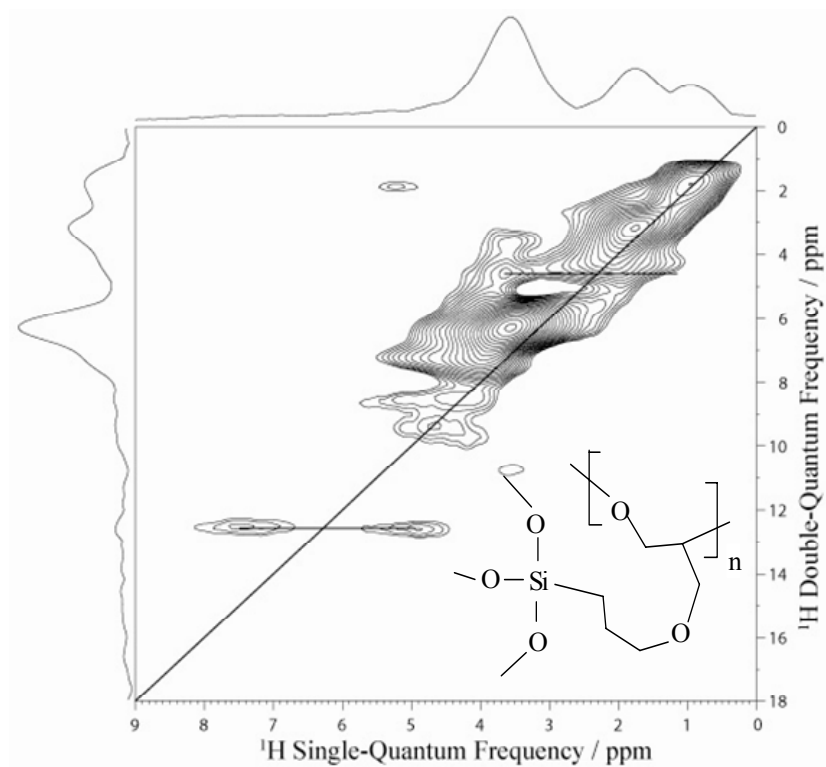
By comparing the fast MAS and CRAMPS spectra of the samples with C factors 0 and 100 (30G and 100 II 30G), the resonance at 0.8 ppm is sharper in the MAS spectra than in the CRAMPS one. The residual linewidth of the peak in the CRAMPS spectra can be determined to a large extent by the distribution of the isotropic chemical shift due to the existence of a variety of CH_3 structures and hydrogens in position a. In contrast ^1H - ^1H dipolar interactions affect the linewidths in the MAS-only spectra.

With increasing C factor from 100 to 2000 for 30G samples and to 1500 for 60G samples, it can be observed that the resonance at 3.4 ppm which can be due to hydrogens in PEO chains ($-\text{O}-\text{CH}_2-[-\text{CH}_2-\text{CH}_2]_n-\text{O}-$) and diol [124, 290] increases in intensity and for higher C factors (from 1000 for 30G and 1500 for 60G) this peak is the main contribution to the spectra. This peak can also have a contribution from hydrogens in position d from GPTMS. Also with increasing C factor from 1000 to 2000 for 30G the peak becomes broader suggesting a more extensive and rigid organic network and stronger dipolar couplings. In the meantime the peaks at 4.5 and 7 ppm from amino acids decrease in intensity and are visible as shoulders suggesting that gelatin has been incorporated into the silicate network. At these C factors a shoulder for 30G compositions (Figure 6.9 a and b) and a well defined peak for 60G (Figure 6.8) was detected at 2.6 ppm due to hydrogens f from GPTMS residues. This suggests that some epoxide rings from GPTMS molecules remain intact and are not opened by gelatin molecules. This is in agreement with ^{13}C CP MAS NMR results. Also the sharpness of the peaks for the 1500 II 60G sample suggest a residual mobility, confirming that short and relatively mobile PEO are formed.

The ^1H DQ CRAMPS spectra recorded for C factors 0 for both 30G and 60G, as well as 500 for 30G and 1500 for 60G are presented in Figures 6.10 and 6.11. Despite the broadening of the spectra a few on-diagonal and cross-peaks can be observed.

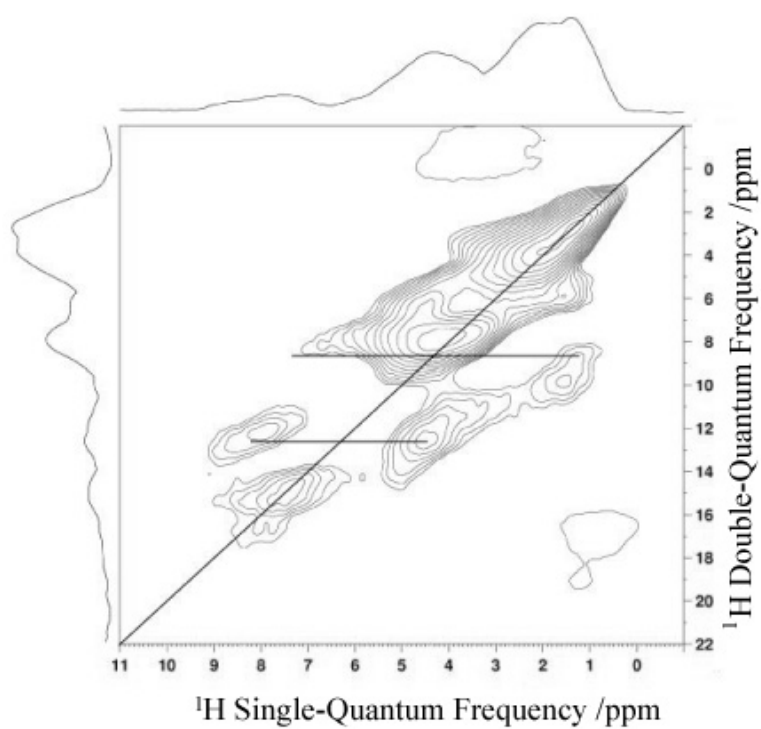


(a)

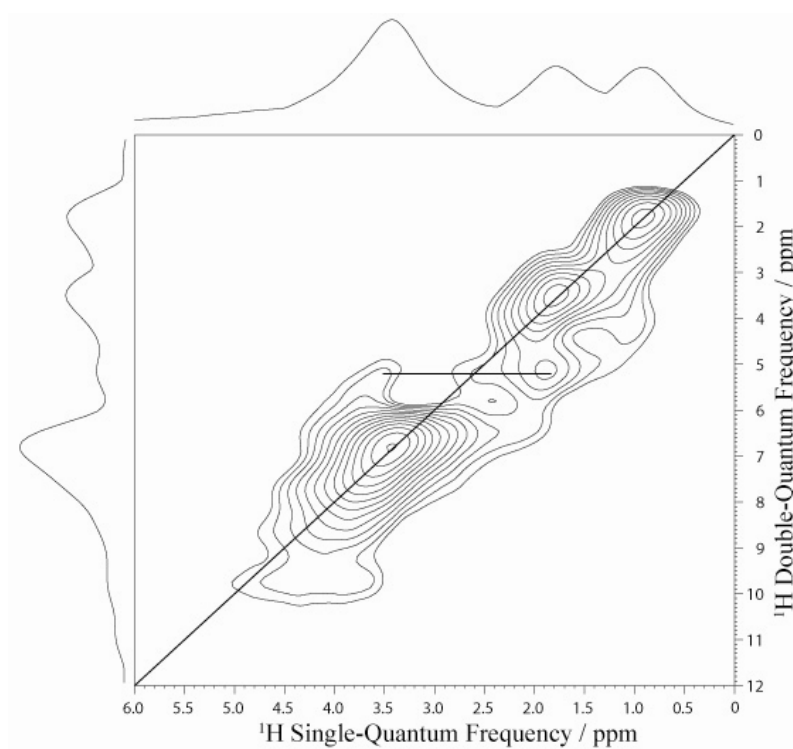


(b)

Figure 6.10. Two-dimensional ^1H (500 MHz) DQ CRAMPS spectrum of hybrids with C-factor 0 (a) and 500 (b) for 30% gelatin. PEO chains bent conformation is inserted.



(a)



(b)

Figure 6.11. Two-dimensional ^1H (500 MHz) DQ CRAMPS spectrum of hybrids with C-factor 0 (a) and 1500 (b) for 60% gelatin.

For the 30G sample with C factor 0 (Figure 6.10 a), intermolecular cross-peak correlations between SiOH (at 1.3-1.5 ppm) and both CH₂ and NH₃⁺ from amino acids (at 3.8 and 6.2 ppm, respectively) can be observed, suggesting that the gelatin has been incorporated in the silica network and weak interactions (van der Waals, electrostatic or hydrogen bonding) of a physical nature between the two networks take place. An inter- and/or intramolecular correlation between a CH₂ (at 3.2-3.8 ppm) and both NH₃⁺ (at 6.2 ppm) and NH (6.8 ppm) amide forms from amino acids are detected. On-diagonal peaks from both NH₃⁺ and NH can be observed, as inter- and/or intramolecular interactions from amino acids in gelatin molecules.

For C factor 500 having 30% gelatin (Figure 6.10 b) a correlation between hydrogens in position a at 0.8 ppm from GPTMS residues and PEO or diol at 3.5 ppm can be detected. Also a correlation between protons a and b is not observed. Consequently, an intramolecular bent conformation for PEO chains can be deduced. Intermolecular proximities in PEO are less likely to take place due to steric restrictions. Another intermolecular correlation can be observed between a CH (at 4.5 ppm) and NH₃⁺ (at 7.2 ppm) from amino acid molecules of the gelatin. An important feature is the absence of the on-diagonal peak corresponding to close proximity of two NH₃⁺ indicating that they are not close in space. This supports the hypothesis that GPTMS has created a link between gelatin and the silica network and therefore the gelatin is immobilized in the silicate network. Also the PEO formed can induce steric hindrance and conformational constraints.

For 60% gelatin in a silica matrix with C factor 0 (60G, Figure 6.11 a) an intermolecular cross-peak correlation between a SiOH (1.5 ppm) and NH₃⁺ (7.2 ppm) is observed, similar to 30G. Another intra and/or intermolecular correlation between a CH (at 4.5 ppm) and NH amide form (at 8.5 ppm) from gelatin can be detected. The deshielding of NH₃⁺ and NH amide forms from gelatin can be due to a stronger interaction with the inorganic matrix and the higher concentration of the organic phase.

For C factor 1500 (Figure 6.11 b), just an off-diagonal peak between hydrogens in position b from GPTMS chains and PEO chains is observed, suggesting a bent conformation of PEO chains similar with 30G sample. The lack of other

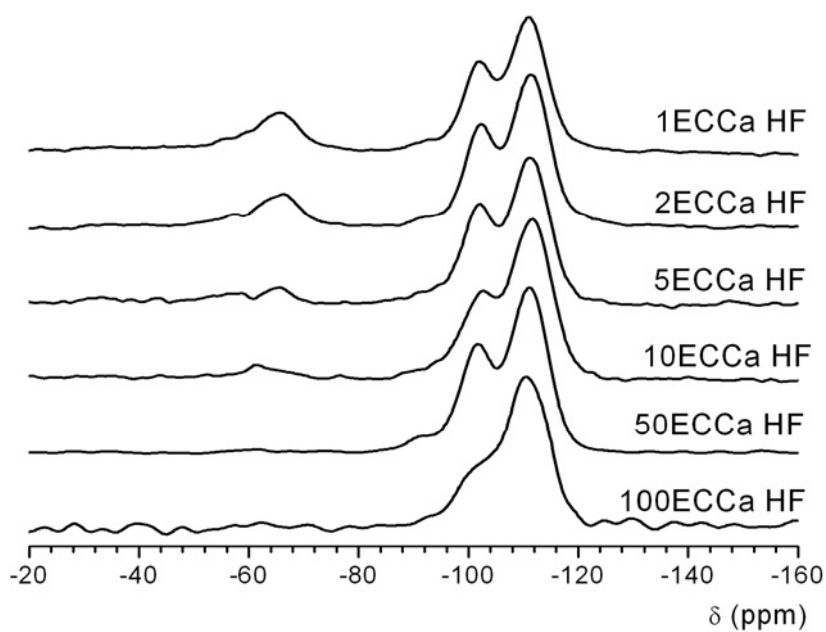
intermolecular correlations can be due to the mobility of the species, which was deduced from ^{13}C CP and ^1H MAS NMR spectra for this sample.

6.3.2. Silica-calcium oxide-(γ -PGA) organic-inorganic hybrids

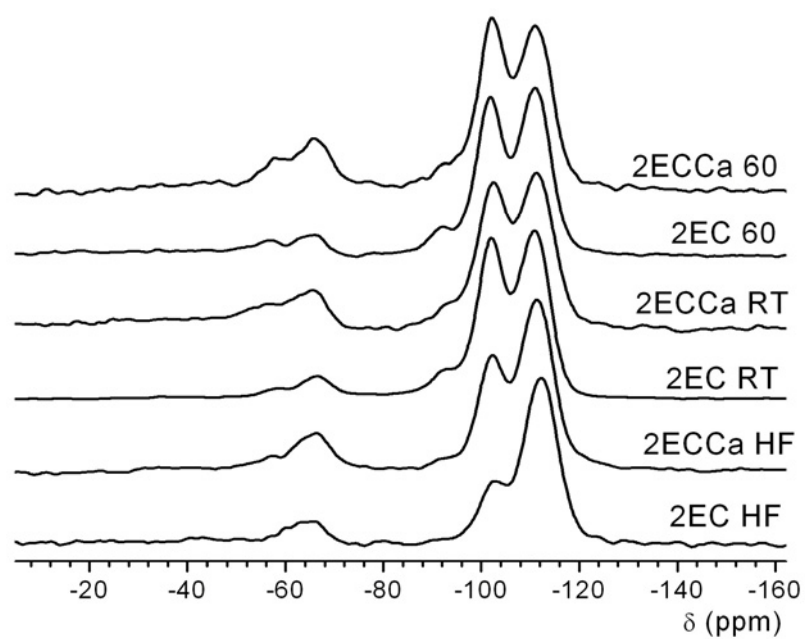
The influence of the γ -PGA:GPTMS mole ratio (X_{EC}) and the synthesis conditions (samples gelled with HF, at room temperature and at 60°C) on the growth of inorganic and organic networks when CaCl_2 has been used as the calcium source have been investigated.

^{29}Si MAS NMR spectra of 40 wt% γ -PGA and 60 wt% bioactive silica (70 mol% SiO_2 and 30 mol% CaO) organic-inorganic hybrids synthesised using HF as catalyst for X_{EC} from 100 (100ECCa HF) to 1 (1ECCa HF) are shown in Figure 6.12 a, with a comparison between gels made with HF, at room temperature and 60 °C with and without calcium for $X_{\text{EC}}=2$ in Figure 6.12 b. The ^{29}Si MAS NMR results with the deconvolution of spectra for all samples are summarised in Table 6.2, where both T^n and Q^n species can be detected.

In all samples the silica matrix condensed well, forming Si-O-Si bonds as shown by the dominance of Q^4 species in the hybrids. The samples synthesized using HF as catalyst have a higher concentration of Q^4 and lower concentration of Q^3 species for the same X_{EC} compared with samples gelled at room temperature and 60 °C. This is due to the influence of HF as a catalyst in the gelling process when highly branched clusters are obtained [96]. The proportion of T^n species, particularly the T^3 , were found to decrease with increasing X_{EC} ratio. This shows that the GPTMS was successfully condensed in the hybrid and that with increased GPTMS a higher degree of inorganic/organic crosslinking was taking place. The proportion of Q^4 was found to increase with increasing X_{EC} (decreasing T^n), while the Q^3/Q^4 ratio was generally observed to decrease. This observation suggests that with a higher concentration of GPTMS the silica particles were smaller therefore more Q^3 species were present. This indicates that the increase in crosslinking decreased the silica particle size and increased inorganic/organic interaction. However, the overall degree of condensation (D_c) between these samples is similar (Table 6.2), indicating that the proportions of bridging to non-bridging oxygens in the hybrids were similar, i.e., the overall network connectivity of the samples were similar.



(a)



(b)

Figure 6.12. ^{29}Si MAS NMR spectra of (a) hybrids for X_{EC} ranging from 1 to 100 using HF as catalyst and (b) a comparison between gels made with HF, at room temperature and 60 °C with and without calcium for $X_{\text{EC}}=2$.

Table 6.2. ^{29}Si MAS NMR data of class II silica-calcium oxide- γ -PGA hybrids, giving the spectral deconvolution into different T^n and Q^n species.

Sample	T^1			T^2			T^3			Q^2			Q^3			Q^4			D_c (%)
	δ (ppm)	FWHM (ppm)	I (%)																
SiO ₂ -CaO- (γ -PGA) using CaCl ₂ as calcium precursor																			
100ECCa HF	-	-	-	-	-	-	-62.3	4.57	2	-92.5	5.03	2	-101.4	8.58	25	-111.0	9.04	71	92.7
50ECCa HF	-	-	-	-	-	-	-61.1	5.1	1	-92.1	8.1	6	-101.5	7.1	33	-111.1	8.1	60	87.8
50EC HF	-	-	-	-60.7	5.2	1	-65.3	5.2	1	-92.6	8.5	4	-101.7	7.7	23	-111.5	8.3	71	91.9
10ECCa HF	-	-	-	-	-	-	-65.5	7.2	2	-93.6	9.3	5	-102.1	7.4	29	-111.6	8.3	62	90.3
							-61.1	4.3	2										
10ECCa RT	-	-	-	-56.1	5.9	2	-65.6	5.5	2	-93.9	9.1	9	-102.1	6.6	37	-111.2	8.3	49	85.6
							-59.8	2.7	1										
10ECCa 60	-	-	-	-55.4	3.3	1	-66.3	10.6	3	-92.3	6.5	5	-101.9	7.8	44	-111.2	7.8	45	75.0
							-59.0	3.5	2										
5ECCa HF	-	-	-	-57.4	5.1	3	-65.2	5.2	4	-94.4	5.7	4	-101.8	6.7	31	-111.2	8.1	58	89.3
5ECCa RT	-	-	-	-57.1	5.7	3	-65.8	5.0	4	-92.7	5.1	6	-102.1	5.3	41	-111.1	7.7	45	74.5
							-62.1	2.7	1										
5ECCa 60				-55.7	5.2	2	-64.6	9.1	7	-93.9	9.2	11	-102.0	7.1	38	-110.8	8.0	42	73.8
2ECCa HF	-52.7	5.9	1	-57.1	4.1	2	-65.6	8.8	12	-93.0	7.5	4	-102.0	6.6	28	-111.4	8.0	53	89.7
2ECCa RT	-	-	-	-55.2	10.5	7	-65.3	8.6	10	-93.7	6.6	5	-102.2	6.9	34	-111.4	8.1	44	86.7
2ECCa 60	-52.7	4.6	1	-57.9	6.0	5	-66.0	7.9	12	-93.3	7.9	6	-102.0	6.6	34	-111.1	8.1	41	85.2
2EC HF	-	-	-	-59.2	6.0	2	-65.0	7.9	9	-92.6	5.5	1	-102.5	7.3	22	-112.3	8.0	66	93.3
2EC RT	-	-	-	-58.0	6.9	2	-66.5	7.4	6	-93.1	7.6	8	-101.9	6.4	37	-110.8	7.7	47	74.3
2EC 60	-	-	-	-56.5	6.0	3	-65.2	7.0	5	-92.2	6.8	7	-101.7	6.5	38	-110.9	7.6	47	85.0
1ECCa HF	-	-	-	-56.4	8.4	5	-65.6	8.7	16	-92.9	7.2	4	-101.7	6.6	26	-111.0	8.0	49	89.8
1ECCa RT	-53.3	5.0	2	-57.0	4.3	4	-65.4	8.5	17	-93.1	7.3	7	-101.7	6.3	30	-110.7	8.0	40	86.3
1ECCa 60	-53.0	6.6	4	-57.7	3.8	5	-65.4	8.3	16	-93.4	7.5	5	-102.0	6.4	29	-111.2	8.0	41	85.9
SiO ₂ -CaO- PGA using calcium poly(γ -glutamate) as calcium precursor																			
2EC CaPGA aged	-	-	-	-58.7	10.2	11	-67.0	9.2	13	-92.5	7.3	4	-101.9	8.9	26	-110.9	8.9	46	76.3

FWHM, δ and I represent the linewidth full-width half-maximum, ^{29}Si chemical shift and relative intensity, respectively. Errors associated with measurements are — FWHM \pm 1 ppm, $\delta \pm$ 2 ppm and Integral \pm 2%.

In the calcium-free hybrids, when HF was used as catalyst, a higher proportion of Q⁴ species was observed compared to the calcium-containing hybrids (Table 6.2). The Q⁴ species decreased from 71% to 60% for X_{EC} = 50 and for X_{EC} = 2 from 66% to 53% when calcium was used. Also the Q³ concentration increased from 23% to 33% for X_{EC} = 50 and decreased from 28% to 22% for X_{EC} = 2. This indicates that the incorporation of calcium in the hybrid samples leads to a more polymerised chain-like silica network (see below). This is also supported from the lower D_c for samples without calcium. Therefore the Ca²⁺ ion interacts with the gelling catalyst HF by lowering its catalytic activity. The time for gel formation supports this, where the calcium-containing 2ECCa gelled in 60 minutes while the calcium-free 2EC gelled in less than 2.4 minutes. For samples synthesized at room temperature and 60 °C using HCl as catalyst, the proportion of Q⁴ decreased just slightly and compared with samples synthesized with HF, the Q³ concentration decreased when calcium was used, as the catalyst and the calcium salt have the same anions (Cl⁻). Also the D_c was observed to be lower comparing samples made with HF. For all three reaction conditions the Tⁿ species have been found to increase for calcium containing samples indicating that calcium increases the crosslinking between functionalized γ -PGA and silica network (see Figure 3.15). The results from ²⁹Si MAS NMR also suggests that calcium is not incorporated in the silica matrix at this stage and that the calcium is present in the gelling solution.

When calcium poly(γ -glutamate) as the salt of γ -PGA was used (2EC CaPGA aged) the concentration of Tⁿ species in ²⁹Si MAS NMR spectra is higher comparing the samples with the same X_{EC}=2 made from CaCl₂ and using HCl as catalyst (Table 6.2). This can be due to the fact that aging leads to more extensive organic-inorganic crosslinking between phases. This is supported by a lower concentration of Q³ species compared with 2ECCa RT and 2ECCa 60 samples. However, the D_c is comparable with samples synthesised at room temperature and 60 °C.

¹³C CP MAS NMR spectra for silica-calcium oxide-PGA with X_{EC}=1 synthesised using different conditions (gelled with HF (1ECCa HF), at room temperature (1ECCa RT) and at 60 °C (1ECCA 60)) are shown in Figure 6.13 a, with an insert showing the PGA structure.

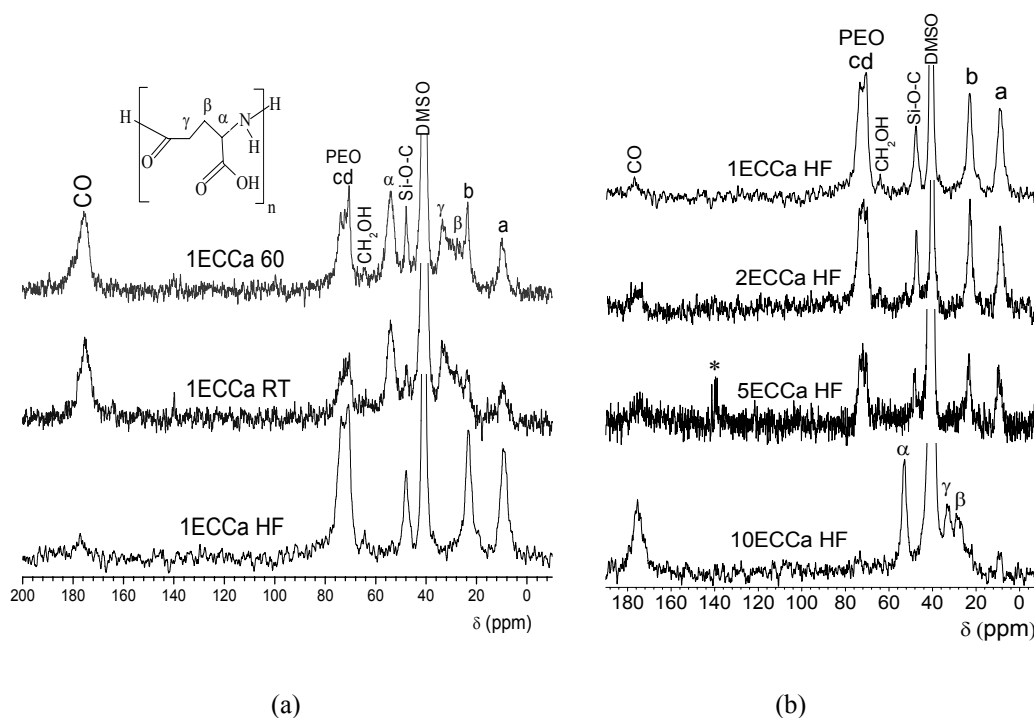


Figure 6.13. ^{13}C CP MAS NMR of silica-CaO-(γ -PGA) hybrids for $X_{\text{EC}}=1$ gelled with HF at room temperature and at 60 °C (a) and for different X_{EC} (1, 2, 5 and 10) gelled with HF (b). * denotes spinning sideband.

As can be observed the efficiency of CP is strongly reduced. This is probably due to high mobility as DMSO used in the synthesis is still present in the system (the peak around 40 ppm [303]) and the fact that samples having calcium adsorbed water. Also it is possible that a fast reorientation of the molecules could reduce the CP efficiency. However GPTMS is covalently coupled to the γ -PGA by the ring opening reaction of the epoxy ring (see Figure 3.15) as the signals corresponding to carbons in positions e and f are absent from the spectra. For samples made with HF, the peaks corresponding to carbons α , β and γ from PGA at 53.8, 26.5 and 33.1 ppm [303-306], respectively are very low in intensity suggesting that the polymer is either highly mobile or is incorporated in the matrix.

The peak corresponding to terminal diol (CH₂OH) at 64 ppm [285] is very low in intensity in comparison with hybrid samples containing gelatin. This can be due to the fact that the diol reacted with silanols to form Si-O-C bonds, with the corresponding resonance at 48 ppm, which is higher in comparison with hybrid samples containing gelatin. In the 70-75 ppm region beside the carbons c and d, the

PEO chains are present. The sharpness of the peaks suggests that these species are relatively mobile and short PEO chains are formed.

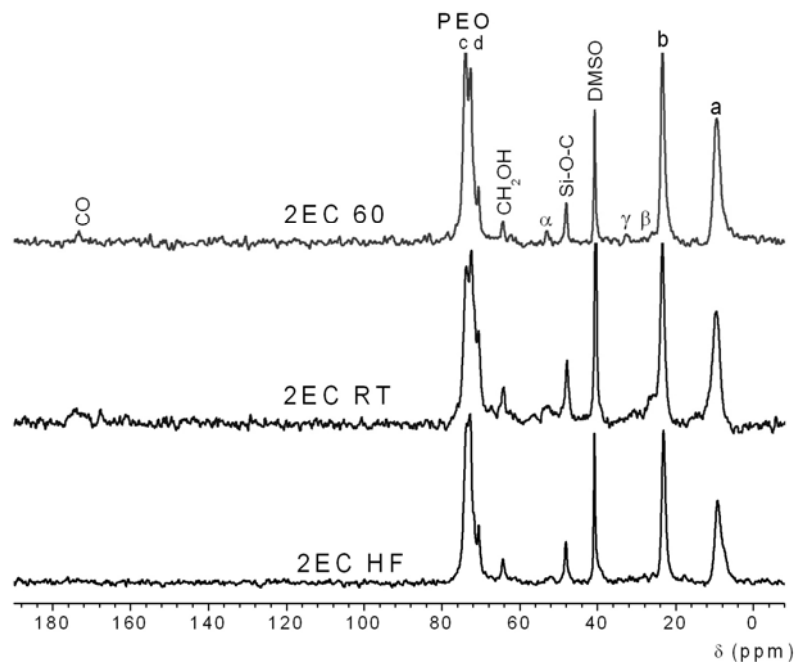


Figure 6.14. ^{13}C CP MAS NMR of silica-(γ -PGA) hybrids without calcium for $X_{\text{EC}}=2$ gelled with HF at room temperature and at 60 °C.

When calcium has not been used, the efficiency of CP is increased, as can be observed in Figure 6.14. DMSO is still present but in lower concentration. Also the peaks corresponding to polymer are very low in intensity as it is incorporated in the network. However when HF was used as catalyst, the PGA is almost completely incorporated, similar to the case with calcium. The peak closest to silicon atom in GPTMS (C_a) is found in different structural environments from one molecule to another and has a restricted mobility due to the rigidity of the inorganic network as is suggested by its broadening (Figure 6.13 a and b and Figure 6.14).

The ^1H MAS NMR spectra of silica-CaO-(γ -PGA) hybrids with X_{EC} from 1 to 10 gelled with HF and for calcium free samples for $X_{\text{EC}}=2$ gelled under different conditions are shown in Figure 6.15 a and b, respectively.

For silica- γ -PGA hybrids containing calcium (Figure 6.15 a) the spectra present mainly the resonances from DMSO and H_2O at 2.6 and 5-6 ppm [303], respectively.

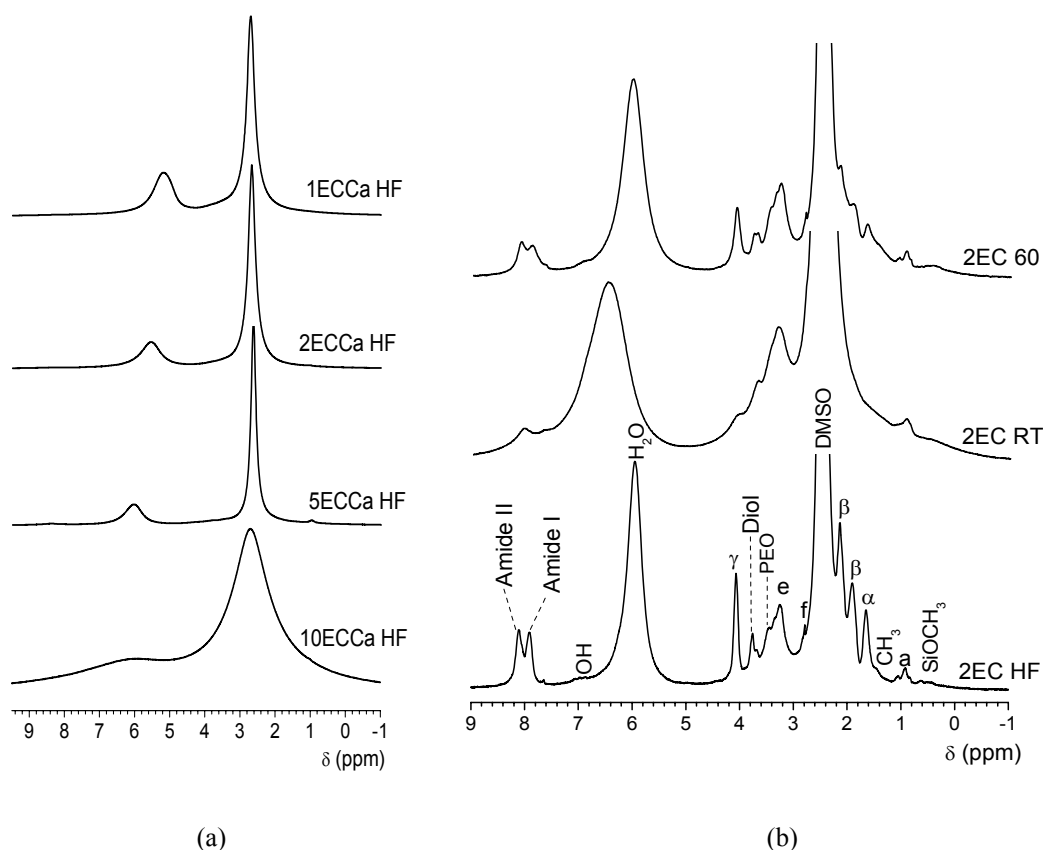


Figure 6.15. ^1H MAS NMR spectra of (a) hybrids for X_{EC} ranging from 1 to 10 using HF as catalyst and (b) hybrids made with HF, at room temperature and 60 °C without calcium for $X_{\text{EC}}=2$.

However for $X_{\text{EC}}=10$ (10EC Ca HF) the resonances are broader due to a higher concentration of γ -PGA in the system and consequently stronger dipolar couplings. This is in accordance with ^{13}C CP MAS NMR spectra where for this sample mainly the resonances from γ -PGA polymer were present. When calcium has not been used (Figure 6.15 b), due to a lower concentration of DMSO and water other resonances can be distinguished in the spectra. The two β - CH_2 inequivalent protons corresponding to γ -PGA give signals at 1.65 and 1.90 ppm, with γ - CH_2 and α -CH protons at 2.14 and 4.07 ppm, respectively [303, 304, 306, 307]. The two amide peaks corresponding to the protonated NH_3^+ and NH amide forms (Amide I and Amide II) appear at 7.90 and 8.11 ppm [303]. For samples synthesised with HF (2EC HF) these peaks are sharp, indicating a high degree of mobility. This could explain the lack of signal in ^{13}C CP MAS NMR spectra for these species. At room temperature and 60 °C, these peaks are broader, as the polymer probably has an increased rigidity due to the inorganic and organic network. The peaks corresponding

to GPTMS residues appear at 0.9, 2.78 and 3.25 ppm for hydrogens in positions a, f and e respectively [124] (see GPTMS structure in Figure 6.5). The presence of protons attached to carbons e and f in the epoxide ring shows that some epoxide rings remain intact but are probably highly mobile as the peaks are sharp and have not been detected by ^{13}C CP. Also the peak corresponding to $\text{Si}(\text{OCH}_3)$ in GPTMS appears as a very small and broad resonance at 0.5 ppm suggesting that almost all of the methoxide groups have been hydrolysed and condensed to give siloxane bonds. The protons bonded to carbons in PEO formed by the reaction of epoxies (Scheme 6.1, eq. 6.4.) and to diols (Scheme 6.1, eq. 6.4.) can be distinguished at 3.45 and 3.75 ppm, respectively [124, 290]. The DMSO solvent presents an intense and sharp peak at 2.5 ppm [303]. Water resonance depends on the water content in the sample. Hydrogen bonded SiOH appear at 7.00 ppm [222, 233] as a broad resonance. For samples gelled at RT (2EC RT) and 60 °C (2EC 60) the resonances are broader in comparison with sample gelled with HF (2EC HF), suggesting a restricted mobility and stronger dipolar coupling between protons. The residual methyls from TEOS appear at 1.4 ppm as a shoulder and is low in intensity suggesting that most of the alkoxide has been reacted.

A comparison between the ^{13}C CP MAS spectra of silica-(γ -PGA) hybrids and calcium-containing sample for $X_{\text{EC}}=2$ when different calcium sources have been used are shown in Figure 6.16 a, with an insert for the CO region for 2EC CaPGA aged sample.

The ^{13}C CP MAS NMR spectrum for the sample synthesised using the calcium salt of γ -PGA shows that the resonance corresponding to α -CH, β -CH₂ and γ -CH₂ of γ -PGA are broader and slightly shifted compared with the 2ECCa sample made with CaCl_2 . The change in α - and β -carbons signals at 54.7 and 28 ppm in the 2EC CaPGA aged sample compared with 53.5 and 26.5 ppm in the 2ECCa RT sample, respectively are most significant reflecting the proximity of these carbons to the ionisable carboxyl group. The carbons in the γ position are similar at 33.1 and 33.0 ppm for the two samples. These changes in chemical shifts for the α and β carbons can be attributed to an effect of ionisation of the carboxyl group due to an electrostatic effect exerted by calcium ions coordinated to it [304].

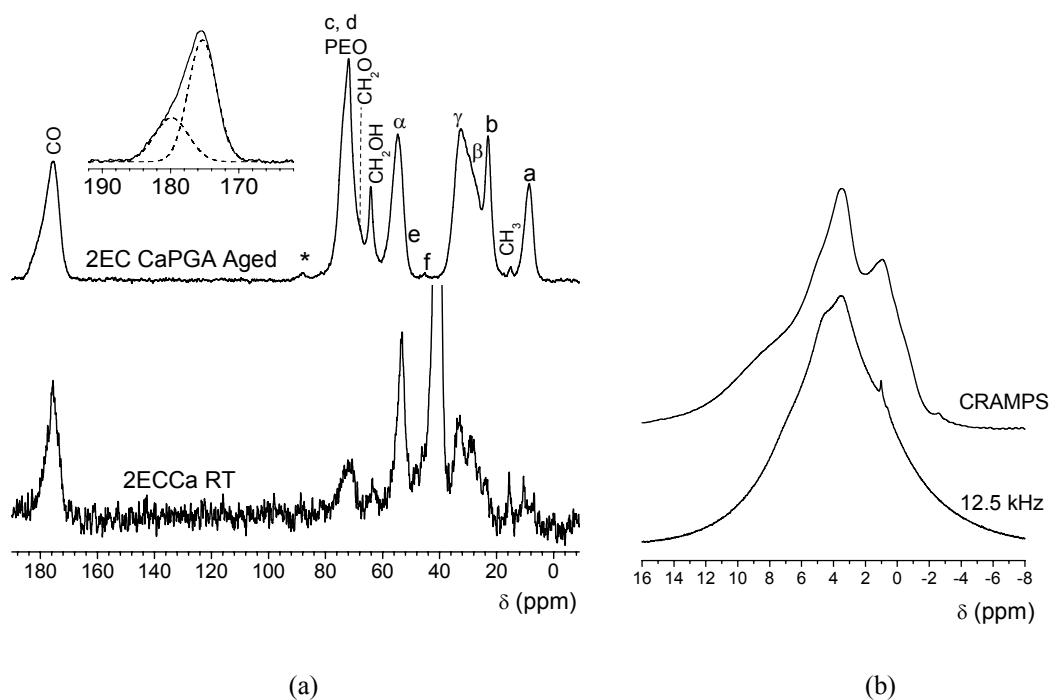


Figure 6.16. (a) A comparison between ^{13}C CP MAS NMR spectra for $X_{\text{EC}}=2$ when CaCl_2 (2ECCa RT) and calcium salt of γ -PGA (2EC CaPGA Aged) have been used and (b) ^1H MAS at 12.5 kHz and CRAMPS using windowed DUMBO-1 sequence spectra of 2EC CaPGA aged sample.

* denotes spinning sideband of CO resonance.

Also the resonances are broader for the 2EC CaPGA aged sample indicating that γ -PGA residues are bound to calcium ions in particular α and β resonances are closer to Ca^{2+} than γ . The broadening can indicate a constraint of the residues due to the inorganic and organic networks. The carbonyl and carboxyl resonances appear at 175.4 and 179.9 ppm respectively (insert in Figure 6.16 a), where the COO^- is broader compared with the CO resonance (linewidths of 5.7 and 4.8 ppm, respectively), suggesting that it is close to calcium. Short PEO chains are formed as is suggested by the sharpness of the resonance in the 70-75 ppm region. The presence of C_f is evident as a small contribution at 44 ppm, suggesting that PGA have opened the epoxide ring and a link between organic and inorganic networks has been created, but some of the epoxide rings remained intact.

The ^1H MAS NMR spectra at 12.5 kHz and CRAMPS using DUMBO as the decoupling sequence for the 2EC CaPGA aged sample (Figure 6.16 b) show the resonances corresponding to hydrogens in position a from GPTMS and to PEO chains at 0.9 and 3.43 ppm [124, 290], respectively. The spectra show an extended

organic network, with short polymer chains, as the main resonance corresponds to PEO hydrogens. The peak at 4.56 ppm as a broad resonance can have contributions from H₂O and α -CH protons [303, 304, 306]. The protons from amide groups appear around 8 ppm as a broad component, suggesting strong dipolar couplings, as well as possible exchange between free and bound carboxyl to calcium ions [304].

⁴³Ca NMR in natural abundance for X_{EC}=2 when CaCl₂ (2ECCa HF) and the Ca(γ -PGA) (2EC CaPGA aged) are used as calcium precursors, are presented in Figure 6.17.

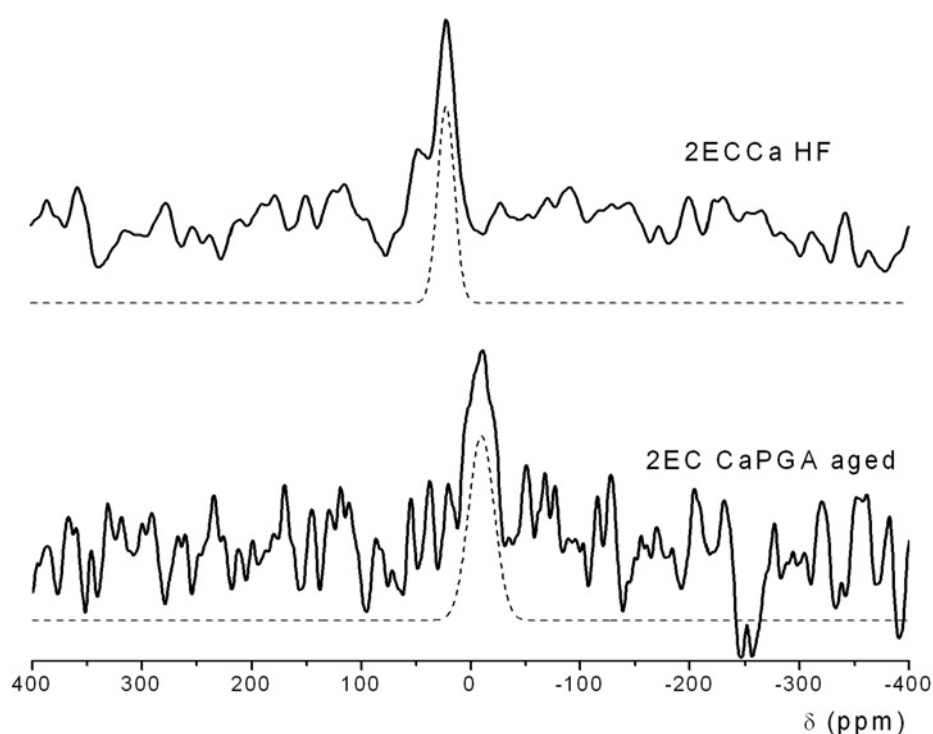


Figure 6.17. ⁴³Ca MAS NMR of silica-CaO-PGA hybrids when CaCl₂ and CaPGA have been used as calcium precursors. The dash lines represent the fit.

The signal of the aged sample is reduced compared with the sample made with HF. This is probably due to the fact that by aging, calcium has a greater dispersion in chemical shift and the signal is reduced. As can be observed the peak positions for the two samples are different, suggesting different environments for calcium. For sample synthesised from CaCl₂ using HF as catalyst (2ECCa HF) the peak position at 21.4 ppm (with a FWHM of 18 ppm) is between those of CaCl₂ and

CaF₂ at 53.1 and -17.2 ppm, respectively, as reported in literature [192]. This might suggest calcium environments between CaCl₂ and CaF₂ for this sample. When calcium poly(γ -glutamate) has been used as the calcium source (2EC CaPGA aged) the peak position at -9 ppm is closed to the calcium oxalate at -8.8 ppm [193]. This suggests that calcium ions are in close environments to oxalate and probably attached to COO⁻ in calcium poly(γ -glutamate) as was shown in Figure 3.16.

6.4. Conclusions

To test the hypothesis that GPTMS condensed into the silicate network linking the inorganic and organic networks, multinuclear ²⁹Si MAS NMR, ¹³C CP MAS NMR, ¹H MAS and CRAMPS and ⁴³Ca MAS NMR spectroscopy were employed in this chapter for two systems. Firstly, silica-gelatin compositions of 30 and 60 wt% gelatin with C factors (mole ratio of GPTMS/gelatin) of 0-2000 and 0-1500, respectively have been studied. From ²⁹Si NMR, for silica-gelatin class I hybrids (C factor 0), an increase in the silica network connectivity was observed on increasing the gelatin concentration, while ¹³C CP MAS NMR showed predominantly the residues from amino acids of gelatin. As the hybrid's molar ratio of GPTMS:gelatin increased, there was a notable increase in the T species in the ²⁹Si MAS NMR spectra, indicating an increase in inorganic-organic coupling. Increasing the C-factors up to 2000 and 1500 for 30G and 60G compositions, respectively, the predominant signals in ¹³C CP MAS NMR, as well as in ¹H MAS and CRAMPS NMR spectra were from short PEO chains and the diol formed, as well as from GPTMS molecules, as the gelatin has been incorporated. The ¹H DQ CRAMPS spectra suggest a bent conformation of PEO for both concentrations of gelatin. Inter- and intramolecular correlations between amino acid residues in gelatin have been detected, as well as between amino acids and the silicate network. ¹H and ¹³C NMR suggest higher mobility of the species for the 60G composition with a C factor of 1500.

Another system that has been studied was 40 wt% γ -PGA and 60 wt% bioactive silica (70 mol% SiO₂ and 30 mol% CaO) when two calcium salts, CaCl₂ and Ca(γ -PGA) have been used in the synthesis of the hybrids. ²⁹Si NMR indicates that the functionalised γ -PGA and the silica were successfully cross-linked to each other, and as the amount of GPTMS used in synthesis increased the proportions of Tⁿ

to Q^n increased as well, indicating higher degrees of cross-linking between the organic and inorganic phases in the hybrids. The presence of DMSO combined with the higher mobility of the species when CaCl_2 was involved, leads to a reduced efficiency of ^{13}C CP in these samples. The spectra indicate that efficient promotion of epoxide ring opening of GPTMS was reached by functionalised γ -PGA when both calcium salts were used. When HF was used, high mobility has been detected in both ^{13}C CP and ^1H MAS NMR spectra. For both calcium salts as calcium precursor, short and relatively mobile PEO is formed in the system. ^{43}Ca NMR suggests different environments for the hybrids when CaCl_2 and $\text{Ca}(\gamma\text{-PGA})$ have been used as calcium sources. The results from ^{13}C CP, ^1H and ^{43}Ca MAS NMR suggest that calcium ions are coordinated to carboxyl when calcium poly(γ -glutamate) has been used. The multinuclear solid state NMR showed that GPTMS was successful in providing a covalent link from the organic phase, either gelatin or poly(γ -glutamic) acid, to the inorganic silicate network, which is essential to the hybrid design.

7.

INHIBITIVE EFFECT OF SERUM PROTEINS IN THE MECHANISM OF APATITE GROWTH ON BIOACTIVE GLASSES

7.1. Introduction

The first bioactive glass concerning the melt-quench quaternary system SiO_2 , CaO , Na_2O and P_2O_5 , *Bioglass*[®] 45S5, reported by Hench *et al.* [7] opened the field of research of bioactive materials. Since its discovery diverse studies have been performed in order to understand the formation of the hydroxyl carbonate apatite (HCA) layer [11, 13, 30, 43]. The HCA layer deposition mechanism has been described in Chapter 1. Compared to melt-quench compositions, where the glasses are bioactive only for silica contents below 60% [31], sol-gel derived glasses showed bioactivity for silica contents up to 90% [39-41]. To study the bioactivity of materials, Kokubo *et al.* [15] proposed the simulated body fluid (SBF), an aqueous acellular solution that simulates the concentration of inorganic ions and pH of human plasma [207]. Bovine and human serum have also been used for the *in-vitro* studies of the protein adsorption on biomaterials [13, 308-311]. It was found that the presence of proteins from serum inhibit the HCA layer deposition on *Bioglass*[®] [13, 310, 311].

Solid state NMR studies of the structures of the synthetic apatites [191, 198-200, 252, 259-261, 270, 277, 312, 313], calcified tissues [314-321] and the mechanism of apatite layer deposition on bioactive glasses from both melt-quench [322-325] and sol-gel [210, 251] derived glasses have been reported in the literature. ^{29}Si [322-325] and ^{31}P [210, 251, 322-325] have been extensively used and two-dimensional (2D) heteronuclear correlation (HETCOR) studies have been employed in the study of spatial connectivities of the bioactive glass interfaces [251]. Improvements in resolution have been obtained for quadrupolar nuclei by using advanced techniques like MQ MAS (multiple-quantum magic angle spinning) [161,

162]. ^{23}Na MQ MAS have been recently reported for *Bioglass*[®] [326, 327] and other melt-quench bioactive glasses containing Na_2O in the composition [280, 328, 329].

In this work a comparative study to follow the mechanism of apatite nucleation using a multinuclear solid state NMR approach on both melt-quench bioactive *Bioglass*[®] (BG) and sol-gel derived 70S30C (*TheraGlass*[®], TG) compositions immersed for different period of time using two bioactive media, pure SBF (pSBF) and SBF complemented with 10% foetal bovine serum (sSBF) has been performed.

7.2. Experiment details

The protocols followed for the bioactivity tests on both *TheraGlass*[®] and *Bioglass*[®] have been described on Chapter 3. The ^1H , ^{31}P and ^{13}C CP MAS NMR spectra were recorded using the same parameters as in Chapter 5. ^{29}Si MAS NMR spectra of the bioactive glasses were performed using a Varian InfinityPlus 300 spectrometer (7.05 T) operating at 59.62 MHz, using a Varian 7.5 mm probe spinning at 4 kHz. A 3 μs pulse ($\sim 30^\circ$) was applied with a 60 s recycle delay. ^{29}Si NMR spectra were referenced to TMS at 0 ppm. The two-dimensional ^1H - ^{31}P and ^1H - ^{29}Si HETCOR experiments have been recorded on a Bruker Avance II⁺ 600 spectrometer. Ammonium dihydrogen phosphate and kaolinite, respectively, have been used as external references at 0.9 and -92 ppm. For ^1H - ^{31}P HETCOR experiments a contact time of 1 ms, recycle delay of 3 s and 160 scans have been used for each of the 128 t_1 slices. For ^1H - ^{29}Si HETCOR experiments a contact time of 5 ms and recycle delay of 3 s were used. The number of scans and t_1 slices differ for the 2 samples, 688 and 1376 scans have been used for each of the 84 and 44 t_1 slices for pSBF 7d TG and sSBF 7d TG samples, respectively. One-dimensional ^{23}Na MAS NMR spectra have been performed on a Bruker Avance II⁺ 600 spectrometer operating at 158.7 MHz with a Bruker MAS probe spinning at 10 kHz. A 0.5 μs pulse length with a 1 s recycle delay have been used. The ^{23}Na triple-quantum MAS spectra have been recorded using the pulse sequence and parameters as were described in *section 3.3.5.3*. A recycle delay of 1 s was used and 360 acquisitions were co-added for each of the 128 t_1 slices. The f_1 and f_2 spectral widths were 100 kHz. One-dimensional spectra have been recorded for the sample at spinning speed of

20 kHz before to perform the MQMAS experiment. Solid NaCl has been used as reference with a chemical shift of 7.2 ppm.

7.3. Results and discussion

The ^1H MAS NMR spectra of melt-quench *Bioglass*[®] (BG) and sol-gel *Theraglass*[®] (TG) derived glasses, as synthesised and immersed in pSBF and sSBF for 2h, 1d and 7d, are shown in Figure 7.1 a and b, respectively.

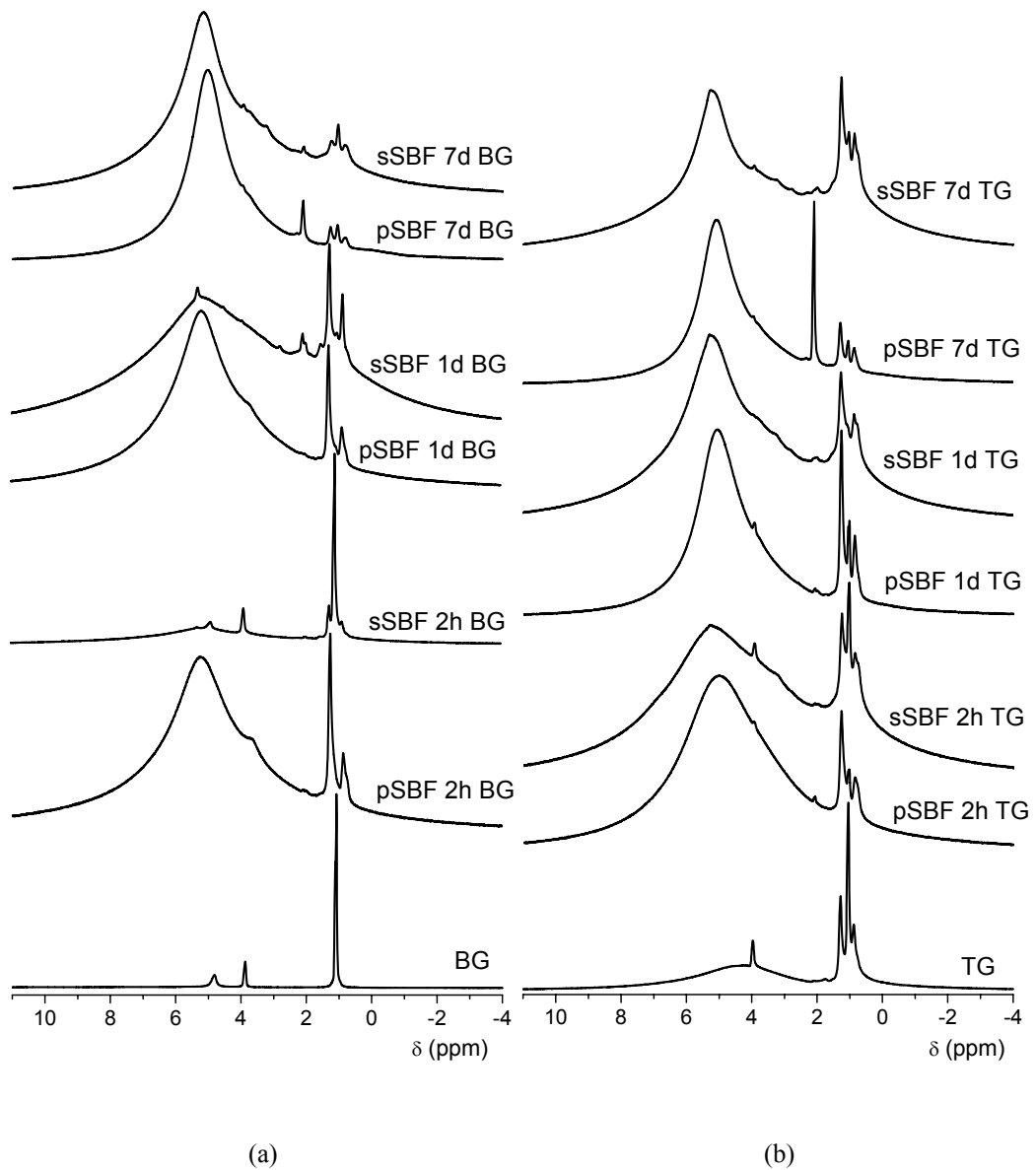


Figure 7.1. ^1H MAS NMR spectra of BG (a) and TG (b) glasses, as synthesised and immersed in pSBF and sSBF for 2h, 1d and 7d, respectively.

For both BG and TG as synthesised samples, the tall sharp peak at 1.1 ppm is due to isolated free hydroxyls coordinated to calcium cations formed from water adsorption on silica surface [216]. The BG sample has also Na^+ ions in the composition, but the free hydroxyls are preferentially coordinated to the calcium, as sodium has lower strength field compared to calcium [216]. However for BG sample which it has the highest contribution, as the formation of free hydroxyls is also favoured by more depolymerised networks (this will be further supported from ^{29}Si measurements) [216]. For the TG sample the peak at 4.1 ppm is due to fluid water as inclusions [231, 249] while the broader component around 5 ppm in both samples (TG and BG) is from physisorbed water. The higher contribution of the last peak in the TG sample is due to the inherent porosity of the sol-gel glasses compared to melt-quenched ones [42, 43]. The TG sample shows two other peaks at 1.3 and 0.8 ppm from alkoxide residues used in the sol-gel synthesis and a small broad peak at 2.1 ppm due to isolated silanols. The absence of isolated silanols in the BG sample can be due to the bulk properties of this sample when OH can be closer to oxygens atoms and form hydrogen-bonded silanols, with the corresponding peak at 3.8 ppm. When the two glasses are immersed in the two bioactive media, pSBF and sSBF, the ^1H NMR spectra present visible changes. Firstly, with increasing immersion time from 2 h to 7 days for both pSBF and sSBF, the appearance of the peak at 1.8 ppm due to isolated SiOH is visible with increasing intensity as the soaking time increases and becomes the most intense contribution for the pSBF 7 d samples. For 2 h immersion time, sSBF sample compared with the pSBF ones present similar behaviour to the as synthesised samples, the only difference is the increased intensity of the peaks at 1.3 and 0.8 ppm due to residues from organics present in the serum. Also the peak at 1.1 ppm becomes smaller in intensity with increasing soaking time, as the polymerisation of the network increases and for the BG sample soaked in pSBF the broad components at 1.3 and 0.9 ppm can be due to the OH coordinated to calcium involved in hydrogen bonding with water molecules present from the SBF or with SiO^- groups, when the resonance corresponding to isolated OH disappears or becomes broader. However for 7 days of soaking for BG sample in both mediums the peaks from OH coordinated to calcium, isolated or hydrogen-bonded, decreased visible in intensity. Also a peak around 0 ppm, as a very broad shoulder, appears for both BG and TG soaked in pSBF for 7 days, due to the structural OH of the apatite.

For both glasses, in pSBF rather mobile species are present compared with sSBF where now the peaks are broader and the mobility is constrained due to steric hindrances and stronger dipolar couplings due to proteins from the serum. Also in sSBF the peaks at 3.2 ppm are due to hydrogen-bonded SiOH, with either water molecules or organics, and this resonance is visible just in BG samples immersed in pSBF. However, the peak from isolated SiOH become smaller in serum, as some of them become hydrogen bonded with the appearance of the corresponding peak at 3.2 ppm. As SiOH are sites which encourage apatite growth, a higher concentration of hydrogen bonded-silanols in serum could influence the apatite formation.

To further confirm the protein adsorption on the glass surfaces, ^{13}C CP MAS NMR have been performed on both TG and BG glasses (Figure 7.2).

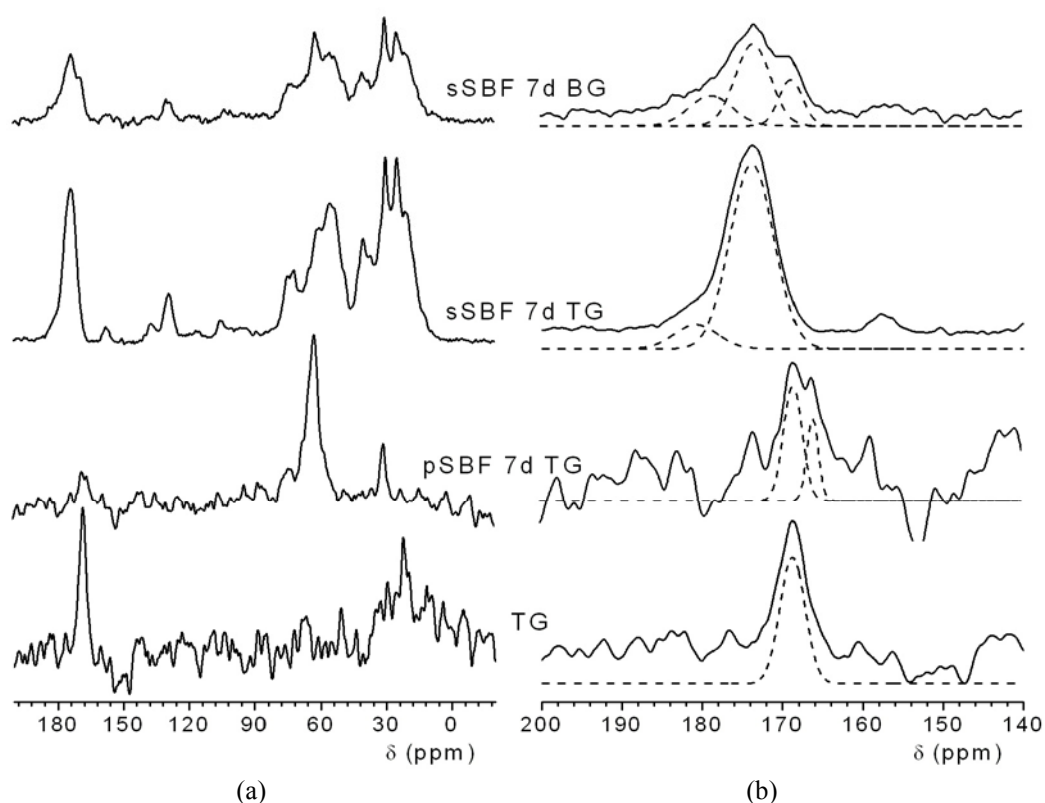


Figure 7.2. ^{13}C CP MAS NMR spectra of TG and BG glasses (a), with the carbonate and organic carbonyl region (b) fitted (dash lines).

For as-synthesised TG sample, the presence of residual organics from TEOS precursor can be detected around 22 ppm. The peak at 168.8 ppm with a linewidth of

3.6 ppm is due to calcite [257, 258] formed from CO₂ adsorption on the glass surface. For the TG sample immersed in pSBF for 7 days (pSBF 7d TG), the ¹³C CP MAS NMR spectrum shows peaks around 30 and 60 ppm corresponding to CH₃ and CH₂O respectively from alkoxide. Also a small contribution from carbonates can be detected in the 160-170 ppm region. Beside the calcite, the peak at 168.5 ppm can be attributed to the formation of type B substituted apatite [260, 313], as it is still present even after 7 days of soaking the sample in pSBF. The peak at 166.0 ppm as a small resonance having a linewidth of 1.7 ppm can be attributed to type A substituted apatite [259, 260]. Thus an AB-type substituted apatite was observed on the TG sample immersed for 7 days in pSBF.

For both TG and BG samples immersed in sSBF for 7 days, the adsorption of proteins on the surface can be observed, where for the sSBF 7d TG, the intensity of the peaks is higher than for the sSBF 7d BG sample, as more proteins are adsorbed due to porosity of sol-gel derived glasses. In the 0-75 ppm region, the aliphatic organic fraction of amino acid residues of proteins from serum is present, with the following chemical shifts (ppm) [296-301]: 20.2 (Leu δ , Val γ,γ' , Thr γ), 25.0 (Pro γ , Glu β , Leu δ), 30.3 (Pro β , Arg β , Lys β), 37.9 (Hyp β , Asp β , Lys ϵ , Leu β , Phe β , Ile β), 42.9 (Gly α , Arg δ), 48.3 (Pro δ), 55.6 (Ala α), 62.4 (Ser β , Val α , Thr α , Ile α), 67.9 (Thr β), 71.2 (Hyp γ). The peak at 128.9 ppm corresponds to aromatic Phe δ,ϵ , while the peak at 158.0 ppm to Arg ϵ . The strong signal in the region around 170 ppm (Figure 7.2 b) derives from the superposition of the organic amino acidic carbonyl and the inorganic carbonate components. This region has been fitted for the two samples using the DMFIT software [224]. For the sSBF 7d TG sample, one component at 173.8 ppm (FWHM = 6.4 ppm) with a shoulder at 180.8 ppm (FWHM = 6.4 ppm) having a ratio of 7:1 can be attributed to organic carboxyl of proteins from serum, free and bound to calcium ions, respectively. The peaks can also have a contribution from the organic carbonyl (CO) of proteins from serum. The presence of organic carboxyl and carbonyl as a broad component prevents a clear observation of the carbonate peaks from substituted apatite. Similar results have been obtained for archaeological bone and tooth samples after acetic acid treatment [330] when carbonate and bicarbonate ions deposited in bones as carbonate (CO₃²⁻) salts, such as calcite, have been eliminated. The authors attributed the peak at 174 ppm to both organic carboxyl and structural CO₃²⁻ of substituted apatite. For the sSBF 7d BG

sample, the two peaks at 173.5 and 178.8 ppm with a FWHM of 5.2 and 6.4 ppm, respectively, have a ratio of 2:1, suggesting that more organic carboxyls are bound to calcium ions, compared with the TG sample (Figure 7.2 b). This can be due to the fact that a smaller amount of proteins are adsorbed on BG sample. For BG glass the carboxyl anions can be bound to Na⁺ ions as well. Also the presence of a third peak at 168.8 ppm (FWHM = 3.5 ppm) is from structural carbonate, as the sample has been immersed 7 days in sSBF and can be attributed to carbonate substituted apatite, type B [260]. The ratio between the three peaks is 1:2:1. A very small resonance at 166.0 ppm ascribed to A-type CO₃²⁻ substituted apatite [259, 260] which cannot be detected above the noise in the present spectra, can indicate a possible very small A-type substitution present. No evidence of Na₂CO₃ has been detected at 170 ppm [331]

Therefore for the BG sample an AB-type substituted apatite is obtained in sSBF after 7 days of immersion while for TG sample the carbonate substitution has not been detected because of the organic carboxyl. Higher linewidths for the TG sample might suggest steric restrictions as more proteins have been observed to be adsorbed, reducing the organic carboxyl mobility.

To have further insight into the apatite nucleation on both bioactive media, ³¹P MAS NMR has been recorded on both *Bioglass*[®] (Figure 7.3 a) and *TheraGlass*[®] (Figure 7.3 b) immersed for different times.

Table 7.1. ³¹P MAS NMR data for measured samples, giving the spectral deconvolution into different species.

Sample	δ (ppm)	FWHM (ppm)	I (%)	δ (ppm)	FWHM (ppm)	I (%)	δ (ppm)	FWHM (ppm)	I (%)
BG	-	-	-	-	-	-	8.1	7.1	100
pSBF 2h BG	3.6	5.9	92	-	-	-	9.7	5.6	8
pSBF 2h TG	3.2	5.5	100	-	-	-	-	-	-
sSBF 2h BG	3.7	6.1	88	-	-	-	9.5	5.7	12
sSBF 2h TG	3.3	5.5	100	-	-	-	-	-	-
pSBF 1d BG	3.2	4.9	96	6.6	2.3	4	-	-	-
pSBF 1d TG	3.0	3.0	88	6.0	2.8	12	-	-	-
sSBF 1d BG	3.4	6.1	100	-	-	-	-	-	-
sSBF 1d TG	3.2	5.8	100	-	-	-	-	-	-
pSBF 7d BG	3.0	3.0	85	5.9	3.0	15	-	-	-
pSBF 7d TG	3.0	2.7	87	5.8	2.9	13	-	-	-
sSBF 7d BG	3.2	4.0	91	6.3	3.2	9	-	-	-
sSBF 7d TG	3.2	4.8	100	-	-	-	-	-	-

FWHM, δ and I represent the linewidth full-width half-maximum, ³¹P chemical shift and relative intensity, respectively. Errors associated with measurements are — FWHM ± 1 ppm, δ ± 1 ppm and Integral ±2%.

The deconvolution of the spectra using DMFIT software [224] is presented in Table 7.1.

The ^{31}P MAS NMR spectrum of the *Bioglass*[®] sample (BG) consists of one broad resonance (FWHM = 7.1 ppm) positioned at 8.1 ppm (Figure 7.2 a, Table 7.1) assigned to the phosphorus in an orthophosphate environment [332-334]. The recorded chemical shift is between that of crystalline Na_3PO_4 at 15.6 ppm [274] and that of $\text{Ca}_3(\text{PO}_4)_2$ at 0 [274] and 3 ppm [109, 335]. Therefore phosphorous exists as isolated orthophosphate environments in the BG glass with a combination of Na^+ and Ca^{2+} as balancing cations, removing them from their network modifying role in the silicate network [332, 281, 282].

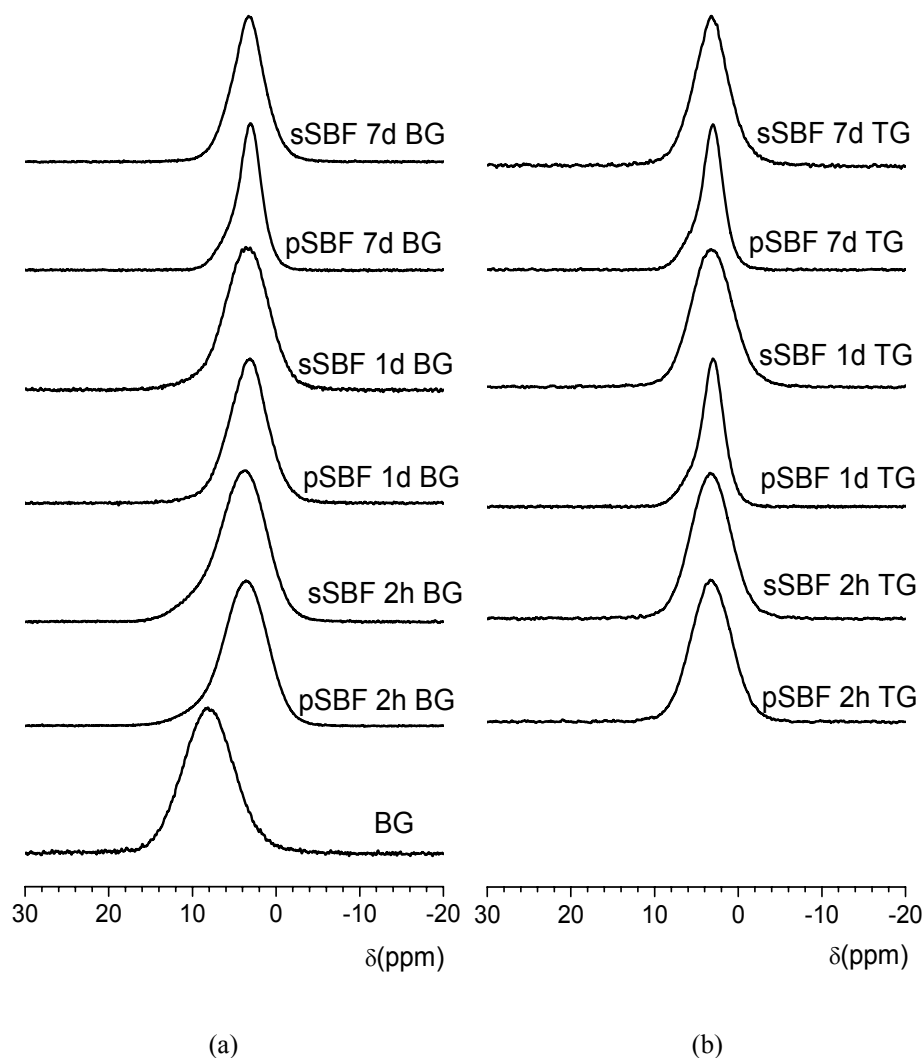


Figure 7.3. ^{31}P MAS NMR spectra of BG (a) and TG (b) for different soaking times in SBF. The spectrum of as-synthesised BG sample is presented (a).

When both BG and TG glasses are immersed in pSBF and sSBF for 2 h, the broad peaks around 3.5 ppm and 3.2 ppm for the two glasses are due to orthophosphate environments balanced by calcium cations. For the BG sample, in both pSBF and sSBF another resonance around 10 ppm, closer to Na_3PO_4 than $\text{Ca}_3(\text{PO}_4)_3$, with a linewidth of 5.6 ppm, is probably PO_4^{3-} closely associated with Na^+ cations with fewer Ca^{2+} cations, compared to the as-synthesized BG sample (Figure 7.3, Table 7.1). As the linewidths suggest, the deposited PO_4^{3-} from the SBF, is disordered and largely amorphous. Similar linewidths have been reported for amorphous calcium phosphate [336].

In pure HAp, HAp that contain ~12% HPO_4^{2-} and HAp with poor crystallinity, the recorded chemical shifts are 2.8, 3.0 and 3.3 ppm [270, 273, 277] with linewidths of 0.5-1 ppm [277]. The recorded ^{31}P chemical shifts for type B HCA (with 3.2-14.5% CO_3^{2-} substituting PO_4^{3-}) were between 2.8-3.0 ppm with linewidths of ~5 ppm, when a small amount of CO_3^{2-} replaces PO_4^{3-} in HAp lattice. The CO_3^{2-} substitution in type A HCA leads to the formation of different chemical environments for the PO_4^{3-} ions with chemical shifts of 5.5, 4.6, 3.8 and 2.5 ppm, and results in a line broadening to ~4 ppm [277]. Therefore the line broadening increases in the order: pure HAp, HAp containing ~12% HPO_4^{2-} , poorly crystallised HAp, type A HCA and type B HCA (3.2-14.5% CO_3^{2-}).

For both samples immersed in sSBF, the linewidths are larger compared with pSBF, suggesting that serum has an inhibiting effect and more disordered calcium phosphate is deposited. Also for TG samples, in both bioactive media the PO_4^{3-} deposited after 2 h has slightly increased ordering compared with the BG sample (Figure 7.2, Table 7.1) as their linewidths suggested.

Increasing the soaking time to 7 days, the linewidth of the 3 ppm resonance decreases for both samples, in pSBF and sSBF (Figure 7.3, Table 7.1), suggesting that a more ordered phosphorus environment are present. A variation of the linewidth with soaking time for BG and TG samples in both bioactive media is shown in Figure 7.4.

The spectra of BG and TG immersed for 1 and 7 days in serum-free medium (pSBF) showed an additional resonance around 6 ppm. As ^{13}C CP MAS NMR spectra of pSBF 7d TG sample (Figure 7.2 b) reveal the presence of CO_3^{2-} in a type

A substituted apatite, this resonance might arise from orthophosphate environments close to carbonate ions.

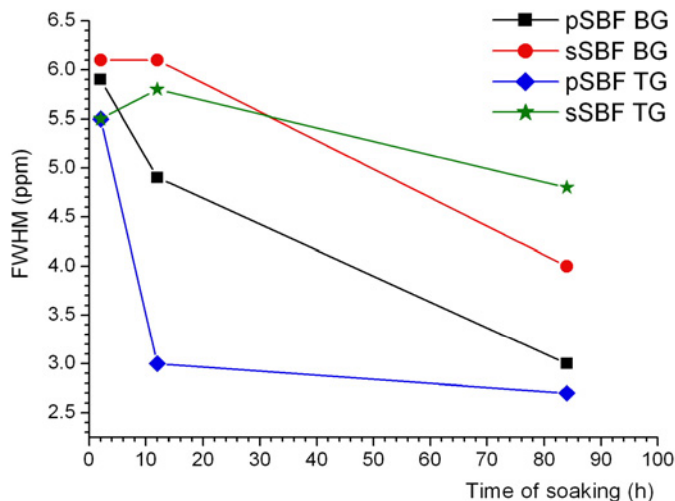


Figure 7.4. The variation of linewidths (ppm) of the 3 ppm resonance with soaking time (h) in pSBF and sSBF for BG and TG samples.

For 1 day immersion this resonance has a higher contribution for the TG sample (12%) compared with the BG sample (4%), while for 7 days of immersion the concentration on both samples is similar. This resonance may also have a contribution from orthophosphate environments balanced by Ca^{2+} with a small contribution from Na^+ charge balanced site. The presence of sodium ions in TG samples arises from SBF. The ^{31}P resonance at 6 ppm is not visible in the ^{31}P MAS NMR spectra of 1 day and 7 days of immersion in sSBF for TG and BG, except for the sSBF 7d BG sample. These phosphates are either absent or are not visible due to the broadness of the peak at 3 ppm.

To study the phosphate and hydrogen site proximities, ^1H - ^{31}P HETCOR has been performed on TG sample immersed for 7 days in pSBF and sSBF (Figure 7.5 a and b, respectively).

In the two-dimensional ^1H - ^{31}P HETCOR spectrum recorded on the pSBF 7d TG sample (Figure 7.5 a), the correlation between the ^1H signal at ~ 0 ppm and the ^{31}P signal at ~ 3 ppm is characteristic of an apatite structure [251, 312, 318, 320].

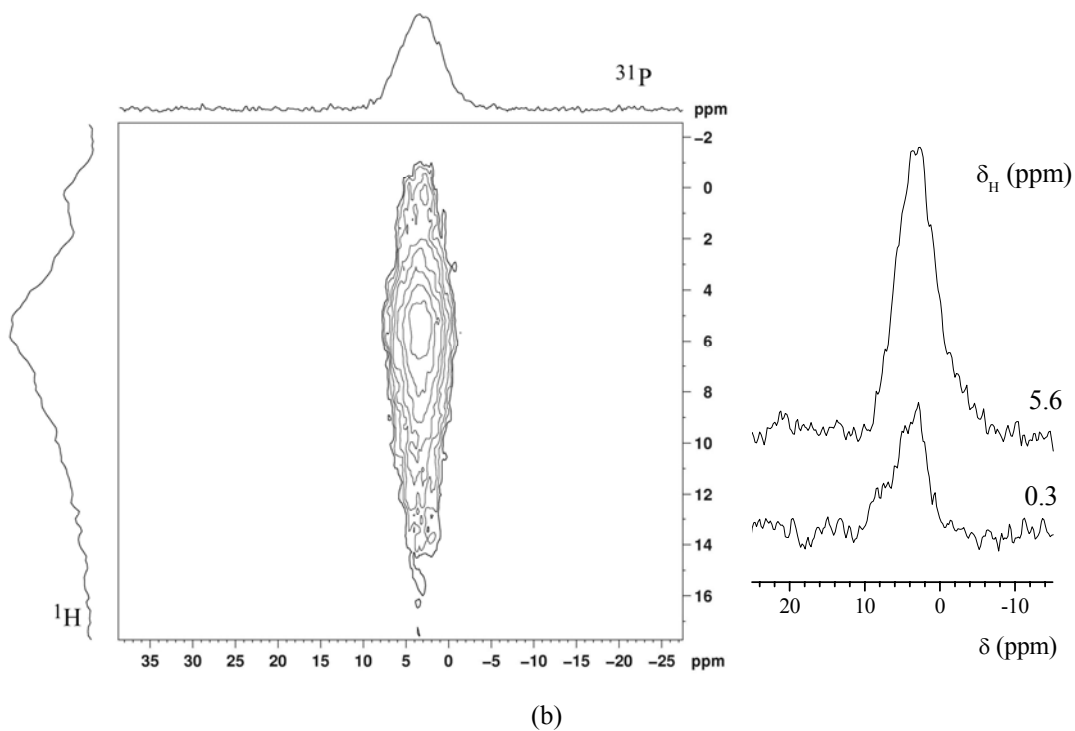
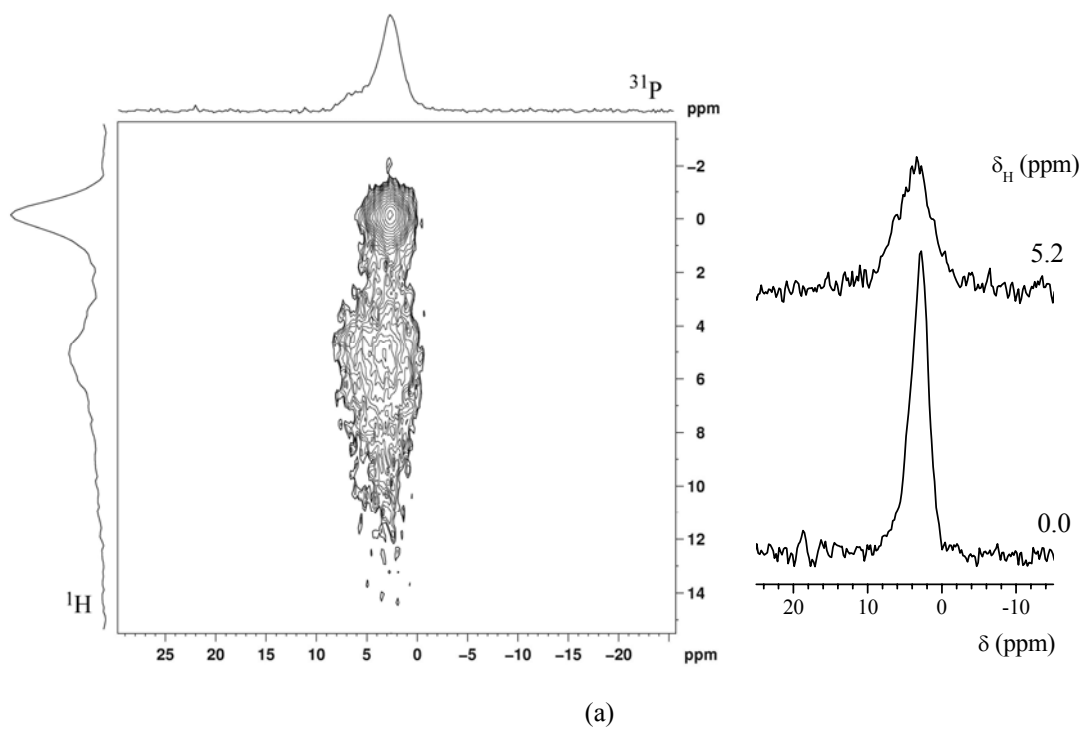


Figure 7.5. ^1H - ^{31}P HETCOR of pSBF 7d TG (a) and sSBF 7d TG (b) samples. On the right, the horizontal slices correspond to ^{31}P NMR spectra extracted from hydrogen sites at 0 and 5 ppm, represented by δ_{H} .

Hence the decreasing linewidths for the peak at ~3 ppm in ^{31}P MAS NMR spectra of samples immersed in pSBF (Figures 7.3 and 7.4, Table 7.1) suggest that the apatite nucleation takes place from amorphous calcium phosphate and becomes more ordered with longer soaking time for both TG and BG samples. The ^{31}P signal at ~ 3 ppm is also correlated with a ^1H signal around 5 ppm from structural and surface water. The ^{31}P component correlated with structural and physisorbed water (slice extracted from HETCOR spectrum corresponding to the ^1H dimension at 5.2 ppm) has a linewidth of 5.4 ppm and the phosphates appear to be more disordered.

These phosphates can originate from amorphous calcium phosphates and phosphate ions hydrogen-bonded to water molecules via molecular motion and/or chemical exchange when HPO_4^{2-} forms:



In the ^1H projection of the HETCOR spectra the highest contribution is at 0 ppm from structural OH of HAp, suggesting that phosphates correlated with water molecules have a lower concentration. This is supported also from the ^{31}P slices extracted for the two hydrogen sites.

Similar correlations have been observed for a 30% SiO_2 -70% CaO composition synthesised by a sol-gel method and immersed in SBF [251] and in animal bones [312, 318, 320] in ^1H - ^{31}P HETCOR spectra.

The ^{31}P peak at ~ 6 ppm is correlated mainly with water at 5 ppm and just a low amount with structural hydroxyl groups at 0.0 ppm, as can be observed in the HETCOR spectrum and from the ^{31}P signal from the horizontal slice extracted from the ^1H dimension at 0.0 ppm, where a shoulder around 6 ppm is visible. This suggests that a small amount of carbonates are in the bulk and the rest are located near the surface. The linewidth of the 2.4 ppm of the peak at 3 ppm supports this hypothesis suggesting that apatite nuclei formed on the glass surface are similar to crystalline HAp.

The ^1H - ^{31}P HETCOR spectrum of the TG sample immersed for 7 days in sSBF (Figure 7.5 b) shows the formation of the apatite, but in lower concentration and is more disordered in comparison with the sample immersed in pSBF. This suggests that serum has an inhibitive effect on the nucleation and growth of apatite

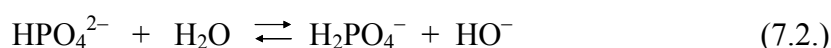
even after 7 days. The proteins have been adsorbed on the surface of the glass, as ^1H MAS and ^{13}C CP MAS NMR spectra suggested (Figures 7.1 and 7.2) and they can form a proteinaceous layer which covers the surface silica layer or the deposited phosphates. The adsorbed protein layer may have reduced further exchange of ions which will retard the formation of HAp, as was suggested by our ^1H - ^{31}P HETCOR spectrum. This would explain also the broader features for ^{31}P MAS NMR spectra (Figure 7.3) observed in serum-containing medium (sSBF) compared with serum-free medium (pSBF) for both BG and TG samples. As ^{13}C CP MAS NMR spectra have shown (Figure 7.2), more proteins have been adsorbed on the TG surface than on BG, suggesting that the formation of the HAp layer could be even more delayed on TG. This accompanies the results from ^{31}P MAS NMR spectra (Figures 7.3 and 7.4) where the peak at 3 ppm is broader for the TG sample (sSBF 7d TG) and the spectrum of BG sample (sSBF 7d BG) presents the contribution at 6 ppm, even if in low concentration (Table 7.1). Also some of the calcium ions have been involved in the reactions with organic carboxyl groups from proteins (Figure 7.2 b) and would decrease the concentration of calcium available for the formation of the phosphate layer and its subsequent nucleation in the HAp. These findings are in agreement with previous studies of the effect of serum proteins when the formation of HAp on bioactive glasses has been delayed [13, 310, 311] due to the inhibitive effects from serum.

The proton cross-section could give more information on the structural hydroxyl groups in the apatite structure. The ^1H peak is shifted to 0.3 ppm from 0.0 ppm (as in pSBF 7d TG), as probably the structural hydroxyls in serum are involved weak hydrogen bonding interactions modulated by molecular motion and/or chemical exchange. This leads to a structural disorder resulting in a line broadening to 3.2 ppm in serum containing-medium (sSBF 7d TG sample) from 1.3 ppm in the serum-free medium (pSBF 7d TG sample). A shift to 0.5 ppm from HCA was found in the bone structure for the structural hydroxyl groups in a ^1H - ^{31}P HETCOR spectrum [320].

The ^{31}P signal correlated with the ^1H signal at 0.3 ppm shows the presence of phosphates at 6 ppm (a shoulder in the horizontal projection extracted from ^1H at 0.3 ppm) from type-A carbonate apatite. The apatite component has a linewidth of 4.5 ppm, more disordered than in pSBF. In MAS NMR spectrum of this sample (Figure

7.3 b) it was difficult to distinguish different phosphorus sites because of overlapp of the peaks and the spectrum was fitted well with just one contribution.

The main correlation in the ^1H - ^{31}P HETCOR spectrum of the sSBF 7d TG sample is between orthophosphate ions at 3.2 ppm and water molecules at 5.6 ppm. The ^{31}P resonance at 3.2 ppm in sSBF 7d TG sample is broader than that of pSBF 7d TG sample, suggesting that the orthophosphate ions, PO_4^{3-} and/or HPO_4^{2-} ions deposited on the surface are more disordered. Possible interactions between proteins and phosphate ions can also take place. From the ^{31}P projection, a shoulder around -2.5 ppm can be distinguished, probably from HPO_4^{2-} in interaction with water molecules:

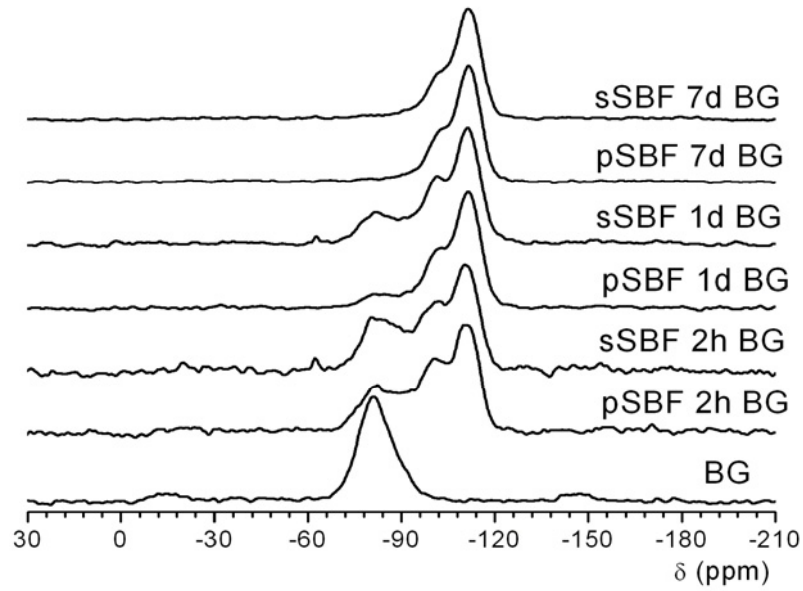


It was shown that at a pH of 7.4, an equilibrium between phosphate ions HPO_4^{2-} and H_2PO_4^- present in the system in these conditions [337] takes place. As SBF has a pH of 7.2, indicates that similar types of orthophosphate ions, $\text{H}_x\text{PO}_4^{(3-x)-}$ are adsorbed on the surface. These species are on the surface of apatite nuclei, as in HPO_4^{2-} substituted HAp the chemical shift of HPO_4^{2-} ions undergoing molecular motion is the same as the PO_4^{3-} ions [270, 273, 277] and discrete, rigid HPO_4^{2-} species have been not found [270]. These findings are in agreement with the results obtained by Vallet-Regi *et al.* [39, 338]. They found on the apatite surface a high proportion of HPO_4^{2-} ions where the Ca/P ratio is 1.2 while in the apatite core the Ca/P ratio was 1.6.

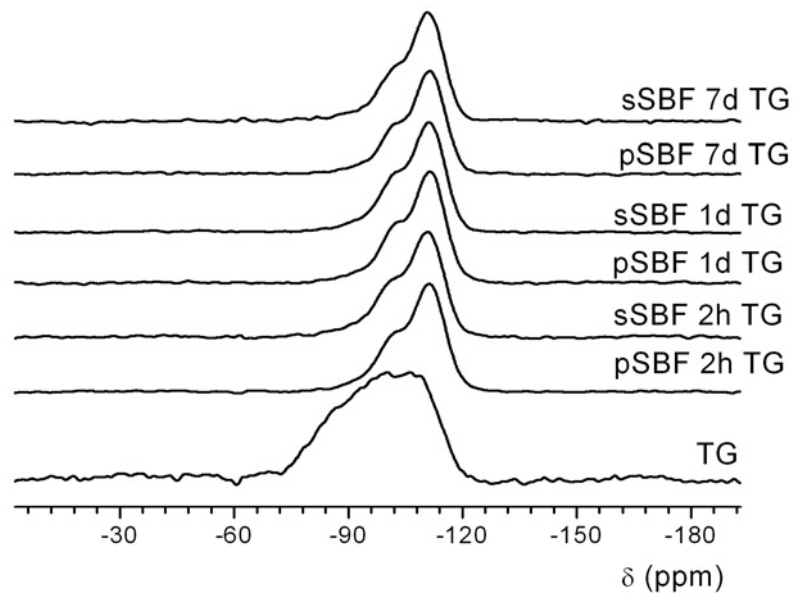
Figure 7.6 shows the ^{29}Si MAS NMR spectra of TG and BG bioactive glasses, as-synthesised and immersed in pSBF and sSBF, respectively, for 2 h, 1 d and 7 d using single-pulse excitation. Simulations were carried out using DMFIT software [224] with Gaussian contributions corresponding to Q^n species and are summarised in Table 7.2.

For TG sample calcium ions act as network modifiers and a less connected silica network is obtained [1], as was described in Chapter 4. The two peaks in the ^{29}Si MAS NMR spectrum of BG sample at -80.9 and -90.7 ppm are assigned to Q^2 and Q^3 units, respectively [332, 333]. The silicate network consists mostly of Q^2 species (87%) with some Q^3 units (13%). From their chemical shift, Q^2 and Q^3

species are associated with both calcium and sodium cations [281, 332, 339], but Q^3 is preferentially associated with Na^+ , $Q^3(Na)$, while Q^2 with Ca^{2+} ($Q^2(Ca)$) [332]. BG has a more depolymerised silicate network than the TG sample.



(a)



(b)

Figure 7.6. ^{29}Si MAS NMR spectra of BG (a) and TG (b) as-synthesised and immersed in SBF for different periods of time.

Table 7.2. ²⁹Si MAS NMR data for measured samples, giving the spectral deconvolution into different Qⁿ species.

Sample	Q ⁰ (Ca, Na)			Q ¹ (Ca, Na)			Q ² (Ca, Na)			Q ³ (Ca, Na), Q ² (H)			Q ³ (H)			Q ⁴		
	δ (ppm)	FWH M (ppm)	I (%)	δ (ppm)	FWH M (ppm)	I (%)	δ (ppm)	FWH M (ppm)	I (%)	δ (ppm)	FWH M (ppm)	I (%)	δ (ppm)	FWH M (ppm)	I (%)	δ (ppm)	FWH M (ppm)	I (%)
TG	-	-	-	-69.2	10.1	2	-82.5	9.9	14	-91.0	10.4	22	-98.9	9.5	22	-108.3	12.4	40
BG	-	-	-	-	-	-	-80.9	11.3	87	-90.7	8.0	13	-	-	-	-	-	-
pSBF 2h TG	-	-	-	-	-	-	-82.4	3.1	1	-92.1	9.4	6	-101.7	9.2	31	-111.5	9.2	62
pSBF 2h BG	-	-	-	-74.9	6.6	5	-81.1	6.9	10	-89.0	11.7	17	-100.7	10.1	28	-111.3	9.3	40
sSBF 2h TG	-	-	-	-	-	-	-84.2	6.2	2	-91.3	7.7	5	-100.8	9.5	30	-111.0	9.9	63
sSBF 2h BG	-62.3	2.5	1	-72.3	6.3	1	-80.7	9.4	18	-88.4	9.2	12	-100.9	12.6	34	-111.3	8.8	34
pSBF 1d TG	-	-	-	-	-	-	-83.7	7.5	1	-92.4	8.9	6	-102.1	9.0	30	-111.7	9.1	63
pSBF 1d BG	-	-	-	-	-	-	-83.0	12.8	10	-92.1	6.0	3	-101.3	9.1	28	-111.6	9.2	59
sSBF 1d TG	-	-	-	-	-	-	-84.1	6.5	1	-92.7	8.6	6	-101.7	8.6	28	-111.3	9.6	65
sSBF 1d BG	-62.7	2.3	1	-71.3	4.7	1	-81.7	11.2	16	-91.7	8.2	8	-101.1	8.6	25	-111.4	9.3	49
pSBF 7d TG	-	-	-	-	-	-	-83.2	6.3	1	-92.2	8.4	5	-102.0	8.8	28	-111.6	9.1	66
pSBF 7d BG	-	-	-	-	-	-	-79.3	7.4	1	-91.7	10.9	5	-102.3	9.2	29	-111.8	8.5	65
sSBF 7d TG	-	-	-	-	-	-	-78.9	7.4	2	-91.2	9.9	6	-101.7	9.1	27	-111.1	9.2	65
sSBF 7d BG	-	-	-	-	-	-	-80.0	11.4	3	-92.0	8.4	5	-101.6	8.6	23	-111.6	9.4	69

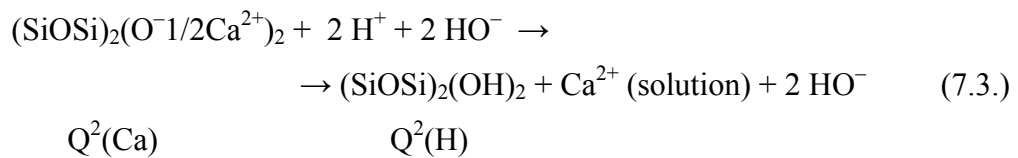
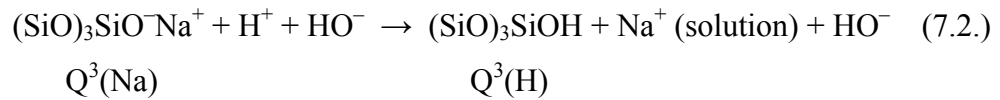
FWHM, δ and I represent the linewidth full-width half-maximum, ²⁹Si chemical shift and relative intensity, respectively.

Errors associated with measurements are: FWHM ± 1 ppm, δ ± 2 ppm and Integral ±2%.

When both glasses are immersed in serum-free (pSBF) and serum-containing (sSBF) bioactive media for 2 h, an increase in Q⁴ units from 40% to 63% (in both pSBF and sSBF) for TG sample and the appearance of Q⁴ species (40% and 34% in pSBF and sSBF, respectively) in the BG sample is observed (Table 7.2). An increase in Q³(H) for TG in both bioactive media and the appearance of these species for BG can also be seen from Table 7.2. Consequently, the concentration of Q³(Ca, Na) and Q²(Ca, Na) for the BG sample and Q²(Ca), Q³(Ca) (or Q²(H)) for the TG sample decreased, while Q¹(Ca) for TG is absent in the spectra (Figure 7.6, Table 7.2).

The increase in the concentration of more polymerised silicate species corresponds to the reconstruction of the silica gel surface layer, with the mechanism proposed by Hench [7, 11] being widely accepted for bioactive glasses degradation. The bioactive process of BG and TG glasses favours the above mechanism, when the first three stages could be observed. In the first step the alkaline and alkaline-earth cations (Na⁺, Ca²⁺) are leached from the silicate network by an exchange with H⁺ or H₃O⁺ from the solution with the formation of SiOH bonds.

As an example in reactions 7.2 and 7.3, the formation of Q³(H) and Q²(H) from Q³(Na) and Q²(Ca) respectively are shown.

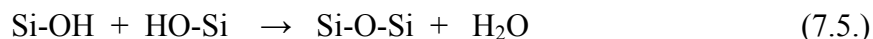


As SBF has a pH of 7.2, some SiOSi bonds can be base hydrolysed with the formation of new SiOH bonds:



From the condensation of silanol units the formation of SiOSi bonds take place with the repolymerisation of a hydrated SiO₂ layer on the surface depleted in

alkaline and alkaline earth cations, which represent the third stage in the reconstruction of silica gel surface layer:



Some SiOSi bonds in $Q^n(\text{Ca}, \text{Na})$ species from the surface can be hydrolysed and due to the presence of Na^+ or Ca^{2+} cations form $Q^n(\text{Ca}, \text{Na})$ species of lower connectivity, as the ^{29}Si MAS NMR results for BG sample immersed for 2 h in pSBF and sSBF suggested, when the formation of $Q^0(\text{Ca}, \text{Na})$ and $Q^1(\text{Ca}, \text{Na})$ take place (Table 7.2).

For TG immersed in pSBF for 2h, compared with the BG sample, a more polymerised silicate network was obtained. This can be explained by the fact that for the TG sample the fraction of network modifying cations in the silicate network was lower as more calcium ions are on the surface of the particles, compared with BG, which is evident in their NMR spectra, where for BG only $Q^2(\text{Ca}, \text{Na})$ and $Q^3(\text{Ca}, \text{Na})$ are obtained. Also the porosity of TG sample favours the leaching of cations as more water is adsorbed and dissolves the cations. The difference is even more predominant when the samples have been immersed in sSBF. Serum inhibits the depletion of the silicate network for the BG sample, where the concentration of Q^4 and $Q^3(\text{H})$ species is lower, due to the fact that the proteins are adsorbed on the BG surface and form a layer which covers the silica layer which may slow down the leaching of the alkaline and alkaline-earth cations from the silicate network. Consequently the silica gel layer formation is delayed due to the inhibitive effects of serum. For the TG sample in pSBF and sSBF (Figure 7.6.b, Table 7.2) there is not a significant difference in the spectra of pSBF and sSBF of 2 h (compare pSBF 2h TG and sSBF 2h TG, respectively).

Increasing the soaking time to 1 and 7 days for the TG sample, the concentration of higher polymerised silicate species (Q^4 and $Q^3(\text{H})$) is almost the same as for 2 h in both bioactive media (Figure 7.6 b, Table 7.2), suggesting that the reconstruction of the silica gel layer takes place after 2 h in both media. The concentration of $Q^2(\text{Ca})$ is around 1-2% in all samples. Even if for the TG sample, more proteins are adsorbed compared with the BG sample, the protein layer does not

influence the silica gel layer formation, as the network modifying cations have been leached from the silicate network.

However, for the BG sample the Q^4 and $Q^3(H)$ species increase gradually as they are immersed for up to 7 days in both bioactive media as more cations are leached from the silicate network (Figure 7.6 a, Table 7.2). For both samples immersed in pSBF and sSBF for 7 days, the concentration of Q^n species is almost the same, suggesting that a similar silica gel layer is formed. For the sSBF 7d BG sample, the concentration of Q^4 species is higher and Q^3 species lower compared with sSBF 7d TG sample.

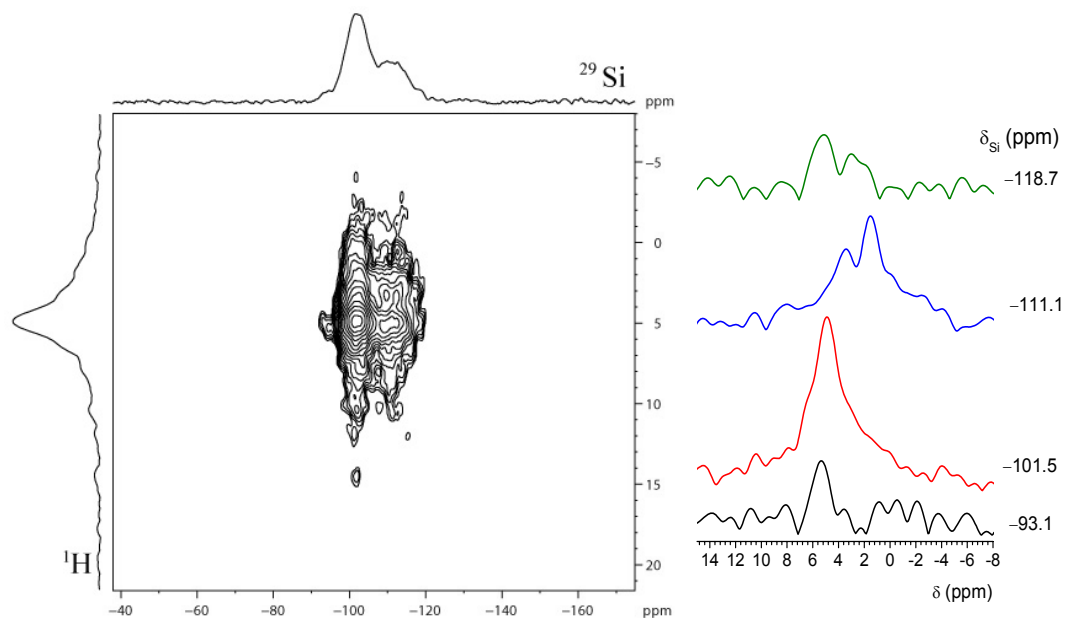
1H - ^{29}Si HETCOR spectra of the TG sample immersed for 7 days in serum-free and serum-containing bioactive media are presented in Figure 7.7 a and b respectively, with vertical slices extracted for the 1H dimension corresponding to each silicon site.

In both samples the presence of SiOP bonds can be detected from the ^{29}Si chemical shift around -120 ppm, due to Q^4 species where the silicon atom is connected by oxygen bridges to 3 phosphorous atoms and to 1 silicon (will be named $Q^4(P)$). The presence of this low concentration species in 2D spectra compared with 1D MAS spectra (Figure 7.6) is due to higher resolution in the 2D. The formation of SiOP bonds can take place from the adsorption of phosphates on the silica gel layer through heteropolymerisation reactions of $SiOH$ or SiO^- species and the POH bonds of the phosphate ions. The formation of SiOP bonds prevents the formation of new $SiOSi$ bonds. The formation of SiOP bonds can explain the variation of chemical shift for Q^n species particularly $Q^3(Ca, Na)$ ($Q^2(H)$), $Q^3(H)$ and Q^4 respectively, to more negative values in the 1D MAS NMR spectra of BG and TG glasses in both bioactive media with increasing time of immersion, because of the presence of first one and then more phosphorus atoms providing a greater shielding of the silicon nucleus [282].

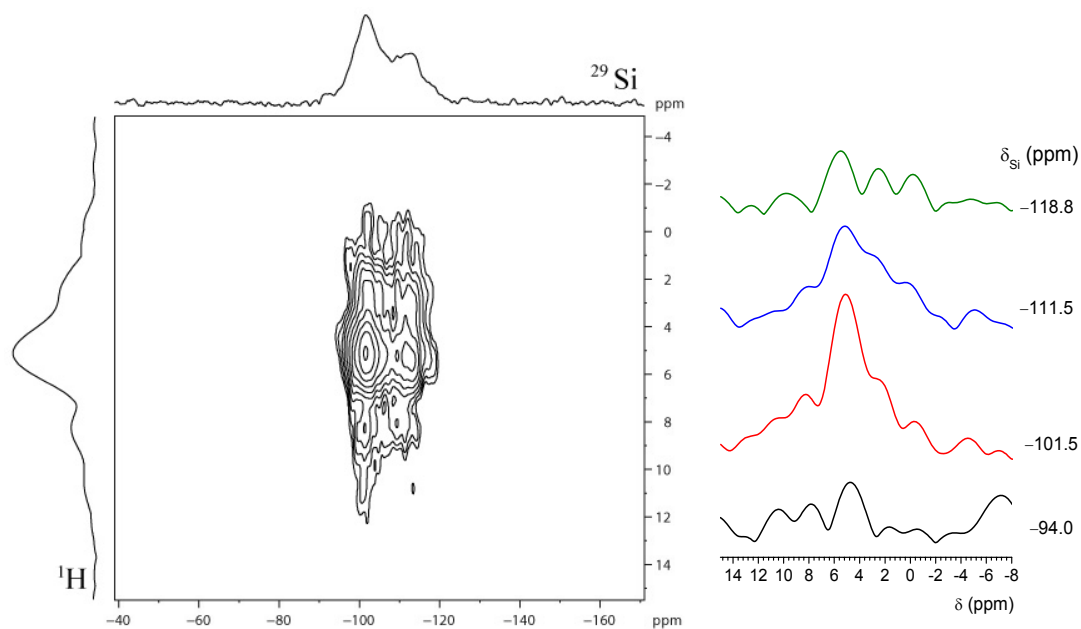
The resonance at -80 ppm has not been detected in the HETCOR spectra of the samples, suggesting that these species are connected to calcium ions and are in the interior of the particle, further from hydrogens. However, in 1D MAS NMR spectra (Figure 7.6, Table 7.2) their concentration was very low (~ 2 -3%).

From the 1H - ^{29}Si HETCOR spectra of both samples it is apparent that the magnetisation was efficiently transferred from water protons (~ 5 ppm) to all silicon

sites. For both samples the magnetisation transfer to Q²(H) (Q³(Ca)) units was just from water molecules.



(a)



(b)

Figure 7.7. ¹H-²⁹Si HETCOR spectra of pSBF 7d TG (a) and sSBF 7d TG (b) samples. To the right, the vertical slices correspond to ¹H NMR spectra extracted from each silicon site represented by δ_{Si} .

However, in the serum-free medium (pSBF 7d TG sample, Figure 7.7 a) the Q^4 sites cross-polarise from water in lower concentration than the other Q^n sites. Some of these sites are probably inaccessible to water molecules. For the Q^4 sites in the pSBF 7d TG sample, the highest contribution for the transferred magnetisation is from isolated SiOH (at 1.5 ppm) and from weakly hydrogen-bonded SiOH at 3.3 ppm. The less efficient transfer of magnetisation from water to some of Q^4 sites in this sample than from silanols can be due to motion of the water molecules reducing the ^1H - ^{29}Si dipolar coupling. For $Q^3(\text{H})$ and $Q^4(\text{P})$ units the magnetisation was also transferred from isolated and weakly hydrogen-bonded silanols, where for $Q^3(\text{H})$ sites the broadening of the peaks can be due to stronger dipolar couplings between adjacent silanols with the formation of intramolecular hydrogen bonding.

In the serum-containing medium (sSBF 7d TG sample, Figure 7.7 b) the most efficient magnetisation transfer for all sites was from water molecules. For $Q^3(\text{H})$, Q^4 and $Q^4(\text{P})$ units the magnetisation has been transferred from weakly hydrogen-bonded silanols. For Q^4 and possibly $Q^3(\text{H})$ species the magnetisation has also been transferred from some hydrogen species at 8 ppm, possibly stronger hydrogen-bonded silanols and/or $-\text{NH}_3^+$ from adsorbed proteins of the serum. Interestingly, for this sample, a possible correlation between structural OH from apatite and $Q^4(\text{P})$ and probably Q^4 units could suggest that some of these units can enter the apatite structure, as the apatite layer was formed later in the serum-containing medium (sSBF). This could also influence the broadness of the ^{31}P MAS NMR spectra of samples immersed in serum even after 7 days (see Figures 7.3 and 7.4, Table 7.1).

Figure 7.8 shows the variation of ^{23}Na MAS NMR spectra of BG glass in pSBF and sSBF with soaking time.

Even if the spectrum of the BG sample, recorded at 10 kHz, presents a broad asymmetric resonance at -1.3 ppm, there appears to be sites within the glass between 2 and 7 ppm with a sharp peak at 4.9 ppm. The broadness of the line is due to the large electric field gradient at the sodium nuclei as evidenced by the tail which extends out to approximately -40 ppm. The sharp feature could be attributed to a possible crystallisation due to surface hydration from water adsorption (see ^1H MAS NMR, Figure 7.1). The spectra of the BG sample immersed for different soaking times in both bioactive media, pSBF and sSBF, are quite similar to each other for 2 h and 1 day. This suggests that the distributions in sodium environments are similar

over the range of these compositions. The spectra present sharper features than present in the BG sample. For the pSBF 7d BG sample the ^{23}Na MAS NMR spectrum shows a sharp feature at -1.3 ppm. The narrowing of the linewidth indicates a smaller electric field gradient experienced by the sodium nuclei.

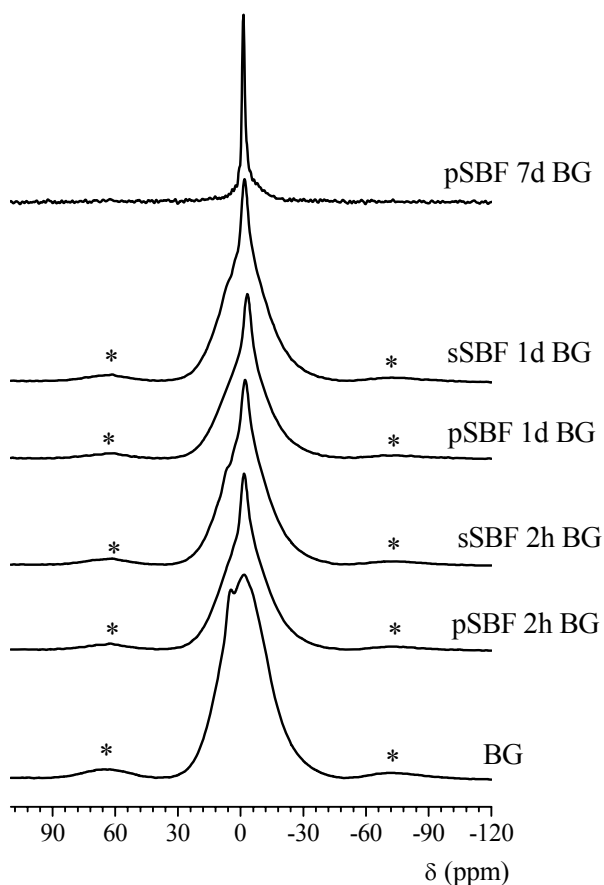


Figure 7.8. ^{23}Na MAS NMR spectra recorded at 14.1 T and a spinning speed of 10 kHz for the BG sample, as-received and immersed in pSBF and sSBF for different periods of time. * denotes spinning sidebands.

The peak position is shifted slightly to more negative values as the glass has been immersed in both bioactive media (to -1.7 , -1.9 , -3.4 and -1.9 ppm for pSBF 2h BG, sSBF 2h BG, pSBF 1d BG and sSBF 1d BG, respectively). More negative peak positions combined with decreasing linewidths for 2 h and 1 day of immersion in both bioactive media can be attributed to a motional averaging of sodium atoms in glass [340, 341]. It was shown [341] that if Na does not undergo motional averaging the peak maxima would become more negative, but the linewidths would increase. In

our samples, this motion can be due to the fact that when BG is immersed in SBF the concentration of Na^+ ions in glass decreases, as was shown by the ^{29}Si MAS NMR results, where an increase in the polymerisation of the structure was observed. However in the serum-containing medium the linewidths are slightly larger compared to those in the serum-free medium, as the mobility and diffusion of cations is slowed down. Also in serum some sodium cations can be complexed with carboxyls from proteins (see ^{13}C CP MAS NMR results). The more negative maxima among these samples can also be attributed to the increase of the mean coordination number of sodium in the glass as the Na concentration decreases and to the higher polymerisation of the silicate network [342]. In all four samples, a sharp contribution around 7.2 ppm appears (for pSBF 2h BG is visible at 20 kHz in Figure 7.9), probably from surface hydration and/or complexation of sodium with chloride ions present from SBF with the formation of NaCl on the surface. The peak position for solid NaCl has been found to be around 7 ppm at 7.05 and 4.7 T, respectively [343-345].

An increase in the chemical shift after 7 days of immersion in pSBF (pSBF 7d BG sample), can be interpreted as follow: the sodium ions have been leached from their modifying role in the silicate network, and the remaining sodiums are on the surface with a decrease in the mean coordination number of Na^+ ions, probably to 6. Sodium is released faster than calcium as the calcium divalent ions are relatively immobile compared to the monovalent sodium ions. This would explain the fact that even if the silica network becomes more polymerised after 7 days of immersion (see ^{29}Si MAS NMR), the peak maximum is increasing again to -1.3 ppm as in the BG glass. The linewidth is similar to crystalline materials (1.5 ppm), as sodium ions have a high mobility and a more ordered phase, probably an ionic compound form from the complexation of sodium cations with anions from SBF is obtained. For this sample the mean coordination number is the predominant factor as sodium ions are on the surface and not in the glass.

The ^{23}Na MAS NMR spectra of BG and pSBF 2h BG samples recorded at 10 and 20 kHz, respectively are shown in Figure 7.9. Analysing the differences in the spectra, it can be observed that the main peak maxima change to -3.8 and -2.5 ppm for BG and pSBF 2h BG samples, respectively, when the spinning speed is increased from 10 to 20 kHz.

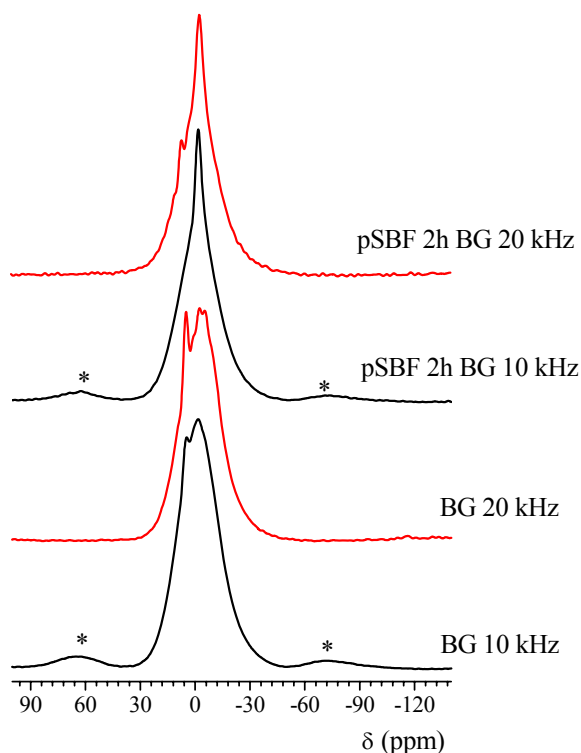
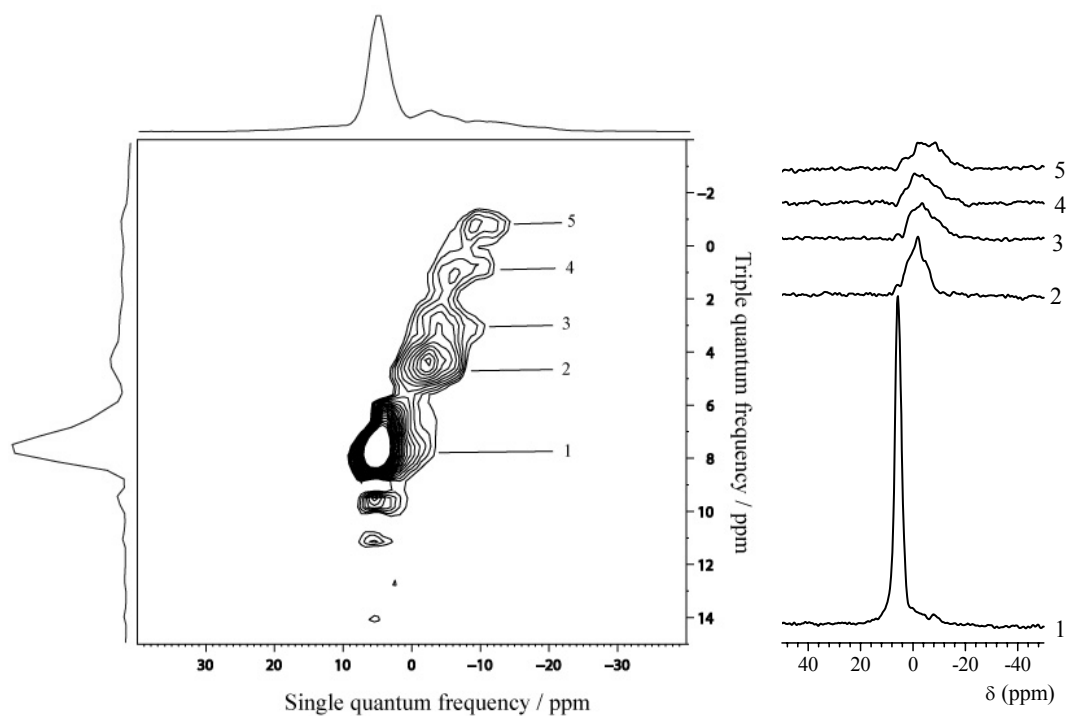


Figure 7.9. ^{23}Na MAS NMR spectra recorded at 14.1T and a spinning speed of 10 and 20 kHz for BG and pSBF 2h BG samples. * denotes spinning sidebands.

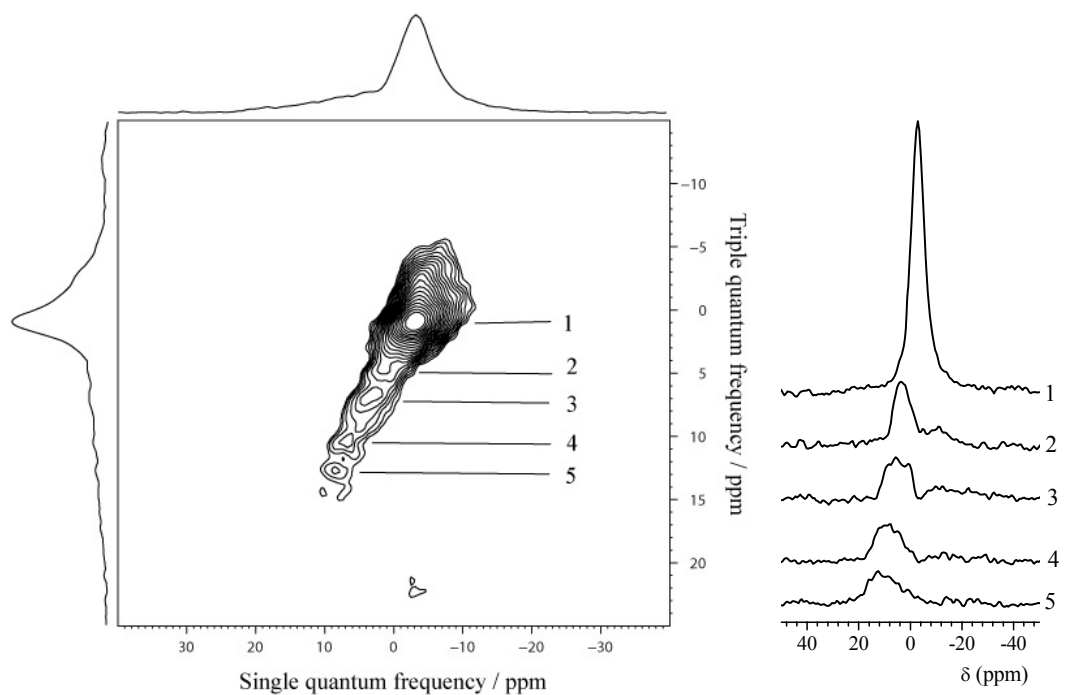
The peak at 7.2 ppm is now visible in spectrum of the pSBF 2h BG sample and the peak position corresponding to ionic species at 5 and 7.2 ppm for the two samples does not change with the spinning speed. The linewidths remain almost the same with increasing spinning speed from 10 to 20 kHz. These changes could be due to a distribution of electric field gradient of sodium present in the glass which is probably narrowed as the spinning speed increases [346].

To go further into the description of the sodium environments, the 2D ^{23}Na MQMAS NMR spectra on the BG and pSBF 2h BG samples have been performed and are shown in Figure 7.10 a and b, respectively.

Horizontal slices through each feature can be extracted from the MQMAS experiment to obtain an MAS lineshape free of overlap from other peaks. Such horizontal slices extracted from the MQMAS NMR spectra are shown on the right hand side for each spectrum and are numbered from 1 to 5.



(a)



(b)

Figure 7.10. ^{23}Na MQMAS spectra recorded at 14.1 T and a spinning speed of 20 kHz of BG (a) and pSBF 2h BG (b) samples.

Horizontal slices from the main features are shown on the right hand side numbered from 1 to 5 for each spectrum.

The quadrupolar parameters obtained from the BG spectrum fit using the DMFIT program [224] are shown in Table 7.3.

Table 7.3. ^{23}Na MQMAS data of BG sample.

Sample		δ_{iso} (ppm)	C_Q (MHz)	η_Q
BG	Peak 1	6.1	0.98	1
	Peak 2	1.2	1.62	1
	Peak 3	-1.2	2.32	0.4
	Peak 4	-3.1	2.25	0.4
	Peak 5	-5.0	2.34	0

δ_{iso} , C_Q and η_Q represent the ^{23}Na isotropic chemical shift, quadrupolar coupling constant and asymmetry parameter, respectively. Errors associated with measurements are: $\delta_{\text{iso}} \pm 1$ ppm, $C_Q \pm 0.1$ MHz and $\eta_Q \pm 0.05$.

The ^{23}Na MQMAS NMR spectrum of the BG sample (Figure 7.10 a) confirms the presence of multiple sodium sites. The spectrum has been fitted using 5 peaks (Table 7.3). One site corresponding to peak 1 gives a distinctively narrow resonance having an isotropic chemical shift at 6.1 ppm (Table 7.3) with a small quadrupolar coupling constant ($C_Q = 0.98$ MHz) and probably arises from the most ionic species in a highly symmetric octahedral geometry. This corresponds to the sharp feature at 4.9 ppm from the 1D MAS spectrum.

This is consistent with the data in the literature [326, 327] where the simulation of the ^{23}Na MQMAS spectrum of *Bioglass*[®] presents at least three distinct sites and one of them has a narrow resonance at $\delta_{\text{iso}} = 6.6$ ppm and a C_Q of 1.2 MHz. The other sites in the BG sample have higher quadrupole coupling constants due to higher electric field gradient at the sodium nuclei.

The site with a δ_{iso} of -5 ppm can be due to sodium carbonates [331, 343, 347, 348] formed on the glass surface from the adsorption of CO_2 . The relatively large C_Q associated with this site might be due to a shorter Na-O distance, when the oxygens of carbonate ions surrounding the Na^+ ions form a distorted octahedral environment [347]. As Na_2CO_3 has two inequivalent sodium sites, ^{23}Na MAS NMR spectra of Na_2CO_3 measured at 14.1 T [348] showed another resonance centred around 5 ppm. Thus the peak at 5 ppm can have also contribution from Na_2CO_3 .

The remaining three peaks having δ_{iso} of -1.2, 1.2 and 3.1 ppm, respectively, could be attributed to sodium ions in a glass, with either silica or phosphate network.

The ^{23}Na MQMAS NMR spectrum of the BG sample immersed for 2 h in pSBF (Figure 7.10 b) shows predominantly one narrow resonance, with an isotropic chemical shift of -1.5 ppm and a $C_Q = 1.2$ MHz. This δ_{iso} is close to that found for

peak 3 in the BG sample, but the C_Q is smaller as a lower electric field gradient must be present at the sodium site. Therefore this site can arise in both samples from Na^+ ions in glass, where for the pSBF 2h BG sample, due to a higher proportion of water and a lower Na^+ content in the glass, the cations can be partially solvated. The other slices shown on the left hand side of this spectrum probably arise from chemical shift dispersion and/or a distribution of electric field gradient. Na_2CO_3 has not been detected, suggesting that it was dissolved in pSBF.

However, MQMAS NMR does not provide quantification of the relative site abundances in the samples, due to the dependence of the multiple-quantum excitation and conversion efficiencies on the quadrupolar parameters.

7.4. Conclusions

In this chapter multinuclear solid-state NMR studies on both BG and TG compositions immersed for different periods of time in serum-free and serum-containing bioactive media have been performed. ^1H MAS NMR spectra showed that in sSBF bioactive medium hydrogen-bonded silanols tended to be formed compared with pSBF where the concentration of isolated silanols seems to increase with the period of soaking. ^1H and ^{13}C CP MAS NMR confirmed that proteins have been adsorbed on the glass surfaces for both compositions, with a higher concentration on sol-gel derived glass. Some of the calcium and sodium ions are bound to the organic carboxyls of proteins from serum. As ^{31}P NMR data of melt-quench and sol-gel derived glasses suggest, increasing the immersion time in both bioactive media led to an increase ordering of phosphate ions. For the first 2 h of immersion the growth of an amorphous calcium phosphate layer takes place followed by an increasingly ordered form of apatite-structured material with increasing immersion time. The serum proteins significantly inhibit the formation of apatite as was suggested from the spatial connectivity determined in ^1H - ^{31}P HETCOR spectra of the TG sample immersed for 7 days in both bioactive media. Carbonate ions enter the apatite structure in small amounts with the formation of an AB substituted apatite. Most of the carbonates are located near the surface. The water molecules are in motion with neighbouring $\text{H}_x\text{PO}_4^{(3-x)-}$ ions possibly in equilibrium with $\text{H}_{x+1}\text{PO}_4^{(2-x)-}$. HPO_4^{2-} ions have been found on the surface of apatite. Serum inhibits the depletion of the silicate network for the BG sample as suggested by ^{29}Si NMR results. Serum proteins

have not been found to inhibit the formation of a silica-rich layer on the TG sample which took place after 2 h in both bioactive media. After 7 d of immersion the silicate layer was similar for both samples. In both media with and without proteins, SiOP bonds have been formed from the adsorbed $H_xPO_4^{(3-x)-}$ ions on the silica surface. Water molecules have to be in the gel layer as the magnetisation from water was efficiently transferred to all silicon sites in 1H - ^{29}Si HETCOR spectra in both bioactive media. Overall our data favours Hench's mechanism of apatite layer deposition in bioactive glasses. The ^{23}Na NMR data confirm the presence of multiple sodium sites in the *Bioglass*[®] composition. With increasing the immersion time in serum-free and -containing media, the sodium concentration in the glass decreases.

8.

OVERALL CONCLUSIONS AND FUTURE DIRECTIONS

8.1. Overall conclusions

Throughout this thesis a multinuclear solid state NMR approach has been applied to a key range of sol-gel derived novel bioactive glasses and nanocomposite tissue scaffolds. First, 70S30C (70 mol% SiO₂ and 30 mol% CaO) composition has been study. The effect of phosphorus in 58S (60 mol% SiO₂, 36 mol% CaO, 4 mol% P₂O₅) composition was studied for two synthesis routes: inorganic and alkoxide. Then the study was extended to organic-inorganic hybrid scaffolds, class I and II, in silica-gelatin and silica-calcium oxide-(γ -PGA) systems. In the last part of this thesis, the mechanism of apatite growth on both melt-quench and sol-gel glass surfaces was revealed.

The stabilisation process produces a loss of residual organic fragments and structural hydroxyls in the 70S30C sol-gel derived bioactive glasses, as ¹H and ¹³C NMR suggested. ²⁹Si MAS NMR indicates that Ca dissolved in the pore liquor in the xerogel stage and incorporated into the silica network during the stabilisation stage increasing the range of Qⁿ species present and correspondingly the disorder of the silicate network. The heterogeneous calcium distribution which results in the large scale nanostructural inhomogeneity of the sol-gel derived 70S30C glass monoliths has been studied. The outside region was found to have a higher concentration of calcium than the centre of the monolith, resulted from the diffusion difficulties of the calcium during the drying stage. Next, solid-state NMR has been applied to the study of two series of samples, TMS-A and TMS-B, synthesised using TMES as a condensation inhibitor and compared with a traditional 70S30C sol-gel derived bioactive glass. ¹H and ²⁹Si NMR supported the hypothesis of the inhomogeneity between the two series. The hydrogen content and the concentration of organic siloxane bonds Si-O-Si(CH₃)₃ were found to increase with TMES concentration which acted as a condensation inhibitor due to a trimethylsilylation mechanism. By

adjusting the dosage of the TMES as a quencher, the distribution of calcium is affected and the overall network connectivity. The incorporation of calcium in the silicate network was sacrificed in the TMS-B samples, even if the homogeneity was improved.

In the next Chapter, bioactive glasses with 58S composition synthesised via inorganic and alkoxide sol-gel routes and thermally treated at different temperatures were analysed. ^1H and ^{13}C CP MAS NMR showed that a small fraction of the residual organic fragments from alkoxides remains in pores even at 800 °C. ^{13}C CP MAS NMR showed the formation of different types of carbonate for the two routes, their stability being higher for samples synthesised via an alkoxide route. ^{31}P MAS and CP MAS NMR revealed different phosphorus environments at lower temperatures. By increasing the temperature, the formation of HAp or fluoroapatite and β -TCP was observed, for samples synthesised via an inorganic route, while via an alkoxide route just disordered orthophosphates tended to be formed in the system. ^{29}Si MAS NMR showed that for the alkoxide route calcium was incorporated at low temperatures, but higher temperatures were needed for the inorganic route. When the glasses approach the glass transition temperature structural densification starts, for both routes, a reorganisation of silicate network was observed with the separation of calcium silicate crystalline phases and cuspidine for the samples synthesised via the alkoxide route.

Having explored the silica-gelatin class I hybrids, from ^{29}Si NMR, an increase in the silicate network connectivity was observed on increasing the gelatin concentration, while ^{13}C CP MAS NMR showed predominantly the residues from amino acids of gelatin. As the hybrid's molar ratio of GPTMS:gelatin increased for class II hybrids, there was a notable increase in the T species in the ^{29}Si MAS NMR spectra, indicating an increase in inorganic-organic coupling. For the highest GPTMS concentration, as the gelatin has been incorporated, the predominant signals in ^{13}C CP MAS NMR, as well as in ^1H MAS and CRAMPS NMR spectra were from short PEO chains, the diol formed and from unreacted GPTMS molecules. Inter- and intramolecular correlations between amino acid residues in gelatin have been detected, as well as between amino acids and the silicate network in the ^1H DQ CRAMPS spectra. Next, the 40 wt% γ -PGA and 60 wt% bioactive silica (70 mol% SiO_2 and 30 mol% CaO) systems when two calcium salts, CaCl_2 and $\text{Ca}(\gamma\text{-PGA})$

were used as calcium precursors, have been studied. ^{29}Si NMR suggests covalent bonding between the organic and inorganic networks from the presence of both T^n and Q^n species. As the amount of GPTMS used in the synthesis increased the proportions of T^n to Q^n increased as well, indicating higher degrees of cross-linking between the organic and inorganic phases in the hybrids. In CaCl_2 containing samples, the high mobility of the species and the presence of the aprotic solvent (DMSO) significantly reduced the ^{13}C CP NMR signal. The results indicate that efficient promotion of epoxide ring opening of GPTMS was reached by functionalised γ -PGA when both calcium salts were used. Short and relatively mobile PEO chains are formed in the system. ^{43}Ca NMR, at natural isotopic abundance, suggests different environments in the hybrid for the two calcium sources. Multinuclear solid state NMR showed that GPTMS was successful in providing a covalent link from the organic phase, either gelatin or γ -PGA, to the inorganic silicate network, which is essential to the hybrid design.

In the last chapter of this thesis, the effect of serum proteins on the apatite growth on both *Bioglass*[®] and *Theraglass*[®] surfaces was studied. ^1H MAS NMR spectra showed that hydrogen-bonded silanols tended to be formed in serum-containing medium instead of isolated silanols found in serum-free medium. ^1H and ^{13}C CP MAS NMR confirmed that proteins have been adsorbed on the glass surfaces for both compositions, with a higher concentration on sol-gel derived glass. ^{31}P NMR data of both glasses suggest that for the first 2 h of immersion the growth of an amorphous calcium phosphate layer takes place followed by an increasingly ordered form of apatite-structured material. ^1H - ^{31}P HETCOR spectra of the *TheraGlass*[®] sample immersed for 7 days in both bioactive media have been useful in establishing the spatial connectivity, when the serum proteins have been found to significantly inhibit apatite formation. Carbonate ions enter the apatite structure in small amounts with the formation of an AB substituted apatite. HPO_4^{2-} ions have been found on the surface of apatite. Serum inhibits the depletion of the silicate network for the *Bioglass*[®] sample, while for the *TheraGlass*[®] sample the formation of a silica-rich layer took place after 2 h in both bioactive media, as suggested by ^{29}Si NMR. SiOP bonds have been detected from ^1H - ^{29}Si HETCOR spectra after 7 days of immersion in both bioactive media. The ^{23}Na NMR data showed the presence of multiple sodium sites in the *Bioglass*[®] composition. The sodium concentration in the glass

decreases with the immersion time in both media and the local structure becomes more ordered.

Overall, this thesis demonstrates the potential of solid-state NMR in the characterisation of sol-gel derived bioactive glasses and scaffolds.

8.2. Future directions

The work contained in this thesis represents only a small step towards the goal of understanding the structure of sol-gel derived bioactive glasses and scaffolds and the interactions between bioactive glasses and living matter.

The preparation of ^{17}O -enriched samples for 70S30C, 58S and $\text{SiO}_2\text{-CaO-(}\gamma\text{-PGA)}$ systems might be able to provide a better understanding on the system by resolving bridging and non-bridging oxygens.

To detect calcium sites in 70S30C, 58S and $\text{SiO}_2\text{-CaO-(}\gamma\text{-PGA)}$ sol-gel glasses and scaffolds, a small number of ^{43}Ca -enriched samples could be synthesised. One or two model crystalline solids could allow MQMAS pulse sequences to be optimised and consequently calcium silicate bioactive glasses and foams could be further studied using advanced ^{43}Ca NMR approaches.

To determine the role of fluorine from the foaming agent (HF) in the structure of 58S glasses and hybrid scaffolds presented in Chapters 5 and 6, ^{19}F NMR could be used.

For the organic-inorganic hybrids explored in this thesis, the study can be extended. For example, $^1\text{H-}^{13}\text{C}$ HETCOR or INEPT (insensitive nuclear enhancement by polarisation transfer) at high spinning speeds or using CRAMPS could be performed to identify H-C proximities in space or through bond. Other biodegradable and/or bioresorbable polymers, like chitosan, PCL and PVA could be added as model polymers to the silica and 70S30C compositions. Compositions with a different polymer/crosslinking agent, like GPTMS, ratio could be studied by solid-state NMR to observe how the polymer type and content affect the silanol content and silicate network connectivity, as well as the state of the bonding between organic and inorganic networks. Also other calcium sources, such as CME could be used, as it does not release toxic by-products and could be incorporated into the hybrid system at low temperatures as was shown throughout Chapter 5.

In the study of the mechanism of apatite formation, beside ^{17}O -enriched *TheraGlass*[®] and *Bioglass*[®] samples, a small amount of SBF could be prepared using ^{17}O -enriched water to perform ^{17}O NMR. Therefore BO and NBO could be identified and the silica layer deposition could be further studied. Moreover, the study concerning proteins effect, could be extended towards the analysis of bioactive glass reactivity in cell-containing solutions, since some of the interactions between cells and foreign materials are often mediated by proteins.

Some of the experiments presented in this thesis could be reproduced on other types of bioactive glasses, for example, bioactive glasses containing other network modifier cations in their composition, like Mg and/or Zn to observe their behaviour in SBF.

Eventually, molecular dynamic simulations of bioactive glasses could be performed to better understand how bioactive materials react with living matter. First, small clusters, in the form of rings or chains, containing Si, O and/or P atoms could be used for simulations. Further, the study can be extended to more complex systems, such as HAp and to try to simulate the mechanism of HCA formation on the bioactive glass surfaces.

9.

REFERENCES

- [1]. S. Lin, C. Ionescu, K. J. Pike, M. E. Smith, J. R. Jones, Nanostructure evolution and calcium distribution in sol-gel derived bioactive glass, *J. Mater. Chem.*, **2009**, *19*, 1276–1282.
- [2]. S. Lin, C. Ionescu, S. Baker, M. E. Smith, J. R. Jones, Characterisation of the inhomogeneity of sol-gel-derived SiO₂-CaO bioactive glass and a strategy for its improvement, *J. Sol-Gel Sci. Technol.*, **2010**, *53*, 255–262.
- [3]. S. Lin, C. Ionescu, E. M. Valliant, J. V. Hanna, M. E. Smith, J. R. Jones, Tailoring the nanoporosity of sol-gel derived bioactive glass using trimethylethoxysilane, *J. Mater. Chem.*, **2010**, *20*, 1489–1496.
- [4]. O. Mahony, O. Tsigkou, C. Ionescu, C. Minelli, L. Ling, R. Hanly, M. E. Smith, M. M. Stevens, J. R. Jones, Silica-gelatin hybrids with tailorable degradation and mechanical properties for tissue regeneration, *Adv. Funct. Mater.*, **2010**, DOI: 10.1002/adfm.201000838.
- [5]. G. Poologasundarampillai, C. Ionescu, O. Tsigkou, M. Murugesan, R. G. Hill, M. M. Stevens, J. V. Hanna, M. E. Smith, J. R. Jones, Synthesis of bioactive class II poly(γ -glutamic acid)/silica hybrids for bone tissue regeneration, *J. Mater. Chem.*, **2010**, DOI: 10.1039/c0jm00930j.
- [6]. G. Poologasundarampillai, B. Yu, S. Yue, P. D. Lee, C. Ionescu, J. V. Hanna, M. E. Smith, R. D. Hamilton, T. Kasuga, J. R. Jones, Inorganic/organic hybrid nanocomposite scaffolds for bone regeneration, submitted to *Biomaterials*.
- [7]. L. L. Hench, R. J. Splinter, W. C. Allen, T. K. Greenlee, Bonding mechanisms at the interface of ceramic prosthetic materials, *J. Biomed. Mater. Res. Symp.*, **1971**, *2*, 117–141.
- [8]. S. F. Hulbert, S. J. Morrison, J. J. Klawitter, Tissue reaction to three ceramics of porous and non-porous structures, *J. Biomed. Mater. Res.*, **1972**, *6*, 347-374.
- [9]. S. F. Hulbert, The use of alumina and zirconia in surgical implants, in *An Introduction to Bioceramics*, L. L. Hench, J. Wilson (eds) World Scientific, Singapore, **1993**, 25-40.
- [10]. C. G. Pantano, A. E. Clark, L. L. Hench, Multilayer corrosion films on Bioglass Surfaces, *J. Am. Ceram. Soc.*, **1974**, *57*, 412-413.
- [11]. L. L. Hench, Bioceramics: From Concept to Clinic, *J. Am. Ceram. Soc.*, **1991**, *74(7)*, 1487-1510.
- [12]. T. Kokubo, Surface chemistry of bioactive glass-ceramics, *J. Non-Cryst. Solids*, **1990**, *120*, 138-151.
- [13]. S. Radin, P. Ducheyne, B. Rothman, A. Conti, The effect of *in vitro* modeling conditions on the surface reactions of bioactive glass, *J. Biomed. Mater. Res.*, **1997**, *37*, 363–375.
- [14]. J. P. Zhong, D. C. Greenspan, Bioglass surface reactivity: from *in vitro* to *in vivo*, in *Bioceramics II* (Eds.: R. Z. LeGeros, J. P. LeGeros), World Scientific, Singapore, **1998**, 415-418.

- [15]. T. Kokubo, H. Kushitani, S. Sakka, T. Kitsugi, T. Yamamuro, Solutions able to reproduce *in vivo* surface-structure changes in bioactive glass-ceramic A-W, *J. Biomed. Mater. Res.*, **1990**, *24*, 721-734.
- [16]. P. Ducheyne, S. Brown, N. Blumenthal, L. L. Hench, A. Krajewski, G. Palavit, A. Ravaglioli, S. Steineman, S. Winderler, Bioactive glasses, aluminum oxide, and titanium: ion transport phenomena and surface analysis, *Ann. N.Y. Acad. Sci.*, **1988**, *523*, 257-263.
- [17]. T. Kokubo, H. Kushitani, C. Ohsuki, S. Sakka, T. Yamamura, Chemical reaction of bioactive glass and glass-ceramics with a simulated body fluid, *J. Mater. Sci.: Mater. Med.*, **1992**, *3*, 79-83.
- [18]. I. D. Xynos, A. J. Edgar, L. D. Buttery, L. L. Hench, J. M. Polak, Gene-expression profiling of human osteoblasts following treatment with the ionic products of Bioglass 45S5 dissolution, *J. Biomed. Mater. Res.*, **2000**, *55*, 151-157.
- [19]. I. D. Xynos, M. V. Hukkanen, J. J. Batten, L. D. Buttery, L. L. Hench, J. M. Polak, Bioglass 45S5 stimulates osteoblast turnover and enhances bone formation *in vitro*: implications and applications for bone tissue engineering, *Calcif. Tissue Int.*, **2000**, *67*, 321-329.
- [20]. L. L. Hench, J. M. Polack, Third-generation biomedical materials, *Science*, **2002**, *295*, 1014-1017.
- [21]. E. Rabkin, F. J. Schoen, Cardiovascular tissue engineering, *Cardiovasc. Pathol.*, **2002**, *11*, 305-317.
- [22]. B. D. Ratner, S. J. Bryant, Biomaterials: where we have been and where we are going, *Annu. Rev. Biomed. Eng.*, **2004**, *6*, 41-75.
- [23]. J. Rho, L. Kuhn-Spearing, P. Zioupos, Mechanical properties and the hierarchical structure of bone, *Med. Eng. Phys.*, **1998**, *20*, 92-102.
- [24]. M. M. Stevens, J. H. George, Exploring and engineering the cell surface interface, *Science*, **2005**, *310*, 1135-1138.
- [25]. J. R. Jones, P. D. Lee, L. L. Hench, Hierarchical porous materials for tissue engineering, *Phil. Trans. R. Soc. A*, **2006**, *364*, 263-281.
- [26]. L. L. Hench, H. A. Paschall, Direct chemical bonding between bioactive glass-ceramic materials and bone, *J. Biomed. Mater. Res. Symp.*, **1973**, *4*, 25-42.
- [27]. D. C. Greenspan, L. L. Hench, Chemical and mechanical behavior of Bioglass-coated alumina, *J. Biomed. Mater. Res.*, **1976**, *10*, 503-509.
- [28]. U. M. Gross, V. Strunz, The anchoring of glass-ceramics of different solubility in the femur of the rat, *J. Biomed. Mater. Res.*, **1980**, *14*, 607-618.
- [29]. L. L. Hench, O. H. Andersson, Bioactive glasses, in *An introduction to bioceramics*, L. L. Hench, J. Wilson, Eds. *Republic of Singapore: World Scientific*, **1993**, 41-62.
- [30]. L. L. Hench, Bioceramics, *J. Am. Ceram. Soc.*, **1998**, *81* (7) 1705-1728.
- [31]. L. L. Hench, Bioactive Ceramics, *Ann. N.Y. Acad. Sci.*, **1988**, *523*, 54-71.
- [32]. T. Nakamura, T. Yamamuro, S. Higashi, T. Kokubo, S. Ito, A new glass-ceramic for bone replacement evaluation of its bonding to bone tissue, *J. Biomed. Mater. Res.*, **1985**, *19*, 685-698.
- [33]. S. Yoshii, Y. Kakutani, T. Yamamuro, T. Nakamura, T. Kitsugi, M. Oka, T. Kokubo, M. Takagi, Strength of bonding between A-W glass-ceramic and the surface of bone cortex, *J. Biomed. Mater. Res.*, **1988**, *22(A)* 327-338.

- [34]. A. E. Fetner, M. S. Hartigan, S. B. Low, Periodontal repair using Perioglas[®] in non-human primates: clinical and histologic observations, *Compend. Cont. Educ. Dent.*, **1994**, *15*, 932–939.
- [35]. J. Wilson, E. Douek, K. Rust, Bioglass[®] middle ear devices: 10 year clinical results. In *Bioceramics 8* (ed. L. L. Hench, J. Wilson & D. C. Greenspan), Oxford: Pergamon, **1995**, 239–245.
- [36]. R. Li, A. E. Clark, L. L. Hench, An investigation of bioactive glass powders by sol–gel processing, *J. Appl. Biomater.*, **1991**, *2*, 231–239.
- [37]. M. M. Pereira, A. E. Clark, L. L. Hench, Calcium phosphate formation on sol–gel-derived bioactive glasses *in vitro*, *J. Biomed. Mater. Res.*, **1994**, *28*, 693–698.
- [38]. F. Balas, D. Arcos, J. Pérez-Pariente, M. Vallet-Regí, Textural properties of SiO₂ CaO P₂O₅ glasses prepared by the sol–gel method, *J. Mater. Res.*, **2000**, *16*, 1345–1348.
- [39]. A. Martínez, I. Izquierdo-Barba, M. Vallet-Regí, Bioactivity of a CaO–SiO₂ binary glasses system, *Chem. Mater.*, **2000**, *12*, 3080–3088.
- [40]. P. Saravanapavan, L. L. Hench, Low-temperature synthesis, structure, and bioactivity of gel-derived glasses in the binary CaO–SiO₂ system, *J. Biomed. Mater. Res.*, **2001**, *54*, 608–618.
- [41]. P. Saravanapavan, L. L. Hench, Mesoporous Calcium Silicate Glasses. I. Synthesis, *J. Non-Cryst. Solids*, **2003**, *318*, 1–13.
- [42]. P. Sepulveda, J. R. Jones, L. L. Hench, Characterization of melt-derived 45S5 and sol-gel-derived 58S bioactive glasses, *J. Biomed. Mater. Res.*, **2001**, *58*, 734–740.
- [43]. P. Sepulveda, J. R. Jones, L. L. Hench, *In vitro* dissolution of melt-derived 45S5 and sol-gel derived 58S bioactive glasses, *J. Biomed. Mater. Res.*, **2002**, *61*, 301–311.
- [44]. J. Pérez-Pariente, F. Balas, J. Román, A. J. Salinas, M. Vallet-Regí, Influence of composition and surface characteristics on the *in vitro* bioactivity of SiO₂–CaO–P₂O₅–MgO sol-gel glasses, *J. Biomed. Mater. Res.*, **1999**, *47*, 170–175.
- [45]. M. Vallet-Regí, A. J. Salinas, J. Román, M. Gil, Effect of magnesium content on the *in vitro* bioactivity of CaO–MgO–SiO₂–P₂O₅ sol-gel glasses, *J. Mater. Chem.*, **1999**, *9*, 515–518.
- [46]. J. Pérez-Pariente, F. Balas, M. Vallet-Regí, Surface and chemical study of SiO₂·P₂O₅·CaO·(MgO) bioactive glasses, *Chem. Mater.*, **2000**, *12*, 750–755.
- [47]. A. Oki, B. Parveen, S. Hossain, A. Adeniji, H. Donahue, Preparation and *in vitro* bioactivity of zinc containing sol-gel-derived bioglass materials, *J. Biomed. Mater. Res.*, **2004**, *69A*, 216–221.
- [48]. R. M. Day, A. R. Boccaccini, Effect of particulate bioactive glasses on human macrophages and monocytes *in vitro*, *J. Biomed. Mater. Res.*, **2005**, *73A*, 73–79.
- [49]. R. N. Du, J. Chang, S. Y. Ni, N. Y. Zhai, Characterization and *in vitro* bioactivity of zinc-containing bioactive glass and glass-ceramics, *J. Biomater. Appl.*, **2006**, *20*, 341–360.
- [50]. A. Balamurugan, G. Balossier, S. Kannan, J. Michel, A. H.S. Rebelo, J. M. F. Ferreira, Development and *in vitro* characterization of sol–gel derived CaO–P₂O₅–SiO₂–ZnO bioglass, *Acta Biomaterialia*, **2007**, *3*, 255–262.
- [51]. M. Bellantone, N. J. Coleman, L. L. Hench, Bacteriostatic action of a novel four-component bioactive glass, *J. Biomed. Mater. Res.*, **2000**, *51*, 484–490.

- [52]. J. R. Jones, L. M. Ehrenfried, P. Saravanapavan, L. L. Hench, Controlling ion release from bioactive glass foam scaffolds with antibacterial properties, *J. Mater. Sci.: Mater. Med.*, **2006**, *17*, 989-996.
- [53]. P. Sepulveda, J. R. Jones, L. L. Hench, Bioactive sol-gel foams for tissue repair, *J. Biomed. Mater. Res.*, **2002**, *59*, 340-348.
- [54]. J. R. Jones, G. Poologasundarampillai, R. C. Atwood, D. Bernard, P. D. Lee, Non-destructive quantitative 3D analysis for the optimisation of tissue scaffolds, *Biomaterials*, **2007**, *28*, 1404-1413.
- [55]. J. R. Jones, O. Tsigkou, E. E. Coates, M. M. Stevens, J. M. Polak, L. L. Hench, Extracellular matrix formation and mineralization on a phosphate-free porous bioactive glass scaffold using primary human osteoblast (HOB) cells, *Biomaterials*, **2007**, *28*, 1653-1663.
- [56]. C. Sanchez, F. Ribot, Design of hybrid organic-inorganic materials synthesized via sol-gel chemistry, *New J. Chem.* **1994**, *18*, 1007-1047.
- [57]. A. P. V. Pereira, W. L. Vasconcelos, R. K. Oréface, Novel multicomponent silicate-poly(vinyl alcohol) hybrids with controlled reactivity, *J. Non-Cryst. Solids*, **2000**, *273*, 180-185.
- [58]. A. I. Martín, A. J. Salinas, M. Vallet-Regí, Bioactive and degradable organic-inorganic hybrids, *J. Eur. Ceram. Soc.*, **2005**, *25*, 3533-3538.
- [59]. C. Savii, C. A. Ionescu, M. I. Popovici, C. S. Enache, R. Radu, Chapter 6. Nonionic organic-inorganic hybrid materials, in *New Trends in Nonionic (Co) Polymers and Hybrids*, E. S. Dragan, Eds. Nova Science Publishers, New York, **2006**, 215-261.
- [60]. Y. Wei, D. Jin, A new class of organic-inorganic hybrid dental materials, *Polym. Prep.*, **1997**, *38*, 122-123.
- [61]. S. Rhee, J. Choi, Preparation of a bioactive poly(methyl methacrylate)/silica nanocomposite, *J. Am. Ceram. Soc.* **2002**, *85*, 1318-1320.
- [62]. D. Tian, S. Blacher, P. Dubois, J. P. Pirard, R. Jérôme, Porous silica obtained from biodegradable and biocompatible inorganic-organic hybrid materials, *J. Sol-Gel Sci. Techn.*, **1998**, *13*, 415-419.
- [63]. S. H. Rhee, Bone-like apatite-forming ability and mechanical properties of poly(ϵ - caprolactone)/silica hybrid as a function of poly(ϵ -caprolactone) content, *Biomaterials*, **2004**, *25*, 1167-1175.
- [64]. L. Ren, K. Tsuru, S. Hayakawa, A. Osaka, Synthesis and characterization of gelatin-siloxane hybrids derived through sol-gel procedure, *J. Sol-Gel Sci. Techn.*, **2001**, *21*, 115-121.
- [65]. L. Ren, K. Tsuru, S. Hayakawa, A. Osaka, Novel approach to fabricate porous gelatin-siloxane hybrids for bone tissue engineering, *Biomaterials*, **2002**, *23*, 4765-4773.
- [66]. T. Coradin, S. Bah, J. Livage, Gelatine/silicate interactions: from nanoparticles to composite gels, *Colloid Surface B*, **2004**, *35*, 53-58.
- [67]. K. Fan, D. Gonzales and M. Sevoian, Hydrolytic and enzymatic degradation of poly(γ -glutamic acid) hydrogels and their application in slow-release systems for proteins, *J. Environm. Polym. Degrad.*, **1996**, *4*, 253-260.
- [68]. A. Sugino, T. Myiyazaki and C. Ohtsuki, Apatite-forming ability of polyglutamic acid gel in simulated body fluid: effect of cross-linking agent, *Key Eng. Mater.*, **2007**, *330-332*, 683-686.
- [69]. W. Zachariassen, Random Network Hypothesis, *J. Amer. Chem. Soc.*, **1932**, *54(10)*, 3841-3851.

- [70]. M. Vallet-Regi, C. V. Ragel, A. J. Salinas, Glasses with Medical Applications, *Eur. J. Inorg. Chem.*, **2003**, 1029-1042.
- [71]. Z. Strnad, Role of the glass phase in bioactive glass-ceramics, *Biomaterials*, **1992**, *13*, 317-321.
- [72]. C. Y. Kim, A. E. Clark, L. L. Hench, Compositional dependence of calcium phosphate layer formation in fluoride Bioglasses[®], *J. Biomed. Mater. Res.*, **1992**, *26*, 1147-1161.
- [73]. R. G. Hill, An alternative view of the degradation of bioglass, *J. Mater. Sci. Lett.*, **1996**, *15*, 1122-1125.
- [74]. D. Arcos, D. Greenspan, M. Vallet-Regi, A new quantitative method to evaluate the *in vitro* bioactivity of melt and sol-gel-derived silicate glasses, *J. Biomed. Mater. Res. A.*, **2003**, *65*, 344-351.
- [75]. D. Arcos, D. Greenspan, M. Vallet-Regi, Influence of the stabilization temperature on textural and structural features and ion release in SiO₂-CaO-P₂O₅ sol-gel glasses, *Chem. Mater.*, **2002**, *14*, 1515-1522.
- [76]. A. E. Clark, L. L. Hench, The influence of surface chemistry on implant interface histology: A theoretical basis for implant materials selection, *J. Biomed. Mater. Res.*, **1976**, *10*, 161-174.
- [77]. A. E. Clark, C. G. Pantano, L. L. Hench, Auger spectroscopic analysis of Bioglass corrosion films, *J. Am. Ceram. Soc.*, **1976**, *59*, 37-39.
- [78]. L. L. Hench, The story of Bioglass[®], *J. Mat. Sci.: Mater. Med.*, **2006**, *17*, 967-978.
- [79]. L. L. Hench, J. M. Polak, I. D. Xynos, L. D. K. Buttery, Bioactive materials to control cell cycle, *Mat. Res. Innovat.*, **2000**, *3*, 313-323.
- [80]. L. L. Hench, Glass and genes: the 2001 W. E. S. Turner memorial lecture, *Glass Technol.*, **2003**, *44(1)*, 1-10.
- [81]. H. Oonishi, L. L. Hench, J. Wilson, F. Sugihara, E. Tsuji, M. Matsuura, S. Kin, T. Yamamoto, S. Mizokawa, Quantitative comparison of bone growth behaviour in granules in bioglass, A-W glass-ceramic and hydroxyapatite, *J. Biomed. Mater. Res.*, **2000**, *51*, 37-46.
- [82]. T. B. Lovelace, J. T. Mellonig, R. M. Meffert, A. A. Jones, P. V. Nummikoski, D. L. Cochran, Clinical evaluation of bioactive glass in the treatment of periodontal osseous defects in humans, *J. Periodontol.*, **1998**, *69(9)*, 1027-1035.
- [83]. N. Patel, S. M. Best, W. Bonfield, I. R. Gibson, K. A. Hing, E. Damien, P. A. Revell, A comparative study on the *in vivo* behaviour of hydroxyapatite and silicon substituted hydroxyapatite granules, *J. Mater. Sci. Mater. Med.*, **2002**, *13*, 1199-1206.
- [84]. R. C. Beilby, R. S. Pryce, L. L. Hench, J. M. Polak, Enhanced derivation of osteogenic cells from murine embryonic stem cells after treatment with ionic dissolution products of 58S bioactive sol-gel glass, *Tissue Eng.*, **2005**, *11*, 479-488.
- [85]. J. E. Gough, J. R. Jones, L. L. Hench, Nodule formation and mineralisation of human primary osteoblasts cultured on a porous bioactive glass scaffold, *Biomaterials*, **2004**, *25*, 2039-2046.
- [86]. H. Oonishi, S. Kutrshtani, E. Yasukawa, H. Iwaki, L.L. Hench, J. Wilson, E. Tsuji, T. Sugihara, Particulate Bioglass[®] and hydroxyapatite as a bone graft substitute, *J. Clin. Orthop. Rel. Res.*, **1997**, *334*, 316-325.
- [87]. I. D. Xynos, A. J. Edgar, L. D. K. Buttery, L. L. Hench, J. M. Polak, Ionic products of bioactive glass dissolution increase proliferation of human

- osteoblasts and induce insulin-like growth factor II mRNA expression and protein synthesis, *Biochem. Biophys. Res. Comm.*, **2000**, 276, 461–465.
- [88]. J. J. Ebelmen, Untersuchungen über die Verbindungen der Borsäure und Kieselsäure mit Aether, *Liebigs Ann. Chem.*, **1846**, 57, 319-355.
- [89]. R. K. Iler, *The Chemistry of Silica*; Wiley: New York, **1955**.
- [90]. J. Rouxel, Chemical reactivity of low-dimensional solids, *Chem. Scr.*, **1988**, 28, 33-42.
- [91]. L. Livage, Sol-gel processing of metal oxides, *Chem. Scr.* **1988**, 28, 9-18.
- [92]. M. Yamane, A. Shinji, T Sakaino, Preparation of a gel from metal alkoxide and its properties as a precursor of oxide glass, *J. Mater. Sci.*, **1978**, 13, 865-870.
- [93]. S. Sakka, K. Kamiya, Glasses from metal alcoholates, *J. Non-Cryst. Solids*, **1980**, 42, 403-421.
- [94]. J. Livage, *Chimie douce: from shake-and-bake processing to wet chemistry*, *New J. Chem.*, **2001**, 25, 1.
- [95]. R. J. P. Corriu, The Control of Nanostructures Solids: A challenge for molecular chemistry, *Eur. J. Inorg. Chem.*, **2001**, 1109-1121.
- [96]. C. J. Brinker, G. W. Scherer, *Sol-Gel Science: The Physics and Chemistry of Sol-Gel Processing*, Academic Press, San Diego, **1990**.
- [97]. M. Nogami, Y. Moriya, Glass formation through hydrolysis of $\text{Si}(\text{OC}_2\text{H}_5)_4$ with NH_4OH and HCl solution, *J. Non-Cryst. Solids*, **1980**, 37, 191-201.
- [98]. C. J. Brinker, Hydrolysis and condensation of silicates: Effects on structure, *J. Non-Cryst. Solids*, **1988**, 100, 31-50.
- [99]. N. N. Khimich, Synthesis of silica gels and organic-inorganic hybrids on their base, *Glass Phys. Chem.*, **2004**, 30, 430-442.
- [100]. L. L. Hench, J. K. West, The sol-gel process, *Chem. Rev.*, **1990**, 90, 33-72.
- [101]. J. Livage, M. Henry, C. Sanchez, Sol-gel chemistry of transition metal oxides, *Prog. Solid State Chem.*, **1988**, 18, 259-341.
- [102]. L. C. Klein, *Sol-Gel Technology for Thin Films, Fibers, Preforms, Electronics and Specialty Shapes*, Noyes Publications: Park Ridge, N.J., **1988**, 37-85.
- [103]. B. E. Yoldas, Modification of polymer-gel structures, *J. Non-Cryst. Solids*, **1984**, 63, 145-154.
- [104]. K. A. Andrianov, *Metal organic polymers*, Wiley, New York, **1965**.
- [105]. M. G. Voronkov, V. P. Mileshkevich, Y. A. Yuzhelevski, *The siloxane bond*, Consultants Bureau, New York, **1978**.
- [106]. C. Savii, L. Almásy, C. Ionescu, N. K. Székely, C. Enache, M. Popovici, I. Sora, D. Nicoara, G. G. Savii, D. S. Resiga, J. Subrt, V. Štengl, Mesoporous silica matrices derived from sol-gel process assisted by low power ultrasonic activation, *Proces. Applic. Ceram.*, **2009**, 3(1-2), 59-64.
- [107]. C. J. Brinker, G.W. Scherer, Sol \rightarrow gel \rightarrow glass: I. Gelation and gel structure, *J. Non-Cryst. Solids*, **1985**, 70, 301-322.
- [108]. <http://www.psrc.usm.edu/mauritz/solgel.html>.
- [109]. K. J. D. MacKenzie and M. E. Smith, *Multinuclear Solid State NMR of Inorganic Materials*, Pergamon Press, **2002**.
- [110]. C. A. Fyfe, *Solid State NMR for Chemists*, C. F. C. Guelph, Ontario, **1983**.
- [111]. H. Eckert, Structural characterization of noncrystalline solids and glasses using solid state NMR, *Progress in NMR Spectroscopy*, **1992**, 2, 159-293.

- [112]. J. J. Fitzgerald and S. M. de Paul, Chapter 1. Solid state NMR spectroscopy of inorganic materials: an overview, in *Solid state NMR of inorganic materials*, **1998**, 2-133.
- [113]. E. M. Purcell, H. C. Torrey, R. V. Pound, Resonance Absorption by Nuclear Magnetic Moments in a Solid, *Phys. Rev.*, **1946**, *69*, 37-38.
- [114]. F. Bloch, W. W. Hansen, M. Packard, Nuclear induction, *Phys. Rev.*, **1946**, *69*, 127.
- [115]. M. H. Levitt, *Spin Dynamics: basics of nuclear magnetic resonance*, Wiley, **2001**.
- [116]. M. J. Duer, *Solid State NMR, Principles and Applications*, Blackwell Science, **2002**.
- [117]. R. K. Harris, *Nuclear Magnetic Resonance Spectroscopy - A Physicochemical View*, Longman Scientific & Technical, Essex, **1994**.
- [118]. M. Mehring, *Principles of High Resolution NMR in Solids*, Springer-Verlag, Berlin, **1983**.
- [119]. J. Mason, Conventions for the reporting of nuclear magnetic shielding (or shift) tensors suggested by participants in the NATO ARW on NMR Shielding Constants at the University of Maryland, College Park, July 1992, *Solid State NMR*, **1993**, *2*, 285-288.
- [120]. G. E. Pake, NMR in hydrated crystals: fine structure of the proton line, *J. Chem. Phys.*, **1948**, *16*, 327-336.
- [121]. C. A. Fyfe, H. Grondey, Y. Feng, G. T. Kokotailo, Investigation of the three-dimensional Si-O-Si connectivities in the monoclinic form of zeolite ZSM-5 by two-dimensional ^{29}Si INADEQUATE experiments, *Chem. Phys. Lett.*, **1990**, *173*, 211-215.
- [122]. L. Olivier, X. Yuan, A. N. Cormack, C. Jäger, Combined ^{29}Si double quantum NMR and MD simulation studies of network connectivities of binary $\text{Na}_2\text{O}\cdot\text{SiO}_2$ glasses: new prospects and problems, *J. Non-Cryst. Solids*, **2001**, *293*, 53-66.
- [123]. C. Coelho, T. Azais, L. Bonhomme-Coury, J. Maquet, D. Massiot, C. Bonhomme, Application of the MAS-J-HMQC experiment to a new pair of nuclei $\{^{29}\text{Si}, ^{31}\text{P}\}$: $\text{Si}_5\text{O}(\text{PO}_4)_6$ and SiP_2O_7 polymorphs, *J. Magn. Reson.*, **2006**, *179*, 114-119.
- [124]. B. Alonso, D. Massiot, F. Babonneau, G. Brusatin, G. D. Giustina, T. Kidchob, P. Innocenzi, Structural control in germania hybrid organic-inorganic materials, *Chem. Mater.*, **2005**, *17*, 3172-3180.
- [125]. D. Laurencin, C. Gervais, A. Wong, C. Coelho, F. Mauri, D. Massiot, M. E. Smith, C. Bonhomme, Implementation of high resolution ^{43}Ca solid state NMR spectroscopy: toward the elucidation of calcium sites in biological materials, *J. Am. Chem. Soc.*, **2009**, *131*, 13430-13440.
- [126]. M. H. Cohen, F. Reif, Quadrupole effects in nuclear magnetic resonance studies of solids, in F. Seitz (Ed.), New York: Academic Press, *Solid state physics*, **1957**, *5*, 321-438.
- [127]. S. E. Ashbrook, Recent advances in solid-state NMR spectroscopy of quadrupolar nuclei, *Phys. Chem. Chem. Phys.*, **2009**, *11*, 6892-6905.
- [128]. E. R. Andrew, The narrowing of NMR spectra of solids by high-speed specimen rotation and the resolution of chemical shift and spin multiplet structures for solids, *Prog. Nucl. Magn. Reson. Spectrosc.*, **1971**, *8*, 1-39.

- [129]. E. R. Andrew, Magic angle spinning, *Int. Rev. Phys. Chem.*, **1981**, *1*(2), 195-224.
- [130]. M. M. Maricq, J. S. Waugh, NMR in rotating solids, *J. Chem. Phys.*, **1979**, *70*, 3300-3316.
- [131]. B. C. Gerstein, R. G. Pembleton, R. C. Wilson, L. M. Ryan, High-resolution NMR in randomly oriented solids with homonuclear dipolar broadening-combined multiple pulse NMR and magic angle spinning, *J. Chem. Phys.*, **1977**, *66*, 361-362.
- [132]. G. Scheler, U. Haubenreisser, H. Rosenberger, High-resolution ^1H -NMR in solids with multiple-pulse sequences and magic-angle sample spinning at 270-MHz, *J. Magn. Reson.*, **1981**, *44*, 134-144.
- [133]. R. K. Harris, P. Jackson, L. H. Merwin, B. J. Say, G. Hagele, Perspectives in high-resolution solid-state nuclear magnetic-resonance, with emphasis on combined rotation and multiple-pulse spectroscopy, *J. Chem. Soc. Faraday Trans.*, **1988**, *84*, 3649-3672.
- [134]. B. C. Gerstein, CRAMPS, In *Encyclopedia of Nuclear Magnetic Resonance*, D. M. Grant and R. K. Harris, Eds., John Wiley & Sons, New York, **1996**, 1501-1509.
- [135]. M. Lee, W. I. Goldberg, Nuclear-magnetic-resonance line narrowing by a rotating rf field, *Phys. Rev.*, **1965**, *140*, A1261.
- [136]. M. Mehring, J. S. Waugh, Magic-angle NMR experiments in solids, *Phys. Rev. B*, **1972**, *5*, 3459-3471.
- [137]. A. Bielecki, A. C. Kolbert, and M. H. Levitt, Frequency-switched pulse sequences- homonuclear decoupling and dilute spin NMR in solids, *Chem. Phys. Lett.*, **1989**, *155*, 341-346.
- [138]. M. H. Levitt, A. Bielecki, A. C. Kolbert, D. J. Ruben, Frequency switched pulse sequences: Homonuclear decoupling and dilute spin NMR in solids, *Solid State NMR*, **1993**, *2*, 151.
- [139]. E. Vinogradov, P. K. Madhu, S. Vega, High-resolution proton solid-state NMR spectroscopy by phase-modulated Lee-Goldburg experiment, *Chem. Phys. Lett.*, **1999**, *314*, 443-450.
- [140]. D. Sakellariou, A. Lesage, P. Hodgkinson, L. Emsley, Homonuclear dipolar decoupling in solid-state NMR using continuous phase modulation, *Chem. Phys. Lett.*, **2000**, *319*, 253-260.
- [141]. A. Lesage, D. Sakellariou, S. Hediger, B. Elena, P. Charmont, S. Steuernagel, L. Emsley, Experimental aspects of proton NMR spectroscopy in solids using phase-modulated homonuclear dipolar decoupling, *J. Magn. Reson.*, **2003**, *163*, 105-113.
- [142]. B. Elena, G. de Paëpe, L. Emsley, Direct spectral optimisation of proton-proton homonuclear dipolar decoupling in solid-state NMR, *Chem. Phys. Lett.*, **2004**, *398*, 532-538.
- [143]. E. Salager, R. S. Stein, S. Steuernagel, A. Lesage, B. Elena, L. Emsley, Enhanced sensitivity in high-resolution ^1H solid-state NMR spectroscopy with DUMBO dipolar decoupling under ultra-fast MAS, *Chem. Phys. Lett.*, **2009**, *469*, 336-341.
- [144]. S. R. Hartmann, E. L. Hahn, Nuclear double resonance in the rotating frame, *Phys. Rev.*, **1962**, *128*, 2042-2053.
- [145]. A. Pines, M. G. Gibby, J. S. Waugh, Proton-enhanced NMR of dilute spins in solids, *J. Chem. Phys.*, **1973**, *59*, 569-590.

- [146]. J. Schaefer and E. O. Stejskal, ^{13}C nuclear magnetic-resonance of polymers spinning at magic angle, *J. Am. Chem. Soc.*, **1976**, *98*, 1031-1032.
- [147]. J. Jeener, Ampère International Summer school, Basko Polje, Yugoslavia, **1971**.
- [148]. W. P. Aue, J. Karhan, R. R. Ernst, Homonuclear broad-band decoupling and 2-dimensional J-resolved NMR spectroscopy, *J. Chem. Phys.*, **1976**, *64*, 4226–4227.
- [149]. R. R. Ernst, G. Bodenhausen, A. Wokaun, *Principles of Nuclear Magnetic Resonance in One and Two Dimensions*, Clarendon Press, Oxford, England, **1987**.
- [150]. G. Bodenhausen, R. Freeman, R. Niedermeyer, D. L. Turner, Double Fourier transformation in high-resolution NMR, *J. Magn. Res.*, **1977**, *26*, 133-164.
- [151]. P. J. Hore, J. A. Jones, S. Wimperis, *NMR: the toolkit*, Oxford Chemistry Primers 92, Oxford University Press, Oxford, **2004**.
- [152]. S. P. Brown, H. W. Spiess, Advanced solid-state NMR methods for the elucidation of structure and dynamics of molecular, macromolecular, and supramolecular systems, *Chem. Rev.*, **2001**, *101*, 4125-4155.
- [153]. H. W. Spiess, Double-Quantum NMR Spectroscopy of Dipolar Coupled Spins Under Fast Magic Angle Spinning, In *Encyclopedia of Nuclear Magnetic Resonance*, D. M. Grant and R. K. Harris, Eds., John Wiley & Sons, Chichester, UK, **2002**, 44-59.
- [154]. P. K. Madhu, E. Vinogradov, S. Vega, Multiple-pulse and magic-angle spinning aided double-quantum proton solid-state NMR spectroscopy, *Chem. Phys. Lett.*, **2004**, *394*, 423-428.
- [155]. S. P. Brown, A. Lesage, B. Elena, L. Emsley, Probing Proton-Proton Proximities in the Solid State: High-Resolution Two-Dimensional ^1H - ^1H Double-Quantum CRAMPS NMR Spectroscopy, *J. Am. Chem. Soc.*, **2004**, *126*, 13230-13231.
- [156]. S. P. Brown, Probing proton-proton proximities in the solid state, *Prog. Nucl. Magn. Reson. Spectrosc.*, **2007**, *50*, 199-251.
- [157]. A. J. Vega, Heteronuclear chemical-shift correlations of silanol groups studied by two-dimensional cross-polarization magic angle spinning NMR, *J. Am. Chem. Soc.*, **1988**, *110*, 1049-1054.
- [158]. B. -J. van Rossum, C. P. de Groot, V. Ladizhansky, S. Vega, H. J. M. de Groot, A method for measuring heteronuclear (^1H - ^{13}C) distances in high speed MAS NMR, *J. Am. Chem. Soc.*, **2000**, *122*, 3465-3472.
- [159]. A. Brinkmann, M. H. Levitt, Symmetry principles in the nuclear magnetic resonance of spinning solids: Heteronuclear recoupling by generalized Hartmann–Hahn sequences, *J. Chem. Phys.*, **2001**, *115*, 357-384
- [160]. X. Zhao, M. Edén, M. H. Levitt, Recoupling of heteronuclear dipolar interactions in solid-state NMR using symmetry-based pulse sequences, *Chem. Phys. Lett.*, **2001**, *342*, 353-361.
- [161]. L. Frydman, J. S. Harwood, Isotropic spectra of half-integer quadrupolar spins from bidimensional magic-angle spinning NMR, *J. Am. Chem. Soc.* **1995**, *117*, 5367-5368.
- [162]. A. Medek, J. S. Harwood, L. Frydman, Multiple-quantum magic-angle spinning NMR: a new method for the study of quadrupolar spins in a solid, *J. Am. Chem. Soc.*, **1995**, *117*, 12779-12787.

- [163]. S. P. Brown, S. Wimperis, Two-dimensional multiple-quantum MAS NMR of quadrupolar nuclei: A comparison of methods, *J. Magn. Reson.*, **1997**, *128*, 42–61
- [164]. P. J. Hore, *Nuclear magnetic resonance*, Oxford Chemistry Primers 32, Oxford University press, **1995**.
- [165]. D. L. Bryce, G. M. Bernard, M. Gee, M. D. Lumsden, K. Eichele, R. E. Wasylishen, Practical aspects of modern routine solid-state multinuclear magnetic resonance spectroscopy: one-dimensional experiments, *Can. J. Anal. Sci. Spectrosc.*, **2001**, *46*, 46-82.
- [166]. T. C. Farrar, E. D. Becker, Pulse and Fourier transform NMR: introduction to theory and methods, Academic Press Inc., New York, **1971**.
- [167]. A. D. Bain, I. W. Burton, Quadrature detection in one or more dimensions, *Concepts Magn. Reson.*, **1996**, *8*, 191-204.
- [168]. P. Bachmann, W. P. Aue, L. Müller, R. R. Ernst, Phase separation in two-dimensional spectroscopy, *J. Magn. Res.*, **1977**, *28*, 29-39.
- [169]. D. J. States, R. A. Haberkorn, and D. J. Ruben, A Two-Dimensional Nuclear Overhauser Experiment with Pure Absorption Phase in 4 Quadrants, *J. Magn. Reson.*, **1982**, *48*, 286-292.
- [170]. D. Marion, K. Wüthrich, Application of phase sensitive two-dimensional correlated spectroscopy (COSY) for measurements of ^1H ^1H spin-spin coupling constants in proteins, *Biochem. Biophys. Res. Commun.*, **1983**, *113*, 967-974.
- [171]. D. Marion, M. Ikura, R. Tschudin, A. Bax, Rapid recording of 2D NMR-spectra without phase cycling - application to the study of hydrogen-exchange in proteins," *J. Magn. Reson.*, **1989**, *85*, 393-399.
- [172]. D. D. Traficante, Phase-sensitive detection. Part II: quadrature phase detection, *Concepts Magn. Reson.*, **1990**, *2*, 181-195.
- [173]. M. E. Smith, E. R. H. van Eck, Recent advances in experimental solid state NMR methodology for half-integer spin quadrupolar nuclei, *Prog. Nucl. Magn. Reson. Spectrosc.*, **1999**, *34*, 159–201.
- [174]. P. P. Man, J. Klinowski, A. Trokiner, H. Zanni, P. Papon, Selective and non-selective NMR excitation of quadrupolar nuclei in the solid state, *Chem. Phys. Lett.*, **1988**, *151*, 143-150.
- [175]. E. L. Hahn, Spin echoes, *Phys. Rev.*, **1950**, *80*, 580-594.
- [176]. O. B. Peersen, X. L. Wu, I. Kustanovich, S. O. Smith, Variable-amplitude cross-polarization MAS NMR, *J. Magn. Reson. Ser. A*, **1993**, *104*, 334-339.
- [177]. G. Metz, X. L. Wu, S. O. Smith, Ramped-amplitude cross-polarization in magic-angle-spinning NMR, *J. Magn. Reson. Ser. A*, **1994**, *110*, 219-227.
- [178]. S. Hediger, B. H. Meier, N. D. Kurur, G. Bodenhausen, R. R. Ernst, NMR Cross-polarization by adiabatic passage through the Hartmann-Hahn condition (APHH), *Chem. Phys. Lett.*, **1994**, *223*, 283-288.
- [179]. B. M. Fung, A. K. Khitrin, K. Ermolaev, An improved broadband decoupling sequence for liquid crystals and solids, *J. Mag. Res.*, **2000**, *142*, 97–101.
- [180]. A. Lesage, Recent advances in solid-state NMR spectroscopy of spin $I = 1/2$ nuclei, *Phys. Chem. Chem. Phys.*, **2009**, *11*, 6876-6891.
- [181]. J. P. Bradley, C. Tripon, C. Filip, S. P. Brown, Determining relative proton-proton proximities from the build-up of two-dimensional correlation peaks in ^1H double-quantum MAS NMR: insight from multi-spin density-matrix simulations, *Phys. Chem. Chem. Phys.*, **2009**, *11*, 6941-6952.

- [182]. S. Dusold, A. Sebald, Dipolar recoupling under magic-angle spinning conditions, *Annual Reports on NMR Spectroscopy*, **2000**, *41*, 185-264.
- [183]. M. H. Levitt, Symmetry-Based Pulse Sequences in Magic-Angle Spinning Solid-State NMR, in *Encyclopedia of Nuclear Magnetic Resonance*, **2002**, *9*, 165-196.
- [184]. A. Brinkmann, M. Edén, M. H. Levitt, Synchronous helical pulse sequences in magic-angle spinning nuclear magnetic resonance: Double quantum recoupling of multiple-spin systems, *J. Chem. Phys.*, **2000**, *112*, 8539-8554.
- [185]. M. Hohwy, H. J. Jakobsen, M. Edén, M. H. Levitt, N. C. Nielsen, Broadband Dipolar Recoupling in the Nuclear Magnetic Resonance of Rotating Solids: A Compensated C7 Pulse Sequence," *J. Chem. Phys.*, **1998**, *108*, 2686-2694.
- [186]. J. P. Amoureux, C. Fernandez, S. Steuernagel, Z Filtering in MQMAS NMR, *J. Magn. Reson. A*, **1996**, *123*, 116-118.
- [187]. S. C. Kohn, R. Dupree, M. E. Smith, Proton environments and hydrogen-bonding in hydrous silicate glasses from proton NMR, *Nature*, **1989**, *337*, 539-541.
- [188]. R. J. Kirkpatrick, R. K. Brow, Nuclear magnetic resonance investigation of the structures of phosphate and phosphate-containing glasses: a review, *Solid State Nucl. Magn. Reson.*, **1995**, *5*, 9-21.
- [189]. R. K. Brow, Review: the structure of simple phosphate glasses, Section 1. Structure, *J. Non-Cryst. Solids*, **2000**, *263-264*, 1-28
- [190]. H. Koller, G. Engelhardt, A. Kentgens, J. Sauer, ²³Na NMR spectroscopy of solids: interpretation of quadrupole interaction parameters and chemical shifts, *J. Phys. Chem.*, **1994**, *98*, 1544-1551.
- [191]. R. Dupree, A. P. Howes, S. C. Kohn, Natural abundance solid state ⁴³Ca NMR, *Chem. Phys. Lett.*, **1997**, *276*, 399-404.
- [192]. Z. Lin, M. E. Smith, F. E. Sowrey, R. J. Newport, Probing the local structural environment of calcium by natural-abundance solid-state ⁴³Ca NMR, *Physical Review B*, **2004**, *69*, 224107-1-7.
- [193]. A. Wong, A. P. Howes, R. Dupree, M. E. Smith, Natural abundance ⁴³Ca NMR study of calcium-containing organic solids: a model study for Ca-binding biomaterials, *Chem. Phys. Lett.*, **2006**, *427*, 201-205.
- [194]. F. Angeli, M. Gaillard, P. Jollivet, T. Charpentier, Contribution of ⁴³Ca MAS NMR for probing the structural configuration of calcium in glass, *Chem. Phys. Lett.*, **2007**, *440*, 324-328.
- [195]. D. L. Bryce, E. B. Bultz, D. Aebi, Calcium-43 chemical shift tensors as probes of calcium binding environments. Insight into the structure of the vaterite CaCO₃ polymorph by ⁴³Ca solid-state NMR spectroscopy, *J. Am. Chem. Soc.*, **2008**, *130*, 9282-9292.
- [196]. A. Wong, D. Laurencin, G. Wu, R. Dupree, M. E. Smith, An Ab Initio quantum chemical investigation of ⁴³Ca NMR interaction parameters for the Ca²⁺ sites in organic complexes and in metalloproteins, *J. Phys. Chem. A*, **2008**, *112*, 9807-9813.
- [197]. C. Gervais, D. Laurencin, A. Wong, F. Pourpoint, B. Woodward, A. P. Howes, K. J. Pike, R. Dupree, F. Mauri, C. Bonhomme, M. E. Smith, New perspectives on calcium environments in inorganic materials containing calcium-oxygen bonds: a combined computational-experimental ⁴³Ca NMR approach, *Chem. Phys. Lett.*, **2008**, *464*, 42-48.

- [198]. D. Laurencin, A. Wong, R. Dupree, M. E. Smith, Natural abundance ^{43}Ca solid-state NMR characterisation of hydroxyapatite: identification of the two calcium sites, *Magn. Reson. Chem.*, **2008**, *46*, 347–350.
- [199]. D. Laurencin, A. Wong, J. V. Hanna, R. Dupree, M. E. Smith, A high-resolution ^{43}Ca solid-state NMR study of the calcium sites of hydroxyapatite, *J. Am. Chem. Soc.*, **2008**, *130*, 2412–2413.
- [200]. H. Pizzala, S. Caldarelli, J.-G. Eon, A. M. Rossi, D. Laurencin, M. E. Smith, A Solid-State NMR Study of Lead and Vanadium Substitution into Hydroxyapatite, *J. Am. Chem. Soc.*, **2009**, *131*, 5145–5152.
- [201]. A. Wong, D. Laurencin, R. Dupree, M. E. Smith, Two-dimensional ^{43}Ca – ^1H correlation solid-state NMR spectroscopy, *Solid State Nucl. Magn. Reson.*, **2009**, *35*, 32–36.
- [202]. A. Trokiner, P. -V. Bellot, Y. Zhdanov, A. Yakubovskii, NMR determination of the Sternheimer antishielding factor of Ca^{2+} , *Solid State NMR*, **2000**, *16*, 171–175.
- [203]. K. Shimoda, Y. Tobu, K. Kanehashi, T. Nemoto, K. Saito, Local environments of slags: the first application of ^{43}Ca 3QMASNMR technique, *Chem. Lett.*, **2005**, *34*, 1588–1589.
- [204]. K. Shimoda, Y. Tobu, K. Kanehashi, K. Saito, and T. Nemoto, First evidence of multiple Ca sites in amorphous slag structure: Multiple-quantum MAS NMR spectroscopy on calcium-43 at high magnetic field, *Solid State NMR*, **2006**, *30*, 198–202.
- [205]. K. Shimoda, Y. Tobu, Y. Shimoikeda, T. Nemoto, and K. Saito, Multiple Ca^{2+} environments in silicate glasses by high-resolution ^{43}Ca MQMAS NMR technique at high and ultra-high (21.8 T) magnetic fields, *J. Magn. Res.*, **2007**, *186*, 156–159.
- [206]. G. M. Bowers, R. J. Kirkpatrick, Natural abundance ^{43}Ca NMR spectroscopy of tobermorite and jennite: Models for the C-S-H structure, *J. Am. Ceram. Soc.*, **2009**, *92*, 545–548.
- [207]. S. Fujibayashi, M. Neo, H. -M. Kim, T. Kokubo, T. Nakamura, A comparative study between *in vivo* bone ingrowth and *in vitro* apatite formation on Na_2O – CaO – SiO_2 glasses, *Biomaterials*, **2003**, *24*, 1349–1356.
- [208]. J. R. Jones, P. Sepulveda and L. L. Hench, Dose-dependent behavior of bioactive glass dissolution, *J. Biomed. Mater. Res.*, **2001**, *58*, 720–726.
- [209]. J. R. Jones, L. M. Ehrenfried, L. L. Hench, Optimising bioactive glass scaffolds for bone tissue engineering, *Biomaterials*, **2006**, *27*, 964–973.
- [210]. L. J. Skipper, F. E. Sowrey, R. Rashid, R. J. Newport, Z. Lin, M. E. Smith, X-ray diffraction and solid state NMR studies of the growth of hydroxyapatite on bioactive calcia:silica sol-gel glasses, *Phys. Chem. Glasses.*, **2005**, *46* (4), 372–376.
- [211]. T. W. T. Tsai, Y. Moua, Y.-H. Tseng, L. Zhang, J. C. C. Chan, Solid-state NMR study of bioactive binary borosilicate glasses, *J. Phys. Chem. Solids*, **2008**, *69*, 2628–2633.
- [212]. R. H. Glaser, G. L. Wilkes, E. Bronnimann, Solid-state ^{29}Si NMR of TEOS-based multifunctional sol-gel materials, *J. Non-Cryst. Solids*, **1989**, *113*, 73–87.
- [213]. D. W. Sindorf, G.E. Maciel, ^{29}Si NMR study of dehydrated/rehydrated silica gel using cross polarization and magic-angle spinning, *J. Am. Chem. Soc.*, **1983**, *105*, 1487–1493.

- [214]. I. -S. Chuang, D. R. Kinney, G. E. Maciel, Interior hydroxyls of the silica gel system as studied by silicon-29 CP-MAS NMR spectroscopy, *J. Am. Chem. Soc.*, **1993**, *115*, 8695-8705.
- [215]. I. -S. Chuang, G. E. Maciel, A detailed model of local structure and silanol hydrogen bonding of silica gel surfaces, *J. Phys. Chem. B*, **1997**, *101*, 3052-3064.
- [216]. X. Xue, M. Kanzaki, Dissolution mechanisms of water in depolymerised silicate melts: Constraints from ^1H and ^{29}Si NMR spectroscopy and ab initio calculations, *Geoch. Cosmoch. Acta*, **2004**, *68*, 5027-5057.
- [217]. K. A. Koyano, T. Tatsumi, Y. Tanaka, S. Nakata, Stabilization of Mesoporous Molecular Sieves by Trimethylsilylation, *J. Phys. Chem. B*, **1997**, *101*, 9436-9440.
- [218]. H. El Rassy, A. C. Pierre, NMR and IR spectroscopy of silica aerogels with different hydrophobic characteristics, *J. Non-Cryst. Solids*, **2005**, *351*, 1603-1610.
- [219]. C. J. Brinker, K. D. Keefer, D. W. Schaefer, R. A. Assink, B. D. Kay, C. S. Ashley, Sol-gel transition in simple silicates II, *J. Non-Cryst. Solids*, **1984**, *63*, 45-59.
- [220]. J. -B. d'Espinose de la Caillerie, M. R. Aimeur, Y. E. Kortobi, A. P. Legrand, Water Adsorption on Pyrogenic Silica Followed by ^1H MAS NMR, *J. Colloid Interf. Sci.*, **1997**, *194*, 434-439.
- [221]. C. C. Liu, G. E. Maciel, The Fumed Silica Surface: A Study by NMR, *J. Am. Chem. Soc.*, **1996**, *118*, 5103-5119.
- [222]. N. Baccile, G. Laurent, C. Bonhomme, P. Innocenzi, F. Babonneau, Solid-State NMR Characterization of the Surfactant-Silica Interface in Templated Silicas: Acidic versus Basic Conditions, *Chem. Mater.*, **2007**, *19*, 1343-1354.
- [223]. F. Meducin, B. Bresson, N. Lequeux, M. D. Noirfontaine, H. Zanni, Calcium silicate hydrates investigated by solid state high resolution ^1H and ^{29}Si nuclear magnetic resonance, *Cement Concrete Res.*, **2007**, *37*, 631-638.
- [224]. D. Massiot, F. Fayon, M. Capron, I. King, S. Le Calvé, B. Alonso, J. Durand, B. Bujoli, Z. Gan and G. Hoatson, Modelling one- and two-dimensional solid-state NMR spectra, *Magn. Reson. Chem.*, **2002**, *40*, 70-76.
- [225]. G. Engelhardt D. Michel, *High-Resolution Solid-State NMR of Silicates and Zeolites*; Wiley: Chicester, **1987**.
- [226]. G. Engelhardt, M. Nofz, K. Forkel, F. G. Wihsmann, M. Mägi, A. Samoson, E. Lippmaa, Structural studies of calcium aluminosilicate glasses by high resolution solid state ^{29}Si and ^{27}Al magic angle spinning nuclear magnetic resonance, *Phys. Chem. Glasses*, **1985**, *26*, 157-165.
- [227]. P. Zhang, P. J. Grandinetti, J. F. Stebbins, Anionic species determination in CaSiO_3 glass using two-dimensional ^{29}Si NMR, *J. Phys. Chem. B*, **1997**, *101*, 4004-4008
- [228]. G. E. Maciel, D.W. Sindorf, Silicon-29 nuclear magnetic resonance study of the surface of silica gel by cross polarization and magic-angle spinning, *J. Am. Chem. Soc.*, **1980**, *102*, 7606-7607.
- [229]. A. van Blaaderen, A. P. M. Kentgens, Particle morphology and chemical microstructure of colloidal silica spheres made from alkoxyxilanes, *J. Non-Cryst. Solids*, **1992**, *149*, 161-178.
- [230]. R. J. Newport, L. J. Skipper, D. Carta, D. M. Pickup, F. E. Sowrey, M. E. Smith, P. Saravanapavan and L. L. Hench, The use of advanced diffraction

- methods in the study of the structure of a bioactive calcia: silica sol-gel glass, *J. Mater. Sci.: Mater. Med.*, **2006**, *17*, 1003–1010.
- [231]. S. C. Kohn, Solubility of H₂O in nominally anhydrous mantle minerals using ¹H MAS NMR, *Am. Mineral.*, **1996**, *81*, 1523-1526.
- [232]. V. F. FitzGerald, R. M. Martin, J. R. Jones, D. Qiu, K.M. Wetherall, R. Moss, R. J. Newport, Bioactive glass sol-gel foam scaffolds: evolution of nanoporosity during processing and in situ monitoring of apatite layer formation using small and wide angle X-ray scattering, *J. Biomed. Mater. Res.*, **2009**, *91A*, 76–83.
- [233]. J. Trébosc, J. W. Wiench, S. Huh, V. S. Y. Lin, M. Pruski, Solid-state NMR study of MCM-41-type mesoporous silica nanoparticles, *J. Am. Chem. Soc.* **2005**, *127*, 3057-3068.
- [234]. A. J. Salinas, M. Vallet-Regí, I. Izquierdo-Barba, Biomimetic Apatite Deposition on Calcium Silicate Gel Glasses, *J. Sol-Gel Sci. Technol.*, **2001**, *21*, 13–25.
- [235]. P. Saravanapavan, J. R. Jones, R. S. Pryce, L. L. Hench, Bioactivity of gel-glass powders in the CaO-SiO₂ system: A comparison with ternary (CaO-P₂O₅-SiO₂) and quaternary glasses (SiO₂-CaO-P₂O₅-Na₂O), *J. Biomed. Mater. Res.*, **2003**, *66A*, 110–119.
- [236]. M. Vallet-Regí, A. J. Salinas, J. Ramirez-Castellanos, J. M. Gonzalez-Calbet, Nanostructure of bioactive sol-gel glasses and organic-inorganic hybrids, *Chem. Mater.*, **2005**, *17*, 1874–1879.
- [237]. S. Padila, J. Román, A. Carenas, M. Vallet-Regí, The influence of the phosphorus content on the bioactivity of sol-gel glass ceramics, *Biomaterials*, **2005**, *26*, 475-483.
- [238]. L. L. Hench, J. K. West, Biological applications of bioactive glasses, *Life Chem. Rep.*, **1996**, *13*, 187–241.
- [239]. Y. Ebisawa, T. Kokubo, K. Ohura, T. Yamamuro, Bioactivity of CaO-SiO₂ based glasses: in vitro evaluation, *J. Mater. Sci.: Mater. Med.*, **1990**, *1*, 239–244.
- [240]. A. Rámila, F. Balas, M. Vallet-Regí, Synthesis Routes for Bioactive Sol-Gel Glasses: Alkoxides versus Nitrates, *Chem. Mater.*, **2002**, *14*, 542-548.
- [241]. M. Vallet-Regí, A. M. Romero, V. Ragel, R. Z. LeGeros, XRD, SEM-EDS, and FTIR studies of *in vitro* growth of an apatite-like layer on sol-gel glasses, *J. Biomed. Mater. Res.*, **1999**, *44*, 416-421.
- [242]. M. Vallet-Regí, A. Rámila, New bioactive glass and changes in porosity during the growth of a carbonate hydroxyapatite layer on glass surfaces, *Chem. Mater.*, **2000**, *12*, 961-965.
- [243]. D. Carta, J. C. Knowles, M. E. Smith, R. J. Newport, Synthesis and structural characterization of P₂O₅-CaO-Na₂O sol-gel materials, *J. Non-Cryst. Solids*, **2007**, *353*, 1141–1149.
- [244]. D. Carta, D. M. Pickup, J. C. Knowles, I. Ahmed, M. E. Smith, R. J. Newport, A structural study of sol-gel and melt-quenched phosphate-based glasses, *J. Non-Cryst. Solids*, **2007**, *353*, 1759–1765.
- [245]. E. Leonova, I. Izquierdo-Barba, D. Arcos, A. López-Noriega, N. Hedin, M. Vallet-Regí, M. Edén, Multinuclear Solid-State NMR Studies of Ordered Mesoporous Bioactive Glasses, *J. Phys. Chem. C*, **2008**, *112*, 5552-5562.
- [246]. D. M. Pickup, S. P. Valappil, R. M. Moss, H. L. Twyman, P. Guerry, M. E. Smith, M. Wilson, J. C. Knowles, R. J. Newport, Preparation, structural characterisation and antibacterial properties of Ga-doped sol-gel phosphate-based glass, *J. Mater. Sci.*, **2009**, *44*, 1858–1867.

- [247]. C. E. Bronnimann, R. C. Zeigler, G. E. Maciel, Proton NMR Study of Dehydration of the Silica Gel Surface, *J. Am. Chem. Soc.*, **1988**, *110*, 2023-2026.
- [248]. Z. R. Hinedi, S. Goldberg, A. C. Chang, J. P. Yesinowski, A ^{31}P and ^1H MAS NMR study of phosphate sorption onto calcium carbonate, *J. Colloid Interf. Sci.*, **1992**, *152*, 141-160.
- [249]. J. P. Yesinowski, H. Eckert, G. R. Rossmant, Characterization of hydrous species in minerals by high-speed ^1H MAS-NMR, *J. Am. Chem. Soc.*, **1988**, *110*, 1367-1375.
- [250]. J. P. Yesinowski, H. Eckert, Hydrogen environments in calcium phosphates: ^1H MAS NMR at high spinning speeds, *J. Am. Chem. Soc.*, **1987**, *109*, 6274-6282.
- [251]. K. S. K. Lin, Y.-H. Tseng, Y. Mou, Y.-C. Hsu, C. -M. Yang, J. C. C. Chan, Mechanistic study of apatite formation on bioactive glass surface using ^{31}P solid-state NMR spectroscopy, *Chem. Mater.* **2005**, *17*, 4493-4501.
- [252]. G. Gasquères, C. Bonhomme, J. Maquet, F. Babonneau, S. Hayakawa, T. Kanaya, A. Osaka, Revisiting silicate substituted hydroxyapatite by solid-state NMR, *Magn. Res. Chem.*, **2008**, *46*, 342-346.
- [253]. F. Tian, L. Pan, X. Wu, F. Wu, The NMR studies of the $\text{P}_2\text{O}_5\text{-SiO}_2$ sol and gel chemistry *J. Non-Cryst. Solids*, **1988**, *104*, 129-134.
- [254]. G. Busca, V. Lorenzelli, Infrared spectroscopic identification of species arising from reactive adsorption of carbon oxides on metal oxide surfaces, *Mater. Chem.*, **1982**, *7*, 89-126.
- [255]. P. Regnier, A. C. Lasaga, R. A. Bern, O. H. Han, K. W. Zilm, Mechanism of CO_3^{2-} substitution in carbonate-fluorapatite: Evidence from FTIR spectroscopy, ^{13}C NMR and quantum mechanical calculations, *Am. Mineral.*, **1994**, *79*, 809-818.
- [256]. M. Cerruti, C. Morterra, Carbonate formation on bioactive glasses, *Langmuir*, **2004**, *20*, 6382-6388.
- [257]. F. M. Michel, J. MacDonald, J. Feng, B. L. Phillips, L. Ehm, C. Tarabrella, J. B. Parise, R. J. Reeder, Structural characteristics of synthetic amorphous calcium carbonate, *Chem. Mater.* **2008**, *20*, 4720-4728.
- [258]. H. Nebel, M. Neumann, C. Mayer, M. Epple, On the structure of amorphous calcium carbonates - a detailed study by solid-state NMR spectroscopy, *Inorg. Chem.*, **2008**, *47*, 7874-7879.
- [259]. K. Beshah, C. Rey, M. J. Glimcher, M. Schimizu, R. G. Griffin Solid State Carbon-13 and Proton NMR Studies of Carbonate-Containing Calcium Phosphates and Enamel, *J. Solid State Chem.*, **1990**, *84*, 71-81.
- [260]. R. M. Wilson, S. E. P. Dowker, J. C. Elliott, Rietveld refinements and spectroscopic structural studies of a Na-free carbonate apatite made by hydrolysis of monetite, *Biomaterials*, **2006**, *27*, 4682-4692.
- [261]. H. E. Mason, A. Kozłowski, B. L. Phillips, Solid-State NMR study of the role of H and Na in AB-type carbonate hydroxylapatite, *Chem. Mater.*, **2008**, *20*, 294-302.
- [262]. S. C. Kohn, R. A. Brooker, R. Dupree, ^{13}C MAS NMR: A method for studying CO_2 speciation in glasses, *Geoch. Cosmoch. Acta*, **1991**, *55*, 3879-3884.
- [263]. J. García, T. López, M. Álvarez, D. H. Aguilar, P. Quintana, Spectroscopic, structural and textural properties of CaO and CaO-SiO₂ materials synthesized by sol-gel with different acid catalysts, *J. Non-Cryst. Solids*, **2008**, *354*, 729-732.

- [264]. S. C. Goel, M. A. Matchett, M. Y. Chiang, W. E. Buhro, A very large calcium dialkoxide molecular aggregate having a CdI_2 core geometry: $\text{Ca}_9(\text{OCH}_2\text{CH}_2\text{OMe})_{18}(\text{HOCH}_2\text{CH}_2\text{OMe})_2$, *J. Am. Chem. Soc.*, **1991**, *113*, 1844-1845.
- [265]. Y. Fukuda, K. Tanabe, Infrared study of carbon dioxide adsorbed on magnesium and calcium oxides, *Bull. Chem. Soc. Jap.*, **1973**, *46*, 1616-1619.
- [266]. S.-P. Szu, L. C. Klein, M. Greenblatt, Effect of precursors on the structure of phosphosilicate gels: ^{29}Si and ^{31}P MAS-NMR study, *J. Non-Cryst. Solids*, **1992**, *143*, 21-30.
- [267]. C. Fernández-Lorenzo, L. Esquivias, P. Barboux, J. Maquet, F. Taulelle, Sol-gel synthesis of $\text{SiO}_2\text{-P}_2\text{O}_5$ glasses, *J. Non-Cryst. Solids*, **1994**, *176*, 189-199.
- [268]. C. Schrotter, A. Cardenas, M. Smahi, N. Hovnanian, Silicon and phosphorus alkoxide mixture: sol-gel study by spectroscopic techniques, *J. Sol-Gel Sci. Technol.*, **1995**, *4*, 195-204.
- [269]. J. Livage, P. Barboux, M.T. Vandenborre, C. Schmutz, F. Taulelle, Sol-gel synthesis of phosphates, *J. Non-Cryst. Solids*, 1992, 147-148, 18-23.
- [270]. W. P. Rothwell, J. S. Waugh, J. P. Yesinowski, High-resolution variable temperature ^{31}P NMR of solid calcium phosphates, *J. Am. Chem. Soc.*, **1980**, *102*, 2637-2643.
- [271]. A. K. Cheetham, N. J. Clayden, C. M. Dobson, R.J. B. Jakeman, Correlations between ^{31}P N.M.R. chemical shifts and structural parameters in crystalline inorganic phosphates, *J. Chem. Soc. Chem. Commun.*, **1986**, 195-197.
- [272]. A. P. Legrand, H. Sfihi, N. Lequeux, J. Lemaître, ^{31}P solid-state NMR study of the chemical setting process of a dual-paste injectable brushite cements, *J Biomed Mater Res Part B: Appl Biomater.*, **2009**, *91B*, 46-54.
- [273]. J. L. Miquel, L. Facchini, A.P. Legrand, C. Rey, J. Lemaître, Solid state NMR to study calcium phosphate ceramics, *Colloids Surf.*, **1990**, *45*, 421-433.
- [274]. I. L. Mudrakovskii, V. P. Shmachkova, N. S. Kotsarenko, V. M. Mastikhin, ^{31}P NMR study of I-IV group polycrystalline phosphates, *J. Phys. Chem. Solids*, **1986**, *47*, 335-339.
- [275]. R. J. B. Jakeman, A. K. Cheetham, N. J. Clayden, C. M. Dobson, A magic angle spinning NMR study of the phase diagram $\text{Ca}_{3-x}\text{Zn}_x(\text{PO}_4)_2$, *J. Solid State Chem.*, **1989**, *78*, 23-34.
- [276]. L. Obadia, P. Deniard, B. Alonso, T. Rouillon, S. Jobic, J. Guicheux, M. Julien, D. Massiot, B. Bujoli, J.-M. Boulter, Effect of sodium doping in β -tricalcium phosphate on its structure and properties, *Chem. Mater.*, **2006**, *18*, 1425-1433.
- [277]. W. P. Aue, A. H. Roufosse, M. J. Glimcher, R. G. Griffin, Solid-state phosphorus-31 nuclear magnetic resonance studies of synthetic solid phases of calcium phosphate: potential models of bone mineral, *Biochemistry*, **1984**, *23*, 6110-6114.
- [278]. M.-F. Hsieh, L.-H. Perng, T.-S. Chin, H.-G. Perng, Phase purity of sol-gel-derived hydroxyapatite ceramic, *Biomaterials*, **2001**, *22*, 2601-2607.
- [279]. L. Linati, G. Lusvardi, G. Malavasi, L. Menabue, M. C. Menziani, P. Mustarelli, A. Pedone, U. Segre, Medium-range order in phospho-silicate bioactive glasses: Insights from MAS-NMR spectra, chemical durability experiments and molecular dynamics simulations, *J. Non-Cryst. Solids*, **2008**, *354*, 84-89.

- [280]. D. S. Brauer, N. Karpukhina, R. V. Law, R. G. Hill, Structure of fluoride-containing bioactive glasses, *J. Mater. Chem.*, **2009**, *19*, 5629–5636.
- [281]. R. Dupree, D. Holland, M. G. Mortuza, The role of small amounts of P₂O₅ in the structure of alkali desilicate glasses, *Phys. Chem. Glasses*, **1988**, *29*, 18–21.
- [282]. M. W. G. Lockyer, D. Holland, R. Dupree, The structure of (5x)P₂O₅·(1–x)K₂O·4(1–x)SiO₂ glasses, *Phys. Chem. Glasses*, **1995**, *36*, 22–30.
- [283]. M. Cerruti, G. Magnacca, V. Bolis, C. Morterra Characterization of sol-gel bioglasses with the use of simple model systems: a surface-chemistry approach, *J. Mater. Chem.*, **2003**, *13*, 1279–1286.
- [284]. M. R. Hansen, H. J. Jakobsen, J. Skibsted, ²⁹Si chemical shift anisotropies in calcium silicates from high-field ²⁹Si MAS NMR spectroscopy, *Inorg. Chem.*, **2003**, *42*, 2368–2377.
- [285]. M. Templin, U. Wiesnev, H. W. Spiess, Multinuclear Solid-State-NMR Studies of Hybrid Organic-Inorganic Materials, *Adv. Mater.*, **1997**, *9* (10), 814–817.
- [286]. P. Innocenzi, A. Sassi, G. Brusatin, M. Guglielmi, D. Favretto, R. Bertani, A. Venzo, F. Babonneau, A novel synthesis of sol-gel hybrid materials by a nonhydrolytic/hydrolytic reaction of (3-glycidoxypropyl)trimethoxysilane with TiCl₄, *Chem. Mater.*, **2001**, *13*, 3635–3643.
- [287]. S. R. Davis, A. R. Brough, A. Atkinson, Formation of silica/epoxy hybrid network polymers, *J. Non-Cryst. Solids*, **2003**, *315*, 197–205.
- [288]. Katayama, N. Yamada, K. Kikuta, M. Awano, Synthesis and Photochromism of Organosiloxane-Based Organic/Inorganic Hybrid Containing an Inorganic Component Derived from Tungstic Acid, *J. Ceram. Soc. Jpn.*, **2006**, *114*(1), 114–119.
- [289]. M. R. Gizdavic-Nikolaidis, Z. D. Zujovic, N. R. Edmonds, C. J. Bolt, A. J. Eastal, Spectroscopic characterization of GPTMS/DETA and GPTMS/EDA hybrid polymers, *J. Non-Cryst. Solids*, **2007**, *353*, 1598–1605.
- [290]. P. Innocenzi, C. Figus, T. Kidchob, M. Valentini, Bruno Alonso, M. Takahashi, Sol-gel reactions of 3-glycidoxypropyltrimethoxysilane in a highly basic aqueous solution, *Dalton Trans.*, **2009**, 9146–9152.
- [291]. L. Ren, K. Tsuru, S. Hayakawa, A. Osaka, Sol-gel preparation and in vitro deposition of apatite on porous gelatin-siloxane hybrids, *J. Non-Cryst. Solids*, **2001**, *285*, 116–122.
- [292]. L. Ren, K. Tsuru, S. Hayakawa, A. Osaka, Incorporation of Ca²⁺ ions in gelatin-siloxane hybrids through a sol-gel process, *J. Ceram. Soc. Jpn.*, **2001**, *109* (5), 406–411.
- [293]. G. Arrachart, C. Carcel, J. J. E. Moreau, G. Hartmeyer, B. Alonso, D. Massiot, G. Creff, J.-L. Bantignies, P. Dieudonne, M. W. C. Man, G. Althoff, F. Babonneau, C. Bonhomme, Organosilicas based on purine–pyrimidine base pair assemblies: a solid state NMR point of view, *J. Mater. Chem.*, **2008**, *18*, 392–399.
- [294]. J. Brus, J. Dybal, Hydrogen-bond interactions in organically-modified polysiloxane networks studied by 1D and 2D CRAMPS and double-quantum ¹H MAS NMR, *Macromolecules*, **2002**, *35*, 10038–10047.
- [295]. P. Avenier, A. Lesage, M. Taoufik, A. Baudouin, A. De Mallmann, S. Fiddy, M. Vautier, L. Veyre, J.-M. Basset, L. Emsley, E. A. Quadrelli, Well-defined surface imido amido tantalum(v) species from ammonia and silica-supported tantalum hydrides, *J. Am. Chem. Soc.*, **2007**, *129*, 176–186.

- [296]. M. Kamihira, A. Naito, K. Nishimura, S. Tuzi, H. Saito, High-resolution solid-state ^{13}C and ^{15}N NMR study on crystalline Leu- and Met-enkephalins: Distinction of polymorphs, backbone dynamics, and local conformational rearrangements induced by dehydration or freezing of motions of bound solvent molecules, *J. Phys. Chem. B*, **1998**, *102*, 2826-2834.
- [297]. I. Ando, T. Kameda, N. Asakawa, S. Kuroki, H. Kurosu, Structure of peptides and polypeptides in the solid state as elucidated by NMR chemical shift, *J. Molec. Str.*, **1998**, *441*, 213-230.
- [298]. D. Huster, J. Schiller, K. Arnold, Comparison of collagen dynamics in articular cartilage and isolated fibrils by solid-state NMR spectroscopy, *Magn. Res. Med.*, **2002**, *48*, 624-632.
- [299]. A. Böckmanna, A. Lange, A. Galinier, S. Luca, N. Giraud, M. Juy, H. Heise, R. Montserret, F. Penina, M. Baldus, Solid state NMR sequential resonance assignments and conformational analysis of the 2×10.4 kDa dimeric form of the *Bacillus subtilis* protein Crh, *Journal of Biomolecular NMR*, **2003**, *27*, 323-339.
- [300]. D. Reichert, O. Pascui, E. R. deAzevedo, T. J. Bonagamba, K. Arnold, D. Huster, A solid-state NMR study of the fast and slow dynamics of collagen fibrils at varying hydration levels, *Magn. Reson. Chem.*, **2004**, *42*, 276-284.
- [301]. A. E. Aliev, Solid-State NMR Studies of Collagen-Based Parchments and Gelatin, *Biopolymers*, **2005**, *77*, 230-245.
- [302]. D. Hoebbel, M. Nacken, H. Schmidt, The Effect of nanoscaled metal oxide sols on the structure and properties of glycidoxypolytrimethoxysilane derived sols and gels, *J. Sol-Gel Sci. Techn.*, **2000**, *19*, 305-309.
- [303]. M. Borbely, Y. Nagasaki, J. Borbely, K. Fan, A. Bhogle, M. Sevoian, Biosynthesis and chemical modification of poly(γ -glutamic acid), *Polymer Bulletin*, **1994**, *32*, 127-132.
- [304]. K. Hikichi, H. Tanaka, A. Konno, Nuclear magnetic resonance study of poly(γ -glutamic acid)-Cu(II) and Mn(II) complexes, *Polymer Journal*, **1990**, *22(2)*, 103-109.
- [305]. Regis D. Gougeon, Marc Reinholdt, L. Delmotte, J. Mieke-Brendle, P. Jeandet, Solid-state NMR investigation on the interactions between a synthetic montmorillonite and two homopolypeptides, *Solid State NMR*, **2006**, *29*, 322-329.
- [306]. G.-H. Hoa, T.-I. Hoc, K.-H. Hsieh, Y.-C. Sud, P.-Y. Line, J. Yang, K.-H. Yanga, S.-C. Yanga, γ -Polyglutamic acid produced by *Bacillus subtilis* (natto): structural characteristics, chemical properties and biological functionalities, *J. Chn. Chem. Soc.*, **2006**, *53*, 1363-1384.
- [307]. Y. Kobayashi, K. Makino, Nuclear magnetic resonance studies of exchange reaction of α -hydrogen of glutamic acid catalyzed by aspartate aminotransferase, *Biochim. Biophys. Acta*, **1969**, *191*, 738-740.
- [308]. M. Bosetti, E. Verne, M. Ferraris, A. Ravaglioli, M. Cannas, In vitro characterisation of zirconia coated by bioactive glass, *Biomaterials*, **2001**, *22*, 987-994.
- [309]. A. Rosengren, S. Oscarsson, M. Mazzocchi, A. Krajewski, A. Ravaglioli, Protein adsorption onto two bioactive glass-ceramics, *Biomaterials*, **2003**, *24*, 147-155.
- [310]. J. Mei, R. M. Shelton, P. M. Marquis, Changes in the elemental composition of Bioglass during its surface development in the presence or absence of proteins, *J. Mater. Sci. Mater. Med.*, **1995**, *6*, 703-707.

- [311]. E. A. B. Effah Kaufmann, P. Ducheyne, S. Radin, D. A. Bonnell, R. Composto, Initial events at the bioactive glass surface in contact with protein-containing solutions, *J. Biomed. Mater. Res.*, **2000**, *52*, 825-830.
- [312]. R. A. Santos, R. A. Wind, C. Bronnimann, ^1H CRAMPS and ^1H - ^{31}P HetCor experiments on bone, bone mineral and model calcium phosphate phases, *J. Magn. Res. B*, **1994**, *105*, 183-187.
- [313]. H. Sfihi, C. Rey, 1-D and 2-D double heteronuclear magnetic resonance study of the local structure of type B carbonate fluoroapatite, *Magn. Res. Colloid Interf. Sci.*, **2002**, *76*, 409-422.
- [314]. Y. Wu, M. J. Glimcher, C. Rey, J. L. Ackerman, A unique protonated phosphate group in bone mineral not present in synthetic calcium phosphates. Identification by phosphorous-31 solid state NMR spectroscopy, *J. Mol. Biol.*, **1994**, *244*, 423-435.
- [315]. A. H. Roufousse, W. P. Aue, J. E. Roberts, M. J. Glimcher, R. G. Griffin, Investigation of the mineral phases of bone by solid state ^{31}P magic angle sample spinning nuclear magnetic resonance, *Biochemistry*, **1984**, *23*, 6115-6120.
- [316]. L. T. Kuhn, Y. Wu, C. Rey, L. C. Gerstenfeld, M. D. Grynpas, J. L. Ackerman, H.-M. Kim, M. J. Glimcher, Structure, composition, and maturation of newly deposited calcium-phosphate crystals in chicken osteoblast cell cultures, *J. Bone Miner. Res.*, **2000**, *15*(7), 1301-1309.
- [317]. Y. Wu, J. L. Ackerman, H.-M. Kim, C. Rey, A. Barroug, M. J. Glimcher, Nuclear magnetic resonance spin-spin relaxation of the crystals of bone, dental enamel, and synthetic hydroxyapatites, *J. Bone Miner. Res.*, **2002**, *17*(3), 472-480.
- [318]. G. Cho, Y. Wu, J. L. Ackerman, Detection of hydroxyl ions in bone mineral by Solid-State NMR spectroscopy, *Science*, **2003**, *300*, 1123-1127.
- [319]. Y. Wu, J. L. Ackerman, E. S. Strawich, C. Rey, H.-M. Kim, M. J. Glimcher, Phosphate ions in bone: identification of a calcium-organic phosphate complex by ^{31}P Solid-State NMR spectroscopy at early stages of mineralization, *Calcif. Tissue Int.*, **2003**, *72*, 610-626.
- [320]. A. Kafalak-Hachulska, A. Samoson, W. Kolodziejek, ^1H MAS and ^1H - ^{31}P CP/MAS NMR study of human bone mineral, *Calcif. Tissue Int.*, **2003**, *73*, 476-486.
- [321]. E. E. Wilson, A. Awonusi, M. D. Morris, D. H. Kohn, M. M. J. Tecklenburg, L. W. Beck, Three structural roles for water in bone observed by Solid-State NMR, *Biophys. J.*, **2006**, *90*, 3722-3731.
- [322]. S. Hayakawa, K. Tsuru, H. Iida, C. Ohtsuki, A. Osaka, MAS NMR Studies of Apatite Formation on 50CaO.50SiO₂ Glass in a Simulated Body Fluid, *Phys. Chem. Glasses*, **1996**, *37*(5), 188-192.
- [323]. S. Hayakawa, K. Tsuru, C. Ohtsuki, A. Osaka, Mechanism of Apatite Formation on a Sodium Silicate Glass in a Simulated Body Fluid, *J. Am. Ceram. Soc.*, **1999**, *82*(8), 2155-2160.
- [324]. E. Fuji, K. Kawabata, H. Yoshimatsu, S. Hayakawa, K. Tsuru, A. Osaka, Structure and biomineralisation of calcium silicate glasses containing fluoride ions, *J. Ceram. Soc. Jpn.*, **2003**, *111*(10), 762-766.
- [325]. H. Aguiar, E.L. Solla, J. Serra, P. González, B. León, F. Malz, C. Jäger, Raman and NMR study of bioactive Na₂O-MgO-CaO-P₂O₅-SiO₂ glasses, *J. Non-Cryst. Solids*, **2008**, *354*, 5004-5008.

- [326]. A. Angelopoulou, V. Montouillout, D. Massiot, G. Kordas, Study of the alkaline environment in mixed alkali compositions by multiple-quantum magic angle nuclear magnetic resonance (MQ-MAS NMR), *J. Non-Cryst. Solids*, **2008**, 354, 333-340.
- [327]. A. Angelopoulou, V. Montouillout, D. Massiot, G. Kordas, Study of alkaline metal ions and glass-formers in glasses with advanced NMR methods and quantum mechanic calculations, *J. Non-Cryst. Solids*, **2010**, 356, 187-200.
- [328]. I. Abrahams, K. Franks, G. E. Hawkes, G. Philippou, J. Knowles, P. Bodart, T. Nunes, ^{23}Na , ^{27}Al and ^{31}P NMR and X-ray powder diffraction study of Na/Ca/Al phosphate glasses and ceramics, *J. Mater. Chem.*, **1997**, 7(8), 1573-1580.
- [329]. L. A. O'Dell, E. A. Abou Neel, J. C. Knowles, M. E. Smith, Identification of phases in partially crystallised Ti-, Sr- and Zn-containing sodium calcium phosphates by two-dimensional NMR, *Mater. Chem. Phys.*, **2009**, 114, 1008-1015.
- [330]. D. Alfano, A. R. Alburnia, O. Motta, A. Proto, Detection of diagenetic alterations by spectroscopic analysis on archaeological bones from the Necropolis of Poseidonia (Paestum): a case study, *J. Cult. Heritage*, **2009**, 10, 509-513.
- [331]. A. R. Jones, R. Winter, G. N. Greaves, I. H. Smith, ^{23}Na , ^{29}Si , and ^{13}C MAS NMR Investigation of Glass-Forming Reactions between Na_2CO_3 and SiO_2 , *J. Phys. Chem. B*, **2005**, 109, 23154-23161.
- [332]. M. W. G. Lockyer, D. Holland, R. Dupree, NMR investigation of the structure of some bioactive and related glasses, *J. Non-Cryst. Solids*, **1995**, 188, 207-219.
- [333]. I. Elyagar, A. E. Aliev, A. R. Boccaccini, R.G. Hill, Structural analysis of bioactive glasses, *J. Non-Cryst. Solids*, **2005**, 351, 173-183.
- [334]. V. FitzGerald, D. M. Pickup, D. Greenspan, G. Sarkar, J. J. Fitzgerald, K. M. Wetherall, R. M. Moss, J. J. Jones, R. J. Newport, A neutron and X-Ray diffraction study of Bioglass[®] with reverse Monte Carlo modeling, *Adv. Funct. Mater.*, **2007**, 17, 3746-3753.
- [335]. G. L. Turner, K. A. Smith, R. J. Kirkpatrick, E. Oldfield, Structure and cation effects on phosphorus-31 NMR chemical shifts and chemical-shift anisotropies of orthophosphates, *J. Magn. Reson.*, **1986**, 70, 408-415.
- [336]. J. Tropp, N. C. Blumenthal, J. S. Waugh, Phosphorus NMR study of solid amorphous calcium phosphate, *J. Am. Chem. Soc.*, **1983**, 105(1), 22-26.
- [337]. W. -H. Yang, R. J. Kirkpatrick, G. Turner, ^{31}P and ^{29}Si Magic-angle sample-spinning NMR investigation of the structural environment of phosphorus in alkaline-earth silicate glasses, *J. Am. Ceram. Soc.*, **1986**, 69(10), C-222-C-223.
- [338]. I. Izquierdo-Barba, A. J. Salinas, M. Vallet-Regí, *In vitro* calcium phosphate layer formation on sol-gel glasses of the CaO-SiO₂ system, *J. Biomed. Mater. Res.*, **1999**, 47, 243-250.
- [339]. J. B. Murdoch, J. F. Stebbins, I. S. E. Carmichael, High-resolution ^{29}Si NMR study of silicate and aluminosilicate glasses: the effect of network-modifying cations, *Am. Mineral.*, **1985**, 70, 332-343.
- [340]. A. M. George, J. F. Stebbins, Dynamics of Na in sodium aluminosilicate glasses and liquids, *Phys. Chem Minerals*, **1996**, 23, 526-534.
- [341]. Y. Kim, R. J. Kirkpatrick, High-temperature multi-nuclear NMR investigation of analcime, *Am. Mineral.*, **1998**, 83, 339-347.

- [342]. X. Xue, J. F. Stebbins, ^{23}Na NMR chemical shifts and local Na coordination environments in silicate crystals, melts and glasses, *Phys. Chem. Minerals*, **1993**, *20*, 297-307.
- [343]. R. Tabeta, H. Saitô, ^{23}Na chemical shifts of some inorganic and organic compounds in the solid state as determined by the magic angle spinning and high power NMR methods, *Chem. Lett.*, **1984**, 293-296.
- [344]. R. Tabeta, M. Aida, H. Saitô, A high-resolution solid-state ^{23}Na NMR study of sodium complexes with solvents, small ligand molecules, and ionophores. ^{23}Na chemical shifts as means for identification and characterization of ion-ion, ion-solvent, and ion-ligand interactions, *Bull. Chem. Soc. Jpn.*, **1986**, *59*, 1957-1966.
- [345]. H. Maekawa, T. Nakao, S. Shimokawa, T. Yokokawa, Coordination of sodium ions in $\text{NaAlO}_2\text{-SiO}_2$ melts: a high temperature ^{23}Na NMR study, *Phys. Chem. Minerals*, **1997**, *24*, 53-65.
- [346]. S. C. Kohn, M. E. Smith, P. J. Dirken, E. R. H. van Eck, A. P. M. Kentgens, R. Dupree, Sodium environments in dry and hydrous albite glasses: improved ^{23}Na solid state NMR data and their implications for water dissolution mechanisms, *Geoch. Cosm. Acta*, **1998**, *62(1)*, 79-87.
- [347]. C. Jäger, K. Heide, Temperature dependence of the ^{23}Na -central lineshape in Na_2CO_3 studied by nuclear magnetic resonance, *J. Phys. C: Solid State Phys.*, **1983**, *16*, L159-L163.
- [348]. M. R. Rowles, J. V. Hanna, K. J. Pike, M. E. Smith, B. H. O'Connor, ^{29}Si , ^{27}Al , ^1H and ^{23}Na MAS NMR study of the bonding character in aluminosilicate inorganic polymers, *Appl. Magn. Reson.*, **2007**, *32*, 663-689.